Chemical wear of carbon-based refractory material by silicomanganese

MSc DISSERTATION

Prepared by

Wesley Kondwani Banda

385660

Submitted to

School of Chemical and Metallurgical Engineering, Faculty of Engineering and the Built Environment, University of the Witwatersrand, Johannesburg, South Africa

Supervisor: Dr. Elias Matinde (Wits)

Co-Supervisor: Dr. Joalet D Steenkamp (Mintek)

October, 2019

Declaration

I declare that this dissertation is my own work. It is being submitted for a Masters of Science at the University of the Witwatersrand, Johannesburg. It has not been submitted before for any other degree or examination at any other university

_____

Signature

_____Day of_____ 20 _____in_____

Abstract

Chemical wear of two carbon-based refractories by SiMn (Silicomanganese) was investigated. Thermodynamic calculations were conducted in FactSage™ 7.2 (FeMn and FactPS database) when temperature was varied at 1550°C, 1600°C and 1650°C for the type K and type SiC refractory. Temperature test work at constant Si mass % were then conducted at static and dynamic conditions. Furthermore, carbon solubility in Mn-Fe-Si-C alloys with Mn:Fe mass ratio of 4.4 at 1550°C, 1600°C and 1650°C was calculated with FactSage 7.2 (FSstel, FeMn and FactPS database). The results from the FactSage calculation and actual test work were in agreement and it was found that the type SiC refractory experienced the most wear. The SEM analyses indicated that SiMn infiltrated both refractories, with the type SiC experiencing infiltration the most due to its porous nature. At 15 mass % Si the alloy was not saturated in SiC resulting in the carbon (type K) refractory experiencing the most wear.

Thermodynamic calculations when Si mass % was varied at 15 mass %, 17 mass % and 18 mass % for the type K and type SiC refractory predicted that the type K refractory would wear out the most. Experimentally it was found that the type K refractory wore out the most and this was due to the solubility of C in the alloy decreasing which allowed more of the type K refractory to dissolve into the alloy. Increasing the Si mass % above 17 resulted in a SiC saturated alloy. The SEM analyses indicated that SiC was precipitated from the alloy and the SiC phases were visible on the type K refractory surface. Infiltration of the alloy into the refractories by capillary action still reached greater depths in the type SiC refractory.

Dynamic motion introduced erosion wear on the refractory surfaces, the impact was insignificant. Main wear mechanism was found to be chemical wear. Finally the type K was found to be the most suited refractory material to use in the hearth area of an industrial furnace as long as the Si mass % in the alloy is maintained below 17 for Mn-Fe-Si-C alloys with Mn:Fe mass ratio of 4.4.

KEYWORDS: carbon solubility, SiC solubility, FactSage™, rotating finger test, ramming paste, refractory test.

Acknowledgements

The MSc journey has been full of blessings. Different people have contributed to the journey directly and indirectly, and I would like to thank my family, friends and colleagues from Mintek for their support. I know that I can do all things through Christ who strengthens me (Philippians 4:13).

I would like to thank Mintek for funding the research study. I would like to thank Transalloys (PTY) Ltd., Elkem Carbon, Norwegian University of Science and Technology and the SAIMM for their support.

I would like to thank Dr Joalet Steenkamp for believing in me and bringing out the best in me even when I have self-doubts. I would like to thank her for being a great supervisor both at work and in my studies. I would like to thank Dr Elias Matinde for his amazing contributions that have made me a better researcher compared to when I had started this journey.

In Emile Coue's words, I believe that every day in every way I am getting better and better.

TABLE OF CONTENTS

LIST OF FIGURES

LIST OF TABLES

CHAPTER 1: BACKGROUND

1.1. Introduction

The study of chemical wear of two carbon-based refractories namely carbon block and carbon ramming paste, in a silicomanganese (SiMn) furnace tap-hole was under taken by Dr. Steenkamp as part of her PhD studies (Steenkamp, 2014). The complex reactions between slag and carbon-based refractories were studied in order to obtain an improved understanding of the potential of chemical wear of the refractory when tapping SiMn slag. Steenkamp, (2014) found that corrosion was the main wear mechanism, where it was experimentally determined that silicon carbide (SiC), and an alloy containing Si and Mn formed as reaction products between the slag and refractory thereby contributing to the chemical wear of the carbon-based refractory. Subsequent thermodynamic calculations on tapped alloy compositions from industrial furnace using tap data collected over three months indicated the potential for SiMn alloy and refractory interaction being a further source of wear, not only of the tap-hole refractory but also of the hearth refractory, (Figure 1.1), (Steenkamp and Pistorius, 2015).

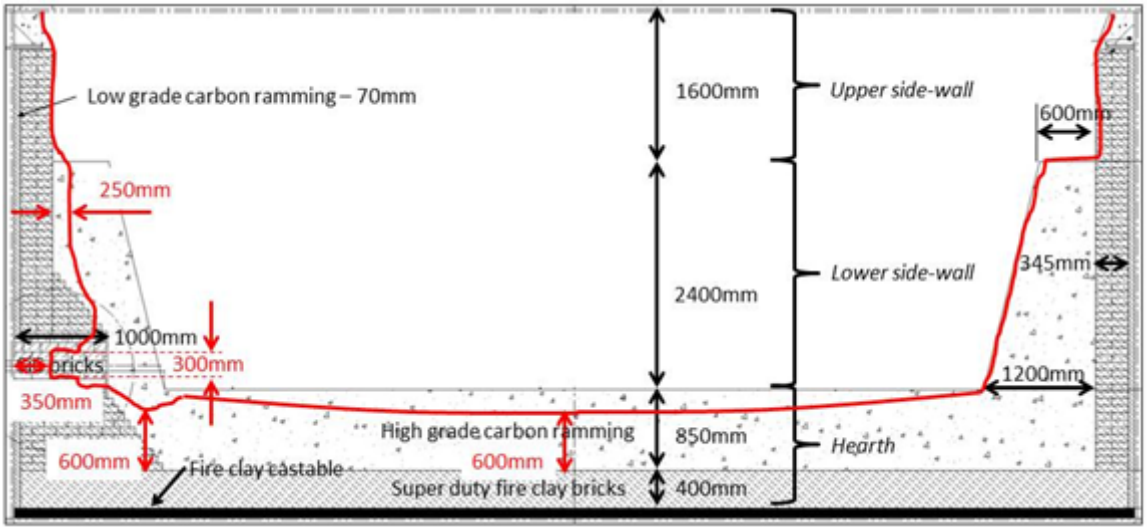

Figure 1.1: Refractory wear profile (red line) of a 48 MVA submerged arc furnace (SAF), used for SiMn production, excavated in 2013 in South Africa superimposed onto the refractory design drawing (black drawing).

Based on these findings, a further investigation of the wear mechanisms of carbon-based refractory by SiMn alloy on laboratory-scale was then required. The objective of the study was to investigate the main wear mechanism of the refractory used in the hearth area of a SiMn

producing furnace, including the differences in the extent of wear between two types of prebaked ramming paste samples using the rotating finger experimental setup. The experiments simulated wear in the hearth and tap-hole of SAFs used in producing SiMn. The study focused on developing and testing a method to allow the measurement of erosion (mechanical) and corrosion wear of the carbon based refractory at different temperatures and alloy composition under inert furnace atmospheric conditions.

1.2. Significance

The wear of the carbon-based refractory by SiMn alloy has not been studied in depth. Most work was done having focussed on iron interactions with the refractories in blast furnaces (Shigeno, Tokuda and Ohtani, 1985; Sun *et al.*, 1998; Dzermejko, Baret and Hubble, 1999). Because the hearth is the most critical part of the furnace, it is important to develop knowledge of the different wear mechanisms taking place in the hearth in relation to principal parameters such as temperature and alloy chemistry. Therefore, this research will provide a good insight into the interactions between the SiMn alloy and the refractory. In the ferroalloys industry, refractory wear is usually estimated on the previous mass balance data collected after a furnace dig-out (Steenkamp and Pistorius 2015). The study allowed the production of accurate refractory wear data to support thermodynamic calculations and observations on industrial scale furnaces, thereby enabling maximum and efficient use of the refractory, improving furnace lining life, as well as potentially preventing furnace burn-throughs.

The study is of interest to the SiMn production industries where refractories are critical to the operation of their furnaces. Refractory failure results in operational downtime, repairs and loss in revenue. It thus serves the SiMn producers best interest to minimize the costs associated with refractory failure. Developing knowledge of different wear mechanisms assists the producers to minimize the main wear mechanisms as well as choose suitable refractory.

1.3. Research objectives

The overall objective of the study was to investigate the wear mechanism of the carbon-based refractory by SiMn alloy. In detail, the study entails the:

1) Development of a rotating finger experimental set-up that will allow the study of the carbon-based hearth refractory wear by SiMn alloy.

2) Characterisation of the refractory and alloy before reaction and post-mortem studies on reacted refractory, based on techniques developed by Steenkamp (Steenkamp, 2014), and other relevant methods to quantify the extent of wear.
3) Comparison of the thermodynamic calculations conducted in FactSage™ to experimental results.
4) Comparison of the extent in wear between the K-type and SiC-type carbon based refractories.

The research topics to address the objectives are as follows:

1. Refractory wear under different laboratory conditions
2. Refractory suitability for use in the hearth area of an industrial furnace producing SiMn
3. Wear mechanism in the type K and type SiC refractory

1.4. Structure of the dissertation

To address the identified research topics, the following aspects have been researched, and form the structure of this thesis:

1. Chapter 1 contains the introduction to the study, providing the definition and background.
2. Chapter 2 contains the literature review of the production of manganese alloys in SAFs, refractories, and wear mechanisms.
3. Chapter 3 contains the methodology and experimental design.
4. Chapter 4 contains the experimental results and they are broken into 3 sections, namely:
    a. Thermodynamics of the interaction of SiMn with the two refractories, type K and type SiC, was modelled. Results for varying temperature and Si-content are provided in the tables.
    b. Static wear tests in which the temperature was varied to study the potential for SiMn alloy to react with K-type and SiC-type refractory was done, for the temperatures 1550°C, 1600°C and 1650°C. The microscopic and mechanical wear results are provided in the form of images and graphs respectively.
    c. Dynamic wear tests, in which the temperature and Si-content of the alloy were varied, was conducted to study the potential for SiMn alloy to interact with the K-type and SiC-type based refractory. Temperatures 1550°C, 1600°C, and 1650°C and Si-content 15, 17, and 18 mass %, were used. The microscopic and

mechanical wear results are provided in the form of images and graphs respectively.

5. Chapter 5 contains the discussions of the key findings.
6. Chapter 6 contains the conclusion, summary of the research topics and recommendation.

CHAPTER 2: LITERATURE REVIEW

2.1. Introduction

Manganese (Mn) and silicon (Si) are crucial constituents in steelmaking as deoxidants, desulfurizers, and alloying elements. Mn alloys have two classes called ferromanganese (FeMn) and SiMn. Si is the primary deoxidizer and Mn is a milder deoxidizer, where the Mn enhances the steel effectiveness due to the formation of stable Mn silicates and aluminates. Mn serves as a desulfurizer and is used as an alloying element in almost all types of steel (Olsen and Tangstad, 2004).

In South Africa, Transalloys is the only SiMn alloy producer as Mogale alloys converted two of its SAFs for the production of FeCr (Steenkamp *et al.*, 2018; Sithole *et al*., 2018). Production of SiMn is achieved in a submerged arc furnace (SAF) of circular design. SAF (see Figure 2.1) has three Söderberg electrodes positioned in a triangular configuration and immersed inside the solid raw material, with its tip immersed in the slag. The electric current is supplied into the furnace by the three electrodes. The electrodes receive power from a single three-phase transformer or three single phase transformers (Steenkamp *et al.*, 2018). The furnace sidewall consist of a steel shell and refractory lining. Carbon based lining is normally used in the hearth (alloy zone) and sidewall areas, with aluminosilicate bricks used to form an insulating lining between the furnace shell and carbon based lining. In the slag zone, graphite tiles, carbon based lining and aluminosilicate bricks are typically installed (Gasik, 2013).

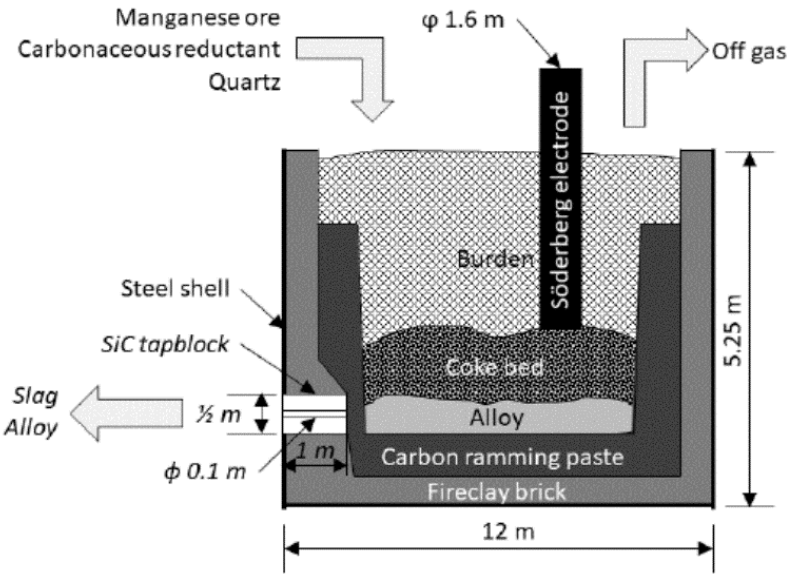

Figure 2.1: Schematic diagram of the SAF producing SiMn (Steenkamp, 2018)

At Transalloys a blend of manganese ores, briquettes, quartz, coal, coke, and recycled material are used as feed material, with the recipe based on mass and energy balance calculations as well as the material costs (Steenkamp *et al.*, 2018). The chemical composition of SiMn produced at Transalloys is typical of ASTM grade C, see Table 2.1, (ASTM A483, 2010; Steenkamp *et al.*, 2018) and the slag product is discarded to the slag dumps as it does not allow for any further recovery of SiMn economically.

Table 2.1: ASTM specification for SiMn alloy (ASTM A483, 2010).

Element	**Grade A**	**Grade B**	**Grade C**
Mn	65-68	65-68	65-68
Si	18.5-21	16-18.5	12.5-16
C, max	1.5	2	3
S, max	0.04	0.04	0.04
P, max	0.2	0.2	0.2

2.2. Refractories

The word ‘refractory’ is defined as ‘resistant to change’, and in the metallurgical industry the refractories are resistant to physical and chemical changes at high elevated temperatures (Mcewan *et al.*, 2011). Refractories are usually non-metallic materials that maintain sufficient physical and chemical stability, to be used for structural purposes in high temperature environments encountered in most process industries (Ewais, 2004). These materials can be exposed to high temperatures above 500ºC and still maintain their strength. Refractory furnace lining serve to reduce the furnace operational costs by reducing the energy losses in a furnace since the process energy, which is the sum of energy required by the process and the energy losses to the environment, is directly linked to operational costs (Steenkamp, 2014). The refractories also serve to protect the furnace shell from high temperatures, which may cause thermo-chemical and/or thermo-mechanical failure (Chesters, 1963; Hancock, 2006). Environmental factors such as mechanical stresses, erosion, and corrosion by hot gases and molten material, may influence the service life of the refractory material (Ewais, 2004).

The first use of refractory could be traced to the period during the transition to the Bronze Age from the Stone Age. The early smelting installations were simple bowl-shaped hearths in pits with above ground stone enclosures. In the Iron Age, around 2000 BC higher temperatures

were required and this resulted in further investigations of refractory that would be suitable for use at elevated temperatures (Mcewan *et al.*, 2011).

Modern refractory technology began in the late 18th century with the growth of the iron industry, then steel industry during the Industrial Revolution. Magnesite and chrome bricks were introduced in the late 1880s, as there was a greater demand for different refractory other than alumina-silicates and silica. Chrome-magnesite bricks were introduced for use in open hearths and steelmaking furnaces after superior hot strength blends of chromite and magnesia were discovered in 1931 (Mcewan *et al.*, 2011).

Some of the principal refractory consuming manufacturing processes include the iron and steelmaking, non-ferrous metal production, cement production, glass, and petrochemical production (Mcewan *et al.*, 2011).

Refractories are classified primarily on the basis of their chemical composition and the forms in which they are used (Routschka, 2008). Refractories are manufactured from compounds that involve the oxides of silicon (Si), aluminium (Al), magnesium (Mg), calcium (Ca), chromium (Cr), and zirconium (Zr) (Ewais, 2004). Refractories are also classified according to their forms, they can either be shaped refractories, which are essentially bricks, or unshaped refractories, also called monolithics (Mcewan *et al.*, 2011).

2.3. Carbon refractories

Carbon-based refractories are classified into two groups, namely carbon bricks or blocks, and carbon-containing monolithic materials. Carbon-based refractories have superior properties relative to other refractories, namely high thermal conductivity, low thermal expansion, high resistance to thermal shock, and chemical inertness to process slag (Ewais 2004; Tomala and Basista 2007).

The raw materials for carbon and graphite refractories include naturally occurring graphite, coal, petroleum coke, coal tar pitch, artificial graphite, coke, gas-calcined anthracite, and electrically calcined anthracite (Ewais, 2004). Binding material include tar-pitches, petroleum pitches, and other organic materials (Ewais, 2004). The mixtures are baked in conventional furnaces at temperatures around 800℃ to 1400℃ to carbonize the binder, with the resulting product containing carbon aggregate particles and carbon binder material (Dzermejko, Baret and Hubble, 1999). The manufacturing process determines the final properties of the refractory material. Porosity in the carbon refractory results from volatile liquids escaping the refractory

material as it is baked, and thus creating cracks and pores that allow for infiltration of process material (Dzermejko, Baret and Hubble, 1999).

Various carbon-based refractories are used in industrial furnaces, namely: different grades of amorphous and hot pressed carbon, conventionally baked and hot-pressed semi-graphite, semi-graphitized carbon, and fully graphitized materials (Dzermejko, Baret and Hubble, 1999). Table 2.2 and 2.3 show the chemical analysis and physical properties of three grades of carbon refractories, respectively. The standard grade is based on dense metallurgical coke and similar products derived from calcined anthracite, while the high conductive grade is based on electro-graphite and calcined anthracite. The petroleum coke grade is based on fully graphitized petroleum coke (Hancock, 2006).

Table 2.2: Chemical analysis based on three grades of carbon refractories (Hancock, 2006).

Product	**fixed carbon**	**ash content**
Standard grade	92	7.5
High conductive grade	90	10
Petroleum coke	98	1

Table 2.3: Physical properties based on three grades of carbon refractories (Hancock, 2006).

Product	**Bulk density g/cm^3**	**apparent porosity %**
Standard grade	1.5	20
High conductive grade	1.6	18
Petroleum coke	1.59	20

Hot-pressing is a unique, proprietary method of manufacturing carbon (Dzermejko, Baret and Hubble, 1999). Relative to the conventional method that takes weeks, hot-pressing may take minutes to bake out binders. It is claimed that 100 times less impermeable carbon is achieved, with relatively higher thermal conductivity, through hot pressing compared to the conventionally baked carbon (Dzermejko, Baret and Hubble, 1999). Micro-pore carbon

refractory has pore diameters of less than 1 micron, thus increasing the resistance to infiltration of the molten material (Tomala and Basista 2007). Improvements in the permeability, as well as pore size reduction in carbonaceous materials, can be achieved by addition of graphite particles, alumina, silicon carbide, or other ceramics (Dzermejko *et al*. 1999; Tomala and Basista 2007). Carbon-based refractories have superior thermal properties, high strength and low wettability towards process materials, which makes them suitable for use in the SiMn refractory lining in the shell, hearth and tap-hole areas (Mølnås, 2011).

2.4. Silicon carbide refractories

Silicon carbide refractories is prepared using petroleum coke, pure silica sand, saw dust, and minor amounts of common salt (Chesters, 1963). The raw materials are electrically heated to a temperature of about 2500°C. Plastic fireclay is added to a dry, graded, and mixed batch of silicon carbide, and isostatic pressing, tamping, or dry pressing is used to shape the batch. The shaped products are then fired at a temperature of at least 1300°C (Chesters, 1963).

Special properties of silicon carbide refractories include high thermal conductivity, thermal shock resistance, high abrasion resistance to various gases, acids, slags and molten metal melts, and high strength up to high temperatures (Chesters, 1963; Hancock, 2006). The disadvantage of the silicon carbide refractory is its tendency to react with oxygen and steam, specifically in the temperature range between 1000 and 1200°C (Hancock, 2006; Routschka, 2008). Silicon dioxide starts forming and coating on the silicon carbide grains at temperatures above 1200°C, which causes expansion in volume of the refractory, and retards the oxidation rate of the silicon carbide refractory (Routschka, 2008).

Silicon carbide exists in two crystalline forms, that is, β and α-silicon carbide (Chesters, 1963; Routschka, 2008). β-silicon carbide has a cubical structure while α-silicon carbide has a hexagonal structure, with the fore-mentioned existing at low temperature modification, and the latter existing after high temperature modifications between 2100 to 2400°C. Silicon carbide dissociates at 2185°C (Hubble, 1999), any further heating above these temperatures results in complete dissociation to silicon and carbon, without passing through a liquid phase (Chesters, 1963). Table 2.4, 2.5 and 2.6 show the β and α-silicon carbide specification data, namely the chemical and phase chemical compositions, and the physical properties as reported by Routschka (2008).

Table 2.4: The chemical compositions of the β-silicon carbide and α-silicon carbide refractories in mass % (Routschka, 2008).

Chemistry	**β-silicon carbide**	**α-silicon carbide**
SiC	90–95	99–100
SiO_2	0–3	0–1
Al_2O_3	0	0–0.1
Fe_2O_3	0–0.5	0–0.1
K_2O	0	0
Na_2O	0	0
CaO	0–0.5	0
Silicon metal	0–0.8	0
Other	0–5	0–0.2

Table 2.5: The phase chemical compositions of the β-silicon carbide and α-silicon carbide refractories in mass % (Routschka, 2008).

Mineralogy	**β-silicon carbide**	**α-silicon carbide**
Silicon carbide SiC	70-80	99-100
Silicon nitride α+β Si_3N_4	5-15	0
silicon oxynitride Si_2ON_2	10-20	0

Sialon	10-20	0
Tridymite	0	0-1
Mullite	0	0
Corundum	0-5	0
Glassy phase, amorphous phase	0-8	0

Table 2.6: The physical properties of the β-silicon carbide and α-silicon carbide refractories (Routschka, 2008).

Physical properties	**β-silicon carbide**	**α-silicon carbide**
Bulk density g/cm^3	2.5-2.7	2.5-2.7
Apparent porosity %	14-20	14-18
Specific surface m^2/g	0.5-1	0-0.1

2.5. Potential refractory wear mechanism

Attack on refractories on a commercial furnace is a complex phenomenon involving not only corrosion wear mechanism but also erosion (Lee and Zhang, 2004). Refractory wear mechanisms in SAF producing manganese ferroalloys in addition may include densification and spalling. Densification is caused by slag or alloy infiltrating pores and/or reacting with the refractory. Spalling is caused by thermal stresses due to thermal gradients across a single refractory body, resulting in the refractory on the hot face fracturing and breaking away due to densification and/or thermal stress. Corrosion occurs when the system is not at equilibrium, where the slag, alloy or a flux reacts (chemical reaction) and/or dissolves (dissolution) the refractory components, in which they are unsaturated (Steenkamp, 2014).

Mølnås, (2011) described erosion as physical wear of refractories as a result of turbulent gas or liquid flow. The wear associated with erosion is related to abrasion, which can be defined as physical wear caused by solids.

In the hearth, refractory integrity depends on uninterrupted cooling. The hearth is normally cooled from the cold face of the refractory and in cases where conductive refractory lining is used, the hearth refractory performance relies on uninterrupted and effective heat transfer through the refractory configuration. Above the critical reaction temperature of the carbonaceous refractory, molten alloy infiltrates the refractory resulting in erosion and wear. During chemical attack, the binder and aggregate are attacked, thus the material strength and properties are compromised (Dzermejko, Baret and Hubble, 1999).

2.6. Chemical (Corrosion) wear mechanism

Researchers define chemical/corrosion wear differently. To illustrate this, Brosnan, (2004) defined corrosion of refractories as refractory wear by loss of thickness and mass from the exposed face of the refractory as a consequence of chemical attack by a corroding fluid in a process in which the refractory and corroding fluid react, approaching chemical equilibrium in the zone of contact between the refractory and the fluid.

Jansson *et al.*, (2004) defined corrosion as any type of interaction between a solid phase and a fluid phase that results in a deleterious effect to either of the phases. Corrosion was described by Jansson *et al*., (2004) consisting of three major categories namely: dissolution, which is a chemical process by which the refractory material is continuously dissolved; penetration or infiltration, by which the slag penetrates into the refractory and causes mechanical effects; and erosion, which is the abrasion process of the refractory material exposed to gas and slag movement.

In a study on corrosion mechanisms between refractory materials and slag, Jansson *et al.*, (2004) observed that the corrosion mechanism started off with dissolution of the refractory materials into the slag, followed by infiltration of the pores and grain boundaries and dispersion of the grains into the slag.

Lee *et al.,* (2002) stated that corrosion wear mechanism on refractory material by slags/alloy involves liquid infiltration and dissolution. The dissolution may be direct or indirect, the latter involving generation of one or more, usually solid, reaction products at the aggregate/slag interface.

Lee *et al.,* (2002) states that chemical wear occurs when many reactions contribute to corrosion, where some of these reactions are heterogeneous, and occur between different phases. In the case of a liquid phase, the corrosion is controlled by direct dissolution of the refractory with or without precipitation, redox reactions, or by complex reactions leading to the formation of a new product. In some cases the new products form a protective layer on the refractory material, protecting it from further wear and wear rate is expected to decrease.

The oxidation and reduction state of the environment can participate in and influence the chemical reactions that take place (Brosnan, 2004). Thus the driving force behind corrosion wear is the chemical potential differences of the components between the refractories and slag and/or alloy (Mattila *et al.,* 2000). The corrosion reactions proceed in a direction towards localized chemical equilibrium. Thus phase equilibrium diagrams or thermodynamic calculation software can be used to analyse corrosion situations and to predict chemical strategies to minimize corrosion and wear rates (Brosnan, 2004).

For the purpose of the study, I will define chemical wear (equation 2.1) as the chemical process between the refractory and a non-saturated alloy which results in the dissolution of the unsaturated component from the refractory (solid phase) into the alloy (liquid phase) and/or precipitation of the saturated components from the alloy (liquid phase) into the refractory (solid phase). Erosion will be defined as the physical wear of the refractory by moving liquid alloy and abrasion will be defined as physical wear of the refractory surface by solids.

$$A_{refractory} \leftrightarrow A_{alloy} \tag{2.1}$$

In Figure 2.2 it can be seen that during corrosion wear mechanism the products formed from chemical reaction may remain attached to the refractory, Figure 2.2(a); be fugitive and move into liquid phase, Figure 2.2(b); or be a combination of the two, Figure 2.2(c) (Lee and Zhang, 2004).

In the study of direct and indirect slag corrosion of oxide and oxide-C refractories by Lee and Zhang, (2004), it was identified that the oxide-C refractory wear mechanism followed 3 stages, where in Figure 2.3(a), there was a formation of a decarburised layer due to oxidation of graphite mainly by iron oxide (FeO) or oxygen in the furnace; in Figure 2.3(b), there was infiltration of the slag into the decarburised layer. Erosion of the oxide grain, followed by slag infiltration aided by high temperature softening of any intragranular silicate bonds, reaction and dissolution of the oxide grain into the slag and molten steel; in Figure 2.3(c), there was

reduction of the oxide grain by high temperature reaction with C, resulting in its exposure and further erosion.

In a study of corrosion on refractories by Brosnan, (2004), 3 stages in which corrosion wear mechanism followed were also identified. In stage 1 of the corrosion wear mechanism on the refractory material, Figure 2.4, the reaction starts off on the refractory surface, and there is little or no slag infiltration, most importantly the infiltration is confined to a depth of less than 100 microns. In stage 2 of the corrosion wear mechanism, Figure 2.4, there is a broad temperature gradient, which cause the slag to penetrate the refractory material. Infiltration is aided by capillary suction as the smallest pores in the refractory draw the liquid slag behind the hot face. In stage 2 there is full infiltration of the refractory material, at depths greater than 100 microns and extensive disruption by corrosion on the refractory surface (Brosnan, 2004). The refractory aggregate particles get penetrated by the slag and the bonding between the aggregates and binder matrix is disrupted, but the bonding still exists. In stage 3, In Figure 2.5, the bonding in the refractory material between the aggregate and binder matrix is minimal. The aggregate particles have been dissolved, leaving behind relics, and The slag itself "appears" to be the only phase holding the residual aggregate particles in place (Brosnan, 2004). In this study the extent of wear in a refractory sample will be identified further using these stages, with stage 1 being minor and 3 being major refractory wear.

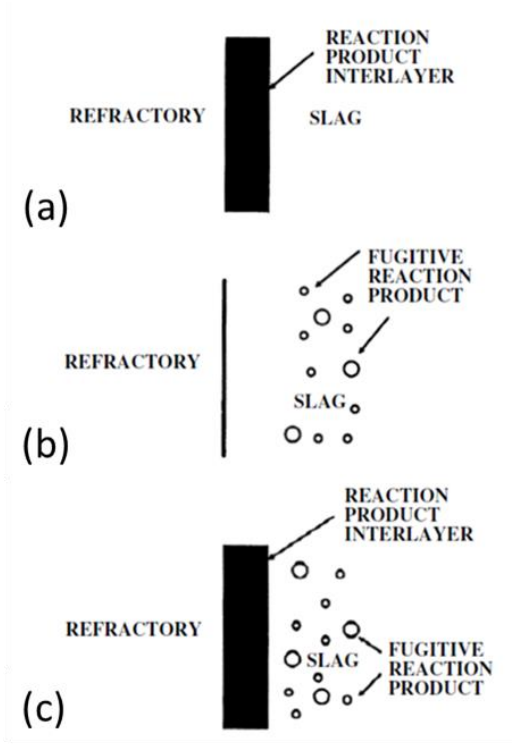

Figure 2.2: Reaction products, (a) attached to the refractory, (b) be fugitive and move into liquid phase, (c) be a combination of the two (Lee and Zhang, 2004)

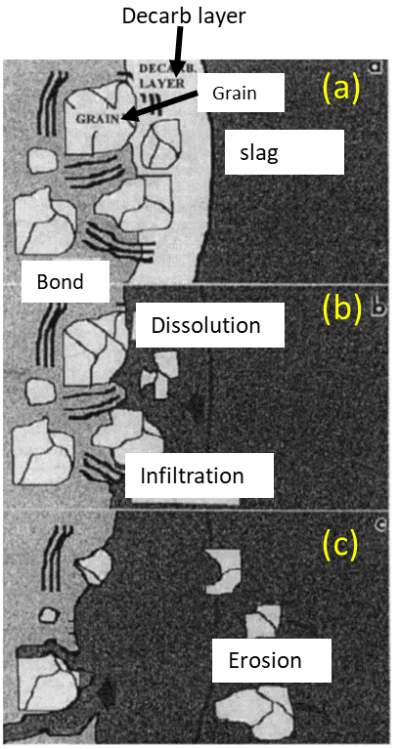

Figure 2.3: Schematic of general mechanism of corrosion of oxide-C refractories(Lee and Zhang, 2004)

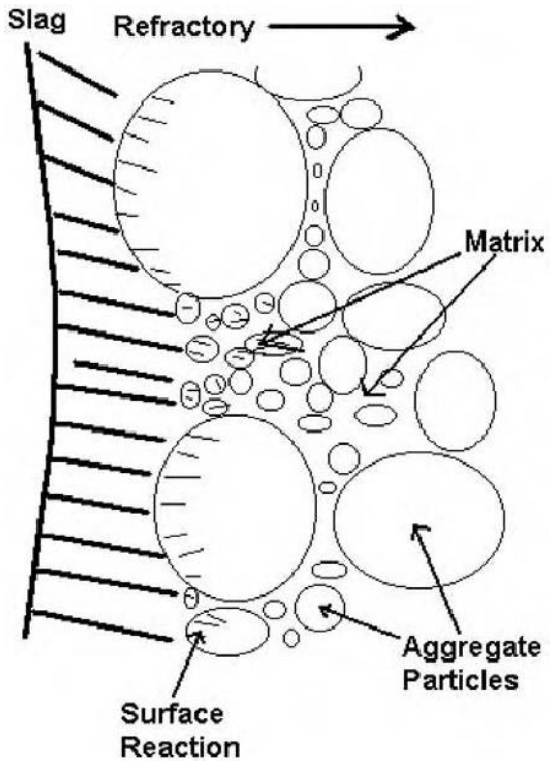

Figure 2.4: Stage 1 of corrosion wear mechanism, showing a bonded refractory (Brosnan, 2004)

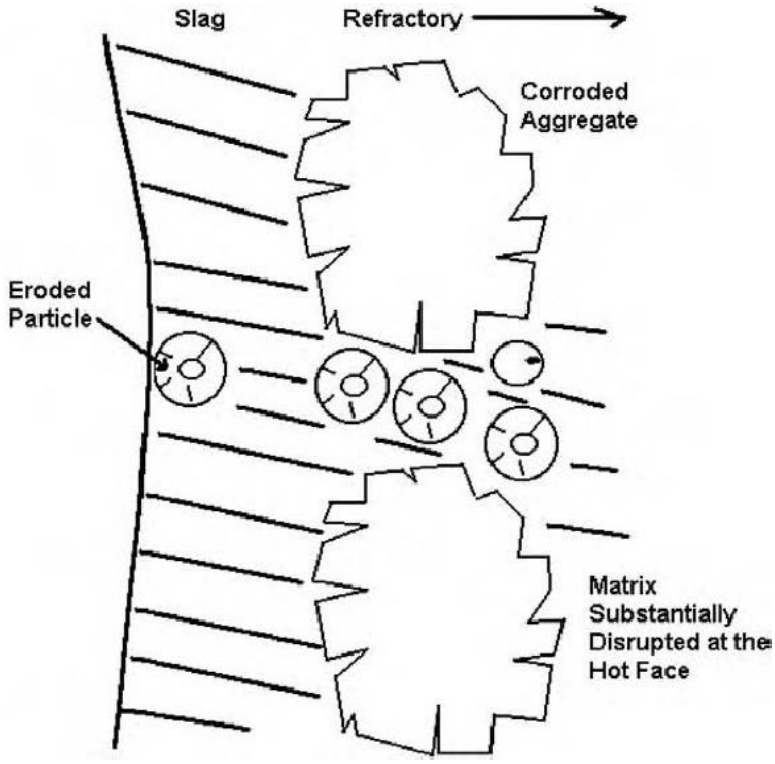

Figure 2.5: Stage 2 of corrosion wear mechanism, showing a bonded refractory (Brosnan, 2004)

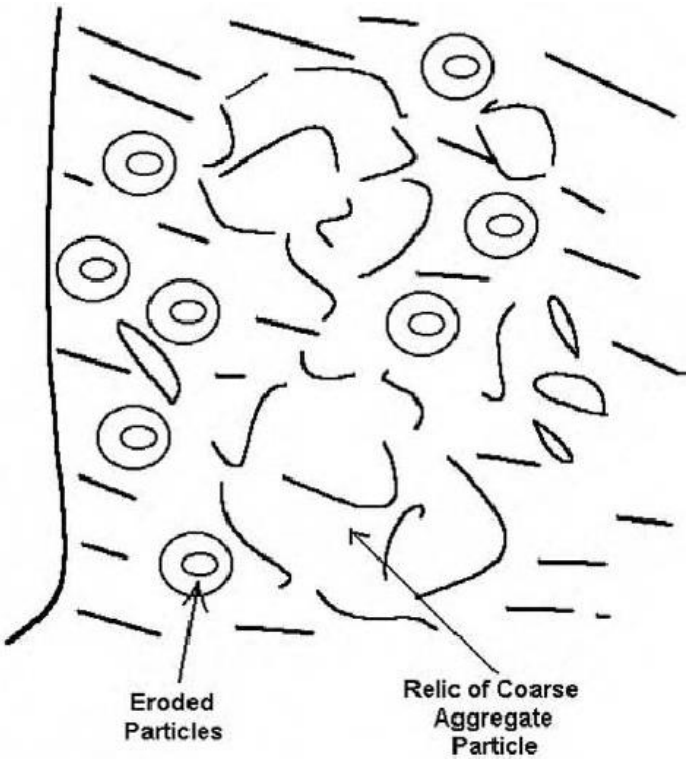

Figure 2.6: Stage 3 of corrosion wear mechanism, showing a bonded refractory (Brosnan, 2004)

2.7. Effect of Porosity on refractory wear

Most refractories contain void space or porosity. This porosity may be open pores that can be penetrated by fluid media and/or it may be closed porosity that is not easily penetrated by fluid media (Brosnan, 2004). Brosnan, (2004) also adds that the presence of open porosity allows corrosive media to penetrate the refractory, causing destructive reactions behind the hot face.

Porosity in refractory material has a direct relationship with refractory wear, such that a more porous material will experience more infiltration by alloy/slag, thus promoting more corrosion if the alloy/slag is unsaturated and erosion. In an apparent porosity range of 12-16% it has been found that slag corrosion rates increase linearly with the percentage of apparent porosity within the refractory (Brosnan, 2004). A study was conducted by Bazan *et al.*, (2011) on the wear of refractories for ceramic filters of different porosity when in contact with C and Mn steel alloys. The tests were conducted in an induction furnace at temperatures, 1560°C, 1600°C, and 1680°C for 20 min, while porosity of the refractories was increased by increasing the addition of various organic materials from 3 to 10 mass %. In the study Bazan *et al.*, (2011) found that corrosion

wear on the refractories increased with increasing porosity, with evident deformation of the refractory material in both the C and Mn steel alloys, see Figure 2.7.

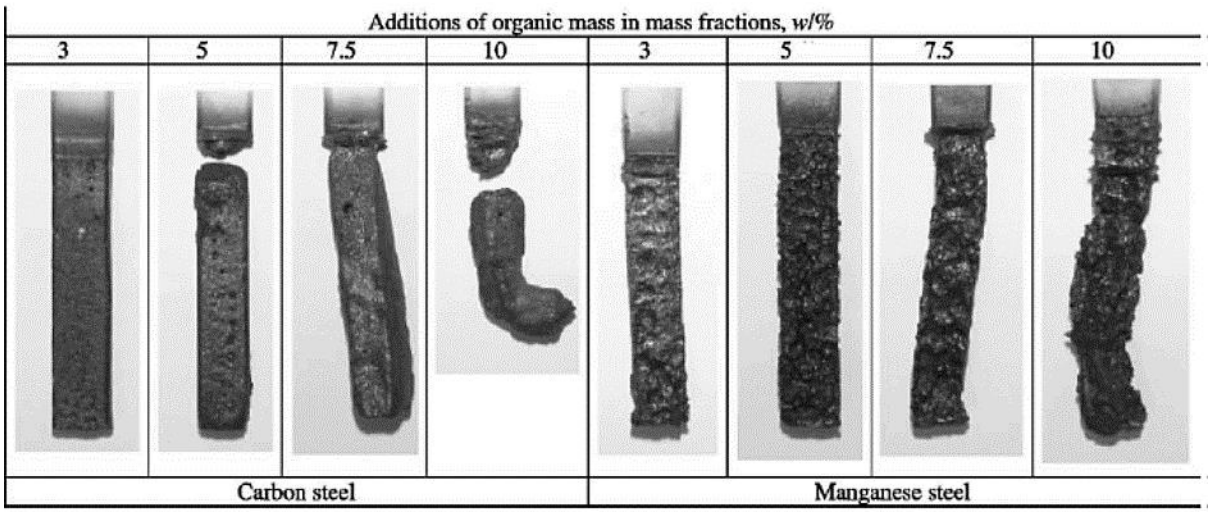

Figure 2.7: Refractory material post-mortem pictures after exposure in C and Mn steel alloys at 1680°C for 20 minutes (Bazan *et al.*, 2011)

2.8. Methods of testing refractories

Different methods have been developed and used in order to attempt to simulate the environment refractories are expose to. The refractory testing methods can either be static, also called dip tests, or dynamic, where the fluid moves relative to the refractory (Lee and Zhang, 2004). Static tests allow the study of corrosion wear mechanism, whilst the dynamic test allow erosion wear mechanism to be studied as well. To understand the phenomenon of corrosion it is necessary to first predict phases that can form during chemical reactions between refractory and process materials using thermodynamic modelling, secondly kinetic factors, lastly simulate the corrosion by relevant laboratory tests and to then compare with actual field results (Poirier *et al.*, 2007). Thermodynamic modelling and laboratory tests were only considered in this study. With chemical wear testing methods and facilities such as induction furnace, rotary kiln, cup tests, etc., together with phase chemical investigations of the post-mortem refractory sample, several boundary layers or zones of attack with different texture can be observed. Penetrated zones where the slag or alloy invaded the refractory matrix, unaltered areas and precipitation zones can be viewed, which can ultimately lead to recommendations to the clients refractory choice for their plant (Poirier *et al.*, 2007; Gregurek *et al.*, 2013).

As discussed in the previous paragraph, there are different ways of testing refractory wear on laboratory scale, with each method having its merits and demerits (Chesters, 1963). Some of the tests described by Mølnås (Mølnås, 2011) included the static plate test, crucible test, and the rotating finger test. The static plate test, shown in Figure 2.8, allows for the wear due to interfacial convection and free density convection to be derived. The static test uses the experimental set-up that involves four platelets (measuring 25 x 10 x 100 mm) immersed 60 mm into glass melts, and held for a period of time. Microscopy and photography techniques are then used to examine the refractory wear once the sample has been sectioned after cooling (Mølnås, 2011). The crucible test shown in Figure 2.9, also known as the cup test, consists of the refractory as the crucible, with the space in it filled with slag or alloy. The crucible and slag are heated to a desired temperature for a specific time, and subsequently cooled, and cut for analysis. To precisely control the temperature, a thermocouple is inserted inside the crucible or within the slag. The change in diameter of the refractory crucible due to refractory wear is then examined, using methods such as scanning electron microscope (SEM), and X-ray diffraction (XRD) analyses (Mølnås, 2011).

The rotating finger or rotating cylinder technique has been used by several researchers in refractory dissolution experiments (Mourao *et al*. 1993; Eric and Demir 2014; Sun *et al*. 1998; Shigeno *et al*. 1985). Figure 2.10 shows the experimental set-up that was used by Mourao *et al*. (1993) to investigate the dissolution rates or carbonaceous materials in liquid iron-carbon melts. Figure 2.11 shows the experimental set up used by Eric and Demir (2014) to investigate the dissolution of chromite in liquid slags. The tests were conducted in an induction furnace which was heated by the graphite susceptor. The crucible with the liquid iron-carbon (Fe-C) melts and the carbonaceous rotating finger was placed inside the graphite susceptor (Mourao, Murthy and Elliott, 1993). The rotation speed was controlled using a motor attached to the rod and the rotating finger. The tests were conducted in an inert atmosphere using argon gas, and temperatures were measured using a type B thermocouple placed between the graphite susceptor and the crucible. Mølnås (2011) stated that the strength of this method was the defined convective flow of alloy or slag around the refractory cylinder or finger, which would simulate the hydrodynamic behaviour between the liquid alloy or slag and refractories at the tap-hole.

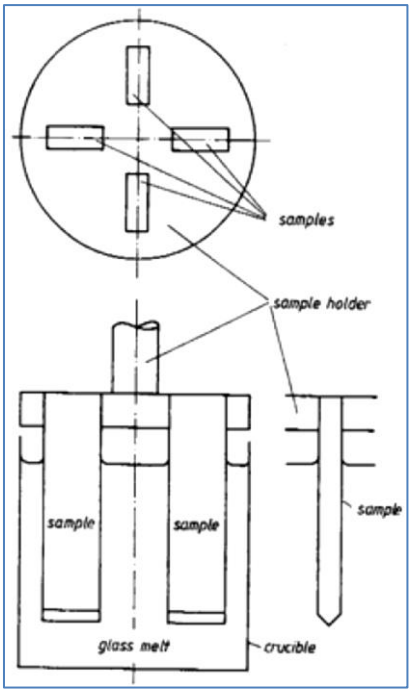

Figure 2.8: Static plate test (Mølnås 2011)

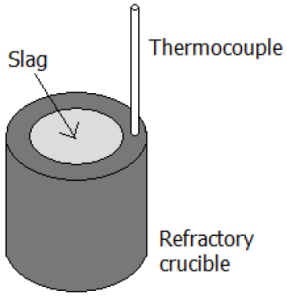

Figure 2.9: Crucible test (Mølnås 2011)

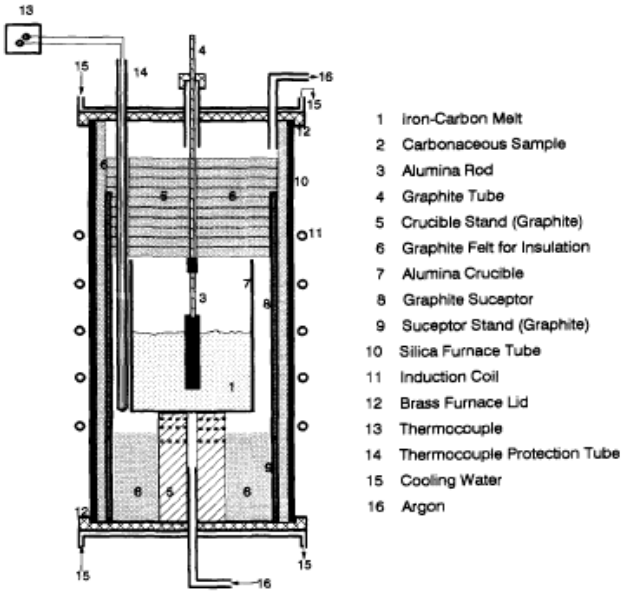

Figure 2.10: The experimental set up of the rotating finger technique used in dissolution experiments (Mourao, Murthy and Elliott, 1993)

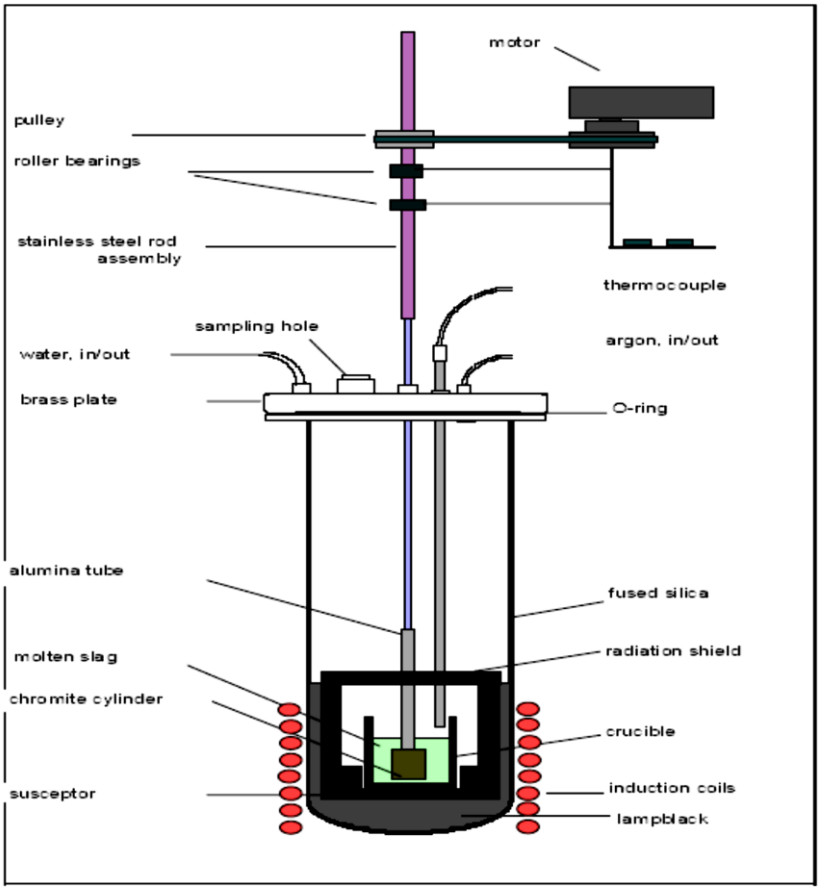

Figure 2.11: The experimental set up of the rotating finger technique used in dissolution experiments (Eric and Demir 2014)

2.9. Chemical wear of refractory material in the FeMn and SiMn industry

Major work on carbon-based material has been done to investigate the interactions of the refractory material with iron and associated iron alloys (Shigeno, Tokuda and Ohtani, 1985; Sun *et al.*, 1998). Sun *et al*. (1998) studied the dissolution of carbon into iron and iron alloys using four independent approaches. The first approach involved the immersion of a graphite cylinder in a molten alloy bath using an electric resistance furnace. The second approach involved the immersion of coke particles in a molten alloy bath using an induction furnace. The third approach involved studying a molten alloy droplet on a graphite plate using an induction furnace. The last approach involved sliding a metal droplet down a graphite spiral in a resistance furnace. Sun *et al.*, (1998) found that the dissolution of carbon refractory increased with an increase in temperature.

Shigeno *et al*. (1985) used the rotating finger technique to investigate the dissolution rate of graphite into iron-carbon melts containing sulfur or phosphorus. It was found that the rate of dissolution of C into the molten alloy decreased by increasing S in the melt. It was also found that poor wetting could retard the rate of C dissolution by reducing the surface area for mass transfer.

Basically, only a few studies have focused on the carbon-based refractory interactions with SiMn slag, and these include studies by Mølnås (2011) and Steenkamp (2014). No substantive literature has been found on the carbon-based refractory interactions with SiMn alloy. Mølnås (2011) investigated the compatibility of five tap-hole refractories, namely ramming paste, silicon carbide tap block, carbon tap block, tap-hole clay and electrode paste, which are used in an industrial SiMn furnace using two industrial SiMn slags. The aim was to investigate the suitability of the selected carbon-based refractories that were used in the SiMn tap-hole. In addition, the study sought to identify critical wear mechanisms at industrial tapping temperatures that would arise as a result of slag and refractory interactions. Mølnås (2011) found that the interactions between slag and the carbon-based refractories caused dissolution of the refractory matrix, and the eventual disintegration of the refractory particles. It was found that both the tap-hole clay and carbon block showed minimal signs of interactions with the slag samples, while the ramming paste failed the compatibility test. Mølnås (2011) recommended further investigation on the electrode paste and silicon carbide tap-hole block as the results were not conclusive.

Aursjø (2015) investigated the effects of carbon lining preparation on the internal morphology of the lining, and how it further affects the degree of wear and intrusion of the refractory by Silicon (Si) alloy. The investigations were done on samples prepared by two different techniques, thus giving two different sample types, namely rammed or layered samples and samples prepared in the Fisher-Sandrammer. In investigating the morphology for the rammed samples, it was found that they had significant differences in average density depending on the position analysed relative to the ramming layers. The top of the rammed layers had higher density and crushed grains, whilst high porosity was found in the bottom rammed layers. In investigating the sample prepared in the Fischer-Sandrammer, it was found that they had uniform densities across the height of the samples, with differences in density across the cross sections due to segregation of the paste. Internal cracks were observed in both refractory samples. To investigate the degree of wear, tests were conducted in an induction furnace at 1600°C, with a reaction time of 40 minutes for all samples. It was found that SiC was formed as a product from the Si alloy and C interaction. The degree of wear increased in areas with high porosity for both samples. In the rammed sample it was in the bottom layers and in the Fischer-Sandrammer samples it was in areas affected by segregation.

Steenkamp (2014) studied the chemical wear of the refractory material in a SiMn furnace tap-hole. The chemical reactions between the slag and refractory, as well as the alloy and refractory, were investigated. Consequently, SiC formation was evident in the cup tests that were conducted on synthetic slag and graphite, which verified the results from thermodynamic calculations. Steenkamp (2014) further investigated two refractories, namely carbon block and carbon ramming paste, to understand their behaviour or wear mechanism when used in the SiMn furnace tap-hole. The wettability studies proved the formation of SiC at 1588ºC, with the slag being wetting towards the refractory in an argon atmosphere, and non-wetting in a CO atmosphere. The cup test experiments confirmed the observations made in the wettability studies for both the carbon block and ramming paste, with the formation of SiC and SiMn when in contact with the industrial slag at the temperature of 1600ºC. These results on the carbon block and ramming paste led to the conclusion that the choice in refractory material (when limited to the two materials studied) was not important on the life of the SiMn tap-hole under the conditions investigated. Finally, the implications of these findings were studied in the excavation and profiling of a 48 MVA SiMn furnace, where the thermodynamic modelling data was supported by the mass flow calculations. Steenkamp (2014) then concluded that one of the mechanisms contributing to SiMn furnace tap-hole wear was the chemical reaction between

the refractories with the slag, and that the chemical wear by slag was definitely not the only wear mechanism applicable, hence the motivation for the present study.

CHAPTER 3: METHODOLOGY

Chapter 3 covers sample preparation, thermodynamic calculations, equipment design and experimental work, validations and assumptions. The detailed furnace procedures are attached in Appendix A, method development for post-mortem sample analysis is attached in Appendix B. Lastly the mechanical testing of the experimental design is attached in Appendix C.

3.1.Introduction

Thermodynamic calculations allow for the theoretical study of the effects of changes in process variables, namely temperature and Si-content, on refractory wear. FactSage™ software was applied to quantify the potential for refractory wear by chemical reaction with, and/or dissolution into, the SiMn alloy. Temperature was varied at 1550°C, 1600°C and 1650°C, and Si content at 15 mass %, 17 mass % and 18 mass %.

The project management life cycle analysis can be seen in Table 3.1 where after the development of the rotating finger experimental equipment and the subsequent trial tests, and optimized tests were ran. The experimental plan can be seen in Table 3.2. The static test samples were analysed by SEM-EDS at the Norwegian University of Technology, where the post-mortem sample analysis method was development and technical results were obtained. The dynamic test samples were analysed by SEM-EDS at Mintek and the technical results reported.

Table 3.1: Project management life cycle analysis.

Starting the project	**Organizing and preparing**	**Carrying out the work**	**Closing the project**
Collection of workplace storage criteria	Decompose project into smaller work packages	Execution phase ran in three phases	Final dissertation
Raw material as-received analysis	Allocate man hours for each work package	**Phase 1:** Material characterisation	SAIMM Journal paper
Assessment of whether any previous work has been done on a similar project	Order the required equipment and raw materials	**Phase 2:** Do modelling calculations to predict experimental results	Index and archive the experimental work records (Mintek internal report)
Design experimental set-up		**Phase 3**: Mechanical equipment testing	
Create project charter		**Phase 4:** Run optimized experimental test work	
Output: Project charter	**Output**: Project management plan	**Output**: EEC11 2016 paper Modelling results Experimental results	**Output:** Thesis Journal paper MINTEK internal final report

Table 3.2: Experimental plan where dynamic tests were conducted at 100 rpm and the composition of the alloy was 15 % except when indicated otherwise.

				Type K				Type SiC			
				Temperature [°C]			Composition (%Si)	Temperature [°C]			Composition (%Si)
Alloy	**Refractory**	**Test number**	**Analysis**	**Static**	**Trial dynamic tests**	**Dynamic**	**Dynamic, 1600°C**	**Static**	**Trial dynamic tests**	**Dynamic**	**Dynamic, 1600°C**
1st	2nd	1	SEM-EDS	1550							
1st	2nd	2	SEM-EDS	1600							
1st	2nd	3	SEM-EDS	1650							
1st	2nd	4	SEM-EDS					1550			
1st	2nd	5	SEM-EDS					1600			
1st	2nd	6	SEM-EDS					1650			
2nd	2nd	7	SEM-EDS		1550*	1550					
2nd	2nd	8	SEM-EDS		1600*	1600					
2nd	2nd	9	SEM-EDS		1650*	1650					
2nd	2nd	10	SEM-EDS						1550*	1550	
2nd	2nd	11	SEM-EDS						1600*	1600	
2nd	2nd	12	SEM-EDS						1650*	1650	
2nd	2nd	(8)	SEM-EDS				15%				
2nd	2nd	13	SEM-EDS				16%				
2nd	2nd	14	SEM-EDS				17%				
2nd	2nd	(11)	SEM-EDS								15%
2nd	2nd	15	SEM-EDS								16%
2nd	2nd	16	SEM-EDS								17%

*Test number not included as these were trial tests. () test 8 and 11 results were used as conditions were similar

3.2.Sample characterisation

3.2.1. Material sourcing and preparation

Industrial SiMn alloy samples were obtained from Transalloys, the only producer of SiMn in South Africa (Steenkamp *et al.*, 2018). Refractory samples were obtained from Elkem Carbon, a Norwegian-based international supplier of carbon-based refractories (Elkem Carbon, 2018).

At Transalloys, (Steenkamp *et al.*, 2018) the alloy is tapped into ladles and then layer cast into alloy beds. Once cooled, the alloy is collected by front-end loader and taken to the alloy handling plant. The sample used in the experiments was collected by hand from the alloy bed. Figure 3.1 shows the sample preparation flow sheet. The as-received alloy was first weighed, crushed and milled to -200 µm. The sample was weighed and split into two sub-samples, one sub-sample was weighed and further split into 20 sub-sub-samples using the 20 cup rotary splitter. Sub-sub-sample number 1 and 2 was used for characterisation, sub-sub-samples 3 to 11 were used for refractory tests using the type K refractory and sub-sub-samples 12 to 20 for refractory tests using the type SiC refractory.

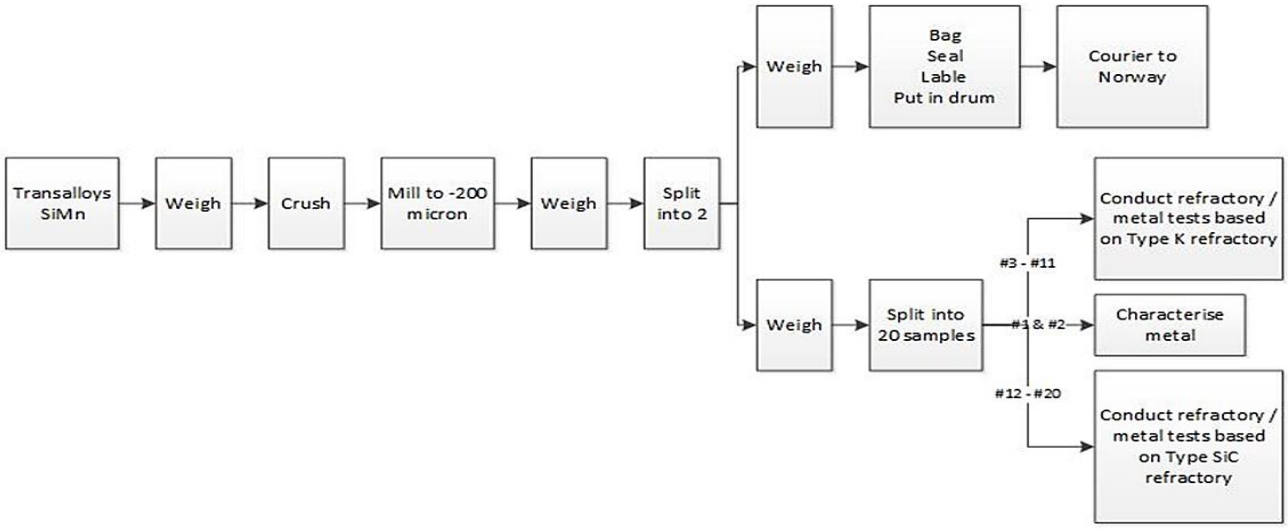

Figure 3.1: SiMn sample preparation flowsheet

The refractory samples were prepared by Elkem Carbon at the research facilities in Kristiansand. Two types of refractory were used: (1) Type K, typically consisting of 80-90% electrically calcined anthracite, 10-20% coal tar pitch and 5% ash content (Elkem Carbon, 2015), and (2) Type SiC, typically containing 60-80% silicon carbide, 10-20% silicon alloy and 10-20% coal tar (Elkem Carbon, 2009). The refractory paste was rammed in a Fisher Sand rammer test machine. The sand rammer is made up of a frame, pendulum and pusher arm weight, and this equipment is used for testing strength of molding sand. The samples were prepared as a larger sample by the sand rammer and density as a function of each stroke, was measured. The rammed samples were placed inside a special high temperature steel box, with coke on all sides to form a coke bed and to reduce oxidation from surrounding air. The samples were heat treated at an increasing rate of 20°C/hour to 950°C, where they were held for 1 hour inside a muffle furnace. In order to cool down the samples, the temperature was reduced from 950°C to 30°C over approximately 20 hours. Cylindrical refractory samples, 50 mm in diameter and 55 mm height, were then core drilled out of the larger sample. The 10 mm diameter holes, to be used to attach the graphite rod, were drilled out afterwards on individual sample cylinders.

In general, testing of refractories can be done by evaluating three components namely, characterisation or data sheet properties, service-related properties, and design-related properties (Baxendale, 2004). The rotating finger experiment discussed in Section 3.4 was used to characterize service-related properties. In Section 3.2, data sheet properties were addressed, which included the chemical composition, bulk density, and apparent porosity, as well as mineral composition. The chemical composition of the as-received SiMn alloy was determined as well. The results of the characterisation was then reported in Chapter 4.

3.2.2. Material characterisation

The bulk chemical compositions of three representative SiMn samples were determined by wet chemistry, X-ray fluorescence (XRF) and the carbon composition in the alloy was determined using ultimate analysis.

Chemical analysis of the refractory material was done to evaluate the concentrations of the elements present. The bulk chemical analyses evaluated include, proximate (ASTM-D3172, 2013), ultimate and ash analyses (ASTM-D3174, 2012).

Proximate analysis (ASTM-D3172, 2013) was done on the refractory samples, where the moisture, ash and volatile matter content were measured, and the fixed carbon was calculated by difference. Moisture content (ASTM-D3173, 2011) of a sample was determined using a drying oven, where the moisture of the sample was obtained by difference of the sample masses before, and after drying. A thermo-gravimetric analyzer (TGA) was used to obtain the volatile matter content and ash content by temperature variations which result in mass changes within the sample as the atmosphere changes from inert to oxidizing. The fixed carbon was determined by difference.

Ultimate analysis was done to obtain elemental analyses of the carbon-based refractories. The results from the ultimate analysis were used to determine the elemental composition of the refractory including carbon, hydrogen, nitrogen, and sulfur. Oxygen was determined by difference (SGS, 2015).

Through the phase chemical analysis, the bulk phase chemical analysis was done using X-ray diffraction (XRD) methods, which provided means of quantifying and characterizing different crystalline phases as well as the amorphous phases present. A Bruker D8 diffractometer with an acceleration voltage of 35kV and cobalt tube with Fe-low beta filter was used with the 2θ angle ranging from 2 to 80 degrees and step size of 0.02° 2θ.

The microscopic examination of the refractory was done using a Zeiss Evo MA15. It allowed the specific phase chemistry of the different phases present in the refractory, characterized through scanning electron microscope-energy dispersive spectroscopy (SEM-EDS). An acceleration voltage of 20 kV was used on the SEM-EDS, and an acceleration voltage of 15 kV was used on the electron microprobe analysis (EMPA). Backscattered electron images (BSE) from the SEM analysis display compositional contrast that result from different atomic number elements, and their distribution. EDS allowed the particular elements to be identified together with their relative compositions (Hafner, 2006). Cameca SX50 Electron Probe Microanalyser (EMPA) provided quantitative analysis of the material with reference to a standard. In an EMPA, a beam of electrons is focused on a specific point, resulting in emission of X-rays of wavelength characteristic of the element present (Chesters, 1963). The beam was generated at 20 kV with a probe current of 30 nA and a spot size of 5μm. EMPA provided a graph with the distribution of the elements, and alternatively backscattered electron images were produced, which can be used to identify different chemical phases (Chesters, 1963). Preparation of the SEM-EDS samples can be seen in Appendix B.

The bulk density of a porous material is the ratio of its mass to its bulk volume (Baxendale, 2004), and was calculated using Equation 3.1. The apparent porosity is the ratio of the open pores in the material to the bulk volume, and was calculated using Equation 3.2. The Archimedean evacuation method was used to measure both the bulk density and apparent porosity. A method based on an ASTM standard C20-00 was developed by Mushwana and Steenkamp (Mushwana and Steenkamp, 2015) which was then used as the standard procedure to do the measurements.

$$\rho = [D/(D - S)(\rho o - \rho L)] + \rho L \quad (3.1)$$

Where:

ρ = Bulk density of the sample (g/cm^3)

ρ_o = Density of auxiliary liquid (g/cm^3)

ρ_L = Density of air (taken as 0.0012 g/cm^3)

$$P = [(W - D)/V] * 100 \quad (3.2)$$

Where,

P = Apparent porosity (%)

W = saturated weight (g)

D = dry mass (g)

V = exterior volume (cm^3), based on *Equation 3.3*

$$V = W - S \quad (3.3)$$

Where,

S = suspended weight (g)

3.3.Thermodynamic Calculations

Historically, refractories were designed and manufactured to be close to equilibrium as possible so that in service changes were limited. Phase diagrams and phase equilibria calculations using

modern software packages such as FactSage™, MTDATA, and THERMOCALC can now be used to complement and limit number of expensive experimental and difficult experimental studies that are needed (Lee, Argent and Zhang, 2002). To gain confidence in the phase equilibria calculations, the calculation results need to be first validated by laboratory scale tests, once validated, the software package can be used to investigate more scenarios. Brosnan, (2004) also states that a full understanding of refractory corrosion includes viewing corrosion as a chemical and physical process and using phase equilibrium diagrams.

FactSage™ was used in this study. The Equilibrium model in FactSage™ 7.2 (Bale *et al.*, 2002) was applied in the thermodynamic calculations. The dataset developed by Tang and Olsen (Tang and Olsen, 2006) for FeMn, and the FactPS, which is the pure substance data base, were applied. The SiMn alloy analysis, reported in Section 4.2, was used as basis for the thermodynamic calculations to predict the potential wear of the SiC and the carbon refractory. Variables tested were temperature and Si composition in the alloy. The temperatures were selected to simulate the typical operating temperatures for SiMn producing furnaces, and were varied from 1550 to 1650°C, with the midpoint temperature of 1600°C being chosen as the baseline temperature. SiMn composition was varied at 15 mass %, 17 mass % and 18 mass % Si. Since Transalloys normally produces grade B SiMn, the modelling was done to include Si alloy mass % in the grade B specification.

3.4.Equipment design

To further investigate the wear predicted by thermodynamic calculations, a rotating experiment was designed and built. Mechanical testing was conducted having temperature as control variable - the detailed results are attached in Appendix C. This section of the report addresses the experimental design used for the optimized tests.

3.4.1. Design experimental set-up

Figure 3.2 shows the design of the rotating finger experimental set-up to be applied in the study. The refractory cylinder with the diameter of 50 mm and height of 55 mm is attached to a cylindrical graphite rod with the height of 550 mm and diameter of 20 mm. The graphite rod is then attached to the refractory cylinder using graphite glue. The graphite rod, attached to the cylinder is then mounted onto an extension arm, which is connected to the rotating motor, for the dynamic rotating motion. The graphite crucible with the outer diameter of 200 mm and height of 250 mm is placed inside the induction furnace to facilitate heat transfer, and alumina

bubbles are added between the graphite crucible and induction furnace chamber to achieve the required height as well as play a role in heat transfer. In addition, the alumina crucible with the outer diameter of 100 mm and height of 115 mm is then placed inside the graphite crucible with alumina bubbles to get the required height inside the graphite crucible. Finally, the SiMn alloy and refractory cylinder interacted inside the alumina crucible when the operating temperature is reached. B-type thermocouples were used to measure the temperatures inside the 25 kW induction furnace. The step by step furnace procedure that was developed to set-up the experiment and run each test is attached in Appendix A.

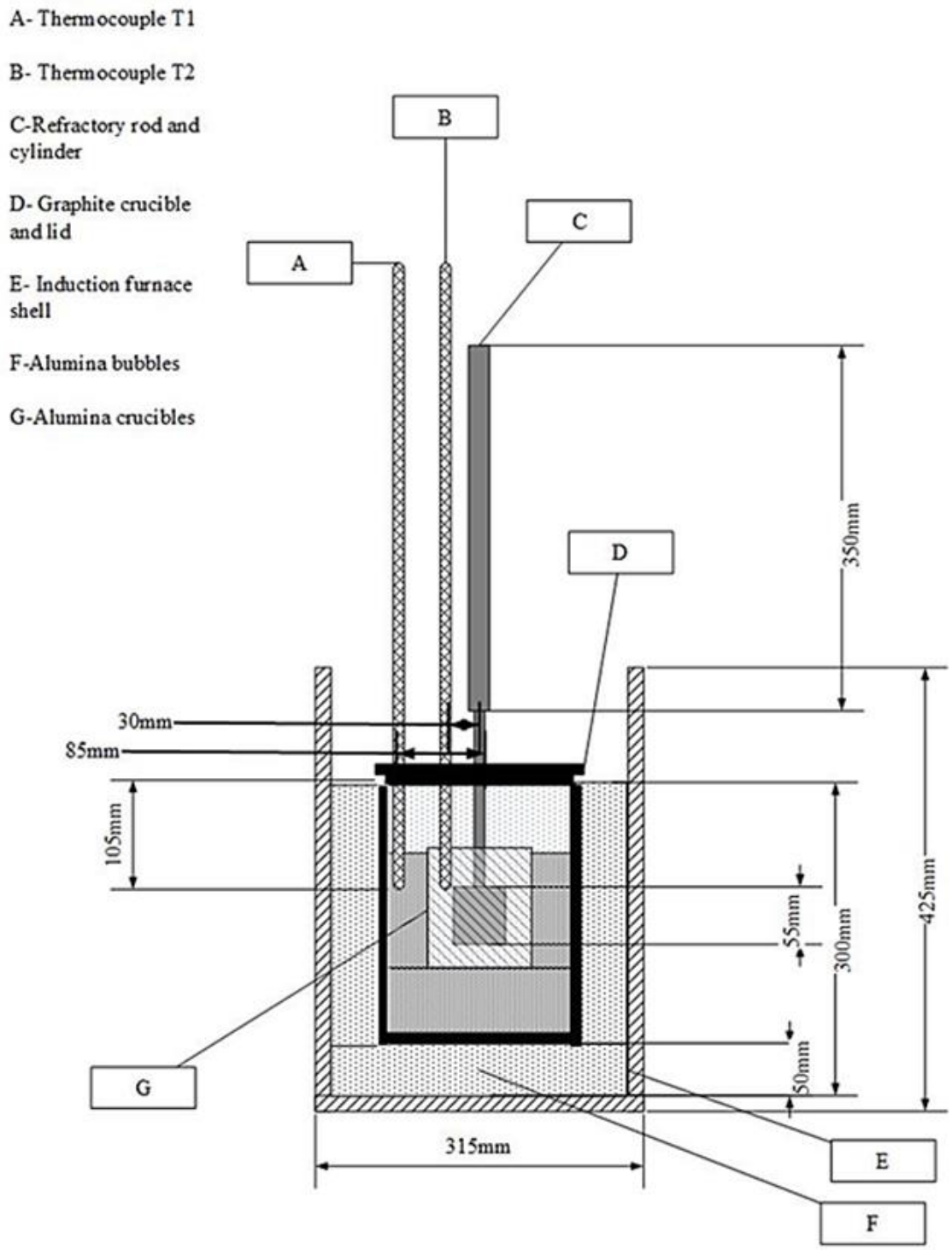

Figure 3.2: Rotating finger experimental set-up

The variables involved in the experiments were temperature, mass per cent Si in the alloy and motor speed. The fixed variables included: reaction time, which was maintained at 90 minutes; the heating rate, which was manually adjusted at increments of 0.5 ampere every 30 minutes, and reaction chamber atmosphere (argon). The controlled variables are listed below. When the

influence of a specific variable on refractory wear was evaluated, all other variables were fixed at the baseline value.

1. Temperature was varied between 1550 and 1650°C, at 50°C intervals. The baseline value for temperature was 1600°C. These values represent the typical temperatures for the SiMn producing furnaces, thus they were chosen to represent their operating conditions.

2. Si content of the alloy was varied between 15, 17 and 18 mass %. The baseline value for Si content of the alloy was 15 mass %. The SiMn composition of the alloy was below grade B, which is normally produced by Transalloys, thus the values chosen cover the composition of the as-received alloy, as well as those specified by the ASTM standard for grade B (ASTM A483, 2010).

3. The motor speed was set at either 0 (static) or 100 rpm (dynamic).

3.5.Temperature validations

Temperature readings from the data logger were validated using the wire-bridge method (Mølnås, 2011). To quantify the error in the temperature reading gold (Au) wire was used. This method was developed between 1981 and 1984, where a study on platinum thermocouple calibration by European laboratories (Matthey, 1988) on 3 types of thermocouples with different rhodium (Rh) and platinum (Pt) combinations, namely: type S (10%Rh-Pt: Pt), type R (13%Rh- Pt: Pt), and type B (30%Rh-Pt: 6%Rh-Pt) was done. It was found that laboratories were able to calibrate new thermocouples to within $\pm 0.4℃$ at the Au melting point and to within $\pm 0.9℃$ at the Pd melting point with mutual agreement inside these figures.

The type B thermocouple hot junction was constructed by clamping a piece of pure metal to the ends of the type B wires as shown in Figure 3.3(a). The thermocouple was then inserted into the induction furnace with a reference type B thermocouple that did not contain a pure metal hot junction. The 2 thermocouples were placed 50 mm apart and 30 mm from the center of the induction furnace. The thermocouples were then heated in an inert atmosphere, and the temperatures were recorded manually at 30 minute intervals, and close to target temperature the temperature was recorded at 5 minute intervals untill the pure metal hot junction melted.

Mølnås (2011) found that at the melting points of gold (1064°C) average measured temperature offsets were -2.1°C with a standard deviation of 2.3°C. The Au hot junctions used in this study can be seen in Figure 3.3(b). Using the Au-wire bridge, at 1064°C, an average offset (based on

3 tests) was 2.6°C with a standard deviation of 1.8°C. This off-set was then used when manually controlling the temperature of the tests. Mølnås (2011) found that the thermocouple reading accuracy increased with increasing temperature. Two type B thermocouples were used in all the rotating finger experiments for improved temperature precision, as well as to allow measurement reading to continue when one thermocouple burns out.

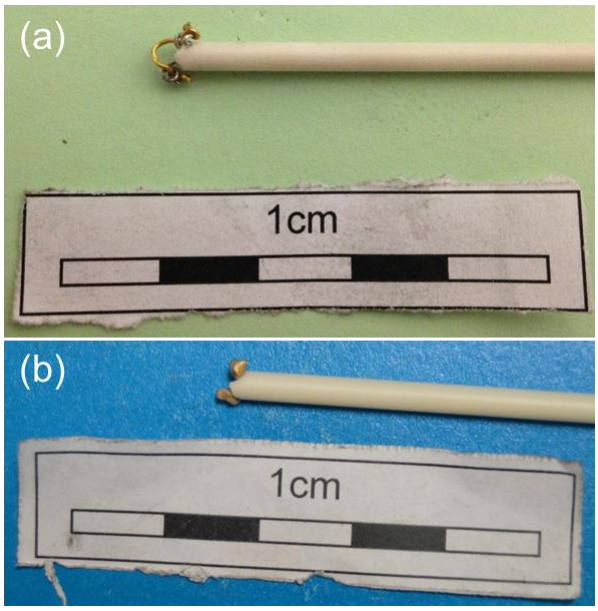

Figure 3.3: (a) Au-wire bridge before experiment, and (b) Au-wire bridge after experiment

3.6.Assumptions

The assumptions used for this study are as follows:

1. The atmosphere is inert and no oxidative reactions took place
2. At equilibrium and reaction temperature the liquid alloy had uniform composition
3. Refractory properties of the first and second batch of samples have negligible differences

CHAPTER 4: RESULTS

4.1. Introduction

Chapter 4 contains results for the optimized test work and raw materials used. The characterisation results of the first as-received refractory samples used for the mechanical test can be viewed in detail in a conference paper by Banda, Steenkamp and Matinde, (2016) focused on characterisation and thermodynamic modelling of the first batch of refractory samples received from Elkem and SiMn alloy from Transalloys.

4.2. Material characterisation

Figure 4.1(a) is the as-received SiMn alloy and Figure 4.1(b) is the corresponding SEM BSE image. The bulk chemical composition of the SiMn alloy 1, which was used for the mechanical equipment testing and static tests, is reported in Table 4.1 and in Table 4.2. The bulk chemical composition for SiMn alloy 2, used for the dynamic tests, is also reported.

The phase chemical analysis of the SiMn alloy indicated that there were two phases present as seen in Figure 4.1, where the two phases can be distinguished by a light grey area (A) and a dark grey area (B). SEM-EDS and EMPA results in Table 4.1 indicate that phase A is a high-Mn and low-Si phase, while phase B is a high-Si phase with lower Mn levels relative to phase A. The presence of carbon was also identified in phase A.

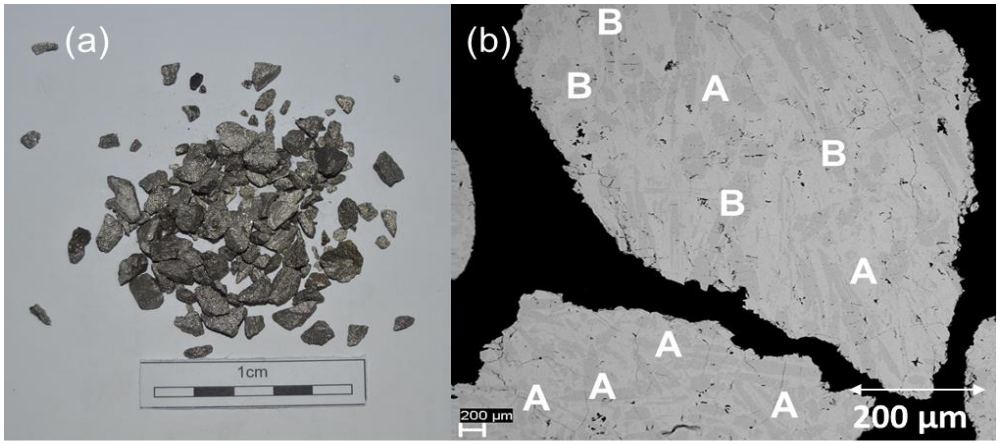

Figure 4.1: SiMn alloy (a) photograph of as-received material and (b) SEM BSE image Images measured at 20 kV acceleration voltage. Scale bar indicates 200 µm.

Table 4.1: Composition of two SiMn alloy phases, present in as-received industrial samples, identified by SEM in Figure 4.1. The calculated average composition was determined by normalised EDS analysis at 20 kV acceleration voltage, with standard deviations indicated in brackets. EMPA, was done on randomly selected grains at 15 kV and 20 nA spot size 5μm.

Area		**C**	**Si**	**Mn**	**Fe**	**Total**
A	SEM-EDS		9.3	75.3	15.5	100.0
	Std. Dev		1.7	5.0	3.4	
	EMPA	2.4	9.7	73.9	14.0	100.0
	Std. Dev	0.2	0.2	1.3	0.8	
B	SEM-EDS		20.4	65.6	14.0	100.0
	Std. Dev		0.4	1.0	0.6	
	EMPA		23.1	62.9	14.9	100.0
	Std. Dev		0.2	0.9	0.9	

Table 4.2: Normalized SiMn alloy XRF and wet chemistry analysis for SiMn alloy 1 used in static tests and Normalized ICP analysis for SiMn alloy 2 used in dynamic tests.

Alloy		**Mn**	**C***	**Si**	**Fe**	**TOTAL**
SiMn1	Average (XRF)	67.5	1.7	15.3	15.5	100
	Std. Dev.	0.19	0.02	0.14	0.11	
	Average (Wet chemistry)	67.3	1.7	14.7	16.3	100
	Std. Dev.	0.08	0.02	0.41	0.11	
SiMn2	Average (ICP_FeMn Metals)	67.8	2.2	14.5	15.5	100
	Std. Dev.	0.3	0.01	0.12	0.15	

**Carbon analysis was done using the ultimate analysis*

In Figure 4.2(a1) and (a2), the as-received Type SiC refractory can be seen and the corresponding SEM-BSE image can be seen in Figure 4.4. In Figure 4.2(b1) and (b2) the as-

received Type K refractory can be seen and the corresponding SEM-BSE image can be seen in Figure 4.3.

In Figure 4.3 the type K refractory SEM-BSE image can be seen to have a major carbon phase, which consists of the carbon aggregate and binder particles, as well as minor intrusions of SiC which may have resulted from surface contamination. In Figure 4.3 the type SiC SEM-BSE image can be seen to have the SiC as the major phase, Si oxide and Si are present as the minor phases.

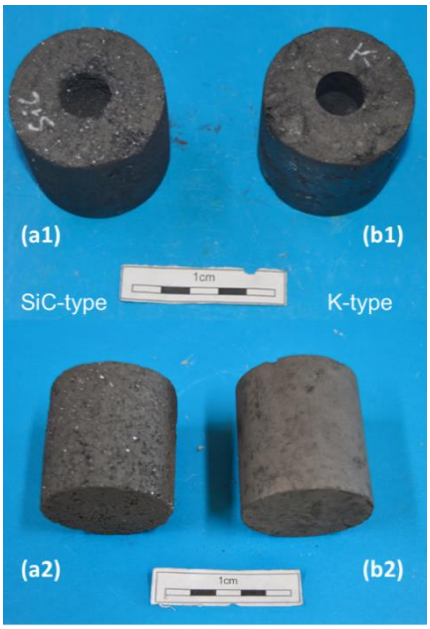

Figure 4.2: (a1) Top view and (a2) side view of the Type SiC refractory cylinder as-received from Elkem, (b1) Top view and (b2) side view of the Type K refractory cylinder as-received from Elkem.

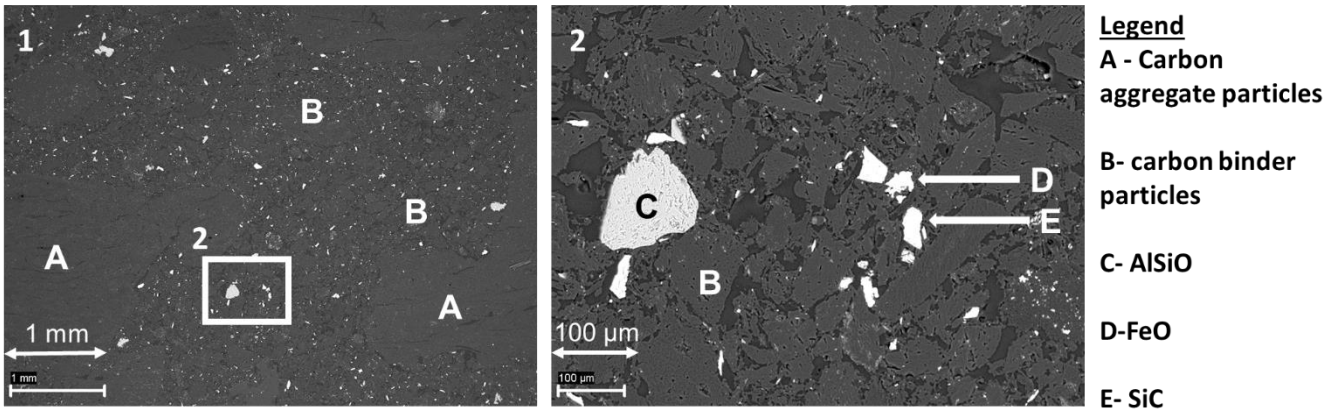

Figure 4.3: Type K Refractory SEM image measured at 20 kV acceleration voltage. Scale bar indicates 1 mm for (1) and 100 µm for (2) which is a magnified portion to view intrusions.

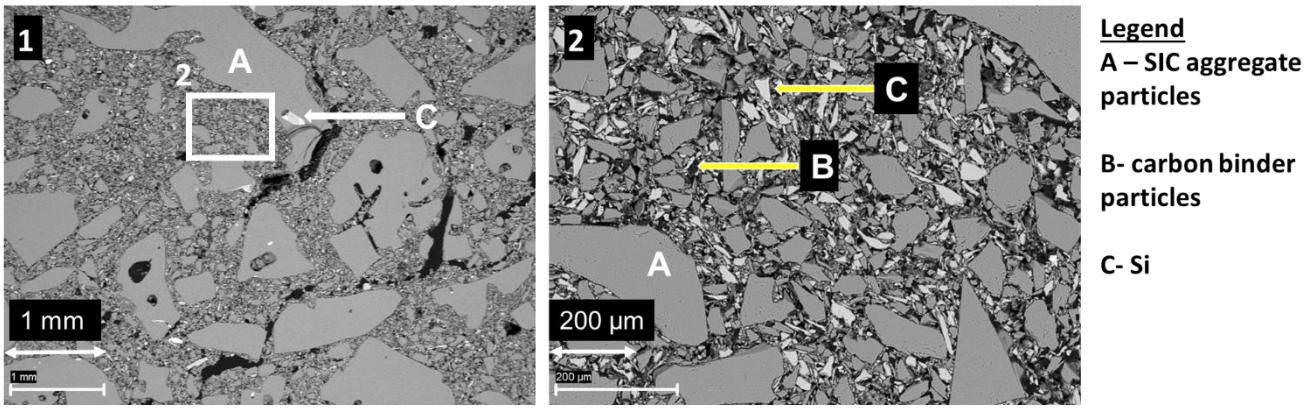

Figure 4.4: Type SiC refractory SEM image measured at 20 kV acceleration voltage. Scale bar indicates 1 mm for (1) and 200 µm for (2) which is the magnified portion to view intrusions.

Table 4.3 and 4.4 contain the proximate and ultimate analysis of the as-received refractory samples from Elkem.

Table 4.3: Proximate analysis of the type K and type SiC refractory as-received from Elkem. The table contains average values of three representative samples and the standard deviation is indicated in brackets. ASTM-D3172, ASTM-D3173, ASTM-D3174, (ASTM-D3172 2013; ASTM-D3173 2011; ASTM-D3174 2012) were used as a standard procedures for the proximate analysis.

	Ash	**Fixed Carbon**	**Moisture**	**Volatile**	**Total**
Type K Refractory	10.9 (7.3)	86.4 (9.9)	0.3 (0.1)	2.4 (2.5)	100.0
Type SiC Refractory	95.9 (1.0)	1.6 (2.7)	0.4 (0.0)	2.4 (1.8)	100.2

Table 4.4**:** Ultimate analysis of the type K and type SiC refractory as-received from Elkem. The table contains average values of triplicated results and the standard deviation is indicated in brackets.

	Hydrogen	**Nitrogen**	**Oxygen**	**Carbon**	**Sulphur**	**Total**
Type K Refractory	0.6 (0.3)	0.4 (0.1)	4.7 (7.6)	96.7 (1.0)	0.1 (0.0)	102.5
Type SiC Refractory	0.2 (0.0)	0.2 (0.0)	0.0 (0.0)	30.7 (0.8)	0.0 (0.0)	31.1

The density and porosity measurement results for the two refractory samples are presented in Table 4.5. The average measured density values are in line with the values supplied by the manufacturer data sheet (Elkem Carbon, 2009, 2015). The calculated porosity value for the type K refractory is also comparable to that given by the manufacturer data sheet. Comparing the bulk densities of the two refractories, it can also be seen that in a given volume, SiC type refractory will have a larger mass than the type K refractory.

Table 4.5: Density and porosity measurement results. The standard deviation for the average measured densities are given in brackets.

	Density (kg/m^3)			**Porosity (%)**	
	Average measured density	Calculated bulk density	Manufacturer data sheet	Calculated porosity	Manufacturer data sheet
Type K Refractory	1480 (0.002)	1818	1460	18	19
Type SiC Refractory	2324 (0.007)	3000	2300	23	Not supplied

4.3. Thermodynamic calculations

Section 4.3 contains the results of the thermodynamic calculations conducted in FactSage™ for the type K and type SiC refractory. The Equilibrium model in FactSage™ 7.2 (Bale *et al.*, 2002) was applied in the thermodynamic calculations. The dataset developed by Tang and

Olsen (Tang and Olsen, 2006) for FeMn, and the FactPS, which is the pure substance data base, were applied. The mass of 100g SiMn alloy and 100g of each refractory was assumed. The type K refractory was assumed to be pure graphite and type SiC was assumed to be pure SiC.

4.3.1. *FactSage*™ refractory mass loss results

Temperature was varied while keeping other variables constant, i.e. Si mass % in the alloy at 14.74. Table 4.6 contains the FactSage™ modelling results, where both refractories show an increase in dissolution into the alloy with an increase in temperature.

Table 4.6: Refractory dissolution with temperature variations.

Temperature (in °C)	**25**	**1550**	**1600**	**1650**
Type K (mass in g)	100	99.5	99.3	99
Type SiC (mass in g)	100	97.7	97	96.2

Table 4.7 contains the modelling results for the type K refractory when the composition of the Si in the alloy was varied and the temperature kept constant at 1600°C. The type K refractory mass loss increased with increasing concentration of Si from 14 to 16 mass %. Increasing the Si mass % to 17 and 18, resulted in decrease in refractory mass loss and precipitation of SiC. A maximum of 2 g SiC was formed at the Si composition of 18 mass %.

Table 4.7: Refractory dissolution and SiC precipitation for the K-type refractory.

Si mass %	**Components (g)**		
	Initial mass	Final mass	SiC precipitation
14	100.0	99.2	0
15	100.0	99.4	0
16	100.0	99.5	0
17	100.0	99.4	0.54
18	100.0	99.0	2.0

Table 4.8 contains the modelling results for the type SiC refractory when the mass % of Si in the alloy was varied and the temperature kept constant at 1600°C. The type SiC refractory mass loss decreases with increasing Si mass %.

Table 4.8: Refractory dissolution and carbon precipitation for the SiC-type refractory.

Si mass %	**Components**		
	Initial mass	Final mass	C precipitation
14	100.0	96.3	0.7
15	100.0	97.7	0.3
16	100.0	98.9	0.0
17	100.0	99.5	0.0
18	100.0	100.1	0.0

4.3.2. FactSage™ alloy composition predictions

Post-mortem alloy analysis was done for both type K, Table 4.9, and type SiC, Table 4.10.

Table 4.9: Type K post-mortem alloy analysis at 1550°C predicted by FactSage™ and from actual static and dynamic tests.

Final alloy composition (mass %)	Mn	C	Si	Fe	Total
As-received (Wet chemistry)	67.8	2.2	14.5	15.5	100.0
FactSage™	67.5	2.7	14.4	15.4	100.0
Actual Static (ICP_FeMn Metals)	66.0	2.3	17.4	14.3	100.0
Actual Dynamic (ICP_FeMn Metals)	65.5	2.6	16.4	15.4	100.0

Table 4.10: Type SiC post-mortem alloy analysis at 1550°C predicted by FactSage™ and from actual static and dynamic tests

Final alloy composition (mass %)	Mn	C	Si	Fe	Total
As-received	67.8	2.2	14.5	15.5	100.0
FactSage™	66.6	2.4	15.8	15.2	100.0
Actual Static (ICP_FeMn Metals)	65.7	2.3	17.9	14.1	100.0
Actual Dynamic (ICP_FeMn Metals)	64.9	2.3	17.7	15.1	100.0

4.4. Mechanical wear analysis

Section 4.3.2 contains the mechanical wear analysis results. Figure 4.5 is upside down in order to show the orientation when ploting the graphs as well as the orientation used to conduct the mechanical wear analysis of the refractory cylinders. The reference point was chosen at the point where the refractory cylinder met the graphite rod, and at 50 mm is at the surface of the refractory fully in contact with the molten alloy. The initial diameter D_i was subtracted from the final diameter D_f in order to calculate the wear thickness. The focus of the mechanical wear analysis was mainly put on the 50mm plane as it was fully in contact with the molten alloy and in an industrial furnace the wear also behaves in a similar manner such that it occurs from the rammed surface moving inwards towards the hearth surface as it can be seen in Chapter 1 Figure 1.1. The method used to measure the wear was calibrated and the results can be seen in Appendix E. In summary the average measured diameter for the type K was 49.64 with the standard deviation of 0.03 and the measurement relative error was 0.72% with the standard deviation of 0.06%. The type SiC average measured diameter was 50.85 mm with the standard deviation of 0.61 mm and the average measurement relative error was 1.69% with the standard deviation of 1.21%. The larger error in type SiC calculations was attributed to quartz granules on the surface of the refractory.

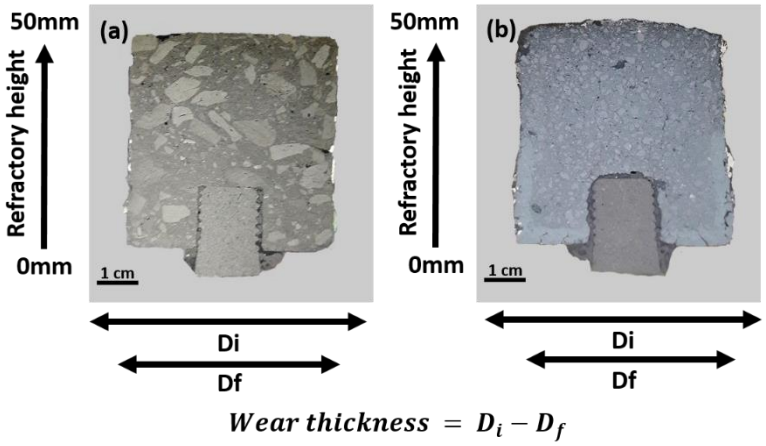

Figure 4.5: (a) type K and (b) type SiC orientation and dimensions used for the wear profile graphs

4.4.1. Static temperature wear tests

In Figure 4.6 at 1550°C, the static mechanical wear of the type K and SiC can be observed. FactSage™ had predicted in Table 4.6, that type SiC would wear more than type K, but the

mechanical wear analysis at 50 mm refractory length (bottom where refractory meets alloy) indicated that type K refractory wore out the most, where the type K refractory lost 2.8 mm and the type SiC lost 2.48 mm in thickness.

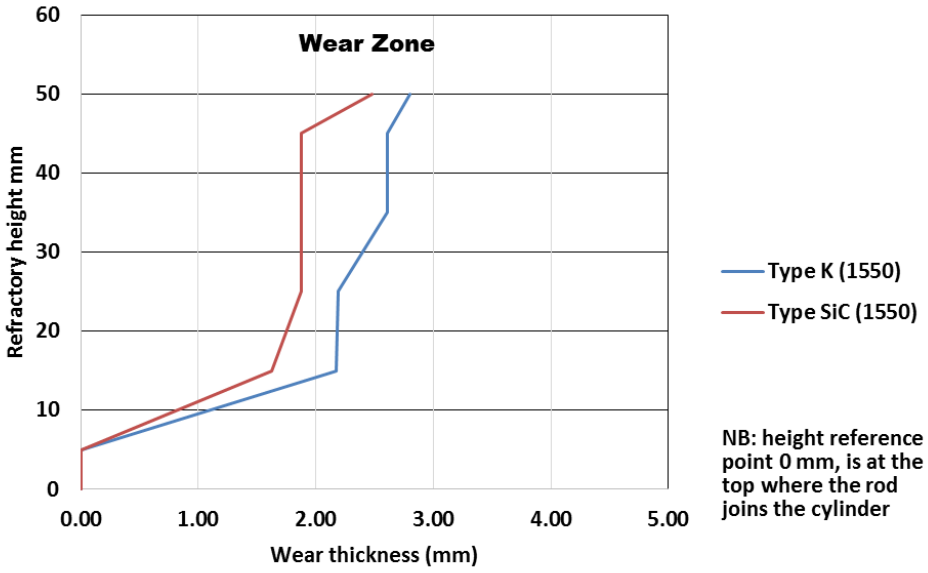

Figure 4.6: Static wear analysis of the type K and SiC at 1550°C

In Figure 4.7 at 1600°C and Figure 4.8 at 1650°C the static mechanical wear of the type K and SiC are in agreement with what FactSage™ had predicted in Table 4.6, as it can be seen in the figures that type SiC experienced more wear with an increase in temperature compared to the type K refractory. In Figure 4.7 at 50 mm type SiC experienced a maximum thickness wear of 4.69 mm, whilst the type K refractory experienced thickness wear of 2.81mm. In Figure 4.8 at 50 mm the type SiC experienced a maximum thickness wear of 7.20 mm, whilst the type K experienced a maximum of 3.48 mm.

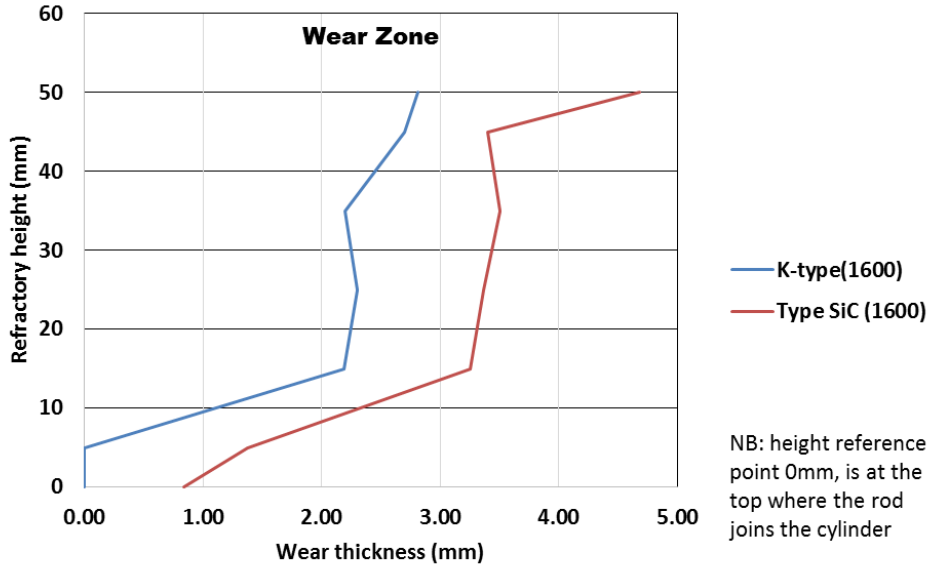

Figure 4.7: Static wear analysis of type K and SiC at 1600°C

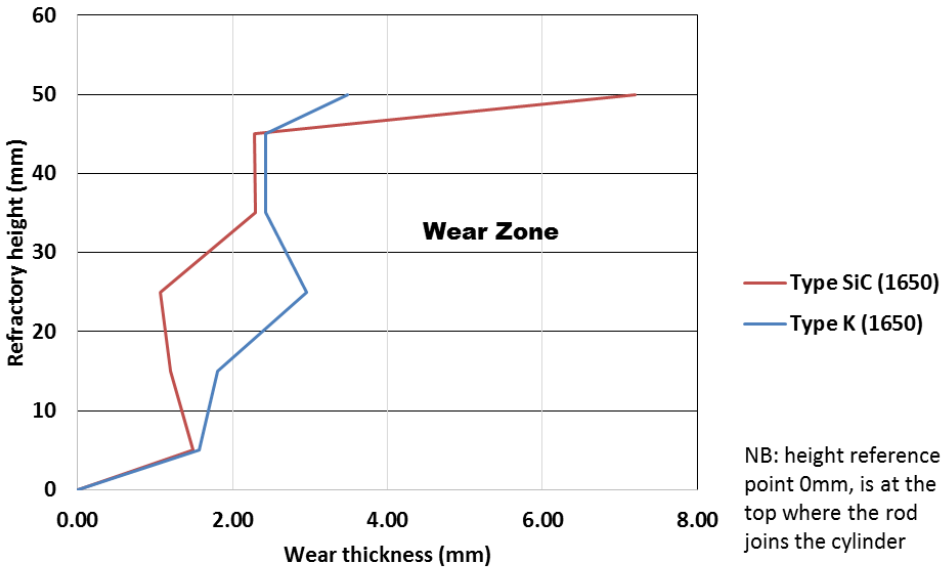

Figure 4.8: Static wear analysis of the type K and SiC at 1650°C

4.4.2. Dynamic temperature wear test

In Figure 4.8 to 4.10 it can be seen that the extent of wear also increased significantly and this was due to the combination of dissolution and erosion resulting from the refractory rotations. In Figure 4.9 at 1550°C the maximum wear experienced at 50 mm by the type SiC and K were 3.10 mm and 2.36 mm respectively. In Figure 4.10 at 1600°C the maximum wear experienced at 50mm by the type SiC and K were 4.77 mm and 2.90 mm respectively. In Figure 4.11 at

1650°C the maximum wear experienced at 50 mm by the type SiC and K were 16.65 mm and 3.12 mm, respectively.

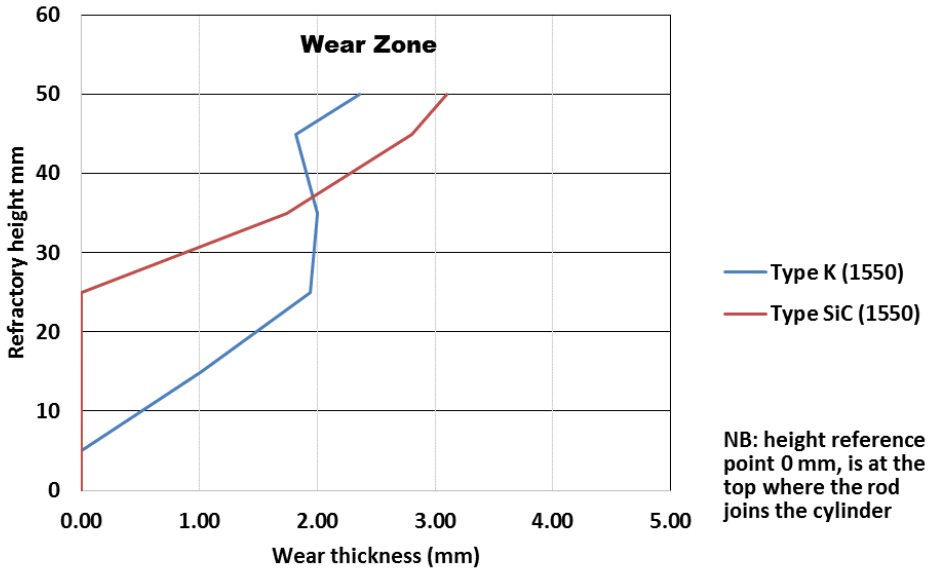

Figure 4.9: Dynamic wear analysis of the type K and SiC at 1550°C

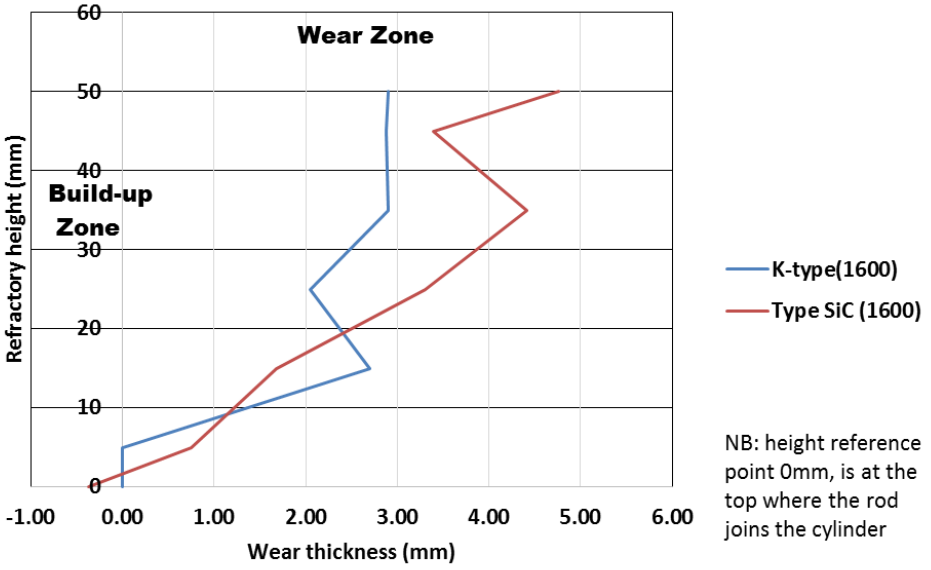

Figure 4.10: Dynamic wear analysis of the type K and SiC at 1600°C

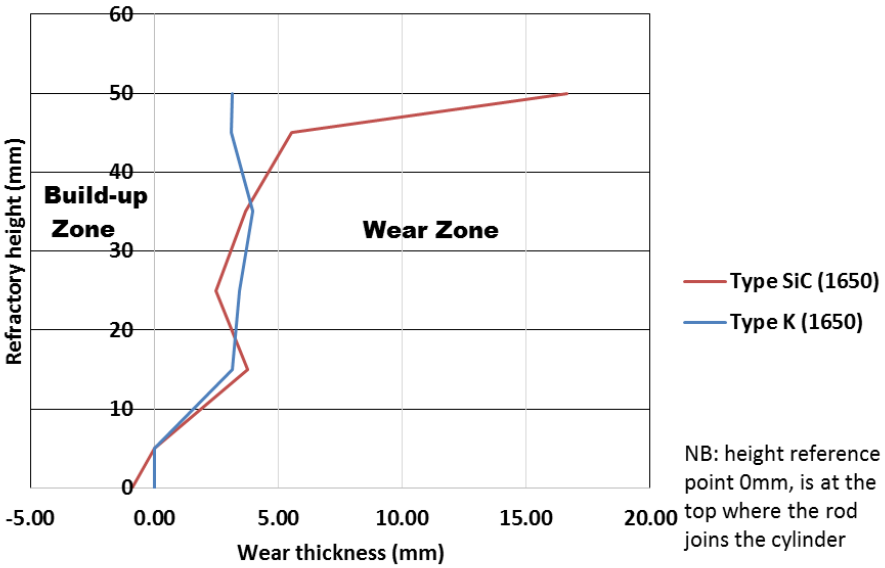

Figure 4.11: Dynamic wear analysis of the type K and SiC at 1650°C

4.4.3. Dynamic composition wear tests

In Figure 4.12 to Figure 4.14 it can be seen that the type SiC refractory still resulted in the most mechanical wear compared to the type K, despite FactSage™ predicting that it would have a decrease in wear with increasing mass % of Si in the alloy. The type SiC refractory experiences less mechanical wear compared to the dynamic temperature wear tests, with the maximum wear experienced at 18 mass % Si, where at 50 mm, 5.60 mm thickness was lost. The type K experienced a maximum wear at 17 mass % Si, where at 50 mm, 5.18 mm thickness was lost, and this was the most the K type had lost, relative to the temperature static and dynamic tests.

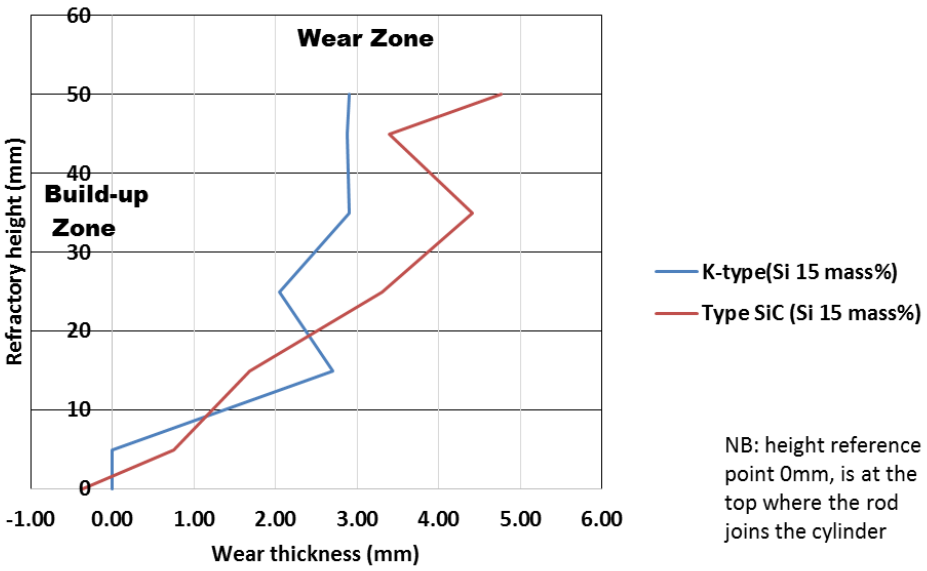

Figure 4.12: Dynamic wear analysis of the type K and SiC at Si 15 mass %

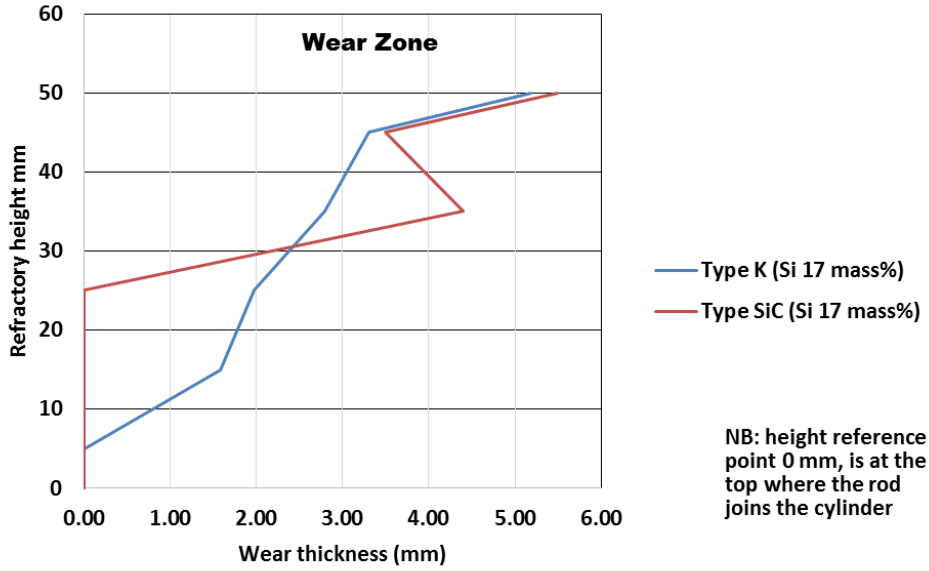

Figure 4.13: Dynamic wear analysis of the type K and SiC at Si 17 mass %

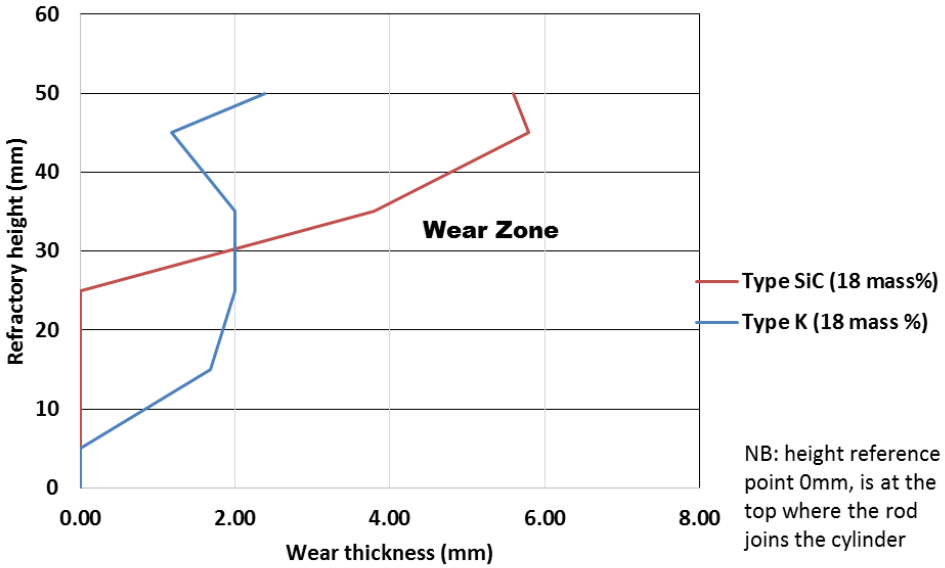

Figure 4.14: Dynamic wear analysis of the type K and SiC at Si 18 mass %

4.4.4. Mechanical wear analysis per refractory per variable

In Figure 4.15 and Figure 4.16 it can be seen that both the type K and SiC respectively, follow the FactSage™ observation, where refractory wear increases with increasing temperature. In Figure 4.17 the refractory wear is seen to increase with increasing mass % of Si from 15 to 17 mass %, and there-after the refractory wear decreases.

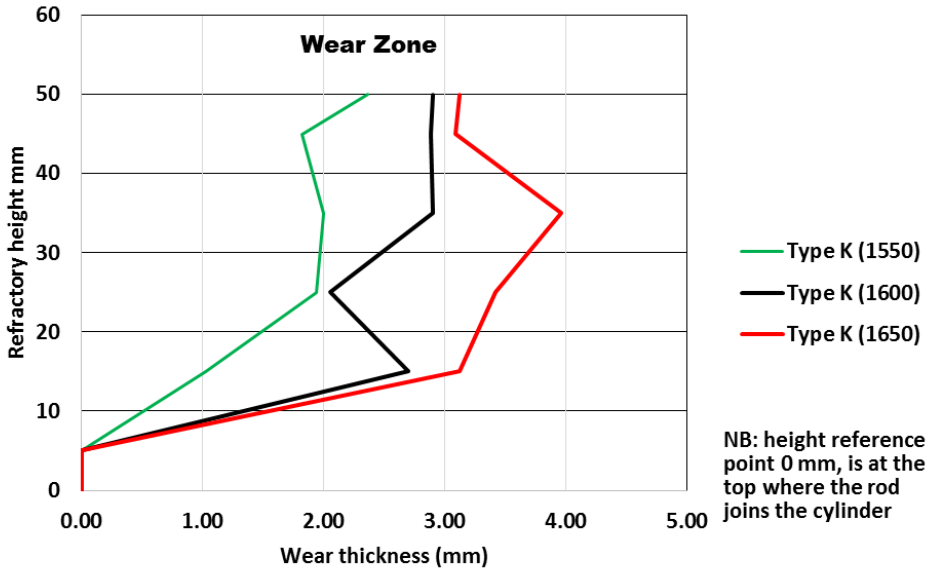

Figure 4.15: Dynamic type K refractory analysis when temperature is varied

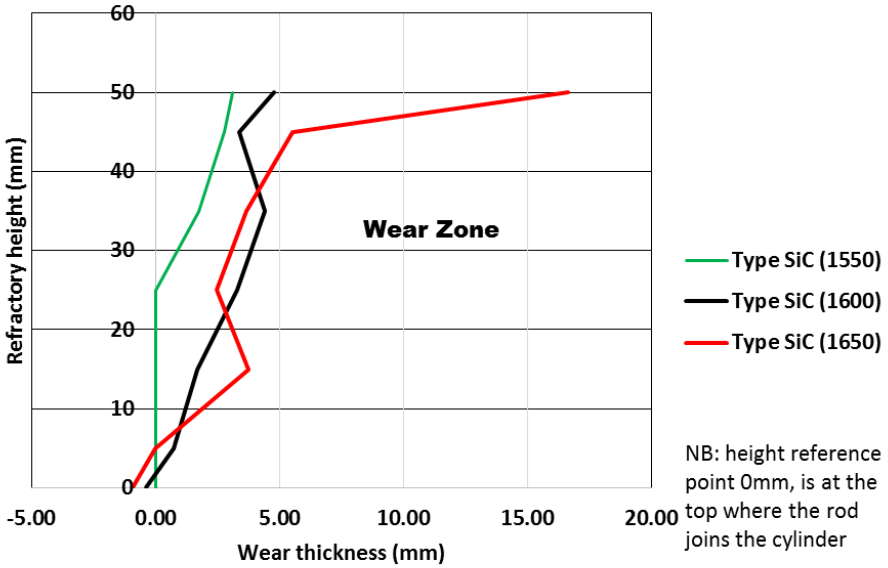

Figure 4.16: Dynamic type SiC refractory analysis when temperature is varied

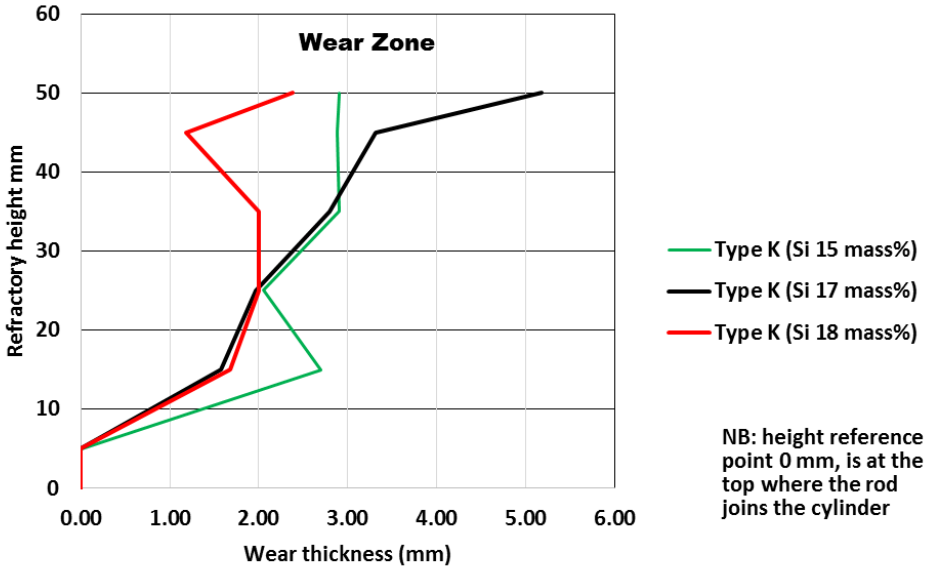

Figure 4.17: Dynamic type K refractory analysis when Si content is varied

In Figure 4.18 type SiC refractory is seen to increase in wear with increase in the mass % of Si. As discussed in Section 4.4.3, this thickness loss was relatively lower than the dynamic and static temperature tests, but was still not in agreement with FactSage™ due to the porous nature of the type SiC, allowing infiltration of the alloy.

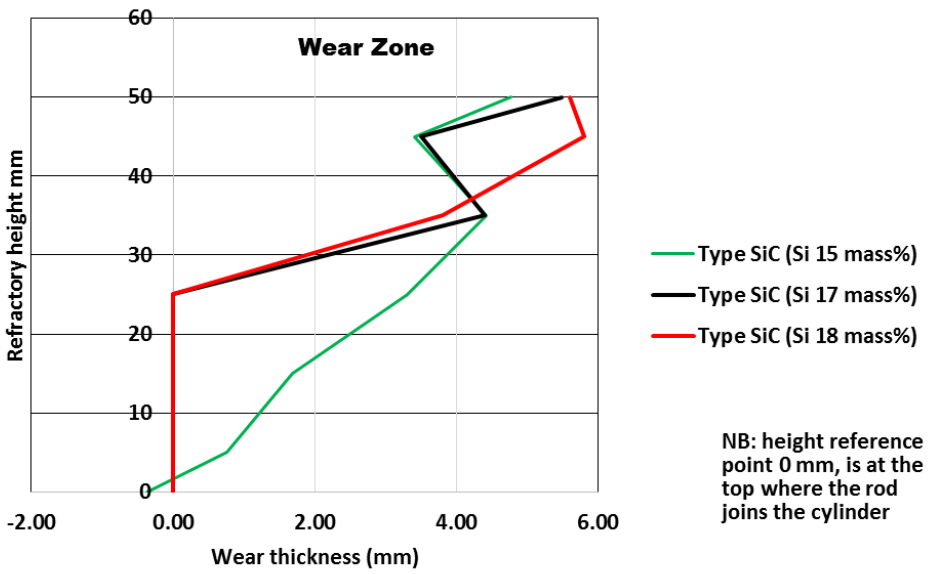

Figure 4.18: Dynamic type SiC refractory analysis when Si content is varied

4.4.5. Mechanical wear analysis per refractory focusing at the static and dynamic conditions when temperature and alloy composition is kept constant.

In Figure 4.19 it can be observed that for the type K refractory, dynamic conditions resulted in minor wear increase with the dynamic and static wear thickness of 2.90 mm and 2.81 mm respectively, with a 0.09 mm increase due to erosion. It can also be seen that the dynamic conditions also resulted in minor wear increase in the type SiC with the dynamic and static wear thickness of 4.77 mm and 4.69 mm respectively, with a 0.08 mm increase due to erosion. In both cases the dynamic curves are relatively furthest to the right, indicating that at different refractory height, more wear took place during the dynamic conditions and this is expected due to the addition erosion wear.

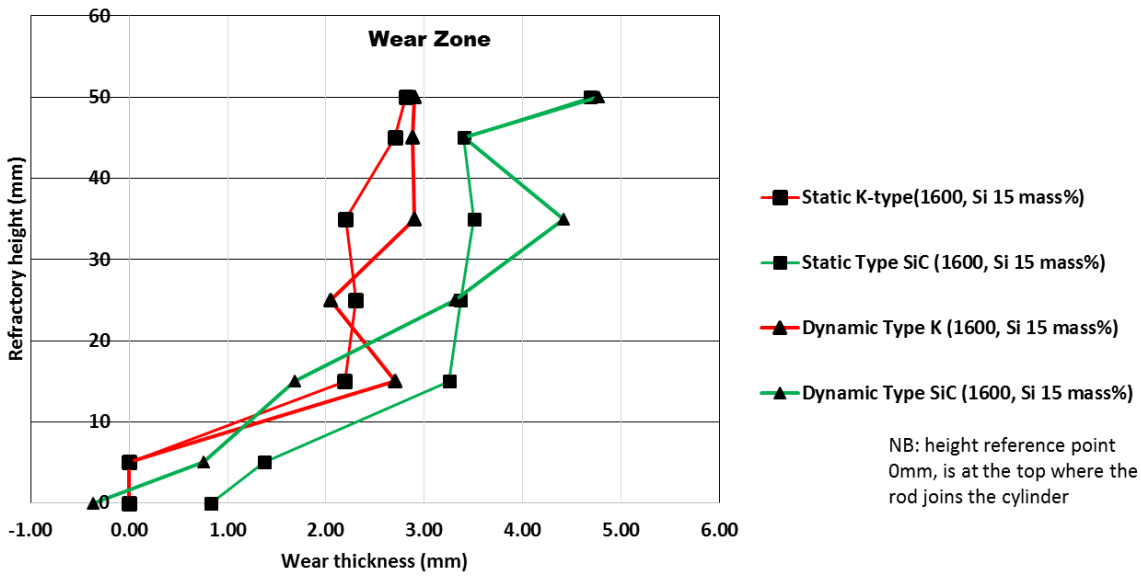

Figure 4.19: Mechanical wear analysis comparison of the dynamic and static, type K and SiC refractory at 1600°C and Si 15 mass%.

4.5. Validating thermodynamic temperature with static tests

Section 0 contains the results from static wear tests conducted to validate the FactSage™ observation in Section 6.2.

4.5.1. Test 1- static-type K at 1550°C

Section 4.5.1 contains SEM-EDS results for test 1 on the type K refractory at 1550°C. Figure 4.20 shows the three areas selected on the refractory cylinder that were in contact with the SiMn alloy and were analysed using the SEM-EDS.

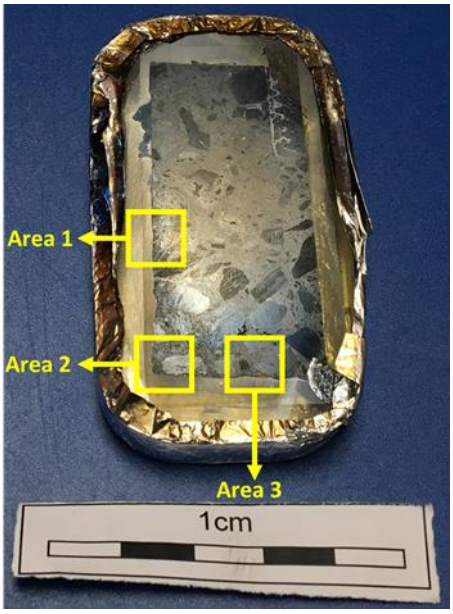

Figure 4.20: Test 1 cross section of the post mortem refractory and areas examined for wear

The static type K SEM-EDS images at 1550° C in Figure 4.20, 4.22 and 4.23 infiltration of SiMn alloy in the refractory can be observed, with the highest SiMn densities identified by bright white areas on the refractory interface, and low SiMn densities in the scattered white areas. The type K extent in wear at 1550°C is in stage 2 evidenced by surface infiltration of the alloy which is greater than 100 microns (Brosnan, 2004).

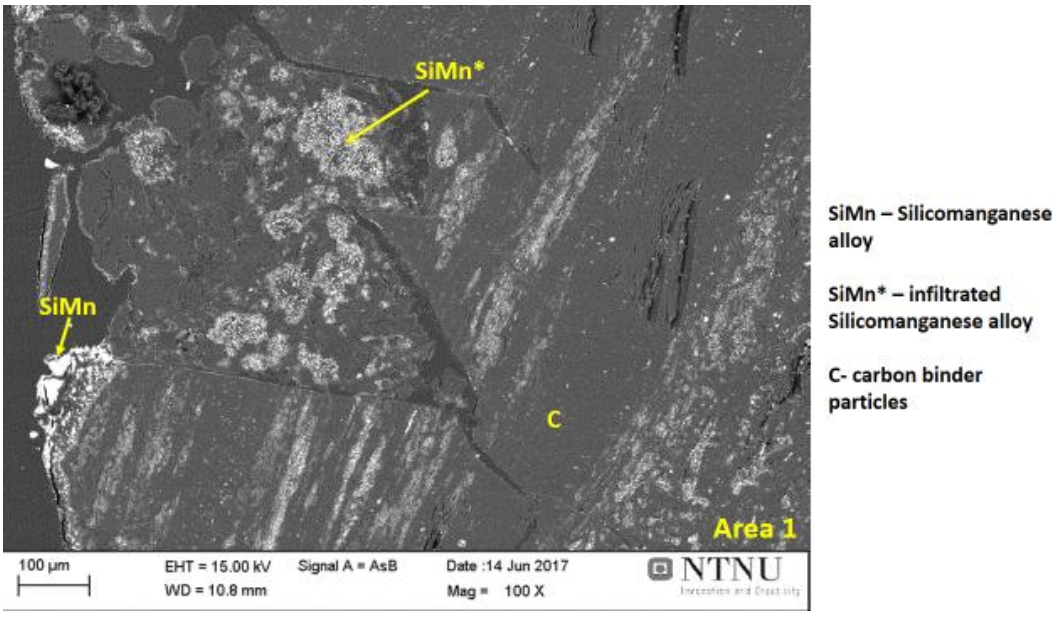

Figure 4.21: Test 1, area 1, K-type Refractory SEM image measured at 15 kV acceleration voltage. Scale bar indicates 100 µm.

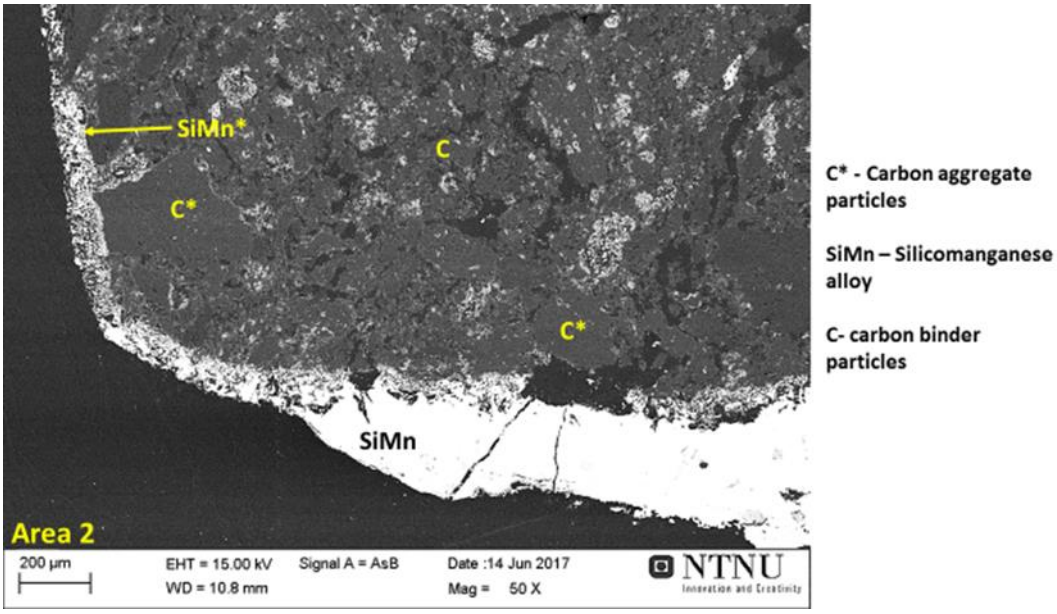

Figure 4.22: Test 1, area 2, K-type Refractory SEM image measured at 15 kV acceleration voltage. Scale bar indicates 200 µm.

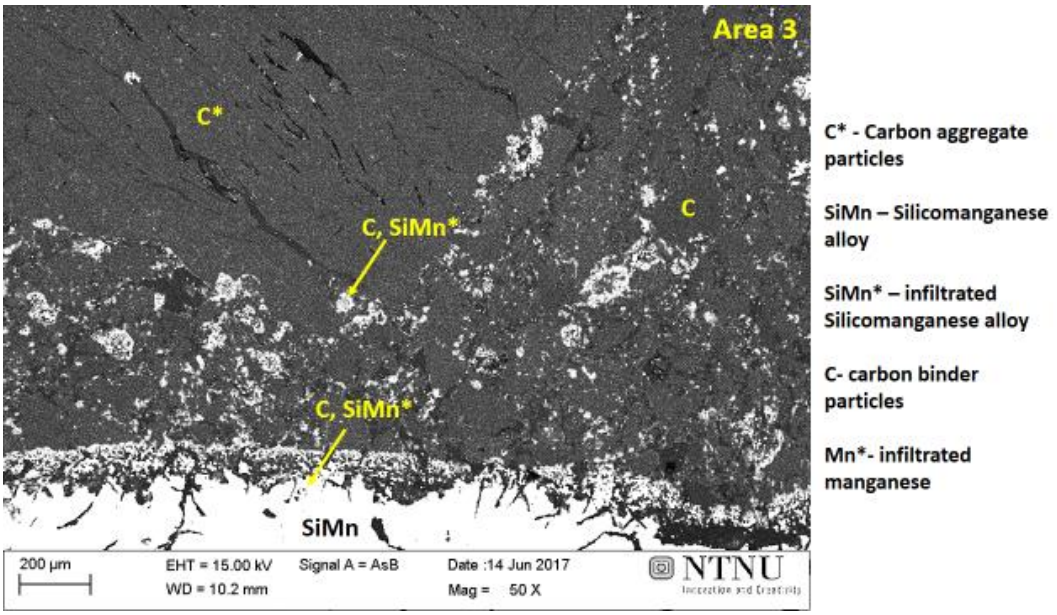

Figure 4.23: Test 1, area 3, K-type Refractory SEM image measured at 15 kV acceleration voltage. Scale bar indicates 200 µm.

4.5.2. Test 2- static- type K at 1600°C

Section 4.5.2 contains SEM-EDS results for test 2 on the type K refractory at 1600°C. Figure 4.24 shows the three areas selected on the refractory cylinder that were in contact with the SiMn alloy and were analysed using the SEM-EDS.

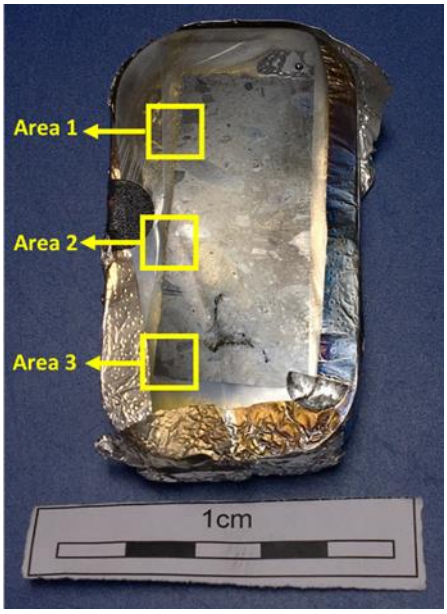

Figure 4.24: Test 2 cross section of the post mortem refractory and areas examined for wear

It is evident in Figure 4.25, 4.26 and 4.27 that infiltration of Type-K refractory by SiMn alloy in the refractory took place. The highest SiMn densities can be identified by bright white areas on the refractory interface, and low SiMn densities in the scattered white areas. The type K extent in wear at 1600°C is in stage 2 evidenced by surface infiltration of the alloy which is greater than 100 microns.

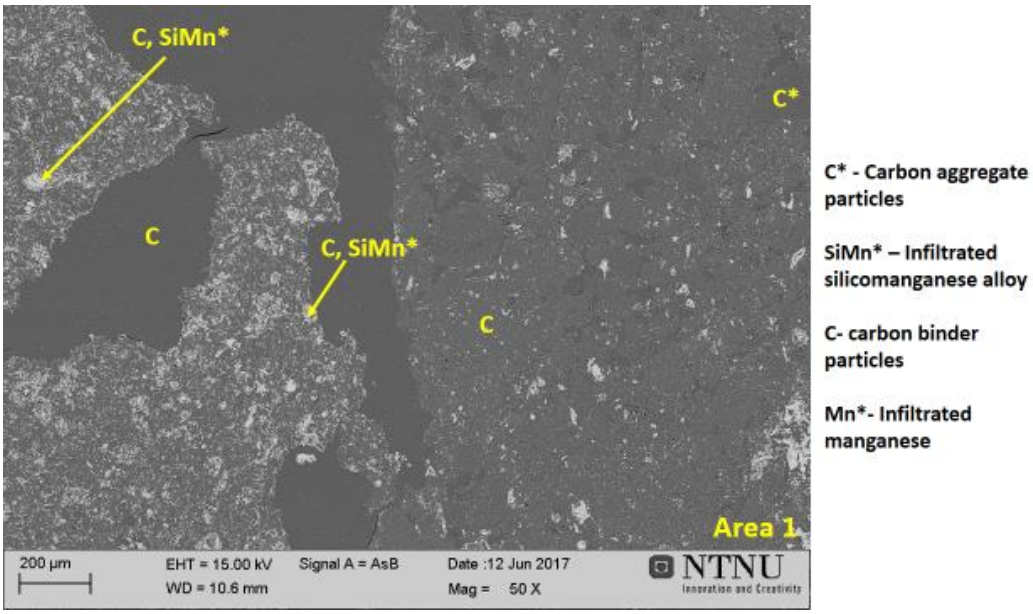

Figure 4.25: Test 2, area 1, K-type Refractory SEM image measured at 15 kV acceleration voltage. Scale bar indicates 200 µm.

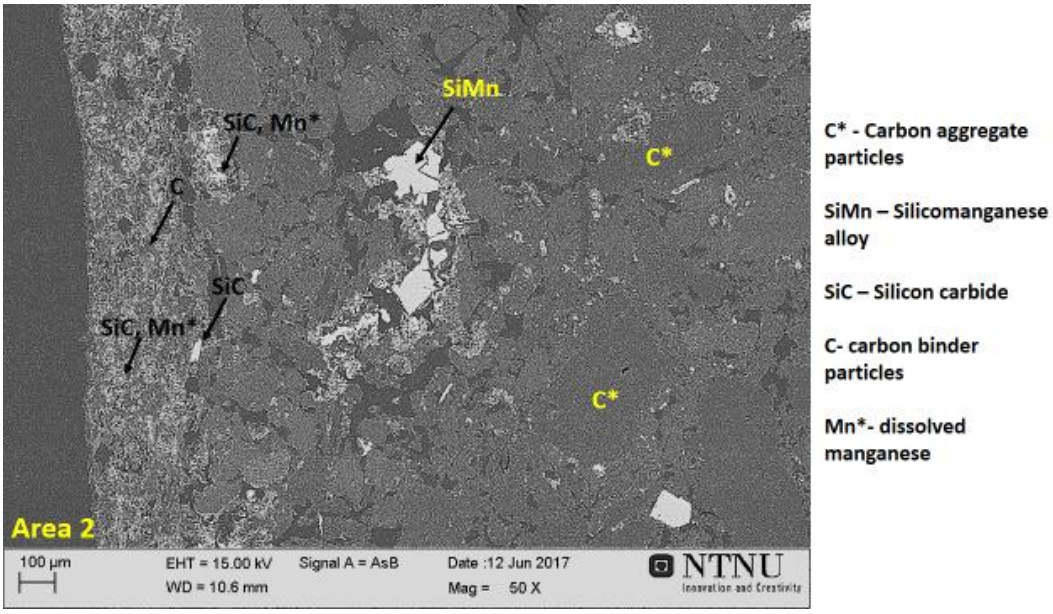

Figure 4.26: Test 2, area 2, K-type Refractory SEM image measured at 15 kV acceleration voltage. Scale bar indicates 200 µm.

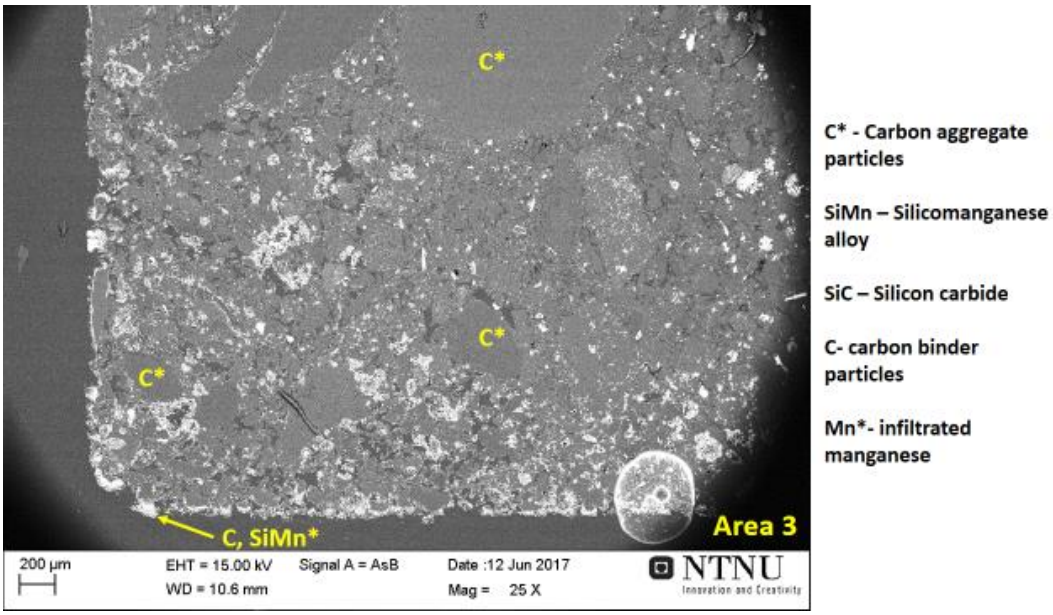

Figure 4.27: Test 2, area 3, K-type Refractory SEM image measured at 15 kV acceleration voltage. Scale bar indicates 200 µm.

4.5.3. Test-3 static- type K at 1650°C

Section 4.5.3 contains SEM-EDS results for test 3 on the type K refractory at 1650°C. Figure 4.28 shows the two areas selected on the refractory cylinder that were in contact with the SiMn alloy and were analysed using the SEM-EDS.

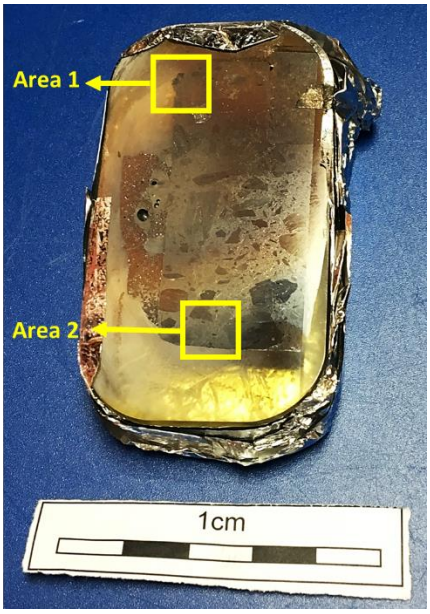

Figure 4.28: Test 3 cross section of the post mortem refractory and areas examined for wear

It is evident in Figure 4.29 and 4.30 that infiltration of SiMn alloy in the refractory takes place. The highest SiMn densities can be identified by bright white areas on the refractory interface, and low SiMn densities in the scattered white areas. The type K extent in wear at 1650°C is in stage 2 evidenced by surface infiltration of the alloy which is greater than 100 microns.

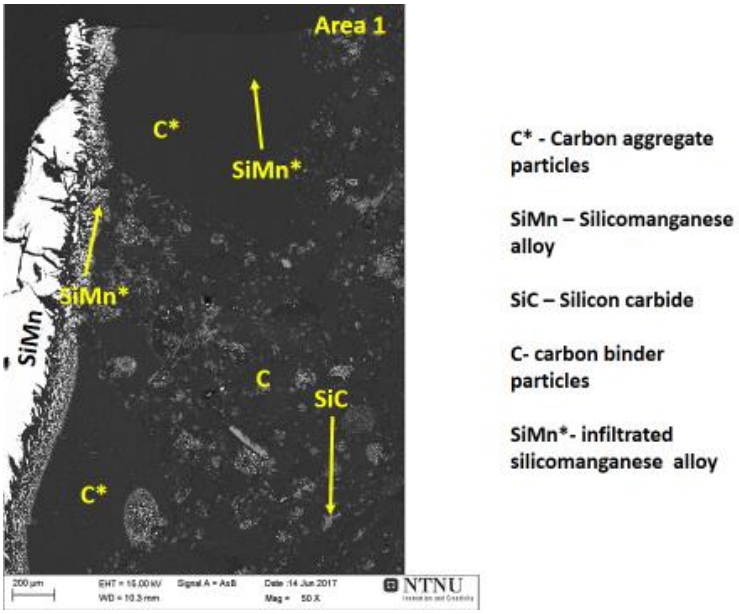

Figure 4.29: Test 3, area 1, K-type Refractory SEM image measured at 15 kV acceleration voltage. Scale bar indicates 200 μm.

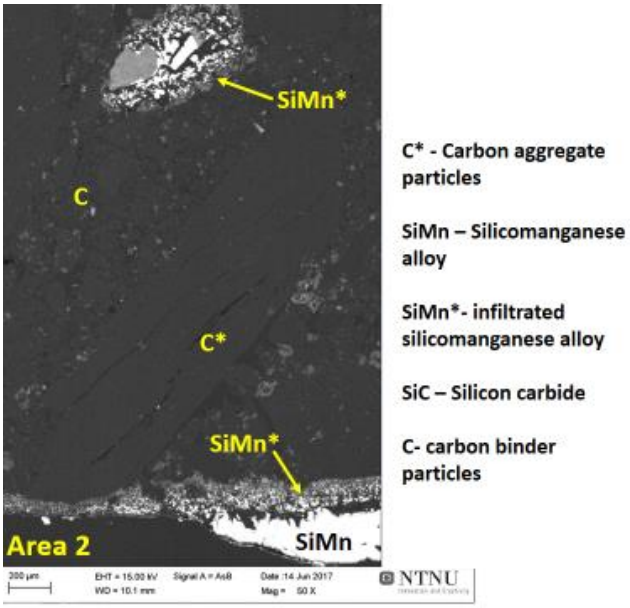

Figure 4.30: Test 3, area 2, K-type Refractory SEM image measured at 15 kV acceleration voltage. Scale bar indicates 200 μm.

4.5.4. Test 4 -static-type SiC at 1550°C

Section 4.5.4 contains SEM-EDS results for test 2 on the type SiC refractory at 1550°C. Figure 4.31 shows the three areas selected on the refractory cylinder that were in contact with the SiMn alloy and were analyzed using the SEM-EDS. It was observed that the major driving force on the wear mechanism was corrosion due to dissolution of the carbon binder particles and SiC aggregates by SiMn. This is evident in Figure 4.32, 4.33 and 4.34, where infiltration of SiMn alloy in the refractory is observed. The type SiC extent in wear at 1550°C is in stage 2 evidenced by surface infiltration of the alloy which is greater than 100 microns.

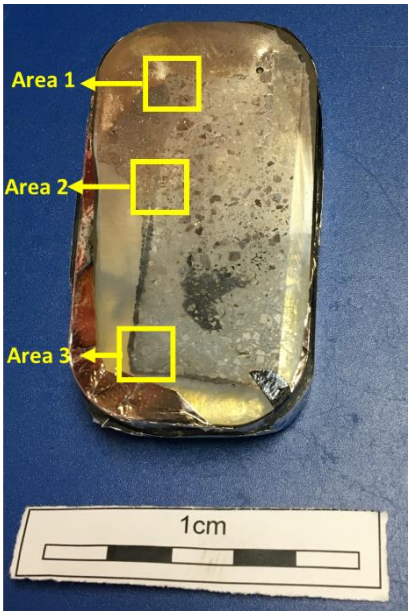

Figure 4.31: Test 4 cross section of the post mortem refractory and areas examined for wear

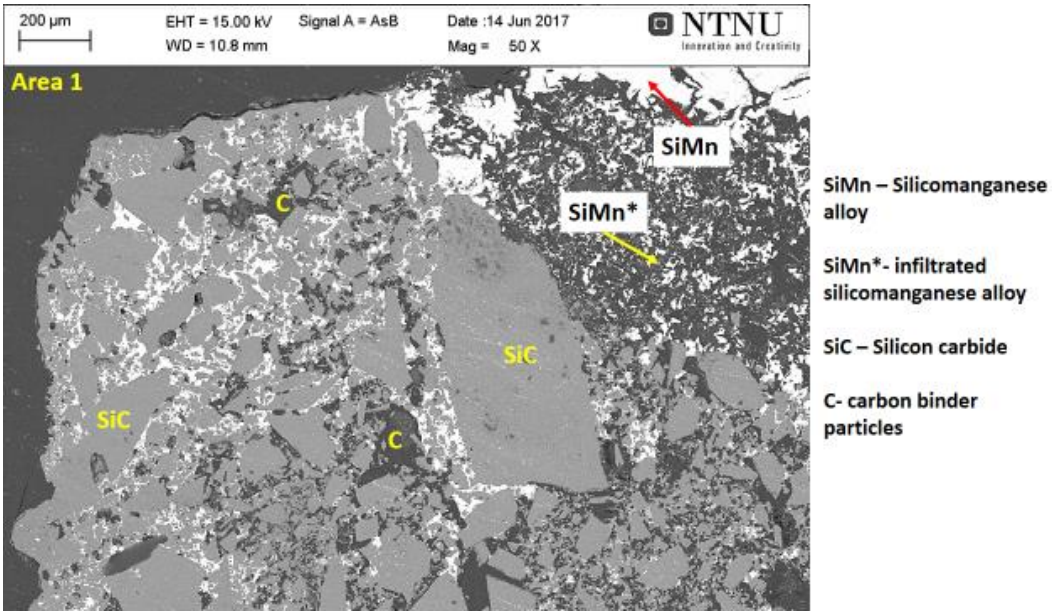

Figure 4.32: Test 4, area 1, SiC-type Refractory SEM image measured at 15 kV acceleration voltage. Scale bar indicates 200 µm.

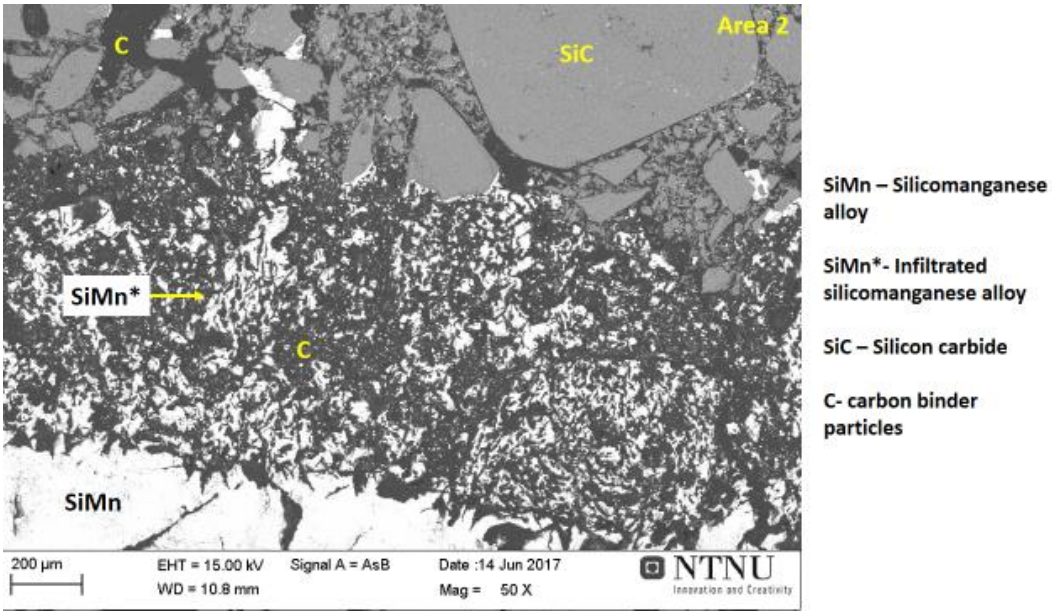

Figure 4.33: Test 4, area 2, SiC-type Refractory SEM image measured at 15 kV acceleration voltage. Scale bar indicates 200 µm.

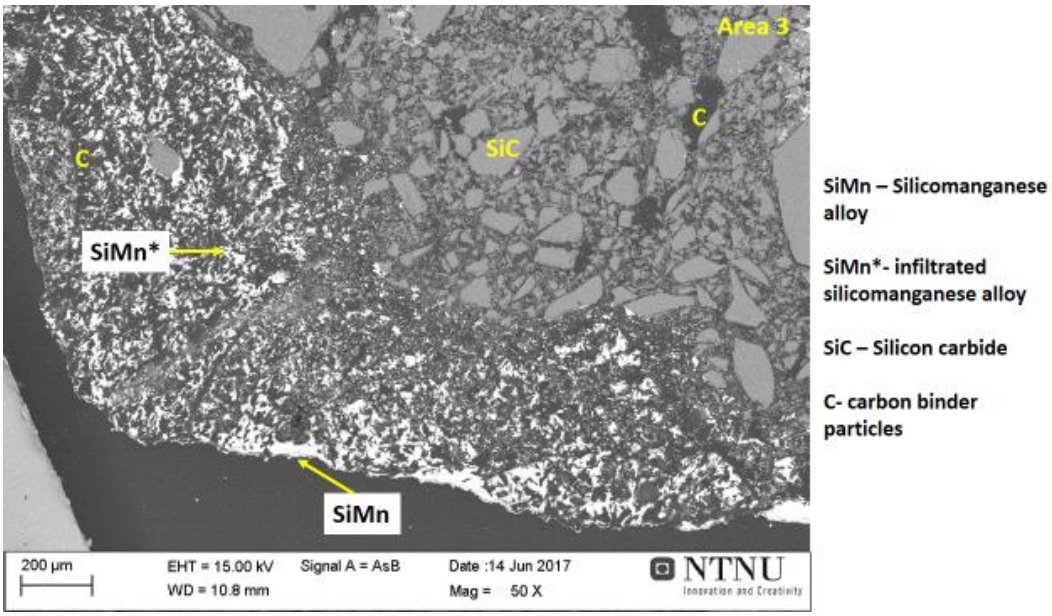

Figure 4.34: Test 4, area 3, SiC-type Refractory SEM image measured at 15 kV acceleration voltage. Scale bar indicates 200 µm.

4.5.5. Test 5-static-Type SiC at 1600°C

Section 4.5.5 contains SEM-EDS results for test 2 on the type SiC refractory at 1600°C. Figure 4.35 shows the two areas selected on the refractory cylinder that were analyzed using the SEM-EDS. Area 1 (Figure 4.36) was chosen to observe extent of infiltration and area 2 (Figure 4.37) as it was in contact with liquid alloy. It was observed that in area 1 the infiltration did not go further into the refractory cylinder and it was mainly around the refractory walls. In area 2 it was observed that there were no reaction products, hence the main driver for the wear mechanism was also corrosion due to dissolution of the C binder in the refractory material which resulted in carbon particles being displaced. The type SiC extent in wear at 1600°C is in stage 2 evidenced by surface infiltration of the alloy which is greater than 100 microns.

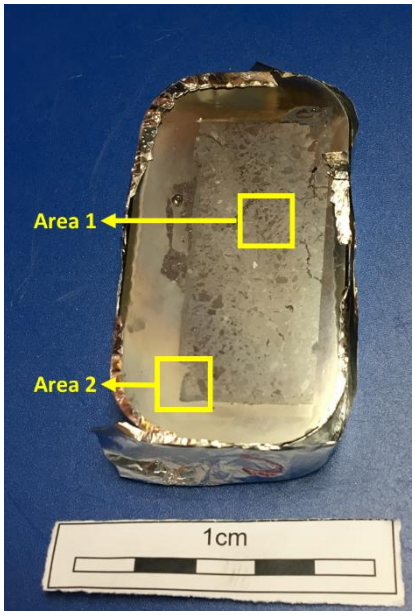

Figure 4.35: Test 5 cross section of the post mortem refractory and areas examined for wear

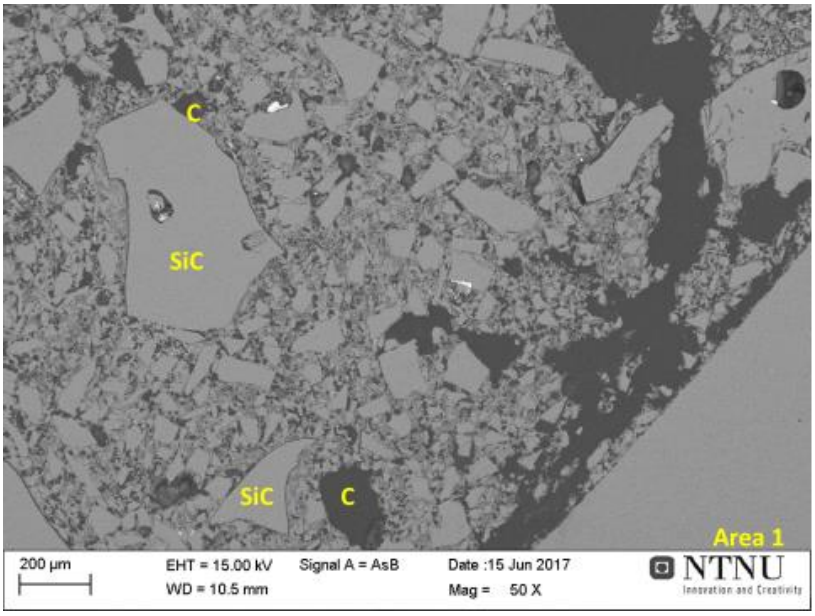

Figure 4.36: Test 5, area 1, SiC-type Refractory SEM image measured at 15 kV acceleration voltage. Scale bar indicates 200 µm.

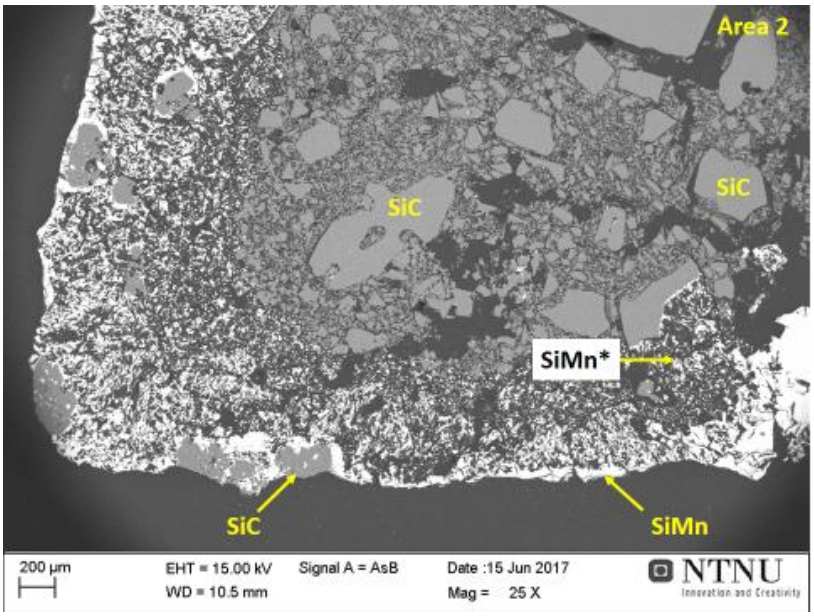

Figure 4.37: Test 5, area 2, SiC-type Refractory SEM image measured at 15 kV acceleration voltage. Scale bar indicates 200 µm.

4.5.6. Test 6-static-type SiC at 1650°C

Section 4.5.6 contains SEM-EDS results for test 2 on the type SiC refractory at 1600°C. Type SiC at 1650°C the infiltration of the alloy was observed to have a similar pattern as in test 4 and test 5 at 1550°C and 1600°C respectively. Three areas were selected as seen in Figure 4.38, namely, area 1 (Figure 4.39), area 2 (Figure 4.40) and area 3 (Figure 4.41). Area 2 was

selected to check the extent of infiltration in the refractory cylinder, and it was observed that in area 2 the infiltration did not go further into the refractory cylinder and it was mainly around the refractory walls. The type SiC extent in wear at 1650°C is in stage 2 evidenced by surface infiltration of the alloy which is greater than 100 microns.

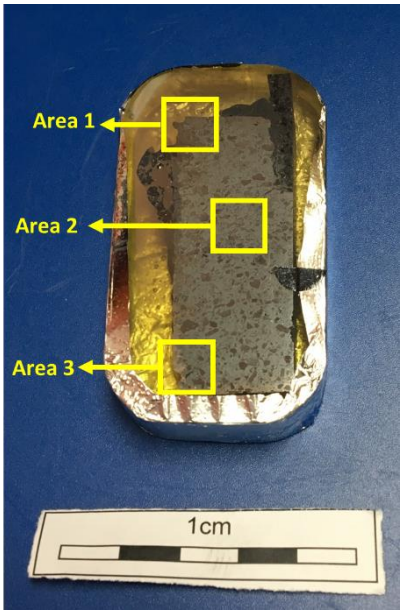

Figure 4.38: Test 6 cross section of the post mortem refractory and areas examined for wear

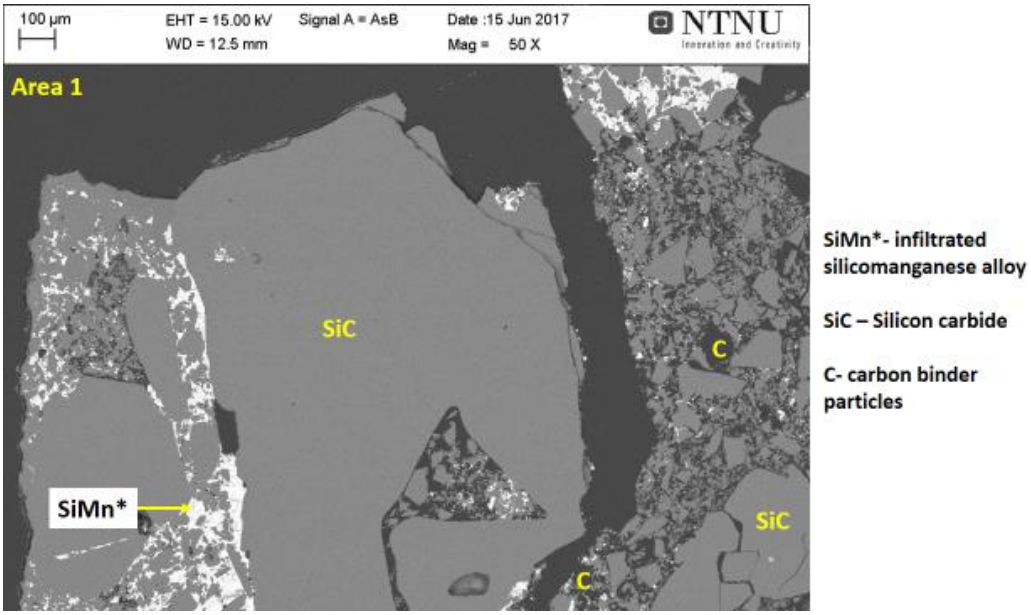

Figure 4.39: Test 6, area 1, SiC-type Refractory SEM image measured at 15 kV acceleration voltage. Scale bar indicates 200 µm.

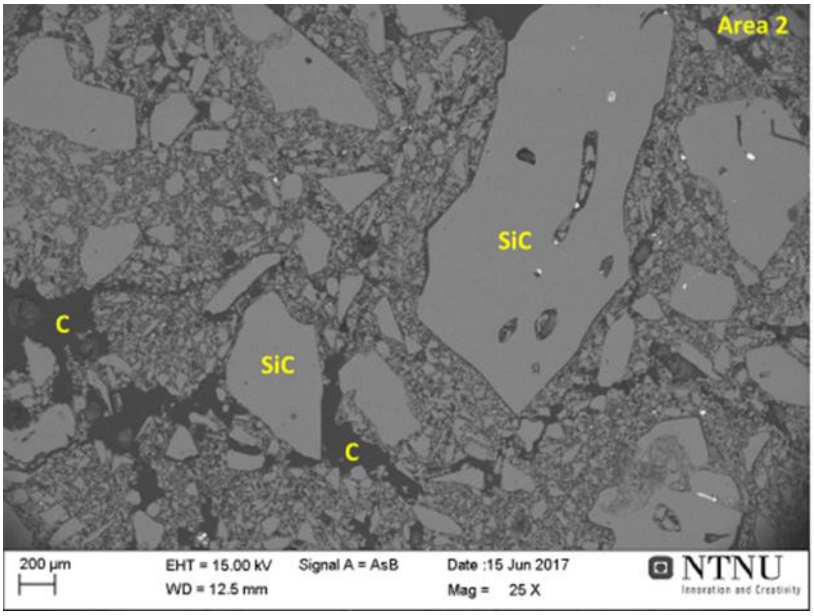

Figure 4.40: Test 6, area 2, SiC-type Refractory SEM image measured at 15 kV acceleration voltage. Scale bar indicates 200 µm.

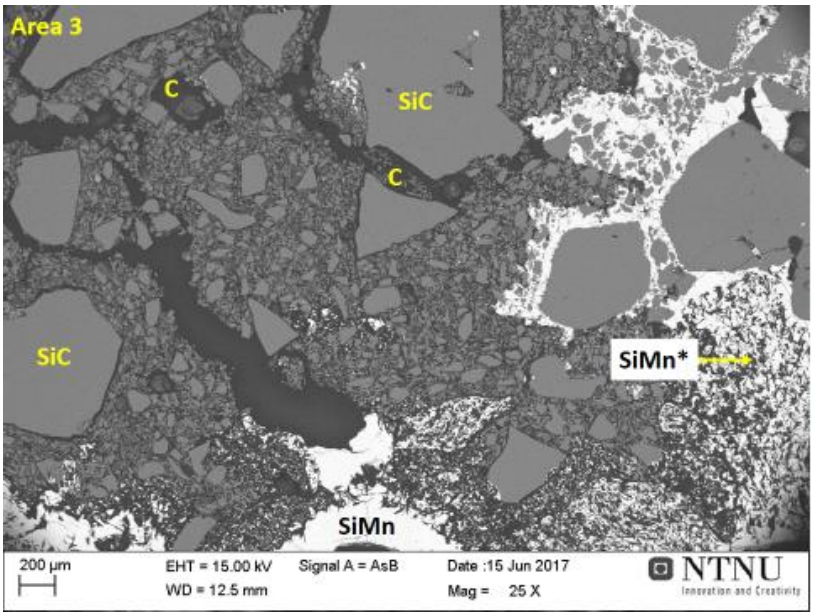

Figure 4.41: Test 6, area 3, SiC-type Refractory SEM image measured at 15 kV acceleration voltage. Scale bar indicates 200 µm.

4.6. SEM-EDS analysis of the refractory wear under dynamic conditions

Section 4.6 reports the SEM-EDS results from the dynamic wear analysis of the refractory wear, when temperature was varied between 1550°C, 1600°C and 1650°C, and Si content at 16 mass % or 17 mass % with the baseline content at 15 mass % and the rotational speed was fixed at 100 rpm, and reaction time was fixed at 90 minutes.

4.6.1. Test 7 –dynamic-type K at 1550°C

Section 4.6.1 contains SEM-EDS results for test 7 on the type K refractory at 1550°C. In Figure 4.42, the cross section of the type K post-mortem refractory can be seen, and different sections were identified for SEM-EDS analysis.

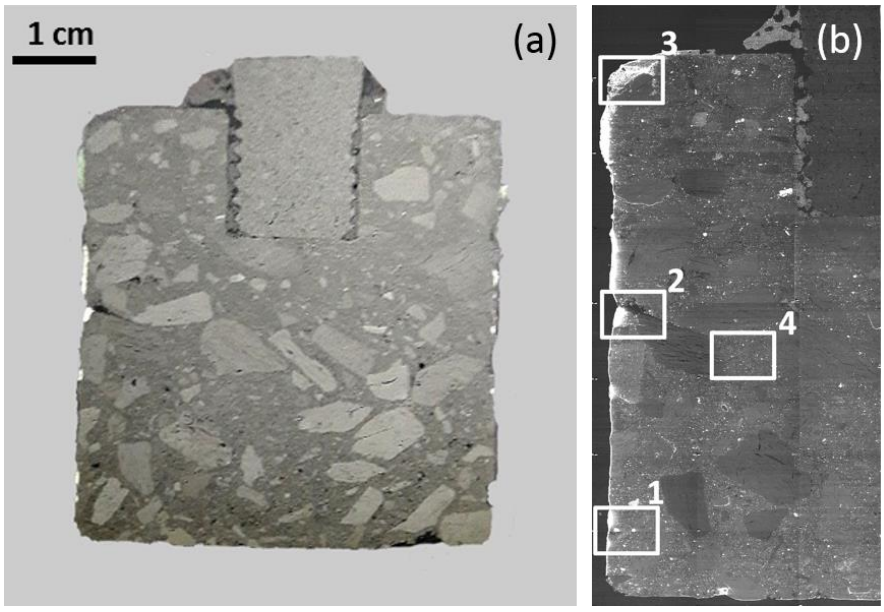

Figure 4.42: (a) Cross section of the test 7 type K post mortem refractory (b) areas examined examined for wear

In comparison to the static type K refractory SEM-EDS analysis at 1550°C in section 6.3.1, where no SiC precipitation could be identified, SiC could be clearly identified in the dynamic type K refractory, evident in Figure 4.43, Figure 4.44, and Figure 4.46. No SiC was observed in Figure 4.45 as it was at the top of the refractory cylinder and there was no direct contact with the SiMn alloy. Infiltration of the alloy in Figure 4.45 could have been the results of the alloy splashing during the refractory cylinder rotations. Alumina and calcium impurities were also identified in the refractory post-mortem investigation. The type K extent in wear at 1550°C is in stage 2, evidenced by surface infiltration of the alloy, which is greater than 100 microns.

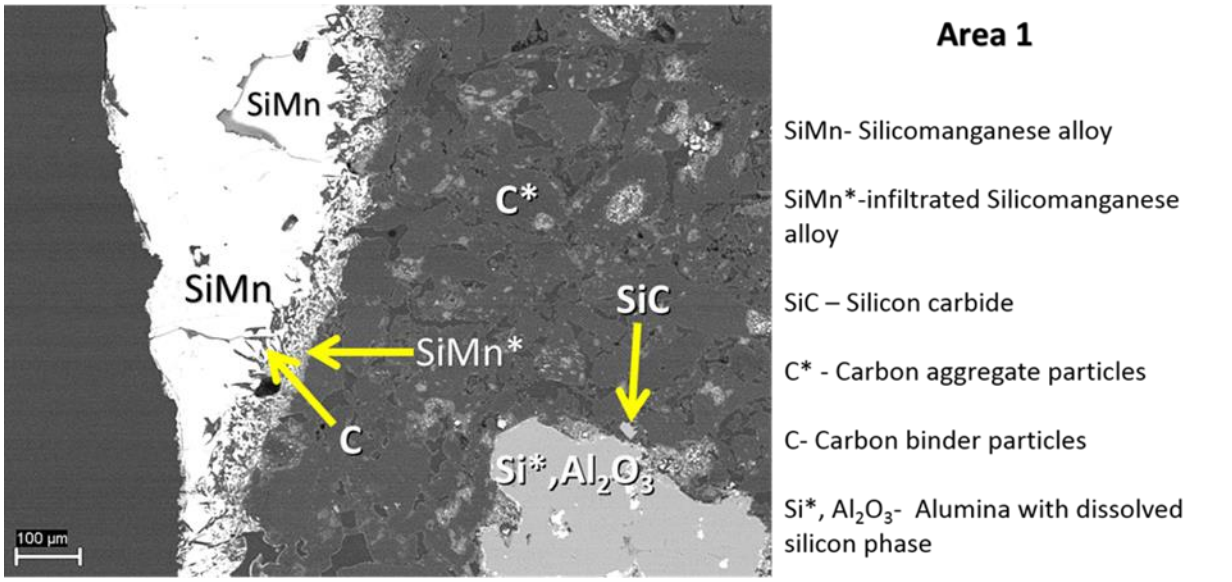

Figure 4.43: Test 7, area 1,-type K refractory SEM image measured at 15 kV acceleration voltage. Scale bar indicates 100 µm

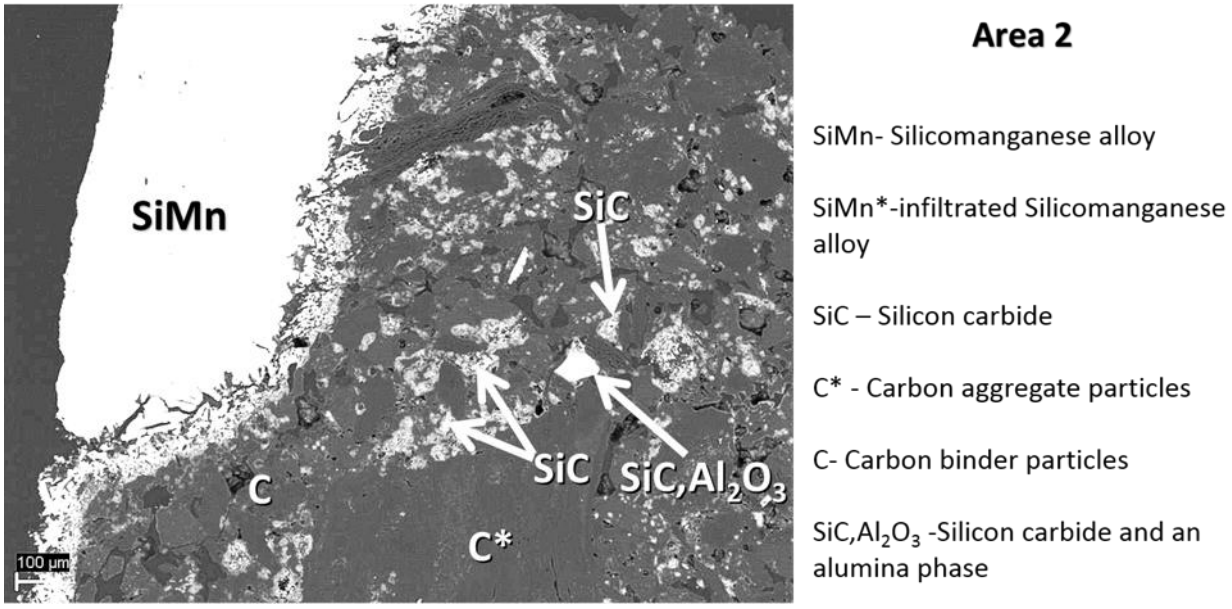

Figure 4.44: Test 7, area 2,-type K refractory SEM image measured at 15 kV acceleration voltage. Scale bar indicates 100 µm

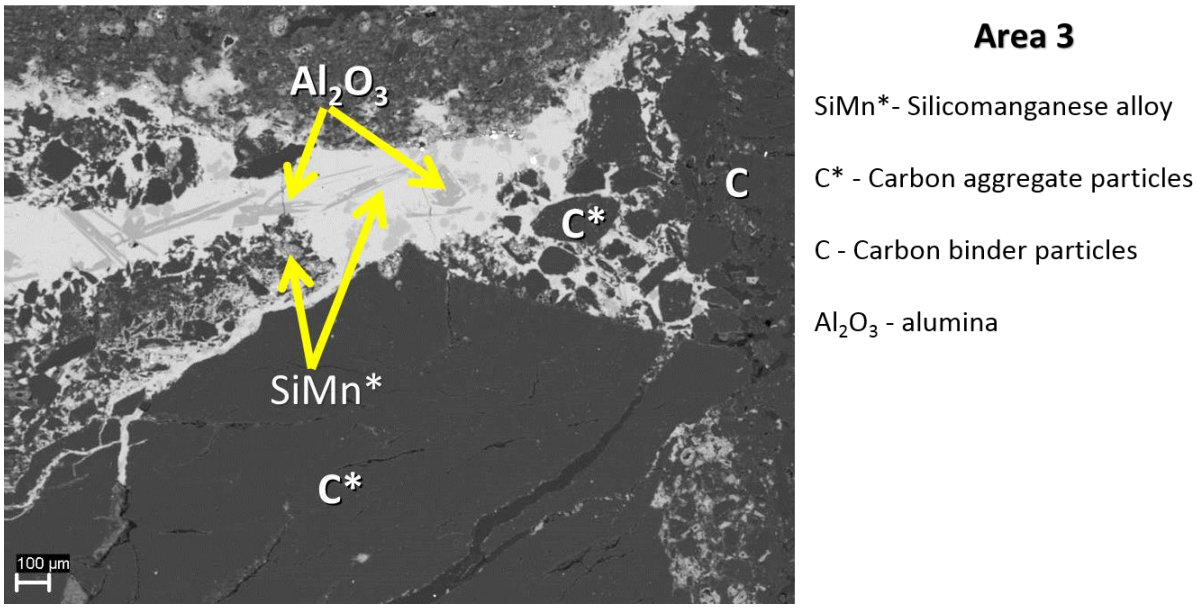

Figure 4.45: Test 7, area 3,-type K refractory SEM image measured at 15 kV acceleration voltage. Scale bar indicates 100 µm

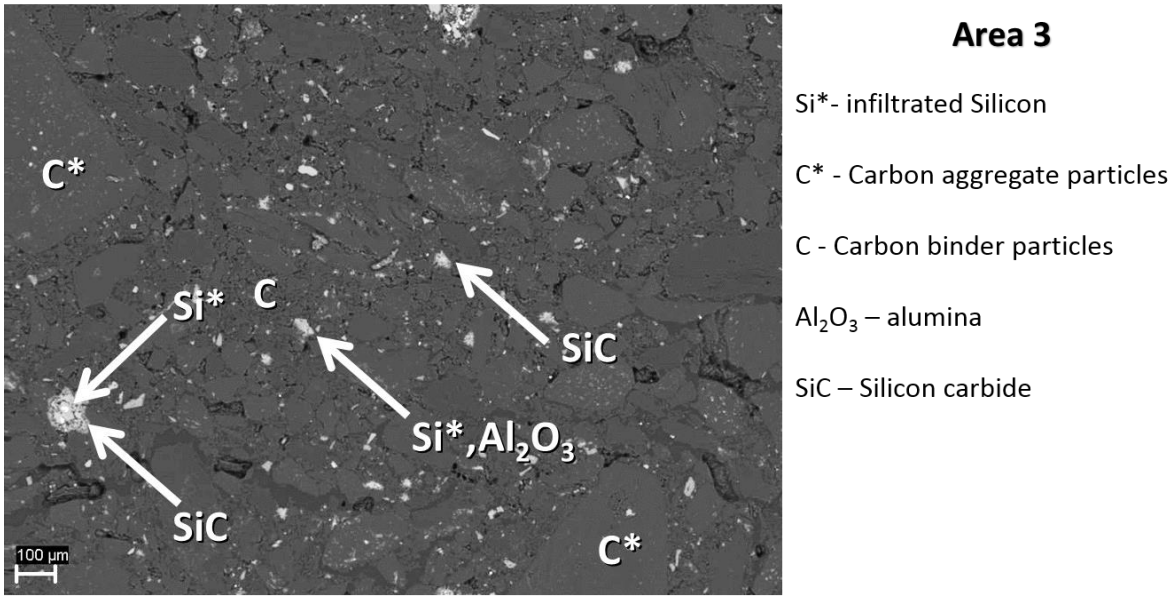

Figure 4.46: Test 7, area 4,-type K refractory SEM image measured at 15 kV acceleration voltage. Scale bar indicates 100 µm

4.6.2. Test 8-dynamic-type K at 1600°C

Section 4.6.2 contains SEM-EDS results for test 8 on the type K refractory at 1600°C. In Figure 4.47 the cross section of the type K post-mortem refractory can be seen with the sections that were identified for SEM-EDS analysis.

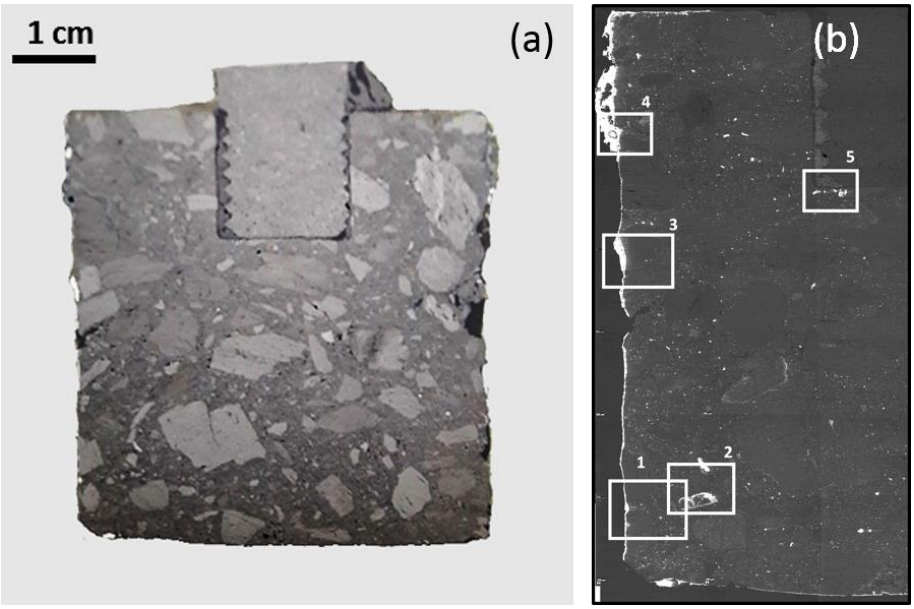

Figure 4.47: (a) Cross section of the test 8 type K post mortem refractory (b) areas examined for wear

In comparison to the static type K refractory analysis at 1600°C in section 6.3.2, where SiC precipitation was observed in Figure 4.26, SiC could also be clearly identified in the dynamic type K refractory. SiC precipitation could be identified on the alloy and refractory interface in Figure 4.44, which serves as evidence that SiC formed at the interface would be eroded away during refractory rotation. In Figure 4.49, dissolution of a carbon aggregate particle is observed and evidence of SiC precipitation can also be seen. In Figure 4.50, and Figure 4.51, only infiltration of the refractory cylinder is observed. Alloy infiltration to a greater distance was also observed in Figure 4.52 with evidence of corrosion due to both dissolution and SiC precipitation. The type K extent in wear at 1600°C is in stage 2 evidenced by surface infiltration of the alloy which is greater than 100 microns.

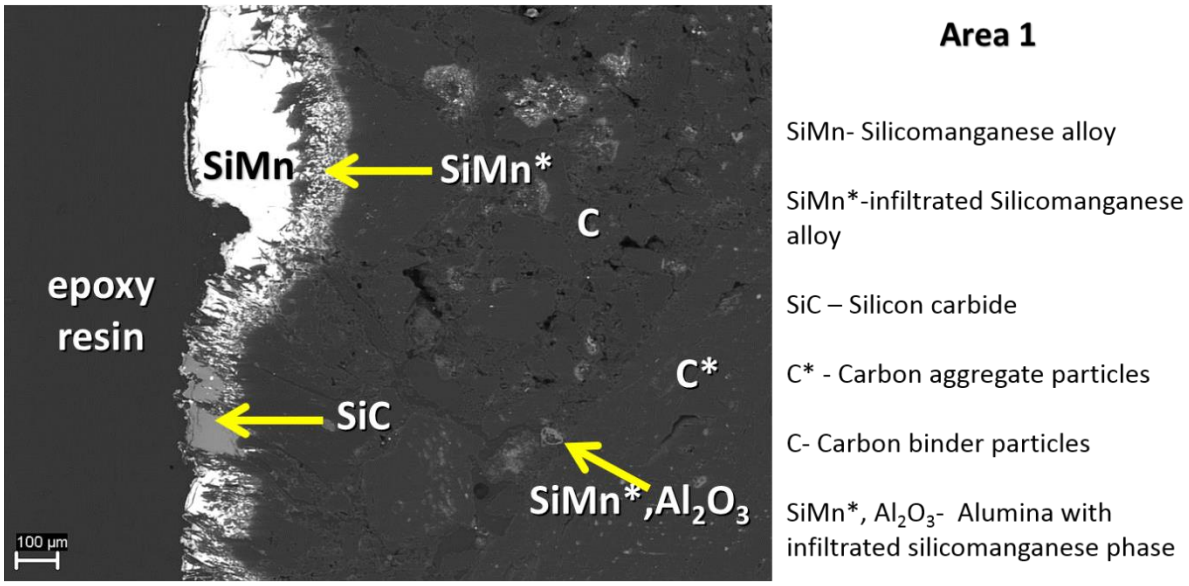

Figure 4.48: Test 8, area 1,-type K refractory SEM image measured at 15 kV acceleration voltage. Scale bar indicates 100 µm

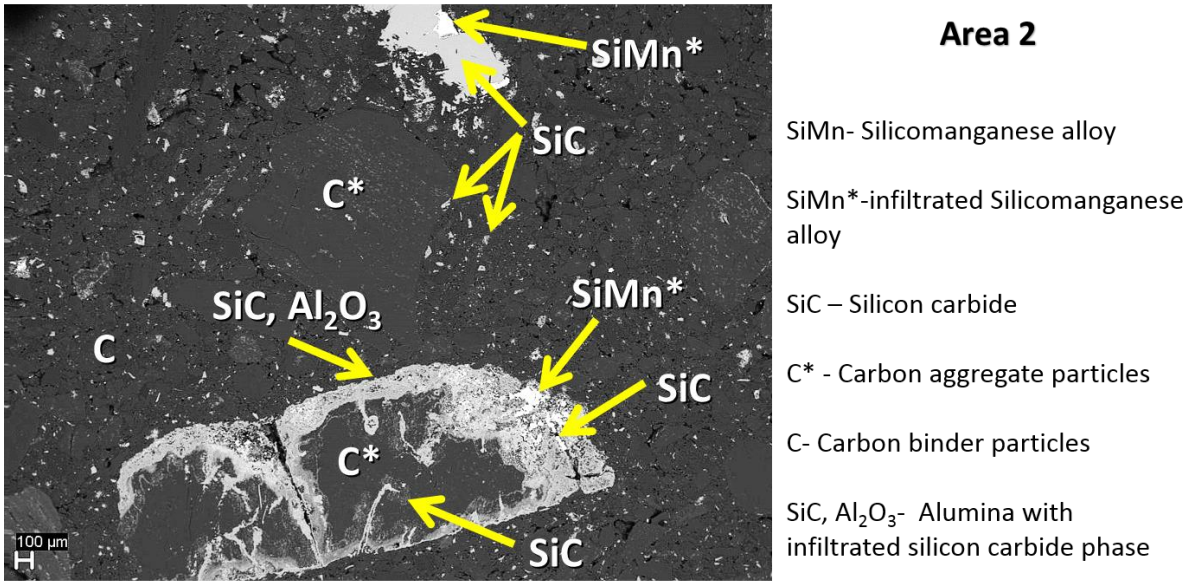

Figure 4.49: Test 8, area 2,-type K refractory SEM image measured at 15 kV acceleration voltage. Scale bar indicates 100 µm

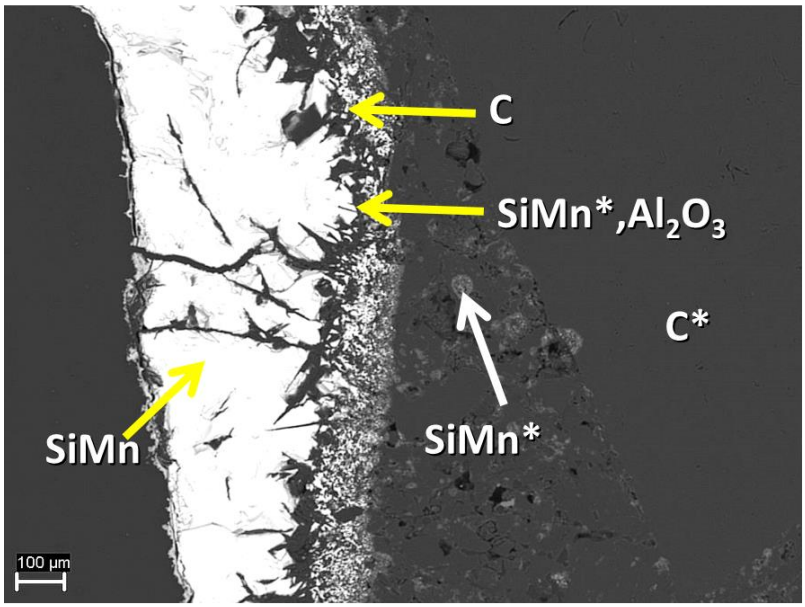

Area 3

SiMn- Silicomanganese alloy

SiMn*-infiltrated Silicomanganese alloy

SiC – Silicon carbide

C* - Carbon aggregate particles

C- Carbon binder particles

SiMn*, Al_2O_3- Alumina with infiltrated silicomanganese phase

Figure 4.50: Test 8, area 3,-type K refractory SEM image measured at 15 kV acceleration voltage. Scale bar indicates 100 µm

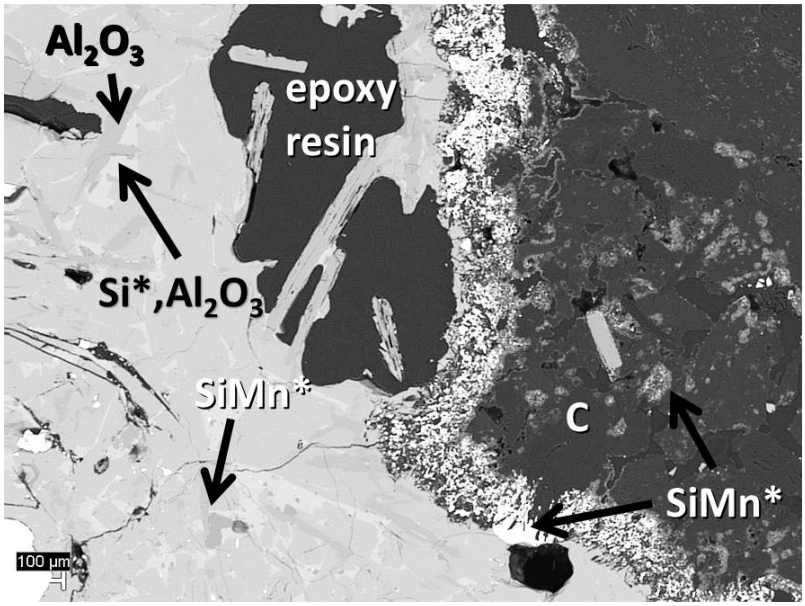

Area 4

SiMn*-infiltrated Silicomanganese alloy

SiC – Silicon carbide

C* - Carbon aggregate particles

C- Carbon binder particles

Si*, Al_2O_3- Alumina with infiltrated silicon phase

Figure 4.51: Test 8, area 4,-type K refractory SEM image measured at 15 kV acceleration voltage. Scale bar indicates 100 µm

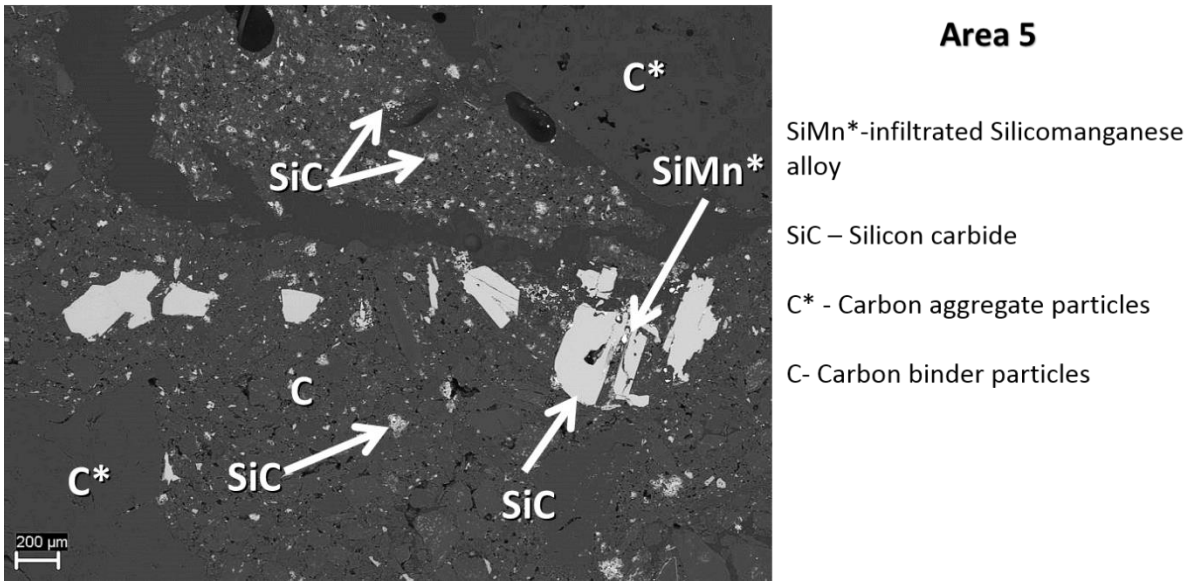

Figure 4.52: Test 8, area 5,-type K refractory SEM image measured at 15 kV acceleration voltage. Scale bar indicates 200 µm

4.6.3. Test 9- dynamic-type K at 1650°C:

Section 0 contains SEM-EDS results for test 9 on the type K refractory at 1650°C. In Figure 4.53 the cross section of the type K post-mortem refractory can be seen with the sections that were identified for SEM-EDS analysis. In comparison to the static type K refractory analysis at 1650°C in section 6.3.3, where SiC precipitation was observed in Figure 4.26, SiC could also be clearly identified in the dynamic type K refractory in Figure 4.56 to Figure 4.58. In Figure 4.55 only infiltration of the alloy is observed. The type K extent in wear at 1650°C is in stage 2 evidenced by surface infiltration of the alloy which is greater than 100 microns.

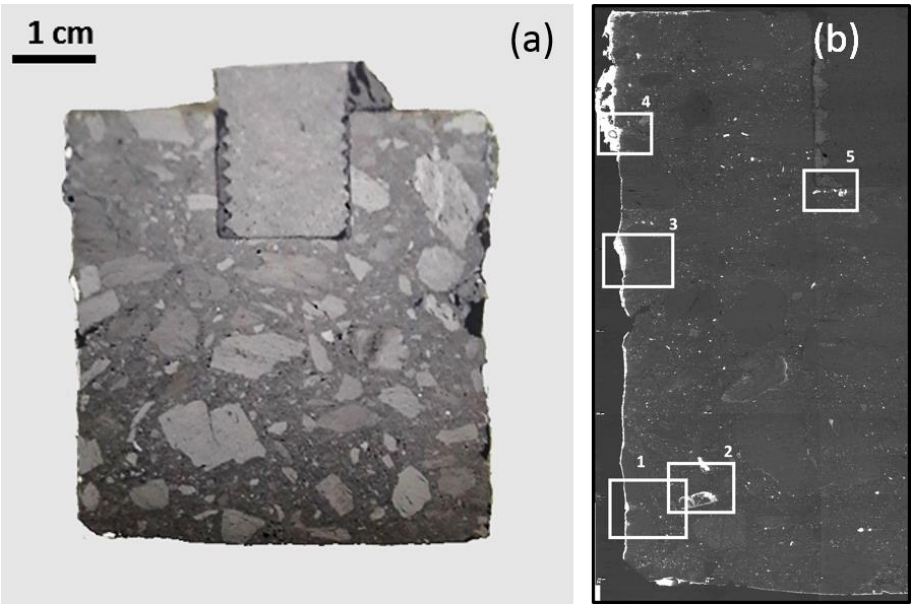

Figure 4.53: (a) Cross section of the test 9 type K post mortem refractory (b) areas examined for wear

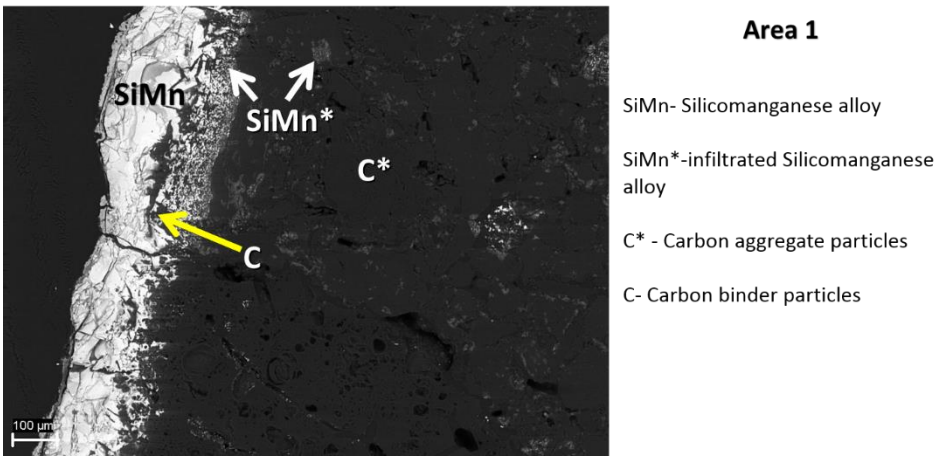

Figure 4.54: Test 9, area 1,-type K refractory SEM image measured at 15 kV acceleration voltage. Scale bar indicates 100 µm

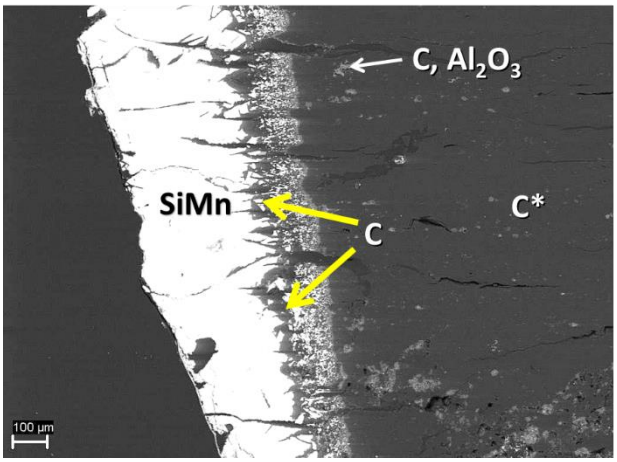

Figure 4.55: Test 9, area 2,-type K refractory SEM image measured at 15 kV acceleration voltage. Scale bar indicates 100 µm

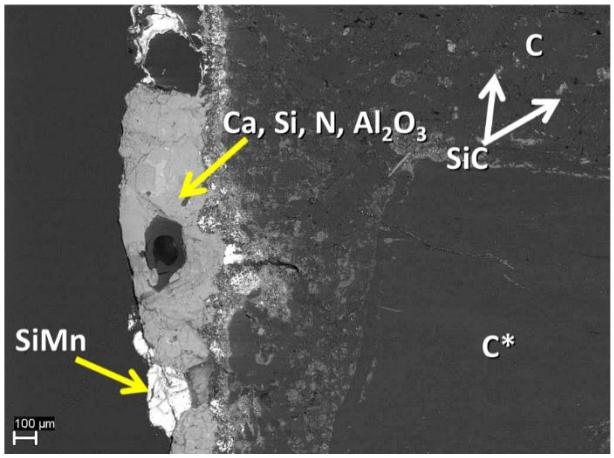

Figure 4.56: Test 9, area 3,-type K refractory SEM image measured at 15 kV acceleration voltage. Scale bar indicates 100 µm

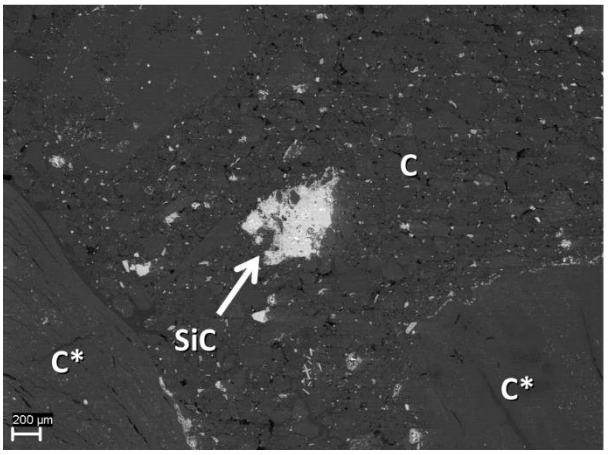

Figure 4.57: Test 9, area 4,-type K refractory SEM image measured at 15 kV acceleration voltage. Scale bar indicates 100 µm

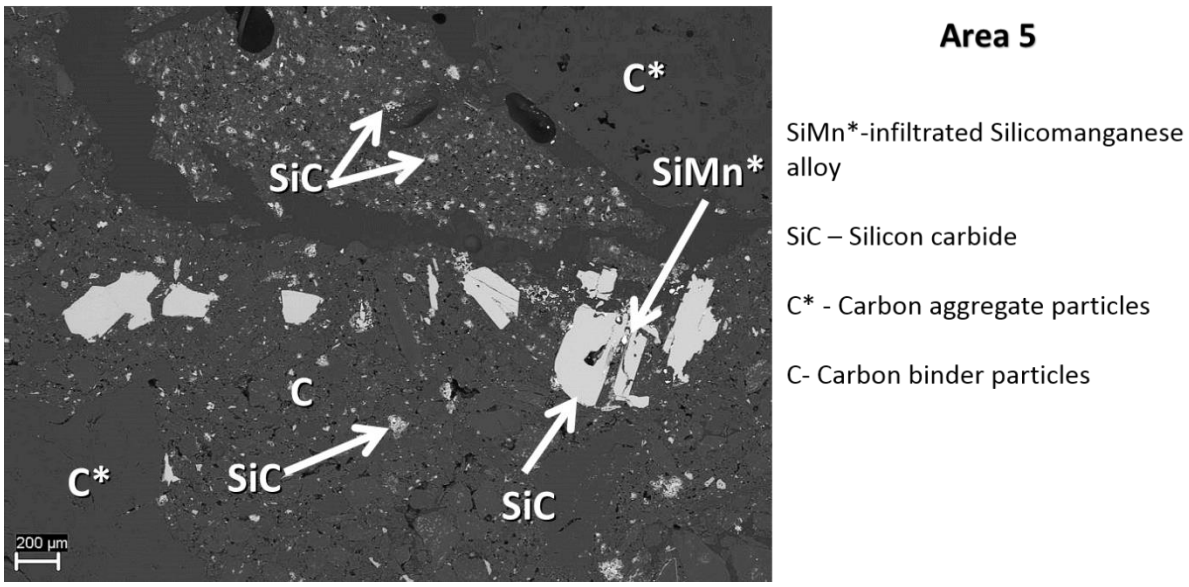

Figure 4.58: Test 9, area 5,-type K refractory SEM image measured at 15 kV acceleration voltage. Scale bar indicates 100 µm

4.6.4. Test 10-dynamic-type SiC at 1550°C:

Section 4.6.4 contains SEM-EDS results for test 10 on the type SiC refractory at 1550°C. In Figure 4.59 the cross section of the type SiC post-mortem refractory can be seen with the sections that were identified for SEM-EDS analysis. In comparison to the static type SiC refractory analysis at 1550°C in section 6.3.4, only alloy corrosion due to dissolution and infiltration could be identified as well in the dynamic SiC post-mortem refractory in Figure 4.60, Figure 4.61, Figure 4.63 and Figure 4.65. In Figure 4.62, Figure 4.64 and Figure 4.66 no infiltration of the alloy was observed. The type SiC extent in wear at 1550°C is in stage 2 evidenced by surface infiltration of the alloy which is greater than 100 microns.

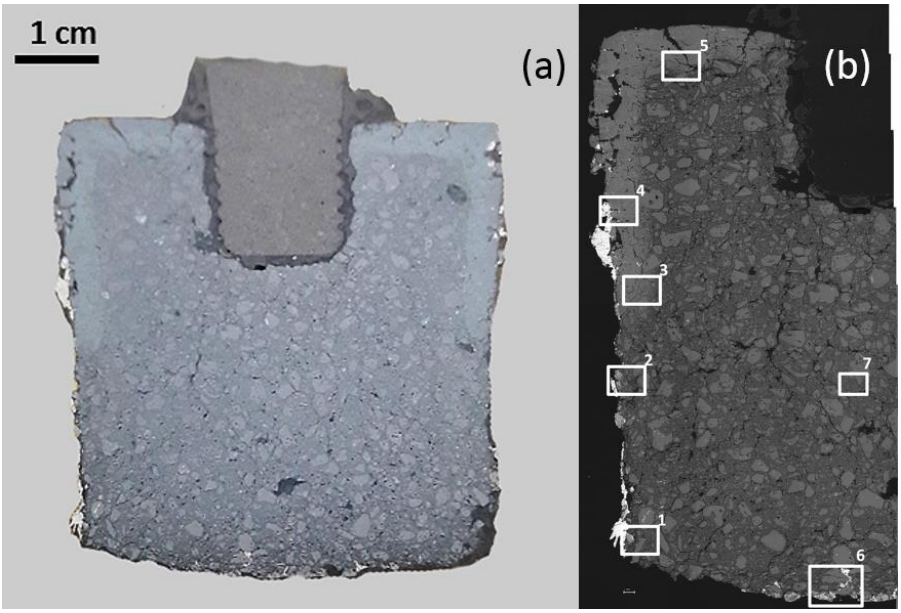

Figure 4.59: (a) Cross section of the test 10 type K post mortem refractory (b) areas examined for wear

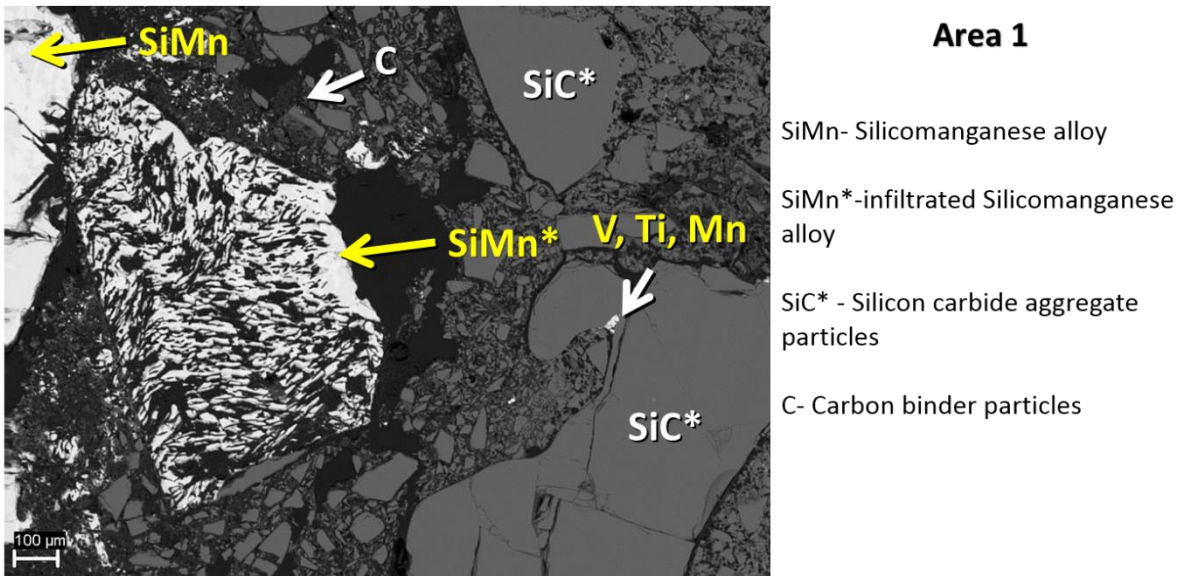

Figure 4.60: Test 10, area 1,-type SiC refractory SEM image measured at 15 kV acceleration voltage. Scale bar indicates 100 µm

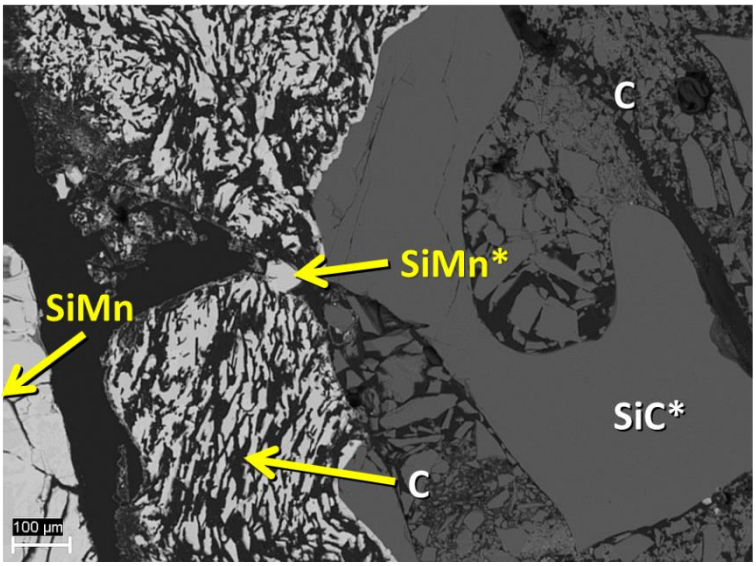

Area 2

SiMn- Silicomanganese alloy

SiMn*-infiltrated Silicomanganese alloy

SiC* - Silicon carbide aggregate particles

C- Carbon binder particles

Figure 4.61: Test 10, area 2,-type SiC refractory SEM image measured at 15 kV acceleration voltage. Scale bar indicates 100 µm

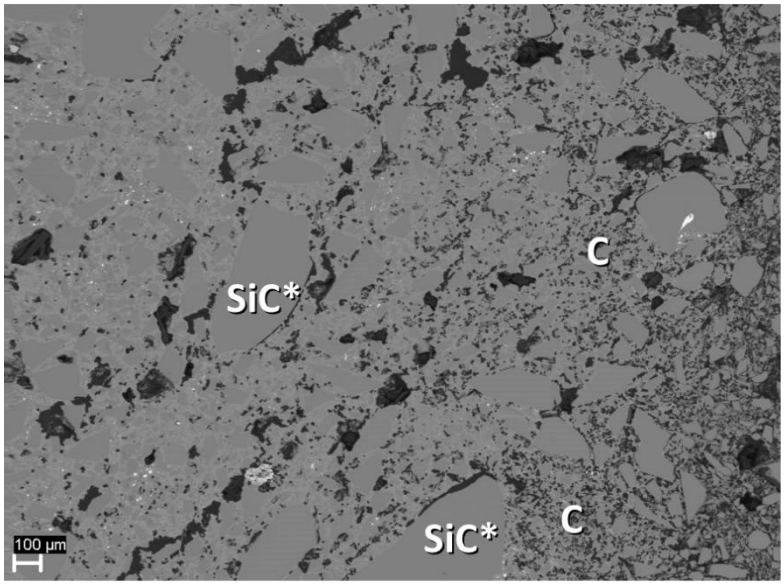

Area 3

SiC* - Silicon carbide aggregate particles

C- Carbon binder particles

Figure 4.62: Test 10, area 3,-type SiC refractory SEM image measured at 15 kV acceleration voltage. Scale bar indicates 100 µm

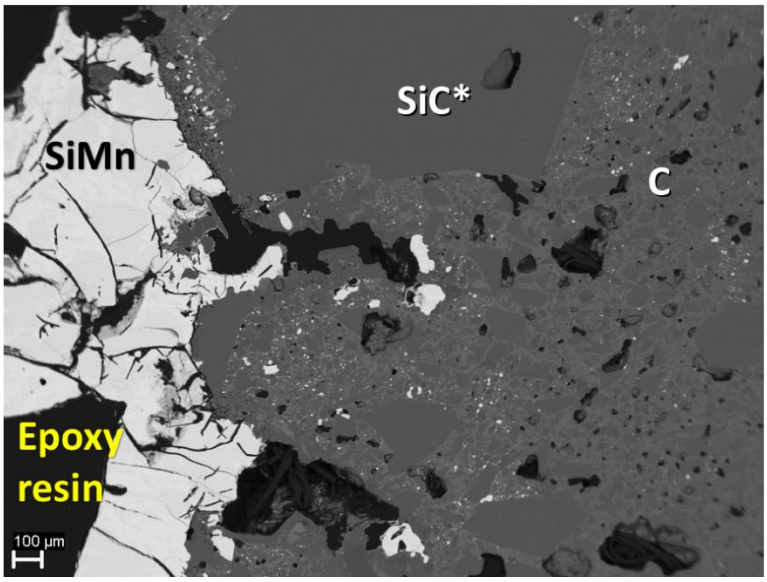

Area 4

SiMn- Silicomanganese alloy

SiC* - Silicon carbide aggregate particles

C- Carbon binder particles

Figure 4.63: Test 10, area 4,-type SiC refractory SEM image measured at 15 kV acceleration voltage. Scale bar indicates 100 µm

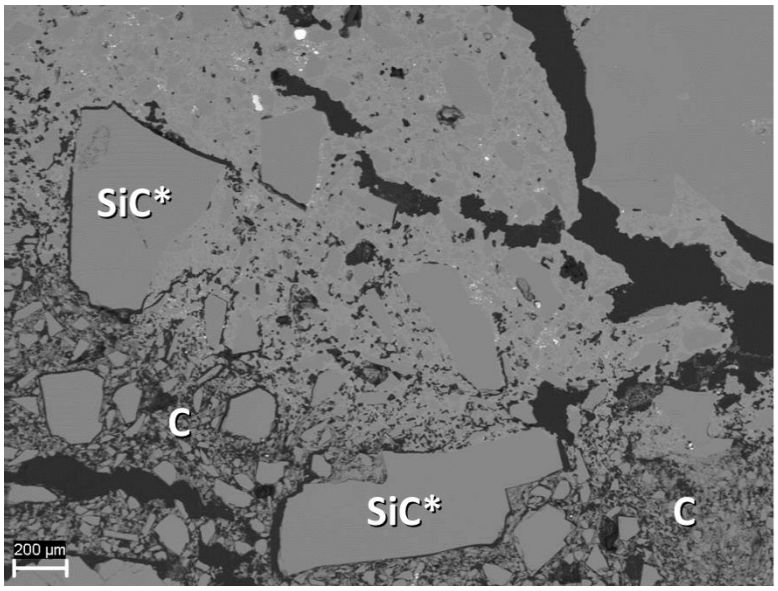

Area 5

SiC* - Silicon carbide aggregate particles

C- Carbon binder particles

Figure 4.64: Test 10, area 5,-type SiC refractory SEM image measured at 15 kV acceleration voltage. Scale bar indicates 200 µm

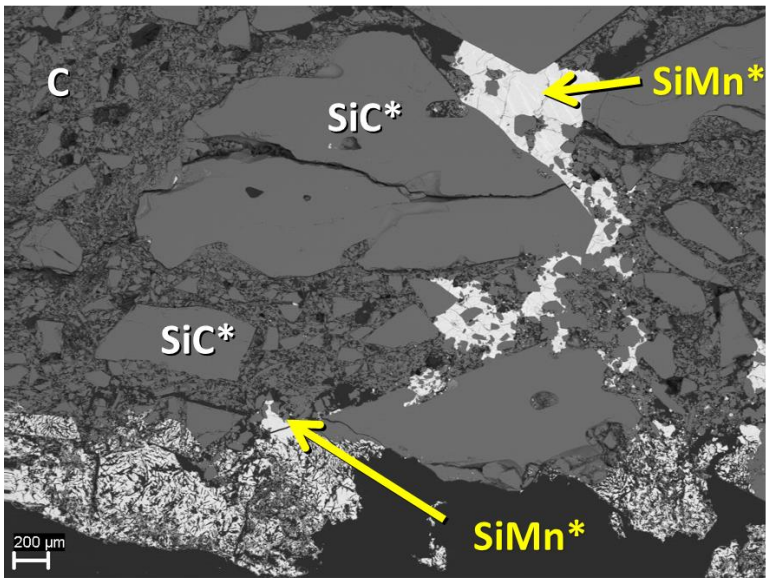

Area 6

SiMn*-infiltrated Silicomanganese alloy

SiC* - Silicon carbide aggregate particles

C- Carbon binder particles

Figure 4.65: Test 10, area 6,-type SiC refractory SEM image measured at 15 kV acceleration voltage. Scale bar indicates 200 µm

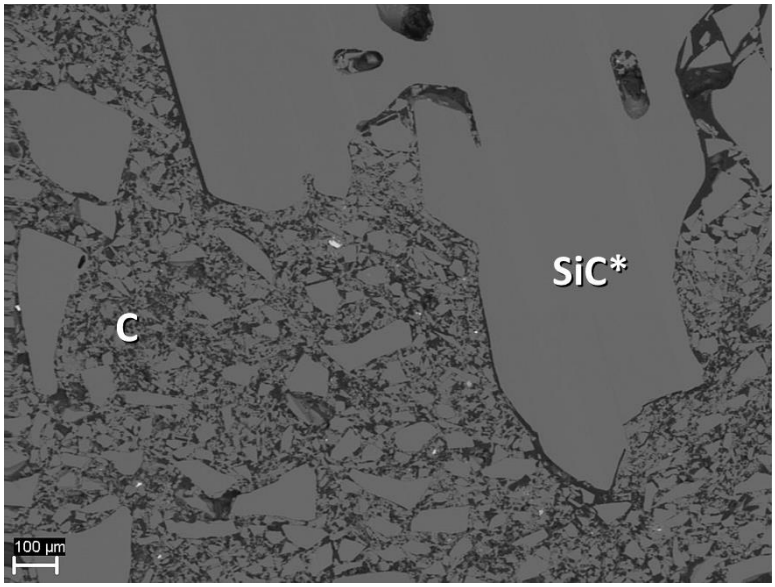

Area 7

SiC* - Silicon carbide aggregate particles

C- Carbon binder particles

Figure 4.66: Test 10, area 7,-type SiC refractory SEM image measured at 15 kV acceleration voltage. Scale bar indicates 100 µm

4.6.5. Test 11-dynamic-type SiC at 1600°C:

Section 4.6.5 contains SEM-EDS results for test 11 on the type SiC refractory at 1600°C. In Figure 4.67, the cross section of the type SiC post-mortem refractory can be seen with the sections that were identified for SEM-EDS analysis. In comparison to the static type SiC refractory analysis at 1600°C in section 6.3.5, only alloy corrosion due to dissolution and

infiltration could be identified as well in the dynamic SiC post-mortem refractory in Figure 4.68 to Figure 4.72. In comparison with the dynamic type SiC at 1550°C, this refractory had more alloy infiltration with the temperature increase. The type SiC extent in wear at 1600°C is in stage 3 evidenced by surface infiltration of the alloy which is greater than 100 microns and aggregate relic formation.

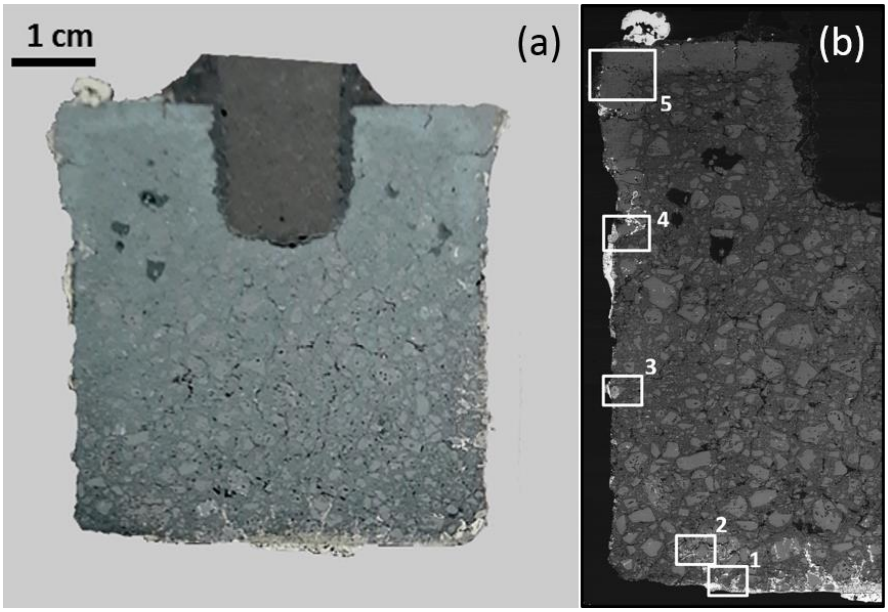

Figure 4.67: (a) Cross section of the test 11 type SiC post mortem refractory (b) areas examined for wear

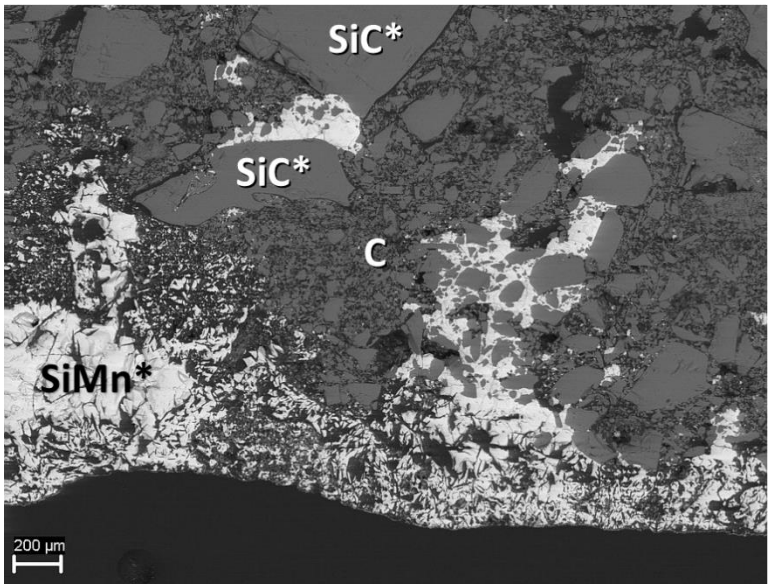

Area 1

SiMn*-infiltrated silicomanganese alloy

SiC* - Silicon carbide aggregate particles

C- Carbon binder particles

Figure 4.68: Test 11, area 1,-type SiC refractory SEM image measured at 15 kV acceleration voltage. Scale bar indicates 200 µm

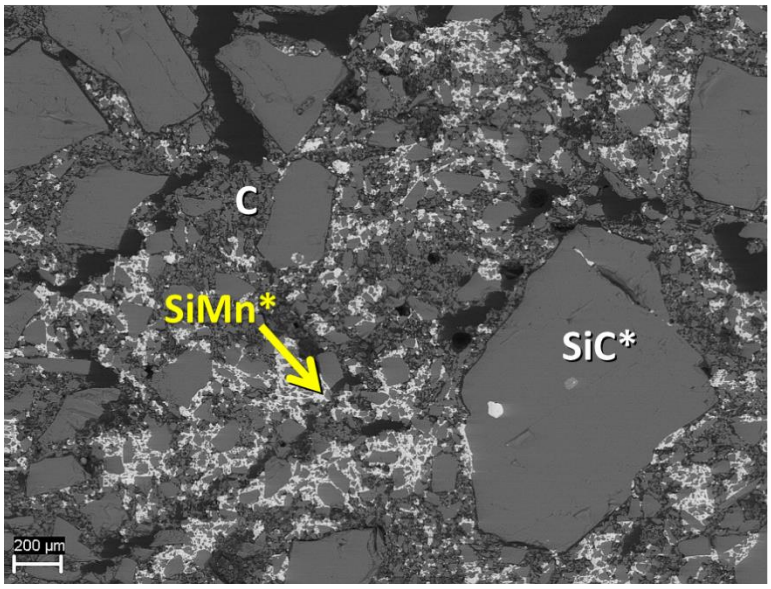

Area 2

SiMn*-infiltrated silicomanganese alloy

SiC* - Silicon carbide aggregate particles

C- Carbon binder particles

Figure 4.69: Test 11, area 2,-type SiC refractory SEM image measured at 15 kV acceleration voltage. Scale bar indicates 200 µm

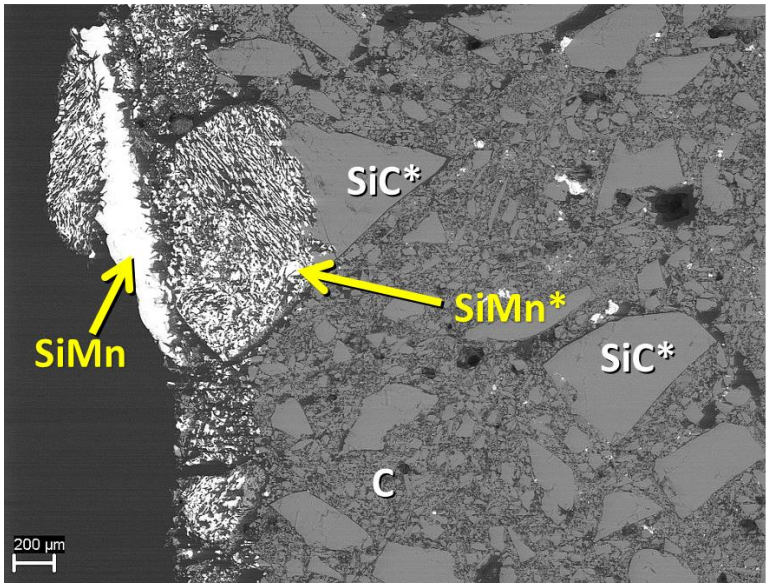

Area 3

SiMn- Silicomanganese alloy

SiMn*- Dissolved silicomanganese alloy

SiC* - Silicon carbide aggregate particles

C- Carbon binder particles

Figure 4.70: Test 11, area 3,-type SiC refractory SEM image measured at 15 kV acceleration voltage. Scale bar indicates 200 µm

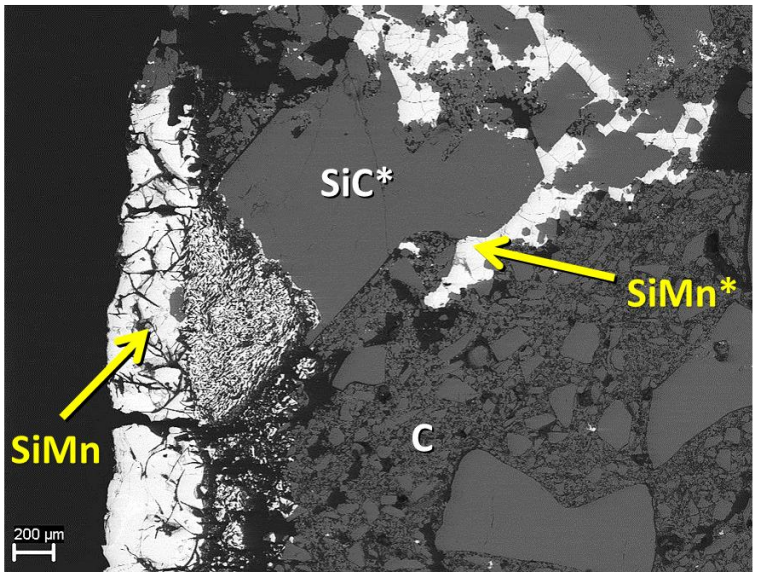

Area 4

SiMn- Silicomanganese alloy

SiMn*- Dissolved silicomanganese alloy

SiC* - Silicon carbide aggregate particles

C- Carbon binder particles

Figure 4.71: Test 11, area 4,-type SiC refractory SEM image measured at 15 kV acceleration voltage. Scale bar indicates 200 µm

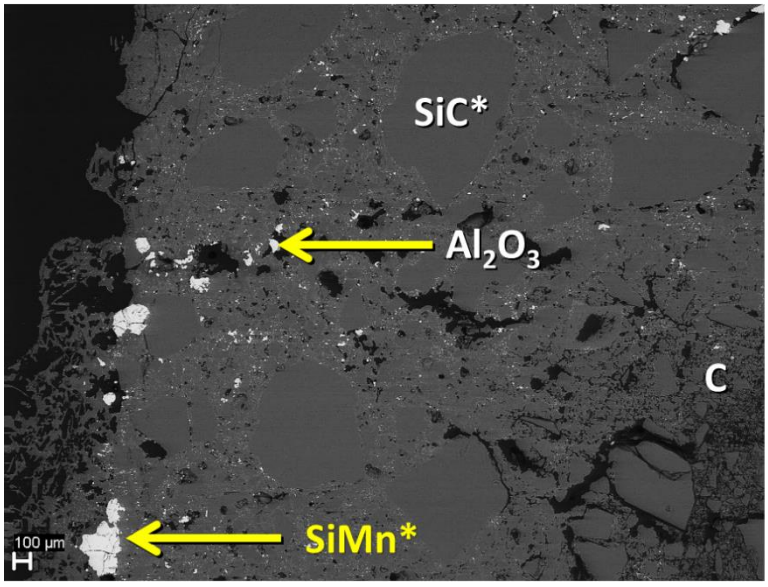

Area 5

Al_2O_3- Alumina phase

SiMn*- Dissolved silicomanganese alloy

SiC* - Silicon carbide aggregate particles

C- Carbon binder particles

Figure 4.72: Test 11, area 5,-type SiC refractory SEM image measured at 15 kV acceleration voltage. Scale bar indicates 100 µm

4.6.6. Test 12-dynamic-type SiC at 1650°C:

Section 4.6.6 contains SEM-EDS results for test 12 on the type SiC refractory at 1650°C. In Figure 4.73 the cross section of the type SiC post-mortem refractory can be seen with the sections that were identified for SEM-EDS analysis. In comparison to the static type SiC refractory analysis at 1650°C in section 6.3.6, only alloy corrosion due to dissolution and

infiltration could be identified as well in the dynamic SiC post-mortem refractory in Figure 4.74 to Figure 4.77. In comparison with both the dynamic type SiC at 1550°C and 1600°C, this refractory had more alloy infiltration with the temperature increase, this observation could have been due to the alloy being superheated and thus making it even less viscous and allowing it to infiltrate the refractory pores a lot easier. The type SiC extent in wear at 1650°C is in stage 3 evidenced by surface infiltration of the alloy which is greater than 100 microns and aggregate relic formation.

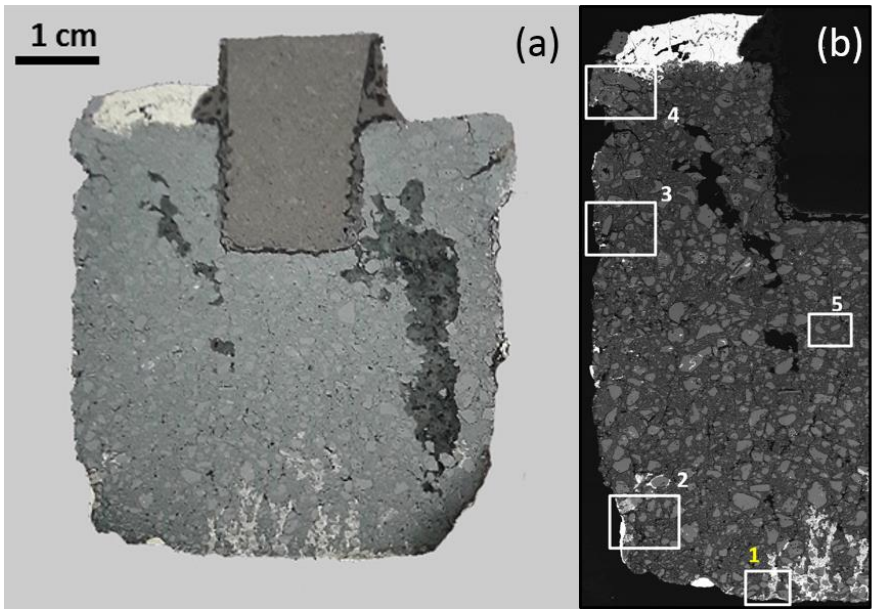

Figure 4.73: (a) Cross section of the test 12 type SiC post mortem refractory (b) areas examined for wear

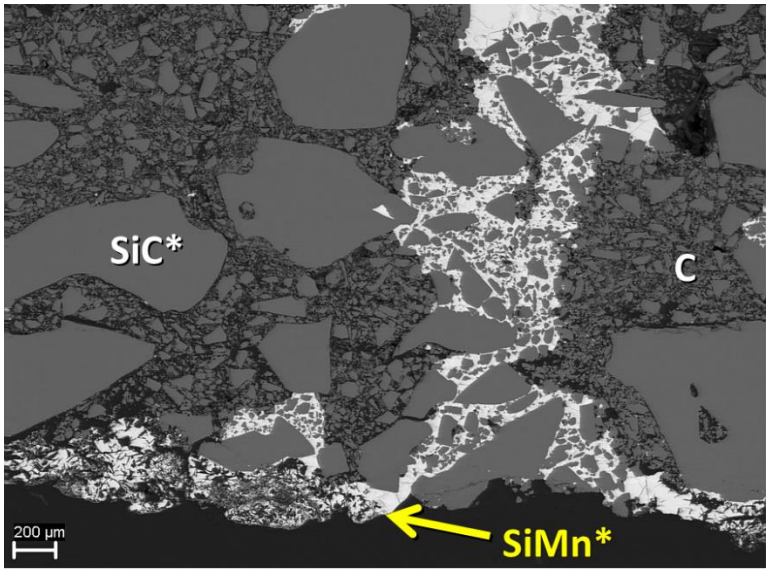

Area 1

SiMn*- Dissolved silicomanganese alloy

SiC* - Silicon carbide aggregate particles

C- Carbon binder particles

Figure 4.74: Test 12, area 1,-type SiC refractory SEM image measured at 15 kV acceleration voltage. Scale bar indicates 200 µm

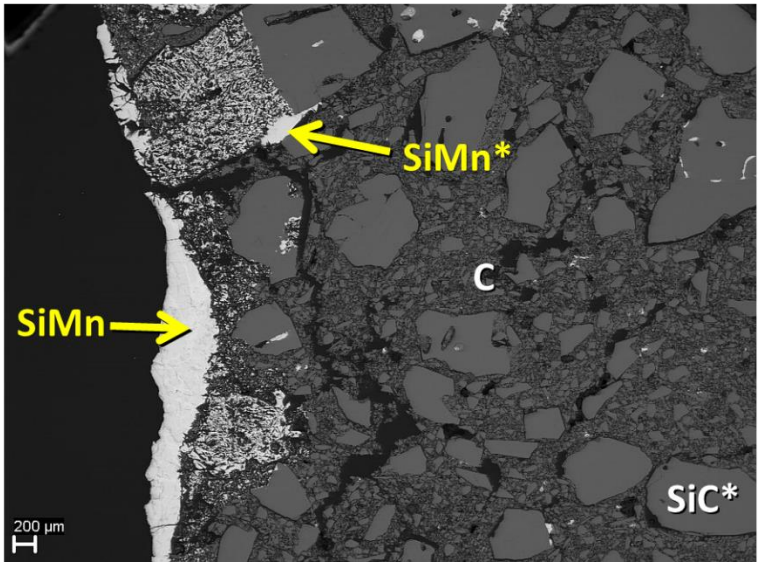

Area 2

SiMn*- Dissolved silicomanganese alloy

SiMn- Silicomanganese alloy

SiC* - Silicon carbide aggregate particles

C- Carbon binder particles

Figure 4.75: Test 12, area 2,-type SiC refractory SEM image measured at 15 kV acceleration voltage. Scale bar indicates 200 µm

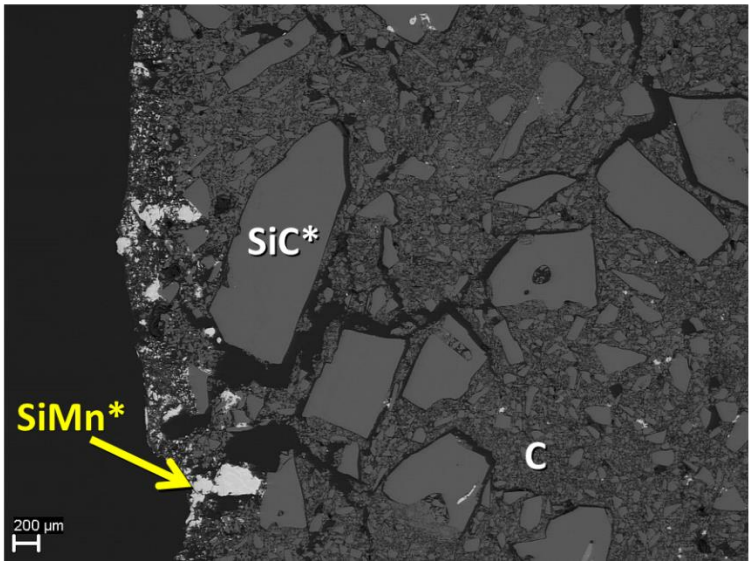

Area 3

SiMn*- Dissolved silicomanganese alloy

SiMn- Silicomanganese alloy

SiC* - Silicon carbide aggregate particles

C- Carbon binder particles

Figure 4.76: Test 12, area 3,-type SiC refractory SEM image measured at 15 kV acceleration voltage. Scale bar indicates 200 µm

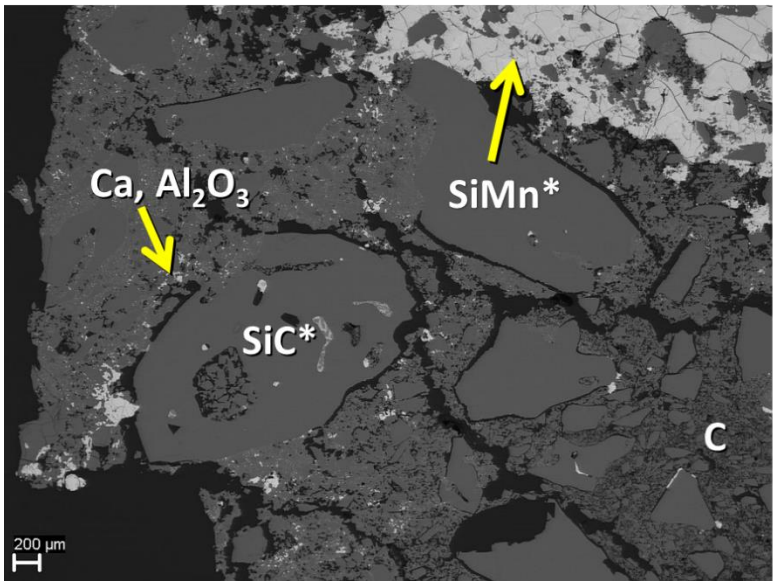

Area 4

Ca, Al_2O_3- Calcium, Alumina phase

SiMn*- Dissolved silicomanganese alloy

SiC* - Silicon carbide aggregate particles

C- Carbon binder particles

Figure 4.77: Test 12, area 4,-type SiC refractory SEM image measured at 15 kV acceleration voltage. Scale bar indicates 200 µm

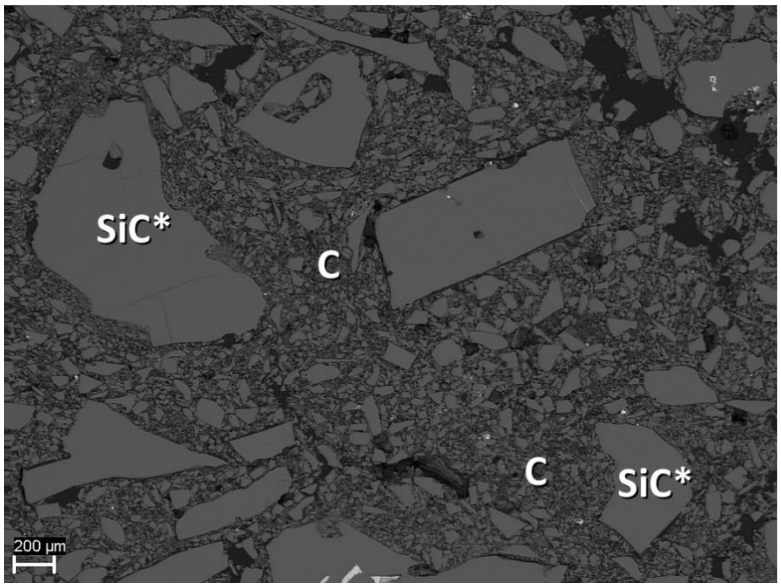

Figure 4.78: Test 12, area 5,-type SiC refractory SEM image measured at 15 kV acceleration voltage. Scale bar indicates 200 µm

4.6.7. Test 13-dynamic-type K at Si=17 mass%

Section 4.6.7 contains SEM-EDS results for test 13 on the type K refractory at Si content of 17 mass %. In Figure 4.79 the cross section of the dynamic type K refractory at 17 mass % Si can be seen with the sections that were identified for SEM-EDS analysis. Corrosion is identified as the main wear mechanism, with SiC precipitation identifiable only in Figure 4.83 to 4.86 and no traces of SiC can be identified in Figure 4.80 to Figure 4.82. In comparison to type K, in section 6.4.2 at 1600°C and 15 mass %, there was less SiC precipitation that took place in all areas examined in section 6.4.2 compared to the test with Si at 17 mass %. This observation is in agreement with the FactSage™ modelled data. The type K extent in wear at Si-content of 17 mass% is in stage 2 evidenced by surface infiltration of the alloy which is greater than 100 microns.

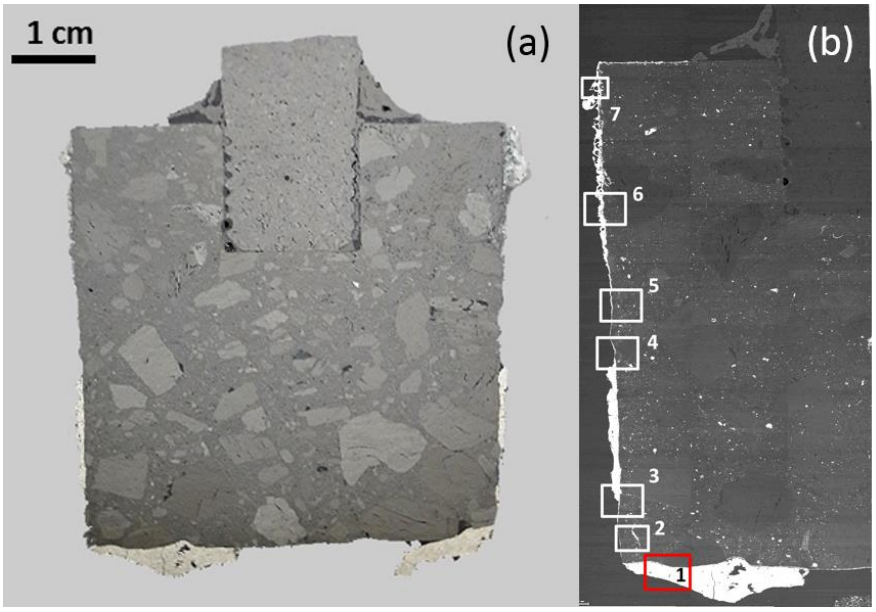

Figure 4.79: (a) Cross section of the test 13 type K post mortem refractory (b) areas examined for wear

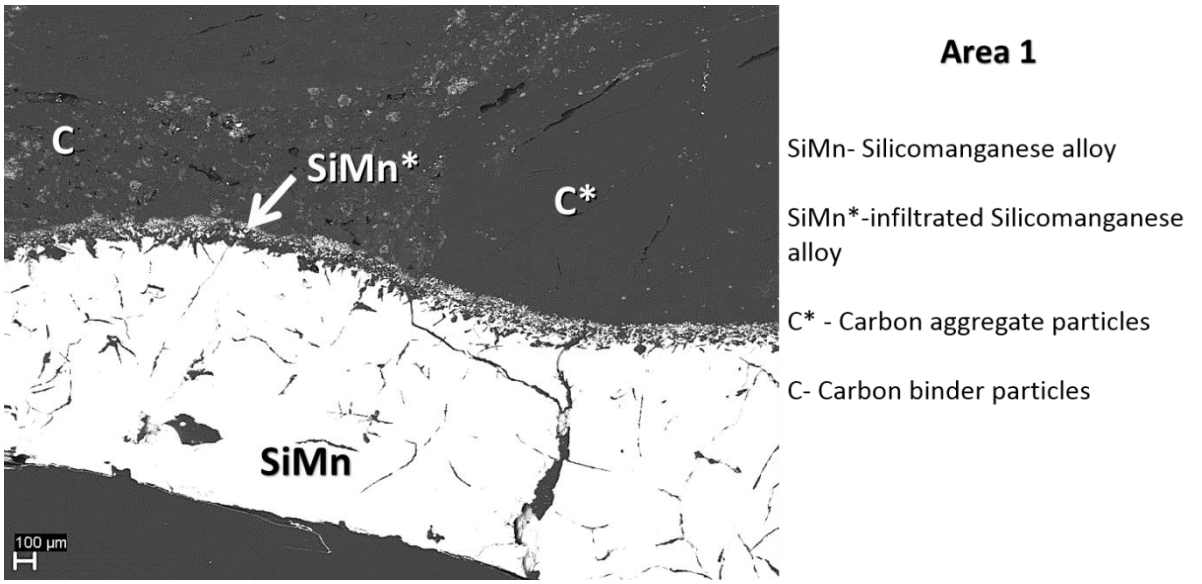

Figure 4.80: Test 13, area 1,-type K refractory SEM image measured at 15 kV acceleration voltage. Scale bar indicates 100 µm

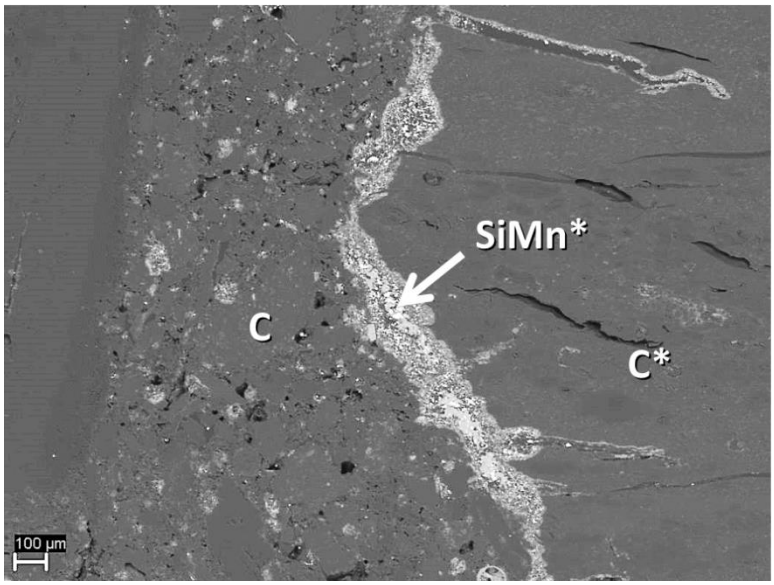

Area 2

SiMn*-infiltrated Silicomanganese alloy

C* - Carbon aggregate particles

C- Carbon binder particles

Figure 4.81: Test 13, area 2,-type K refractory SEM image measured at 15 kV acceleration voltage. Scale bar indicates 100 µm

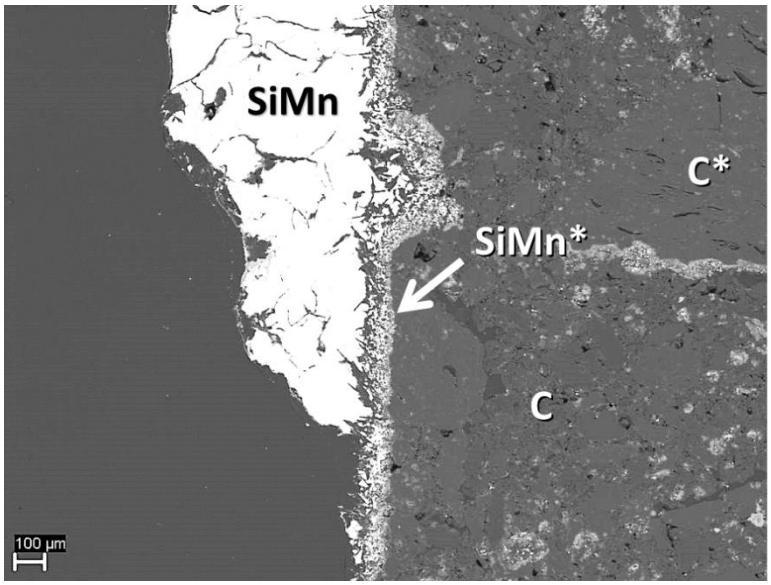

Area 3

SiMn*-infiltrated Silicomanganese alloy

SiMn- Silicomanganese alloy

C* - Carbon aggregate particles

C- Carbon binder particles

Figure 4.82: Test 13, area 3,-type K refractory SEM image measured at 15 kV acceleration voltage. Scale bar indicates 100 µm

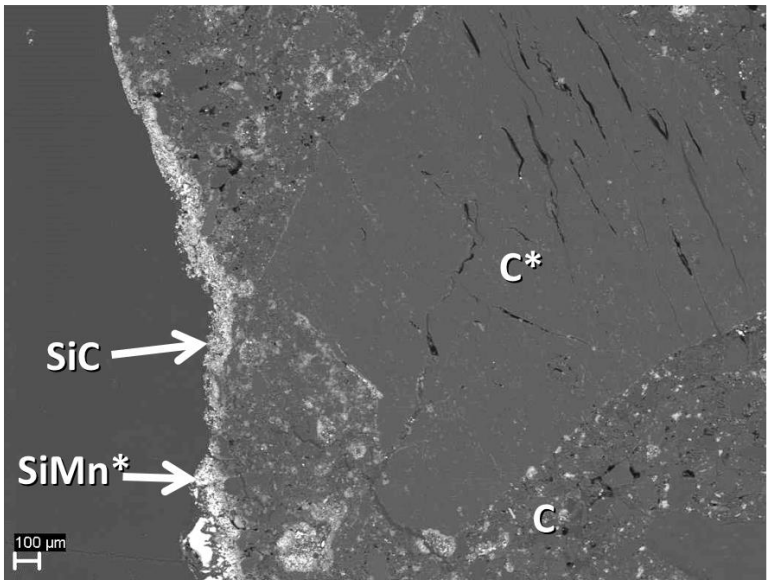

Area 4

SiMn*-infiltrated Silicomanganese alloy

SiC – Silicon carbide

C* - Carbon aggregate particles

C- Carbon binder particles

Figure 4.83: Test 13, area 4,-type K refractory SEM image measured at 15 kV acceleration voltage. Scale bar indicates 100 µm

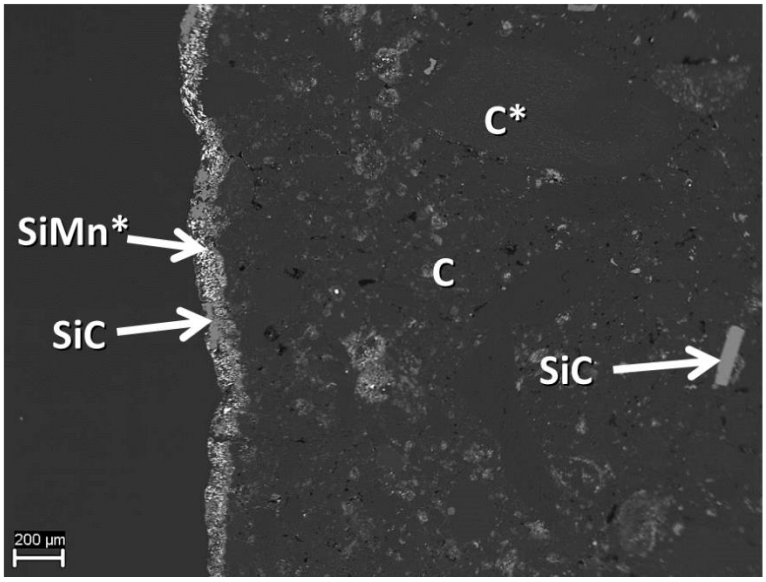

Area 5

SiMn*-infiltrated Silicomanganese alloy

SiC – Silicon carbide

C* - Carbon aggregate particles

C- Carbon binder particles

Figure 4.84: Test 13, area 5,-type K refractory SEM image measured at 15 kV acceleration voltage. Scale bar indicates 200 µm

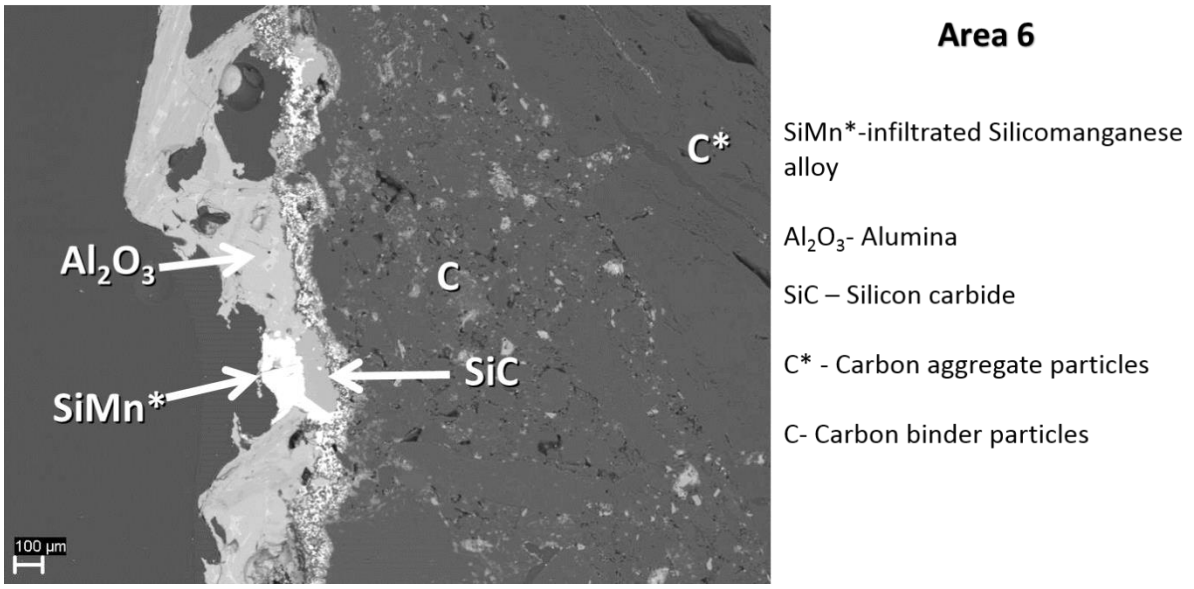

Figure 4.85: Test 13, area 6,-type K refractory SEM image measured at 15 kV acceleration voltage. Scale bar indicates 100 µm

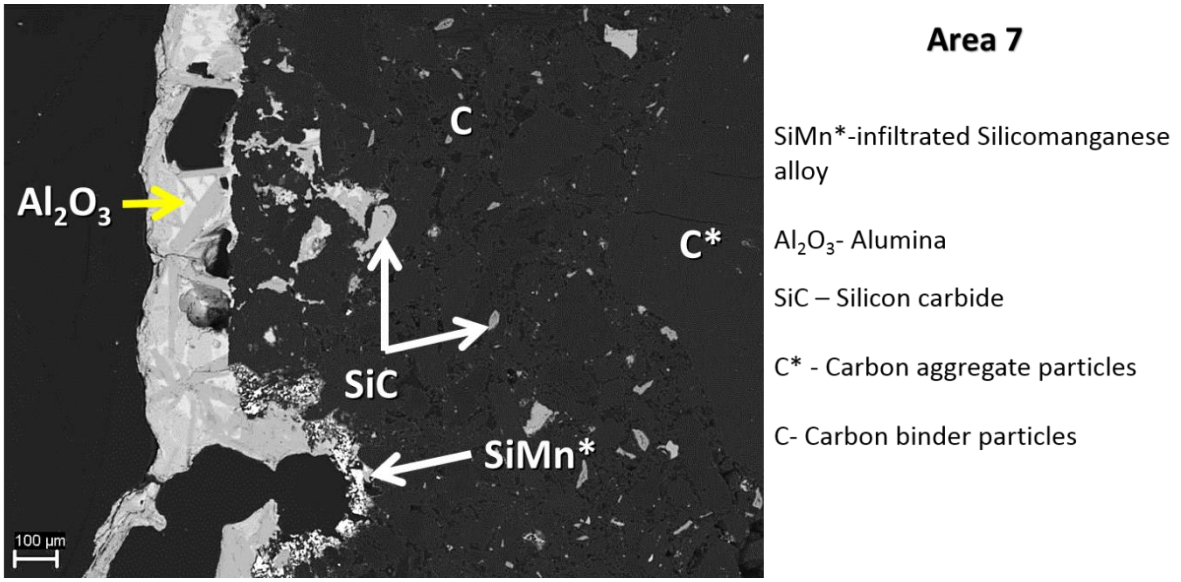

Figure 4.86: Test 13, area 7,-type K refractory SEM image measured at 15 kV acceleration voltage. Scale bar indicates 100 µm

4.6.8. Test 14-dynamic-type K at Si=18 mass%

Section 4.6.8 contains SEM-EDS results for test 14 on the type K refractory at Si content of 18 mass %. In Figure 4.87, the cross section of the dynamic type K refractory at 18 mass % Si can be seen with the sections that were identified for SEM-EDS analysis. In Figure 4.88 to Figure 4.92 with exception to Figure 4.91, SiC precipitation can be seen, with most of it occurring at

the alloy and refractory interface. In comparison to the test 13, test 14 has SiC precipitation with larger areas. This observation is in agreement with the FactSage™ modelled data. The type K extent in wear at Si-content of 18 mass% is in stage 2 evidenced by surface infiltration of the alloy which is greater than 100 microns.

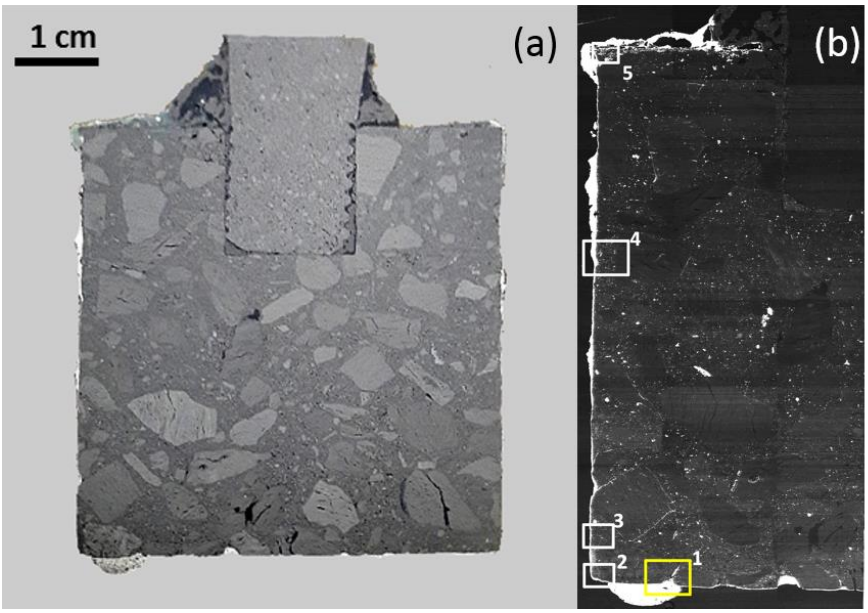

Figure 4.87: (a) Cross section of the test 14 type K post mortem refractory (b) areas examined for wear

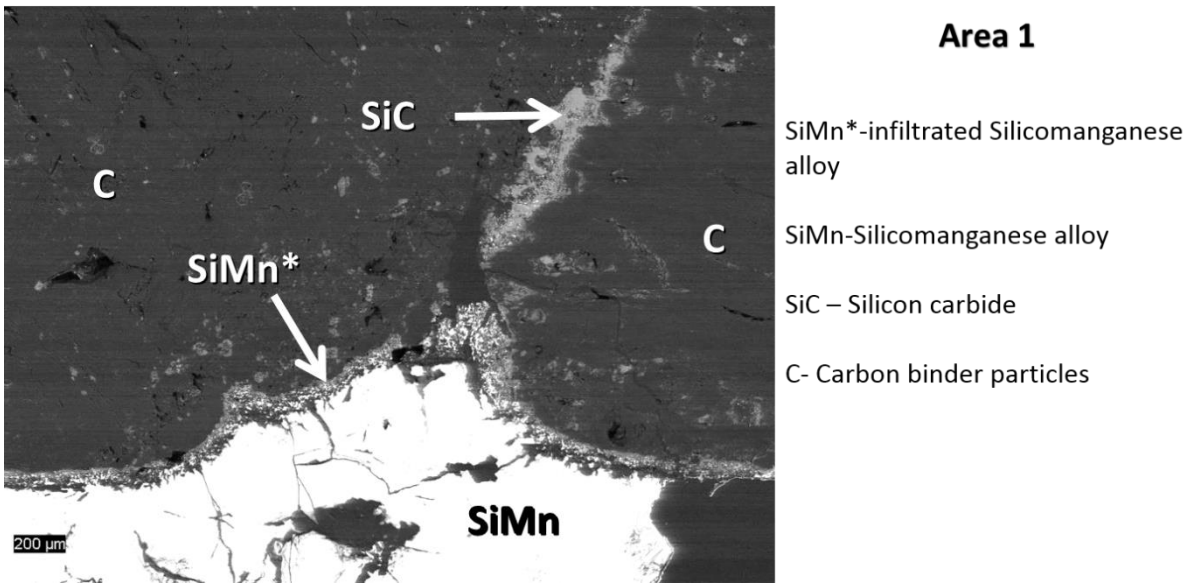

Figure 4.88: Test 14, area 1,-type K refractory SEM image measured at 15 kV acceleration voltage. Scale bar indicates 200 µm

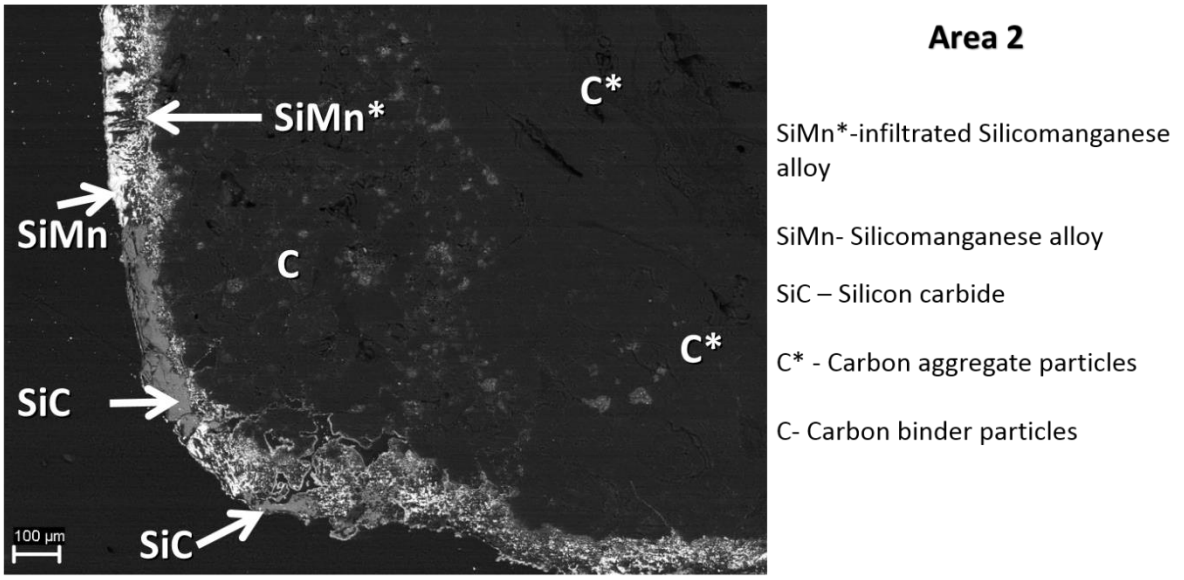

Figure 4.89: Test 14, area 2,-type K refractory SEM image measured at 15 kV acceleration voltage. Scale bar indicates 100 µm

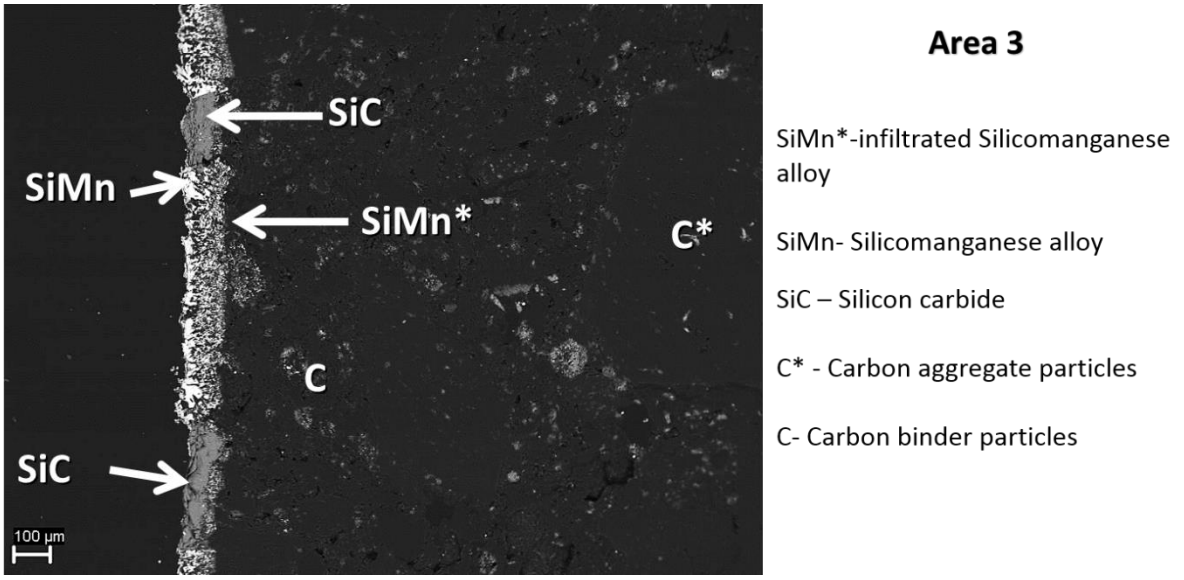

Figure 4.90: Test 14, area 3,-type K refractory SEM image measured at 15 kV acceleration voltage. Scale bar indicates 100 µm

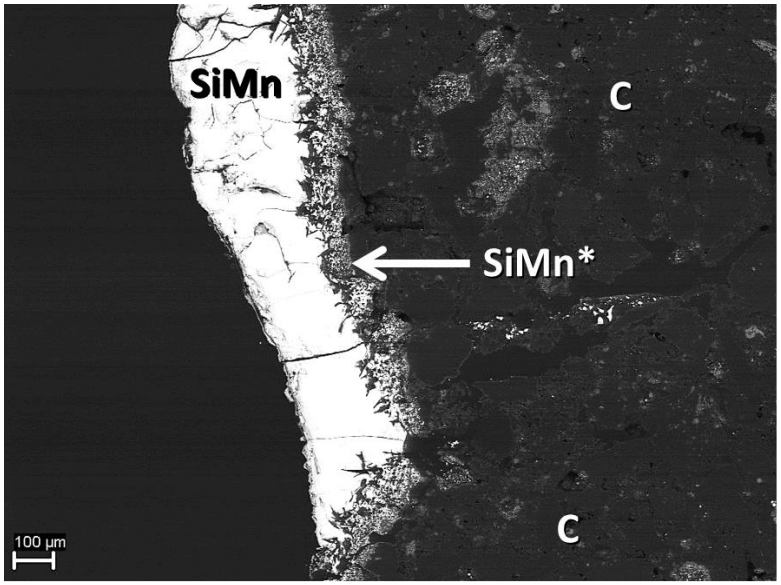

Figure 4.91: Test 14, area 4,-type K refractory SEM image measured at 15 kV acceleration voltage. Scale bar indicates 100 µm

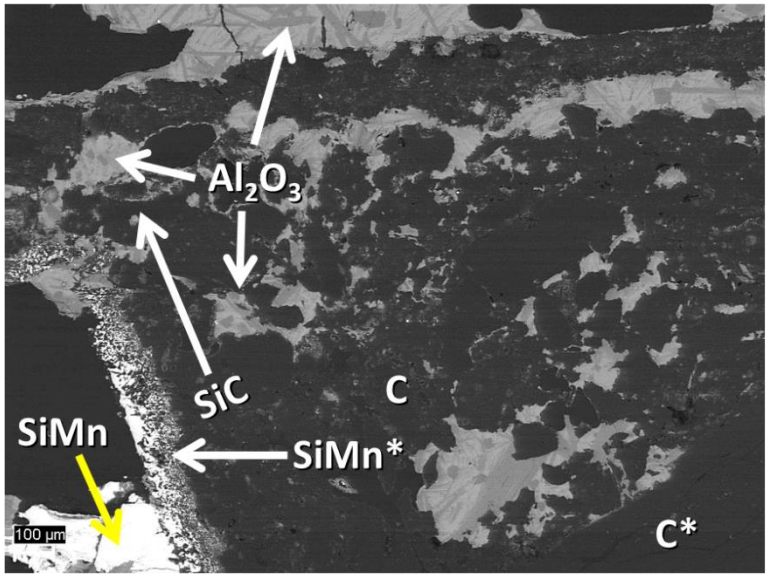

Figure 4.92: Test 14, area 5,-type K refractory SEM image measured at 15 kV acceleration voltage. Scale bar indicates 100 µm

4.6.9. Test 15-dynamic-type SiC at Si=17 mass%

Section 4.6.9 contains SEM-EDS results for test 15 on the type SiC refractory at Si content of 17 mass %. In Figure 4.93, the cross section of the dynamic type SiC refractory at 17 mass % Si can be seen with the sections that were identified for SEM-EDS analysis. The refractory

wear extent in the type SiC refractory at 17 mass % Si-content can be considered to be stage 3 evidenced by surface alloy infiltration of above 100 microns and aggregate relic formations.

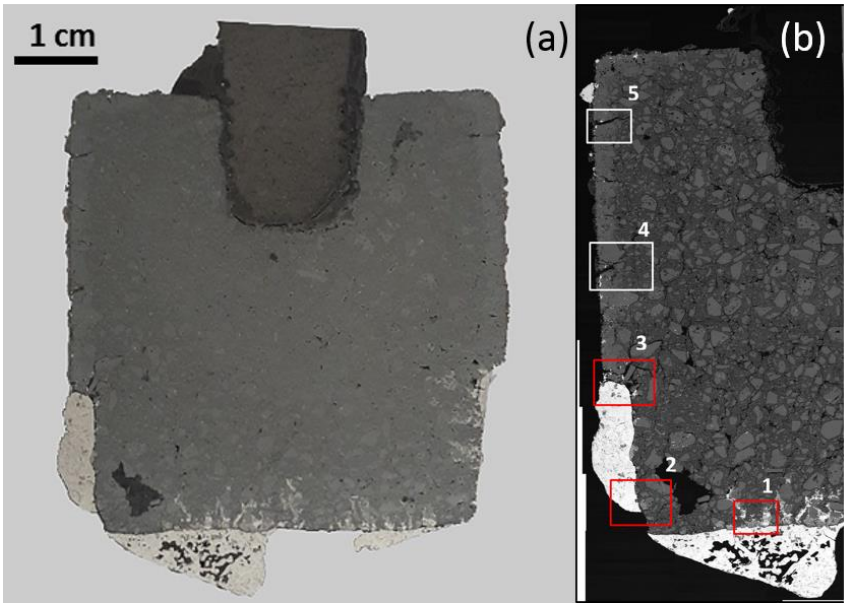

Figure 4.93: (a) Cross section of the test 15 type SiC post mortem refractory (b) areas examined for wear

Corrosion due to dissolution is observed as the main wear mechanism and SiC precipitation could not be clearly identified even at the alloy interfaces. The extent of infiltration in test 15, which can be seen in Figure 4.93 to Figure 4.98, is greater than that in test 11-dynamic-type SiC at 15 mass %, 1600°C, which can be seen in section 6.4.5. In section 6.2 FactSage™ predicted that SiC refractory wear would decrease with an increase in Si content in the alloy, the observation made was contradictory, and this is due to the porous nature of the SiC making it more prone to wear as the alloy infiltrates SiC refractory increasing wear by dissolution.

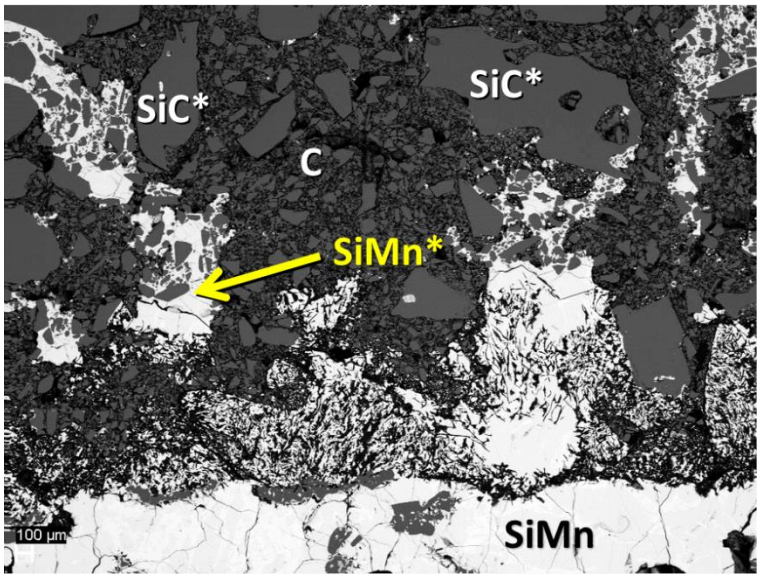

Area 1

SiMn*- Dissolved silicomanganese alloy

SiC* - Silicon carbide aggregate particles

C- Carbon binder particles

SiMn- Silicomanganese alloy

Figure 4.94: Test 15, area 1,-type SiC refractory SEM image measured at 15 kV acceleration voltage. Scale bar indicates 100 µm

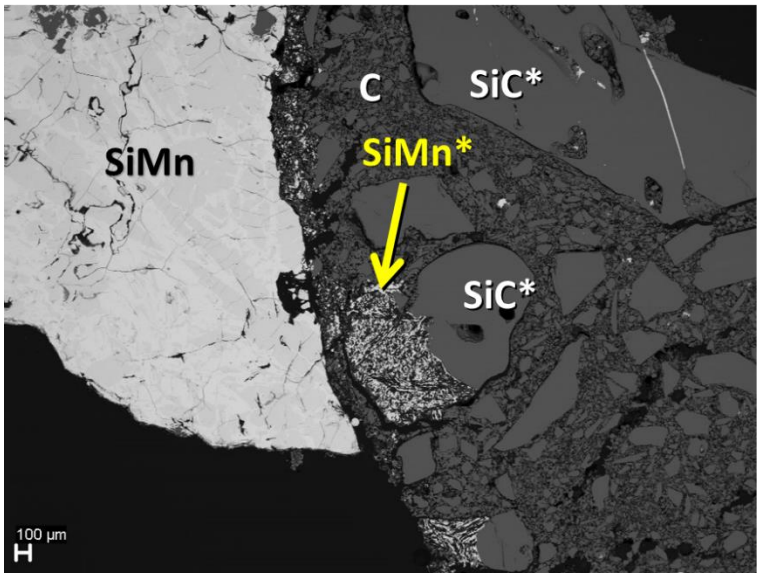

Area 2

SiMn*- Dissolved silicomanganese alloy

SiC* - Silicon carbide aggregate particles

C- Carbon binder particles

SiMn- Silicomanganese alloy

Figure 4.95: Test 15, area 2,-type SiC refractory SEM image measured at 15 kV acceleration voltage. Scale bar indicates 100 µm

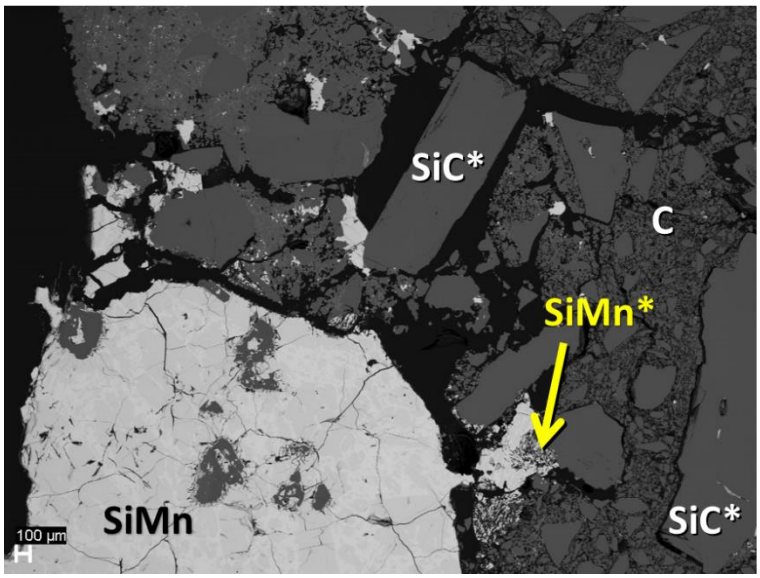

Area 3

SiMn*- Dissolved silicomanganese alloy

SiC* - Silicon carbide aggregate particles

C- Carbon binder particles

SiMn- Silicomanganese alloy

Figure 4.96: Test 15, area 3,-type SiC refractory SEM image measured at 15 kV acceleration voltage. Scale bar indicates 100 µm

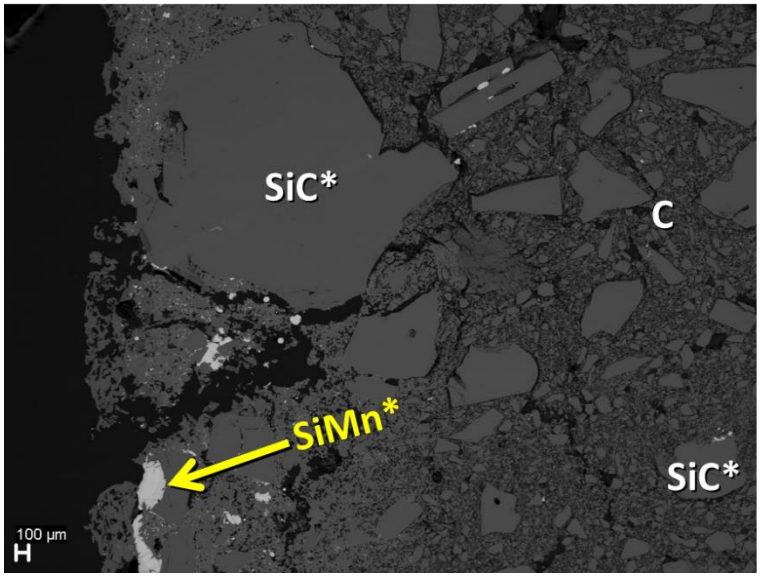

Area 4

SiMn*- Dissolved silicomanganese alloy

SiC* - Silicon carbide aggregate particles

C- Carbon binder particles

SiMn- Silicomanganese alloy

Figure 4.97: Test 15, area 4,-type SiC refractory SEM image measured at 15 kV acceleration voltage. Scale bar indicates 100 µm

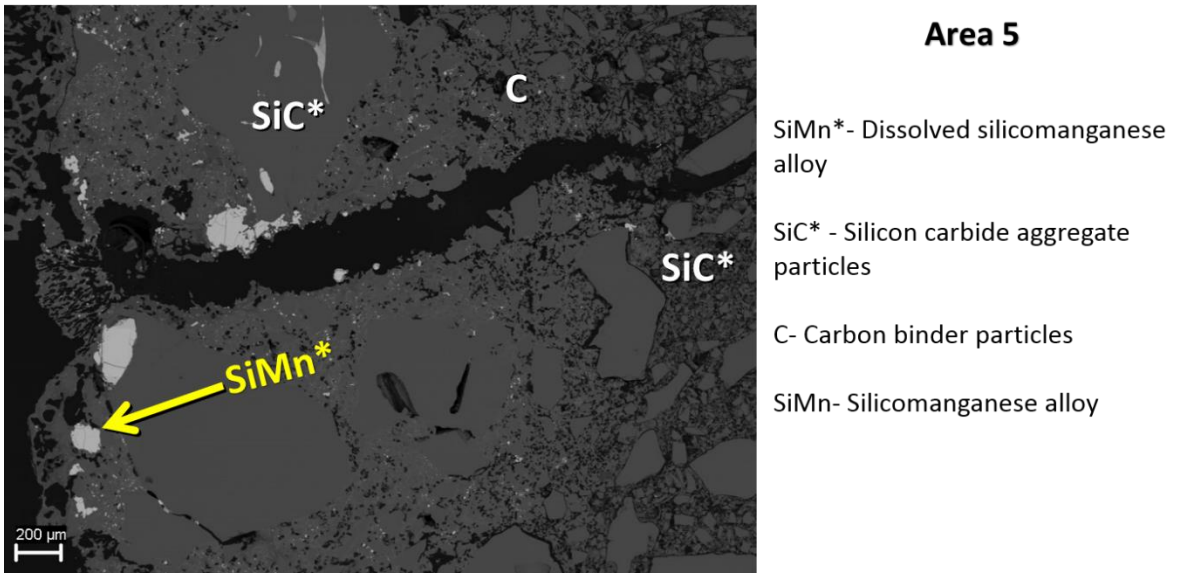

Figure 4.98: Test 15, area 5,-type SiC refractory SEM image measured at 15 kV acceleration voltage. Scale bar indicates 200 µm

4.6.10. Test 16-dynamic-type SiC at Si=18 mass%

Section 4.6.10 contains SEM-EDS results for test 16 on the type K refractory at Si content of 18 mass %. In Figure 4.99, the cross section of the dynamic type SiC refractory at 18 mass % Si can be seen with the sections that were identified for SEM-EDS analysis.

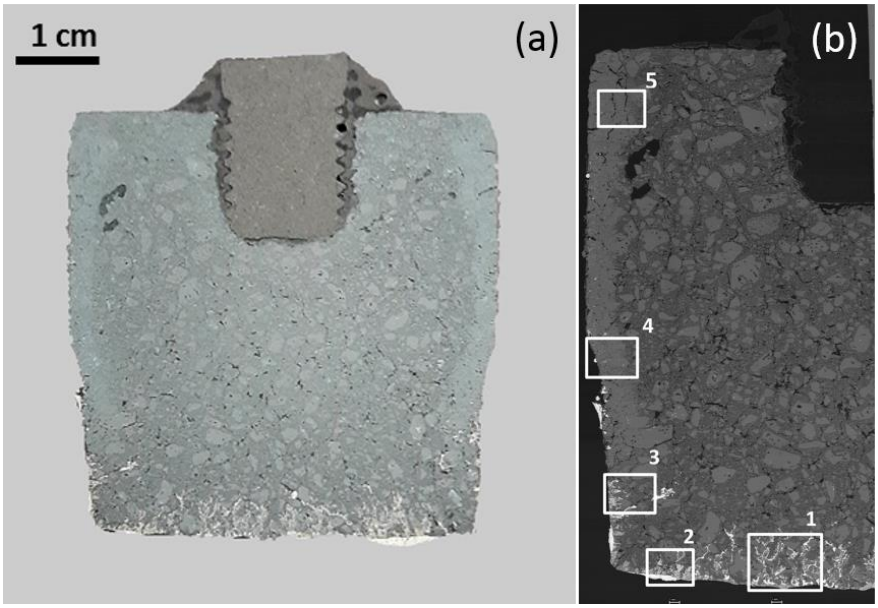

Figure 4.99: (a) Cross section of the test 16 type SiC post mortem refractory (b) areas examined for wear

Corrosion due to dissolution and infiltration is also observed as the main wear mechanism and SiC precipitation could not be clearly identified even at the alloy interfaces. The extent of infiltration in test 16, which can be seen in Figure 4.99 to Figure 4.104, is greater than that in test 15-dynamic-type SiC at 17 mass %. Similarly test 16 had more alloy infiltration due to the porous nature of the SiC thus not supporting the FactSage™ predicted that SiC refractory wear in section 6.2. The refractory wear extent in the type SiC refractory at 18 mass % Si-content can be considered to be stage 3 evidenced by surface alloy infiltration of above 100 microns and aggregate relic formations.

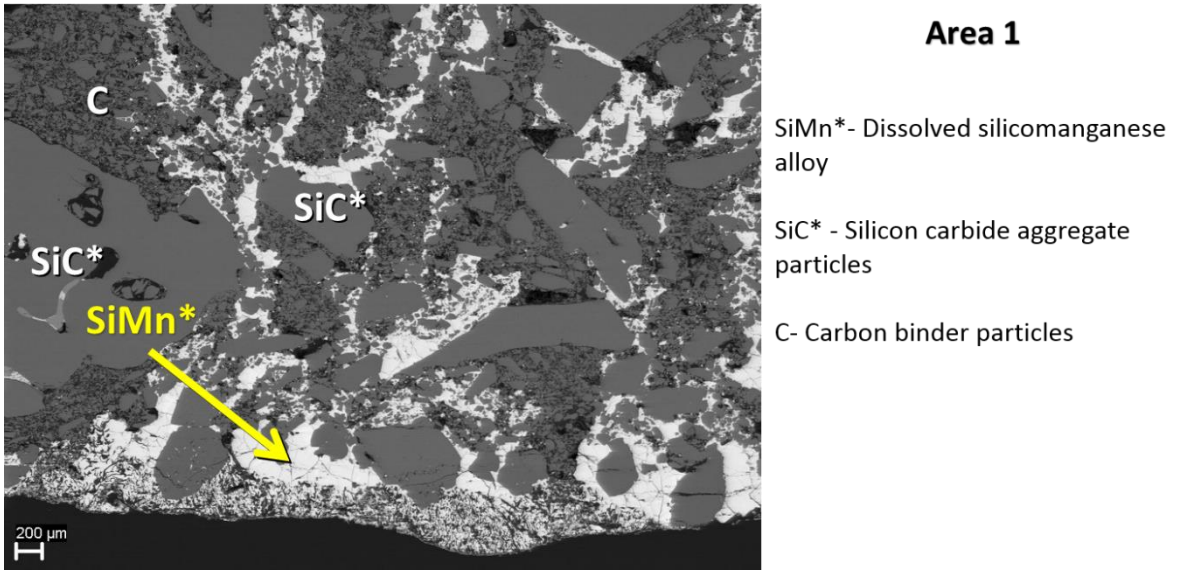

Figure 4.100: Test 16, area 1,-type SiC refractory SEM image measured at 15 kV acceleration voltage. Scale bar indicates 200 µm

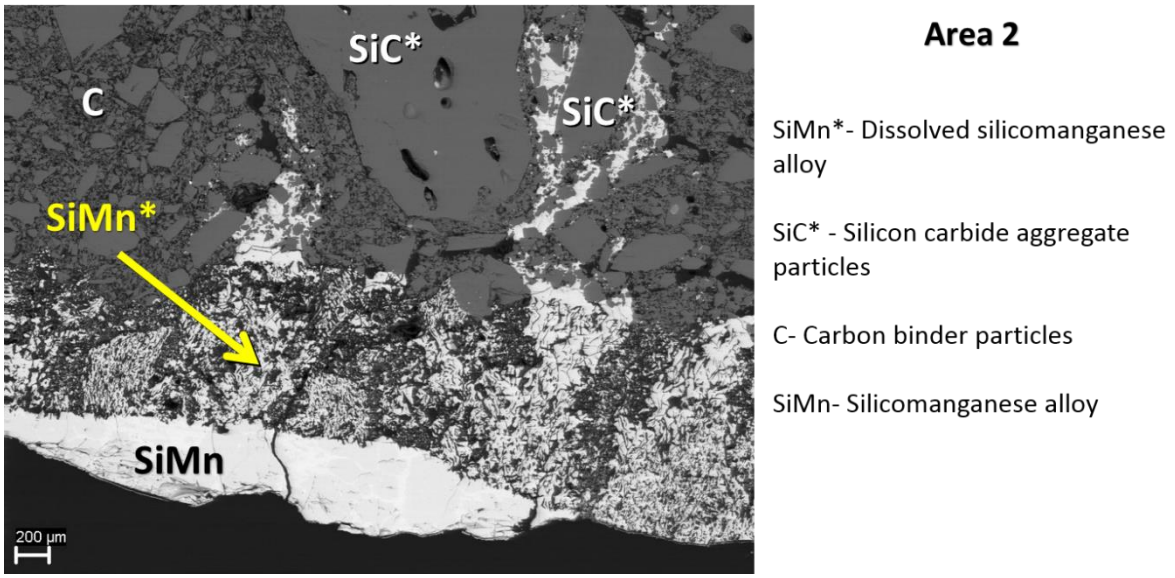

Figure 4.101: Test 16, area 2,-type SiC refractory SEM image measured at 15 kV acceleration voltage. Scale bar indicates 200 µm

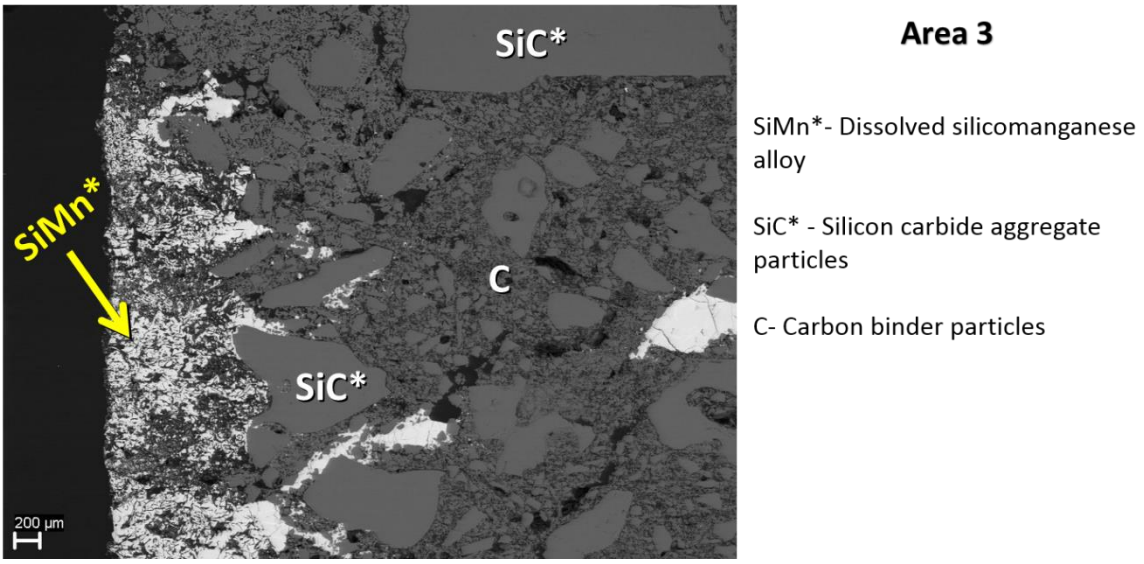

Figure 4.102: Test 16, area 3,-type SiC refractory SEM image measured at 15 kV acceleration voltage. Scale bar indicates 200 µm

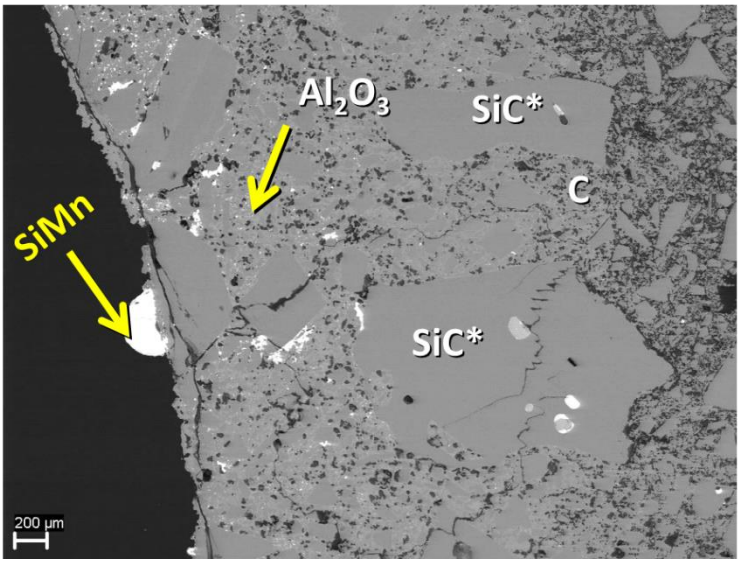

Area 4

SiC* - Silicon carbide aggregate particles

Al_2O_3- Alumina

C- Carbon binder particles

SiMn- Silicomanganese alloy

Figure 4.103: Test 16, area 4,-type SiC refractory SEM image measured at 15 kV acceleration voltage. Scale bar indicates 200 µm

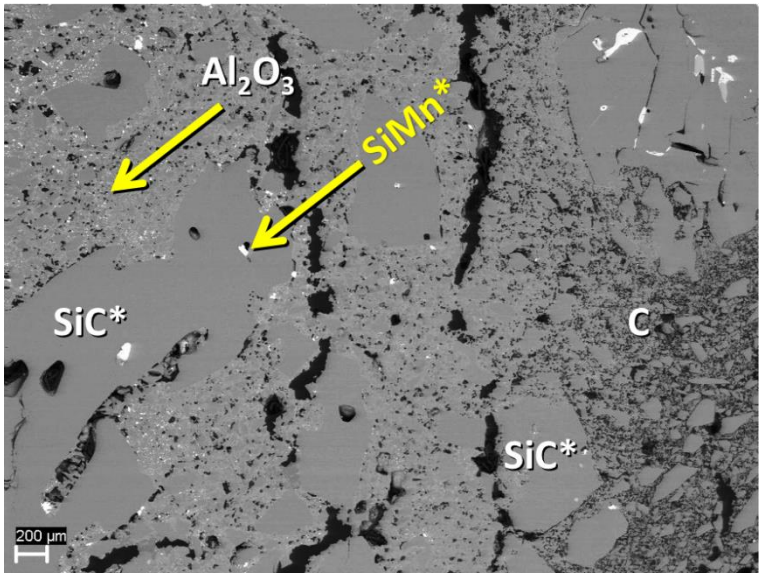

Area 5

SiMn*- Dissolved silicomanganese alloy

SiC* - Silicon carbide aggregate particles

Al_2O_3- Alumina

C- Carbon binder particles

Figure 4.104: Test 16, area 5,-type SiC refractory SEM image measured at 15 kV acceleration voltage. Scale bar indicates 200 µm

CHAPTER 5: DISCUSSION

This chapter discusses the observations made from the experimental work and aims to address the research topics. The test work aimed to address 3 research topics and the first topic aims to evaluate which refractory material performed better at different experimental conditions. The evaluation is done through observation made from FactSage™ calculations, post-mortem refractory sample mechanical wear profiling and SEM-EDS analyses. The second section discusses and evaluate the overall better performing refractory and the second last section discusses the main wear mechanism that contributed the most to the refractory wear.

The research topic was addressed for each of the 3 conditions, i.e when temperature was varied and Si mass % was fixed, when Si mass % was varied and temperature was fixed, and lastly when Si mass % and temperature was fixed and rotational speed was varied. A summary was then included in Table 5.1 to pick out the worst performing refractory.

Table 5.1: Summary of the overall predicted worst behaving refractory and actual wear against the tested variables

Variable	FactSage™	Experimental
Temperature	Type SiC	Type SiC
Si mass %	Type K	Type K
Rotational Speed	-	Type SiC

5.1. Refractory wear under different lab conditions

5.1.1 Effects of temperature

The solubility of C in Mn-Fe-Si-C alloys with Mn:Fe mass ratio of 4.4 at 1550°C, 1600°C and 1650°C was calculated with FactSage 7.2 (FSstel, FeMn and FactPS database) as shown in Figure 5.1. The compositions are given as mass percentages. The as-received alloy composition was unsaturated in both C and SiC, and thus will have a tendency to dissolve both C and SiC refractories. For Si mass % below the dual saturation point on the curve, the stable solid phase at saturation is graphite. SiC is the stable phase at saturation for higher Si mass %. It can be seen in Figure 5.1 that solubility of C increases with increasing temperature from 1550°C to 1650°C and thus it is expected that wear in both refractories would increase with increasing temperature. Consequently, in Table 4.6 it was found from FactSage™ calculations results that

both refractories would dissolve into the alloy as temperature was increased. Furthermore it was found that the type SiC would experience more mass loss compared to the type K. By increasing the temperature from 1550°C to 1650°C at a constant Si mass % of 15, type K refractory will dissolve untill the alloy is C saturated. On the other hand, as temperature increases at constant Si mass %, the alloy remains SiC unsaturated and thus results in the type SiC experiencing more mass loss due to dissolution into the alloy. Experimentally when only temperature was varied and Si mass % was kept constant, the static wear refractory wear profiling shown in Figure 4.7 and 4.8 was in agreement with FactSage™ where the type SiC refractory surface (on the 50mm plane) in contact with the alloy experienced more thickness loss compared to the type K refractory. In Figure 4.6 it can be seen that the results are contradictory and this deviation could have been introduced by the measurement relative error of 1.69 % on the SiC refractory. The type K SEM analyses in Figure 4.21, 4.22 and 4.23 show that the refractory experienced infiltration by the SiMn alloy and dissolution can also be seen by change in the surface shape in Figure 4.23. The type SiC SEM analyses in Figure 4.32, 4.33 and 4.34 show that the refractory also experienced infiltration by the SiMn alloy and not much surface changes can be seen in Figure 4.34 and this could be due to the SiMn alloy filling up the SiC pores instead of eroding its surface.

In addition to the observations made, precipitation of SiC was not visible from the SEM analysis of the type K and type SiC at 1550°C to 1650°C. Therefore at constant Si mass % the wear can be considered as corrosion wear mechanism with the main driving force being dissolution of the refractories into the alloy phase and this observation was in line with observations made by other researchers (Lee *et al*., 2002; Jansson *et al*., 2004; Lee and Zhang, 2004; Steenkamp, 2014). Equation 2.1, in Section 2.6, was then applied in this instance, where for type K, C dissolves into the alloy phase, Equation 5.1, and for type SiC, SiC dissolves into the alloy phase, Equation 5.2, thus reducing the mass of the refractories.

$$C_{refractory} \leftrightarrow C_{alloy} \tag{5.1}$$

$$SiC_{refractory} \leftrightarrow SiC_{alloy} \tag{5.2}$$

The dynamic wear profiling in Figure 4.9, 4.10, 4.11 can be seen that the type SiC refractory behavior was also in agreement with FactSage™ predictions as it can be seen that the type SiC surfaces that were in contact with the SiMn experience more thickness loss compared to the type K surfaces.

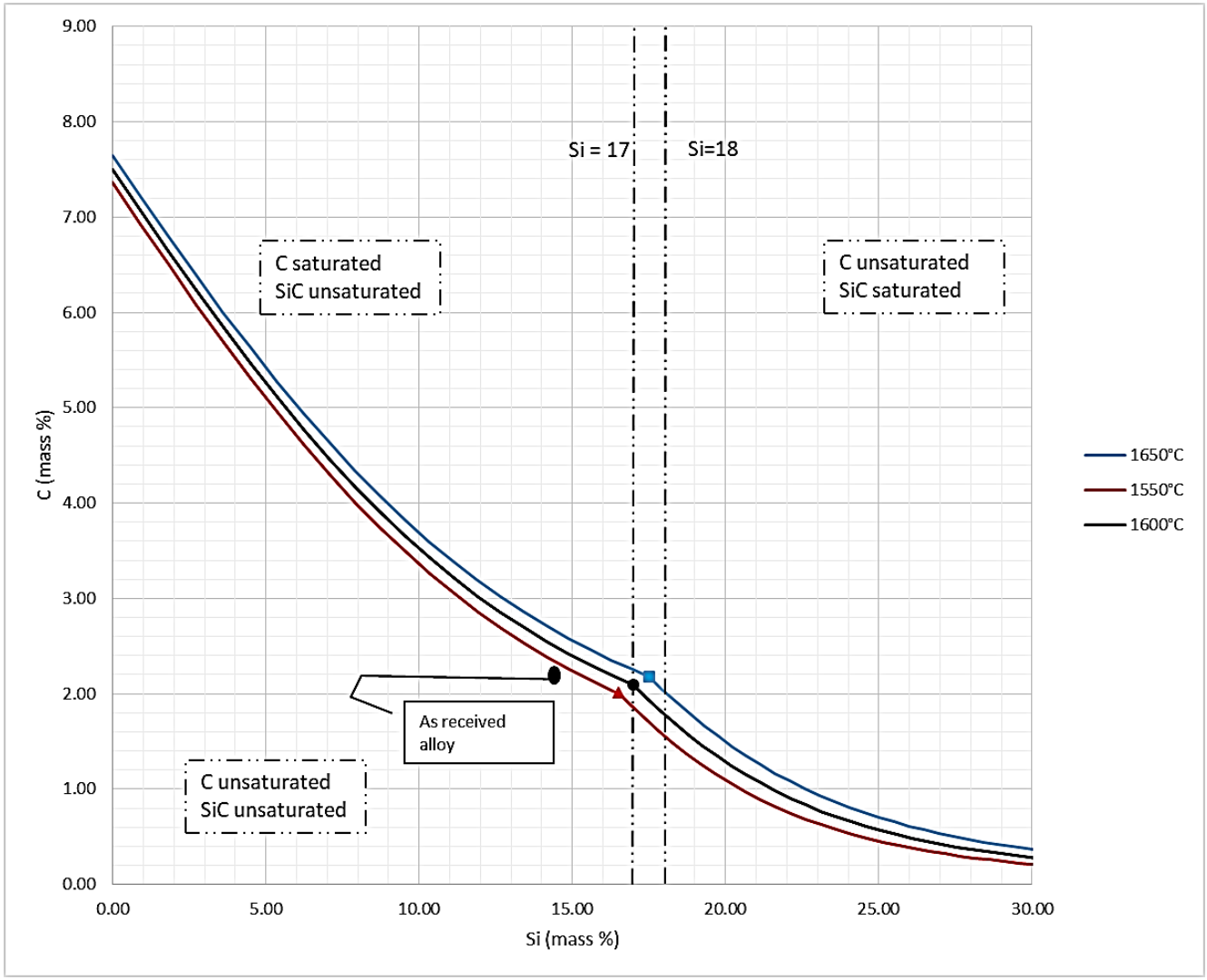

Figure 5.1: Carbon solubility in Mn-Fe-Si-C alloys with Mn:Fe mass ratio of 4.4 at 1550°C 1600°C and 1650°C

5.1.2 Effect of Si content

FactSage™ calculations in Table 4.7 predicted a decrease in mass loss with an increase in Si-content for type K refractory from Si mass % 14 to 16. The predicted mass loss further increased with increasing precipitation of SiC product at 17 and 18 mass % Si. In Figure 4.17 the wear profiling analysis on the type K refractory indicated that the wear increased with increasing Si mass % from 15 to 17 and it then decreased at 18 Si mass % , which was in disagreement with the FactSage™ calculations. At 15 mass % Si the type K SEM analyses in Figure 4.48, 4.49 4.50 and 4.52 show infiltration and SiC precipiation and in Figure 4.51 only

SiMn alloy infiltration was observed. The type K SEM analyses in Figure 4.80, 4.81 and 4.80 at 17 mass % Si, show SiMn alloy infiltration into the refractory and no SiC was observed. On the other hand in Figure 4.83, 4.84, 4.85 and 4.86 infiltration and SiC was observed. The type K SEM analyses in Figure 4.88, 4.89, 4.90 and 4.91 at 18 mass % Si, SiMn alloy infiltration was observed as well as SiC phases, which were identified in all the analysed areas on the refractory surface. In Figure 5.1 it can be seen that solubility of C decreases with increasing Si mass % in the alloy. The type K refractory dissolved into the alloy untill saturation was achieved. Further increasing the Si mass % to 18 resulted in a SiC saturated alloy. It this region SiC was precipitated and type K refractory was expected to dissolve further since the alloy is C unsaturated. There is a possibility that the precipitated SiC formed a protective layer around the refractory hence the reduction in wear at 18 Si mass % (Lee *et al*., 2002; Lee and Zhang, 2004).

The refractory wear extent in the type K refractory when Si mass % was varied (Figure 5.2) can be considered to be stage 2. At this stage the surface alloy infiltration is above 100 microns. The refractory wear extent in the type SiC refractory when Si-content was varied can be considered to be stage 3. At this stage the surface alloy infiltration is above 100 microns and aggregate relic formations are observed, as shown in Figure 5.4. The observation of refractory wear going through different stages was also made by Brosnan, (2004) in the study on corrosion wear mechanisms.

Results from FactSage™ calculations shown in Table 4.8 predicted that the SiC refractory mass loss would decrease with increasing Si mass % while C would be precipitated at 14 and 15 Si mass %. The precipitation of C would decrease with increasing Si mass %. Figure 4.18 shows the type SiC refractory wear area decreased from 15 to 17 Si mass % and further increase to 18 Si mass % results in further reduction in wear, almost similar to the wear at 17 Si mass %. As discussed previously, C and SiC are at dual saturation at 1600°C and 17 mass % Si (Figure 5.1), and thus wear from dissolution is not expected. At 1600°C and 18 mass % Si, the alloy is SiC saturated and C unsaturated and thus the type K refractory was expected to experience more dissolution and none was expected from the type SiC refractory.

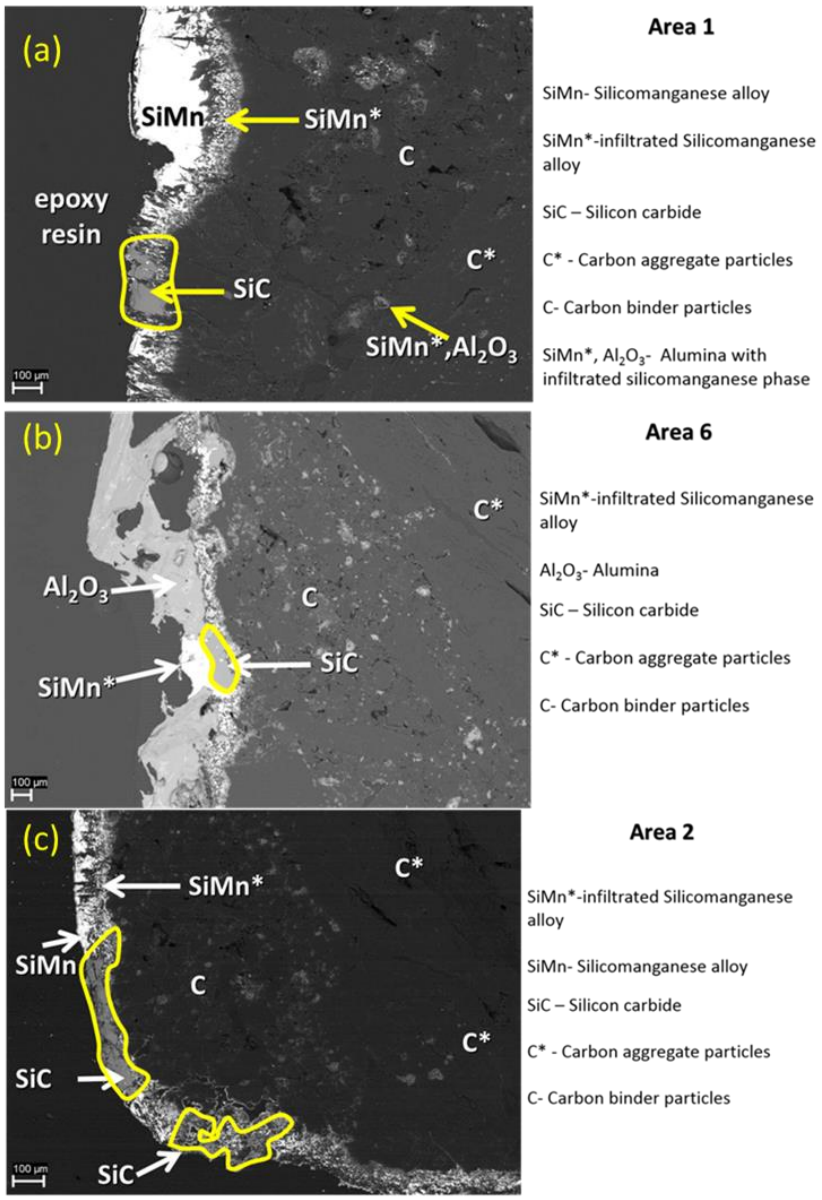

Figure 5.2: Product attachment on the type K refractory surface, (a) 15 mass % Si, (b) 17 mass % Si and (c) 18 mass % Si

5.1.3 Effect of rotational speed

In static tests the refractories experienced chemical wear. In dynamic tests the refractories experienced both chemical and erosion wear. Wear profiling was conducted to assess the effect of rotational speed on the refractories (Figure 4.19). At 1600°C and Si mass % of 15, type K had a slight increase in refractory wear due to erosion. The erosion wear on the type SiC was insignificant. Type SiC experienced more infiltration at static conditions compared to dynamic conditions. The observation was evidenced by the type SiC refractory experiencing expansion compared to the type K. In Table 4.5 it can be seen that the type SiC had a higher porosity

value than the type K refractory thus making the type SiC refractory more susceptible to alloy infiltration. The observations were inline with studies conducted to understand the relationship between refractory characteristics and corrosion wear mechanism, which have indicated that porosity plays a significant role promoting infiltration thus increasing corrosion (Brosnan, 2004; Bazan *et al.*, 2011). SEM analysis comparison at 200 μm magnification of the two refractories (Figure 5.3) shows that the type SiC refractory allowed greater alloy infiltration depth (1087 μm) resulting in refractory expansion, whilst in the type K refraction erosion was relatively on the surface and infiltration depth of (653 μm). Increased alloy infiltration can also be identified as the white areas in the SEM images, where for type SiC in Figure 5.3 (b), there is more white areas (alloy phase) compared to type K, Figure 5.3 (a). The refractory wear extent in both the type K and type SiC refractory at static conditions when temperature was varied, Figure 5.3, can be considered to be stage 2 as is evidenced by greater alloy infiltration depths above 100 microns and aggregate particle dissolution. Alloy infiltration depths of above 100 microns were also observed by Brosnan, (2004) in the study on corrosion wear mechanisms.

Overall at constant temperature and Si mass %, the type SiC experienced more mechanical wear than the type K due to the alloy being SiC unsaturated and not much due to the motion of the refractory.

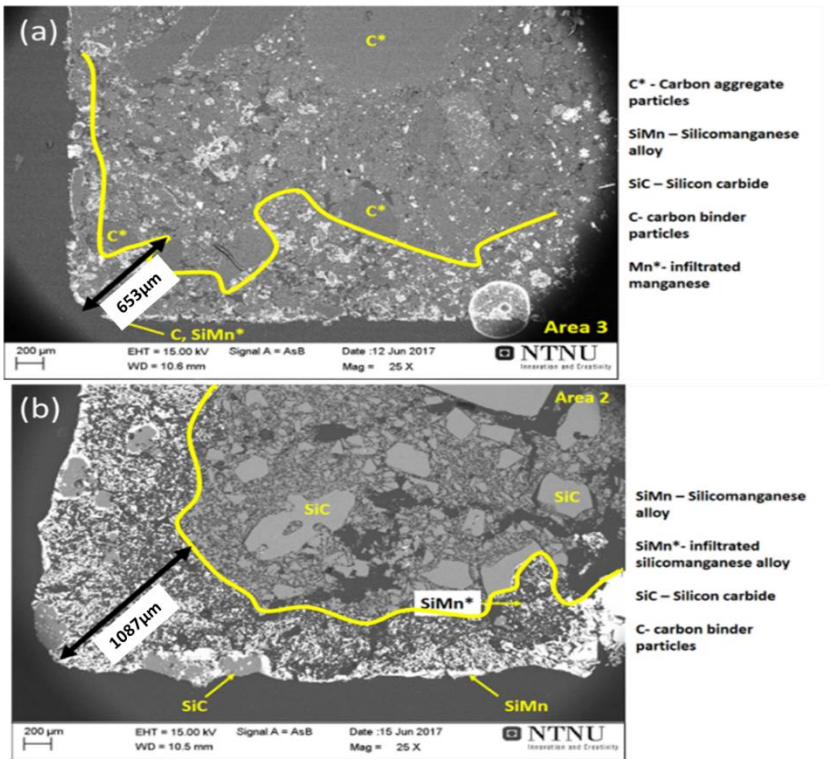

Figure 5.3: Infiltration depth comparison at constant temperature and Si mass % (a) Test 2-static-type K at 1600°C and (b) Test 5-static-type SiC at 1600°C

5.2. Wear mechanism in the type K and type SiC refractory

In Figure 5.4(a) the wear pattern at static conditions for both refractories, was infiltration, and chemical wear. In Figure 5.4(b) the wear pattern at dynamic conditions for refractories, was infiltration, chemical wear, and erosion wear. The main wear mechanism was chemical wear as it was shown that erosion wear had minor impact on the overall mechanical wear analysis at constant temperature and composition. The observation of chemical wear as the main driving force for refractory wear are inline with other studies that were conducted to understand chemical wear mechanisms (Lee *et al*., 2002; Jansson *et al*., 2004; Lee and Zhang, 2004; Steenkamp, 2014).

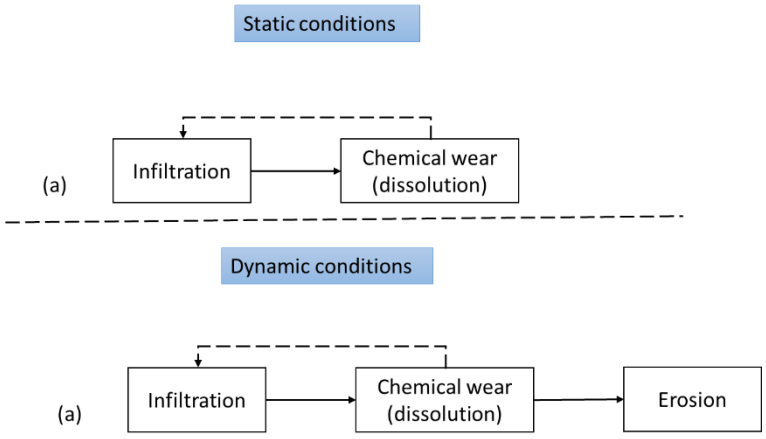

Figure 5.4: Flow diagram of the refractory wear under static and dynamic conditions

5.3. Comparison of the thermodynamic calculations conducted in FactSage™ to experimental results.

This section aims to discuss and compare the merits of the FactSage calculations and how the thermodynamic results apply to the impirical observations by taking a closer look at the assumptions made and the non-equilibrium conditions experienced during the experimental testwork.

Volume loss of the refractories when temperature was varied was calculated using 3D modeling on the Autodesk Fusion 360 free 3D CAD/CAM design software (Figure 5.6). The volume was then converted to mass loss in order to compare with FactSage™. FactSage™ mass loss data was then recalculated with the same initial mass of of the as-received type K and type SiC of 145.29g and 228.15g respectively. The data and calculations used to obtain Figure 5.5 are attached in Appendix F.

Overall in Figure 5.6 it can be observed that the FactSage™ and empirical results had a similar trend where the refractory wear increased with increasing temperature. In addition the type SiC experienced more refractory wear than the type K refractory. There was an observed deviation in the trend for the type SiC at static conditions when temperature was 1650°C and this was due to the refractory experiencing more infiltration of the alloy and thus resulting a slight expansion.

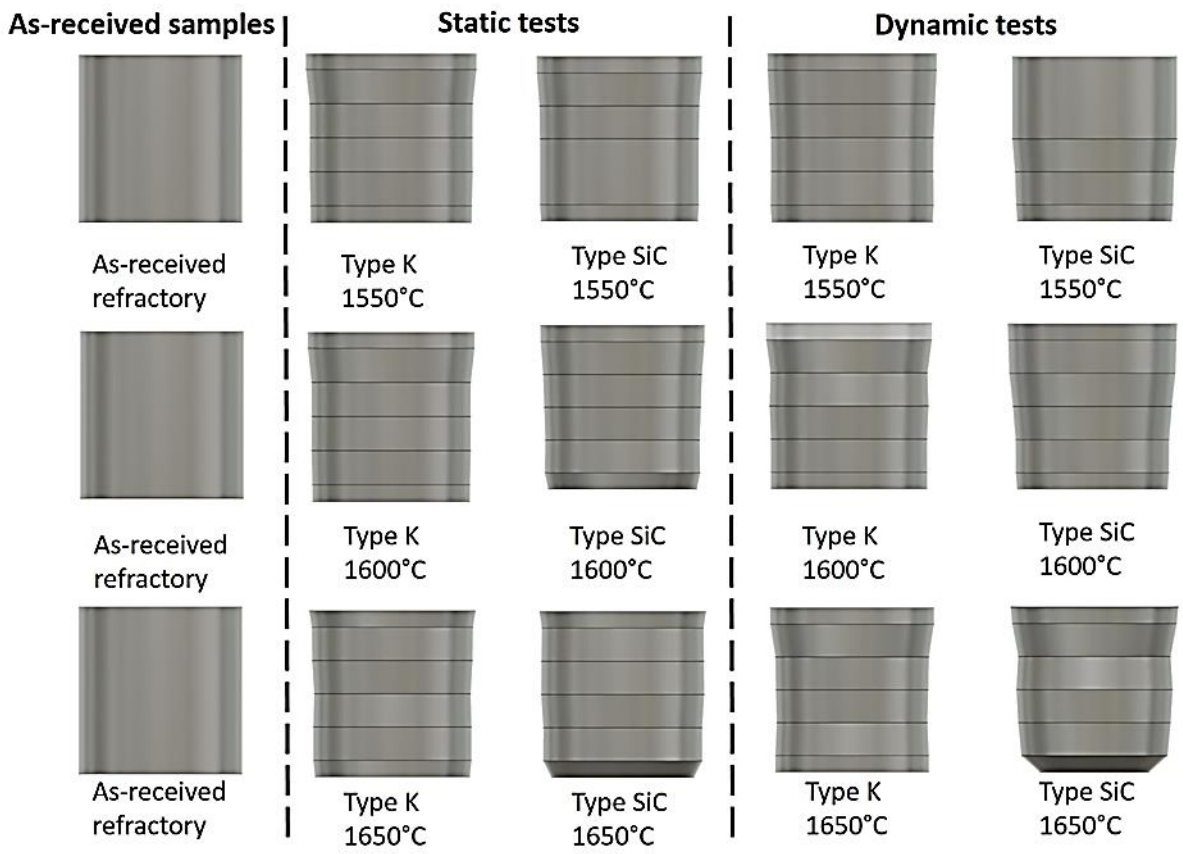

Figure 5.5: 3D refractory wear representation of the actual experimental refractory wear under static and dynamic conditions as temperature was varied with Si mass % fixed.

It can be observed that the refractory wear in the experimental tests was greater than that predicted by FactSage™ due to the preferential attack of the binder phase and resultant loss in structural integrity of the refractories. FactSage™ also does not take into account the kinetics of the chemical reactions taking place, the physical properties of the refractories such as porosity and as well as the fluid dynamics. The deviation in total mass was therefore expected but the general refractory behaviour from the thermodynamics point of view was expected to be in agreement, and this was observed in Table 4.9 and 4.10 where the carbon dissolution into the alloy predicted by FactSage™ at 1550°C and Si mass % of 15 was found to be in agreement with the experimental tests alloy composition.

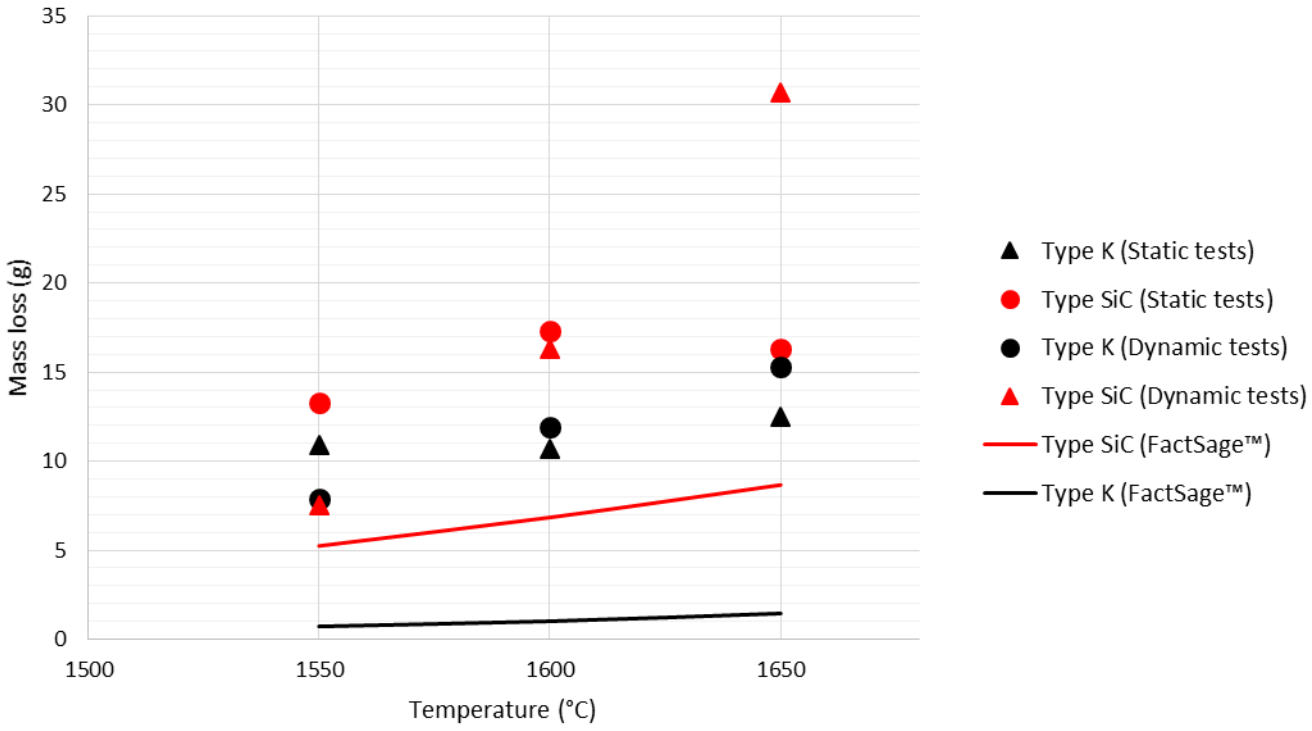

Figure 5.6: Comparison of FactSage™ calculations to the actual experimental refractory wear under static and dynamic conditions as temperature was varied with Si mass % fixed.

5.4. Refractory suitability for use in the hearth area of an industrial furnace producing SiMn

Table 5.1 contains a summary of conclusions from the first research topic. When temperature is varied and Si mass % is constant the type SiC refractory experienced more wear than the type K. Increasing in temperature at constant Si mass % resulted in the alloy being C saturated and SiC unsaturated. Varying Si mass % and keeping temperature constant the type K refractory experienced more wear than the SiC. As increasing Si mass % to 17 and 18% resulted in the alloy being SiC saturated and C unsaturated. Varying rotational speed from static to dynamic, whilst Si mass % and temperature is constant the type SiC refractory experienced more wear than the type K refractory. Though the effect of mechanical wear was not as significant as chemical wear.

In summary the type K is a better suited refractory to use in the hearth area of an industrial furnace as long as the Si mass % in the alloy is below 17 for Mn-Fe-Si-C alloys with Mn:Fe mass ratio of 4.4. In addition the type K physical properties such as low porosity also allows it to be a more versatile refractory by limiting infiltration to the surface.

CHAPTER 6: CONCLUSIONS

Chemical wear of refractories by SiMn was studied in this dissertation. The research objectives were to develop a rotating finger experimental set-up that will allow the study of the carbon-based hearth refractory wear by SiMn alloy. The second objective was to characterise the refractory and alloy before reaction and post-mortem studies on reacted refractory, based on techniques developed by Steenkamp (Steenkamp, 2014), and other relevant methods to quantify the extent of wear. The third objective was to compare the thermodynamic calculations conducted in FactSage™ to experimental results. The final objective was to compare of the extent in wear between the K-type and SiC-type carbon based refractories. This chapter summarizes the experimental work and the highlighted results from the three research topics. In addition, recommendations for further work are summarized.

The compatibility of two ramming pastes – one carbon-based (type K), the other SiC-based (type SiC) – with SiMn alloy were investigated through 6 static tests and 18 dynamic tests in a 25 kW induction furnace at 90 minutes holding time. Temperature and Si mass % were investigated by fixing one and varying the other in order to assess their impact on the two refractory samples. The experimental design and post mortem sample analysis method were developed, tested through 6 dyamic temperature tests and further optimised for the actual experimental test work.

The type K refractory contains 86.4 mass % fixed carbon and 10.9 mass % ash. The type SiC refractory contains 1.6 mass % fixed carbon, Si metal and SiC reported to the ash, with a composition of 95.9 mass %. The alloy sourced for the experimental work is typically a grade C alloy, containing 67.8 mass % Mn, 2.2 mass % C, 15 mass % and 15.5 mass % Fe.

6.1. Refractory wear under different laboratory conditions

Thermodynamically the alloy was not saturated in both C and SiC and hence it was expected that both type K and type SiC would dissolve into the alloy. FactSage™ predicted refractory wear for both refractories when temperature is varied due to chemical wear with the type SiC experiencing the most wear. Increasing temperature at constant Si mass %, the alloy reached saturation but further temperature increase resulted in an increased C solubity into the refractory. At constant Si mass %, the alloy remained SiC unsaturated hence type SiC was expected to wear out the most. Experimentally it was also found that the type SiC experienced more wear than the type K refractory. Microscopical examination indicated greater infiltration

into the type SiC refractory because its porous nature further promoted chemical wear compared to the type K where refractory wear occured on the surface.

FactSage™ further predicted refractory wear for both refractories when Si mass % is varied due to chemical wear with the type SiC experiencing the most wear. Increasing Si mass % at constant temperature, C solubility was decreased and further Si mass % from the dual saturation point when Si mass % was 17 to 18 resulted in the alloy being C unsaturated and SiC saturated. Experimentally it was also found that the type K refractory experienced more wear than the SiC when the Si mass % was varied. SEM analyses indicated greater infiltration into the type SiC refractory because of its porous nature but more chemical wear was experienced by type K with evident SiC precipitation and the particles were observed on the surface of the type K refractory. At constant temperature and Si mass % slight increase in wear was observed due to erosion when dynamic motion was introduced, but it was not as significant as the chemical wear.

6.2. Refractory suitability for use in the hearth area of an industrial furnace producing SiMn

The type K is the most suited refractory material to use in the hearth area of an industrial furnace as long as the Si mass % in the alloy is maintained below 17 for Mn-Fe-Si-C alloys with Mn:Fe mass ratio of 4.4. The type K physical properties such as low porosity minimises the alloy infiltration.

6.3. Wear mechanism in the type K and type SiC refractory

The main wear mechanism was chemical wear. Erosion was introduced with dynamic motion but the effect was insignificant relatively.

6.4. Recommendations for further study

There is opportunity for further test work to assess the impact of other variables that may impact the lifespan of the refractory cylinders, namely:

- The reaction time is important in understanding how wear impacts the service life on the refractories. In a SAF the molten alloy is always in contact with the hearth thus the reaction time is greater than 90 minutes. It is recommended that future studies investigate the time by varying between 60 and 120 minutes at 30 minute intervals. Varying the reaction time will allow an understanding the impact of the reaction kinetics of the main wear mechanism.

- The motor speed, which needs to be varied between 150 rpm and 300 rpms, at 50 rpm intervals. The velocity of the molten material introduces frictional forces and wear due to erosion. Varying the motor speed will help understand the alloy and refractory interactions in areas of low velocity such as the hearth, and areas of high velocity such as the tap-hole area. Modelling of the dynamic conditions would also help understand the transient conditions which have an impact on erosion and abrasion wear mechanisms. It was identified from the testwork that dynamic motion at 100 rpm did not introduce significant erosion wear. Investigation of the effects of rotational speed, which introduce shear force is recommended as a further study to understand fluid dynamics of molten SiMn alloy. The impact of temperature on the viscosity of the alloy would further be required to be investigated as well.

CHAPTER 8: REFERENCES

1. ASTM-D3172 (2013) ‘Standard Practice for Proximate Analysis of Coal and Coke 1’, *Annual Book of ASTM Standards*. West Conshohocken, PA, United States: ASTM International, pp. 1–2. doi: 10.1520/D3172-13.2.
2. ASTM-D3173 (2011) ‘Standard Test Method for Moisture in the Analysis Sample of Coal and Coke 1’, *Annual Book of ASTM Standards*. West Conshohocken, PA, United States: ASTM International, pp. 1–4. doi: 10.1520/D3173-11.2.
3. ASTM-D3174 (2012) ‘Standard Test Method for Ash in the Analysis Sample of Coal and Coke from Coal 1’, *Annual Book of ASTM Standards*. West Conshohocken, PA, United States: ASTM International, pp. 1–6. doi: 10.1520/D3174-11.2.
4. ASTM A483 (2010) ‘Standard Specification for Silicomanganese’, *Annual Book of ASTM Standards.* West Conshohocken, PA, United States: ASTM International, pp. 1–2. doi: 10.1520/F1026-86R08E01.2.
5. AursjØ, S. (2015) *Wear of carbon refractory materials in silicon furnaces*. Norwegian University of Science and Technology, NTNU.
6. Bale, C., Chartrand, P., Degterov, SA., Eriksson, G. (2002) ‘FactSage thermochemical software and databases’, *Calphad*, 26, pp. 189–228.
7. Banda, W., Steenkamp, J. D. and Matinde, E. (2016) ‘Chemical wear of carbon and silicon carbide-based refractory materials by silicomanganese metal’, *in EEC11 - 11th European electric steelmaking conference & expo (25-27 May 2016).*
8. Baxendale, S. (2004) ‘Testing of Refractory Materials’, in *Refractories Handbook*, pp. 435–474.
9. Bazan, J., Socha, L., Martínek, L., Fila, P., Balcar, M., Chmela, J. (2011) ‘Wear of refractory materials for ceramic filters of different porosity in contact with hot metal’, 45(6), pp. 603–608.
10. Brosnan, D. A. (2004) ‘Corrosion of Refractories’, in Schacht, C. A. (ed.) *Refractories Handbook.* New York: Marcel Dekker, Inc., pp. 39–77. Available at: https://www.jurispro.com/files/documents/doc-1066205184-article-1609.pdf.
11. Chesters, J. H. (1963) *Refractories Production and Properties*. London, UK: The iron and steel institute.
12. Dzermejko, A. J., Baret, D. F. and Hubble, D. H. (1999) ‘Ironmaking Refractory Systems’, *Making, Shaping and Treating of Steel - Ironmaking Volume*, pp. 229–258.

13. Elkem Carbon (2009) ‘Elkem Cold Lining Paste Type-SiC, Data Sheet’. Kistiansand, Norway.
14. Elkem Carbon (2015) ‘Type K Lining Paste, Data Sheet’. Kistiansand, Norway.
15. Elkem Carbon (2018) Carbon products. Available at: https://www.elkem.com/carbon/carbon-products/ (Accessed: 10 May 2018).
16. Eric, R. H. and Demir, O. (2014) ‘Dissolution of Chromite in Slags’, *Mineral Processing and Extractive Metallurgy*, 123(1), pp. 2–9.
17. Ewais, E. M. M. (2004) ‘Carbon Based Refractories’, *Journal of the Ceramic Society of Japan*, 112(10), pp. 517–532. doi: 10.2109/jcersj.112.517.
18. Gasik, M. (2013) *Handbook of Ferroalloys: Theory and Technology*. Butterworth-Heinemann.
19. Gregurek D, Ressler A, Reiter V, Franzkowiak A, Spanring A, Prietl T. (2013) ‘Refractory wear mechanisms in the nonferrous metal industry: Testing and modeling results’, *Jom*, 65(11), pp. 1622–1630. doi: 10.1007/s11837-013-0758-1.
20. Hafner, B. (2006) ‘Energy Dispersive Spectroscopy On The SEM: A Primer’, *Characterization Facility, University of Minnesota*, pp. 7–10.
21. Hancock, J. (2006) *Practical Refractories*. Vereeniging, South Africa: Cannon and Hancock cc.
22. Hubble, D. H. (1999) ‘Steel Plant Refractories’, *The Making, Shaping and Treating of Steel - Ironmaking Volume*, pp. 161–228.
23. Jansson, S., Brabie, V. and Bohlin, L. (2004) ‘Corrosion mechanism and kinetic behaviour of refractory materials in contact with CaO-Al 2 O 3 -MgO-SiO 2 slags’, pp. 341–348.
24. Kruger, Joachim; Reuter, Marcus A; Kögler, Carina; Probst, T. (2005) *Metallurgical Furnaces*. Weinheim: Wiley-VHC Verlag GmbH & Co. KGaA.
25. Lee, W. E., Argent, B. B. and Zhang, S. (2002) ‘Complex phase equilibria in refractories design and use’, *Journal of the American Ceramic Society*, 85(12), pp. 2911–2918.
26. Lee, W. E. and Zhang, S. (2004) ‘Direct and indirect slag corrosion of oxide and oxide-c refractories’, in *VII International Conference on Molten Slags Fluxes and Salts*. Cape Town, pp. 309–320.
27. Matthey, J. (1988) ‘Platinum metals review’, *Platinum metals review*, 32, p. 72.
28. Mattila, R. A., Vataneen, J. P. and Härkki, J. J. (2000) ‘Chemical wearing mechanism of refractory materials in a steel ladle slag line’, in *VI International Conference on*

Molten Slags Fluxes and Salts. Stockholm. Available at: https://www.pyrometallurgy.co.za/MoltenSlags2000/pdfs/159.pdf.

29. Mcewan, N., Courtney, T., Parry, R A., Knupfer, P. (2011) 'Chromite — A cost-effective refractory raw material for refractories in various metallurgical applications', (March), pp. 6–9.
30. Miller, D. J., Ruoff, W. H., Strong, S.L., Intermill, A.W., Thoman, T.R., Shao, R.L., (2007) 'Induction furnace for high temperature operation Ep 1 499 179 b1 (12)'.
31. Mølnås, H. (2011) *Compatibility Study of Carbon-Based Refractory Materials utilized in Silicomanganese Production Furnaces (Master's Dissertation)*. Norwegian University of Science and Technology.
32. Mourao, M. B., Murthy, G. G. K. and Elliott, J. F. (1993) 'Experimental Investigation of Dissolution Rates of Carbonaceous Materials', *Metallurgical Transactions B*, 24B (August), pp. 629–637.
33. Mushwana, M. and Steenkamp, J. D. (2015) *Apparent Porosity and Bulk Density Measurements of Samples from an Industrial-Scale Söderberg Electrode*. Randburg, South Africa.
34. NA Sithole, N Rambuda, JD Steenkamp, DA Hayman, and CJ Hockaday. (2018) 'Silicomanganese production at Mogale Alloys', *Journal of The Southern African Institute of Mining and Metallurgy*, 118.
35. Olsen, S. E. and Tangstad, M. (2004) 'Silicomanganese Production – Process Understanding', INFACON X: *Transformation through Technology*, (February), pp. 231–238.
36. Poirier, J., Bouchetou, M.L., Prigent, P., Berjonneau, J. (2007) 'An Overview of Refractory Corrosion: Observations, Mechanisms and Thermodynamic Modeling', *Refractory Application Transactions*, 3(2), pp. 1–12.
37. Routschka, G. (2008) *Pocket Manual Refractory Materials*. Hartmut Wuthnow.
38. SGS (2015) *Proximate and Ultimate Analysis - Mining*. Available at: http://www.sgs.co.za/en/Mining/Analytical-Services/Coal-and-Coke/Proximate-and-Ultimate-Analysis.aspx (Accessed: 1 July 2015).
39. Shigeno, Y., Tokuda, M. and Ohtani, M. (1985) 'The Dissolution Rate of Graphite into Fe-C Melt Containing Sulphur or Phosphorus', *Trans. Jpn. Inst. Met*., pp. 33–43.
40. Silva, S. N., Vernilli, F., Justus, S. M., Marques, O. R., Mazine, A. Baldo, J. B., Longo, E., Varela, J. A. (2005) 'Wear mechanism for blast furnace hearth refractory lining', *Ironmaking & Steelmaking*, 32(6), pp. 459–467. doi: 10.1179/174328105X48160.

41. Steenkamp, J. D. (2014) *Chemical wear of carbon-based refractory materials in a silicomanganese furnace tap-hole*. University of Pretoria.
42. Steenkamp, J. D. (2014) *Chemical Wear of Carbon - Based Refractory Materials In A Silicomanganese Furnace Tap - hole (PhD Thesis)*. University of Pretoria.
43. Steenkamp, J. D., Maphutha, P., Makwarela, O., Banda, W. K., Thobadi, I., Sitefani, M., Gous, J.P., Sutherland, J.J. (2018) 'Silicomanganese production at Transalloys in the twenty-tens', *Journal of The Southern African Institute of Mining and Metallurgy*, 118, pp. 309–320.
44. Steenkamp, J. D. (2018) 'Submerged arc furnace producing silicomanganese according to ore-based process', in *Extraction 2018*.
45. Steenkamp, J. D., Bam, W.G., Ringdalen, E., Mushwana, M., Hockaday, S.A.C., Sithole, N.A. (2018) 'Working towards an increase in manganese ferroalloy production in South Africa — a research agenda', 118(February), pp. 645–654.
46. Steenkamp, J. D. and Pistorius, P. C. (2015) 'Tap-Hole Wear: Analysis of Daily Average Slag And Metal Compositions of A Single SiMn Smelter', in *The Fourteenth International Ferroalloys Congress*, pp. 505–510.
47. Sun, H., Mori, K., Sahajwalla, V., Pehlke, R.D. (1998) 'Carbon Solution in Liquid Iron and Iron Alloys', *High Temperature Materials and Processes*, pp. 257–270.
48. Tang, K. and Olsen, S. E. (2006) 'Computer simulation of equilibrium relations in manganese ferroalloy production', *Metallurgical and Materials Transactions B*, 37, pp. 599–606.
49. Theraja, B. L. (2014) 'Electric heating, Chapter 47', in *Electrical Technology vol. III, 23rd ed*. S. Chand Publishing, pp. 1834–1851.
50. Tomala, J. and Basista, S. (2007) 'Micropore Carbon Furnace Lining', *Infacon XI: Innovation in Ferroalloy Industry*, pp. 722–727.

APPENDIX A: OPERATING PROCEDURE OF THE ROTATING FINGER EXPERIMENTAL SET-UP

Appendix A consist of the procedure that was developed to run the rotating finger experimental set-up, as well as a some of the challenges that were faced while conducting mechanical testing during the trial tests and how they were each addressed in order to optimize the experimental equipment.

The experimental method consists of 20 steps described below;

Step 1

Clean induction furnace and fill in alumina bubbles to the height of 155 mm (from bottom of furnace chamber), see Figure A1.

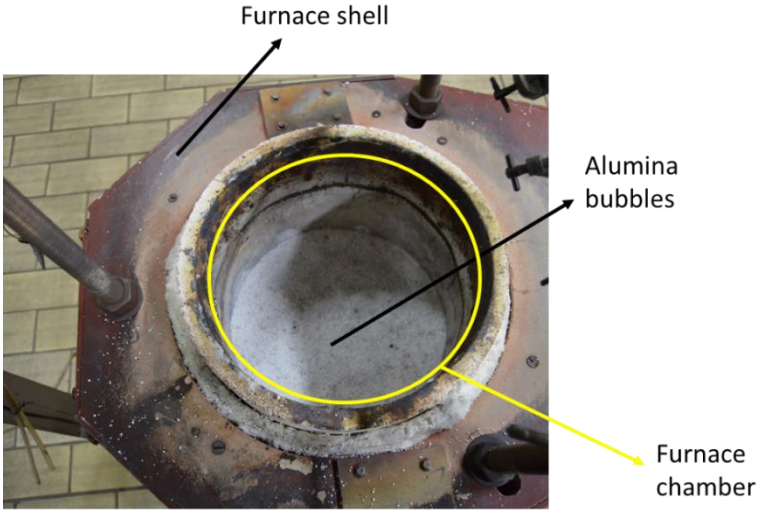

Figure A1: Induction Furnace

Step 2

Insert graphite crucible, used as susceptor, into furnace, see Figure A2.

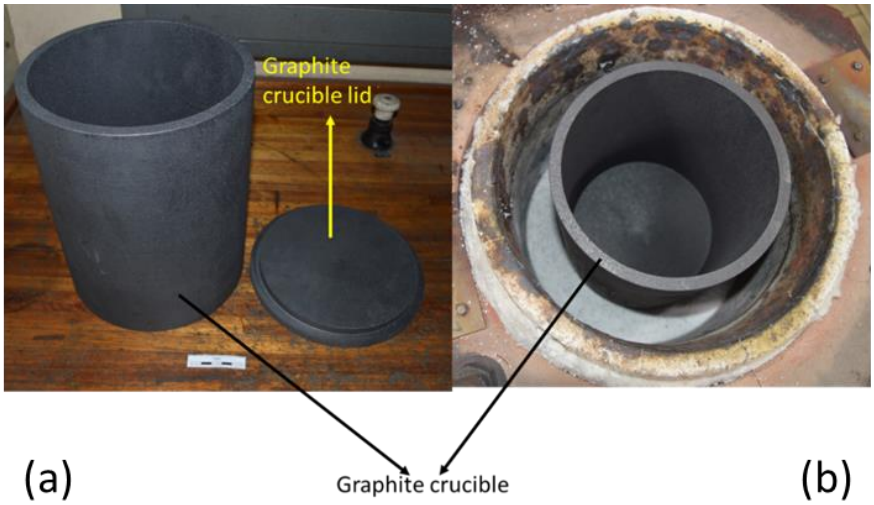

Figure A2: Graphite crucible (a) and graphite crucible inside the induction furnace (b)

Step 3

Fill the gap between graphite crucible and furnace chamber wall with alumina bubbles, see Figure A3.

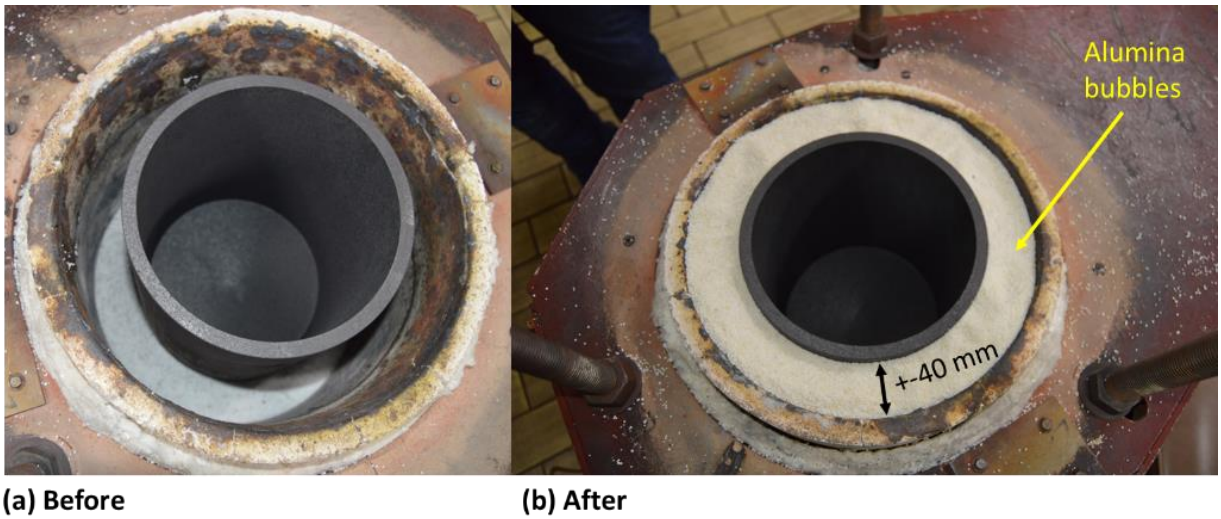

Figure A3: Graphite crucible and induction furnace before (a) and after (b) filling with alumina bubbles

Step 4

Fill graphite crucible with alumina bubbles to the height of 45 mm (from bottom of graphite crucible), see Figure A4.

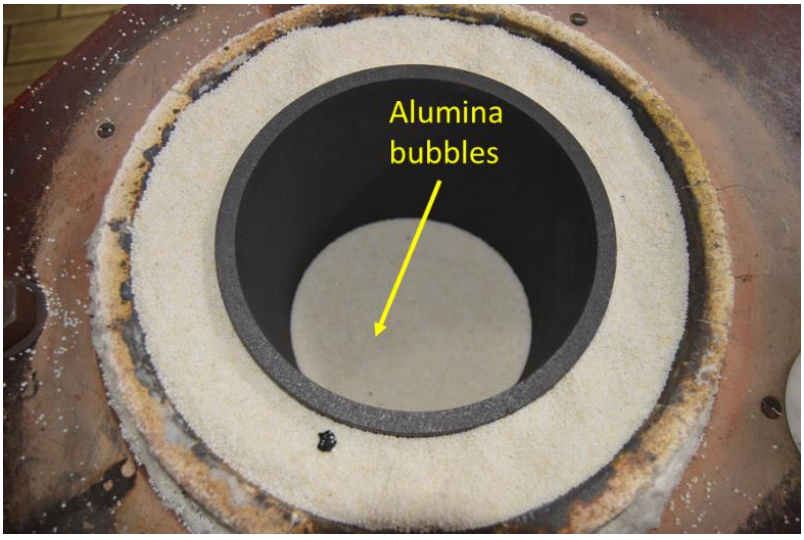

Figure A4: Induction furnace and graphite crucible filled with alumina bubbles

Step 5

Place alumina crucible inside the graphite crucible, see Figure A5.

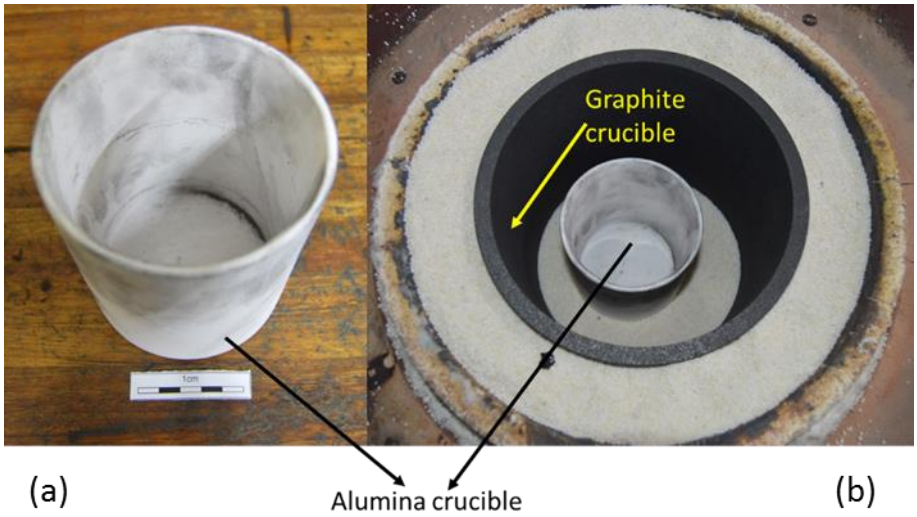

Figure A5: Alumina crucible (a) and alumina crucible inside the graphite crucible (b)

Step 6

Place electric motor stand on the furnace shell, see Figure A6.

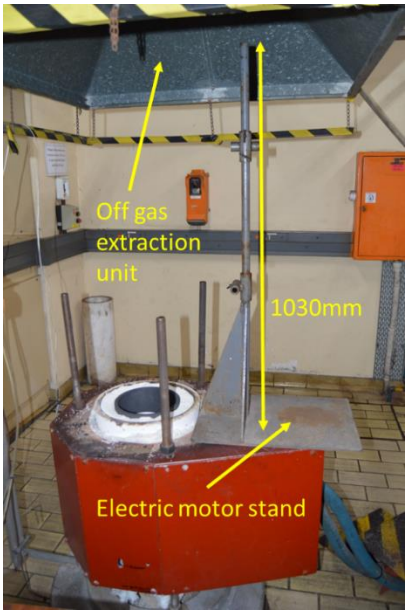

Figure A6: Electric motor stand on the furnace shell

Step 7

Attach rod alignment cylinder to electric motor and connect electric motor to the stand, see Figure A7.

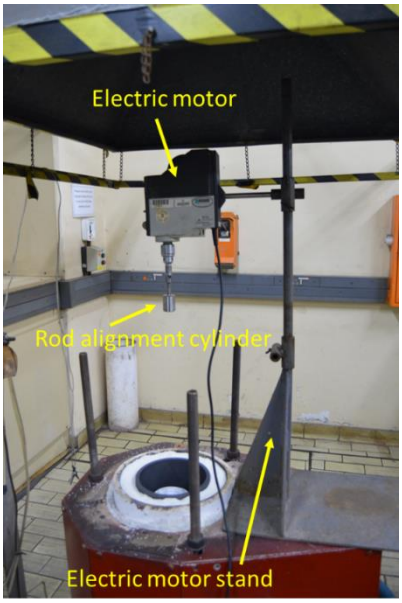

Figure A7: Electric motor stand with motor on the furnace shell

Step 8

Drill holes through the graphite crucible lid, see Figure A8.

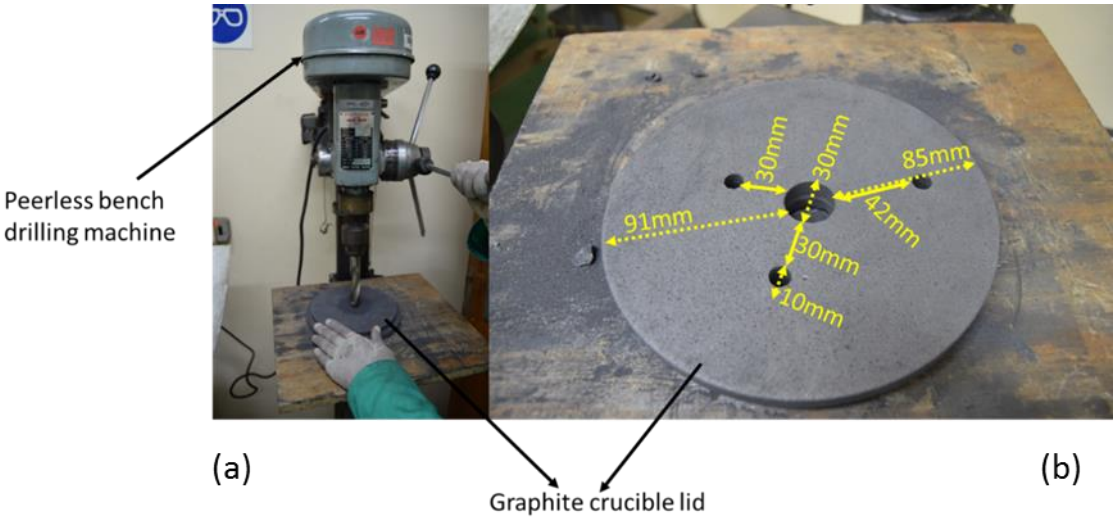

Figure A8: Peerless bench drilling machine (a) and drilled crucible lid (b)

Step 9

Insert rod and refractory cylinder through the lid, and attach the rod to the electric motor by screwing the rod onto the rod alignment cylinder, see Figure A9.

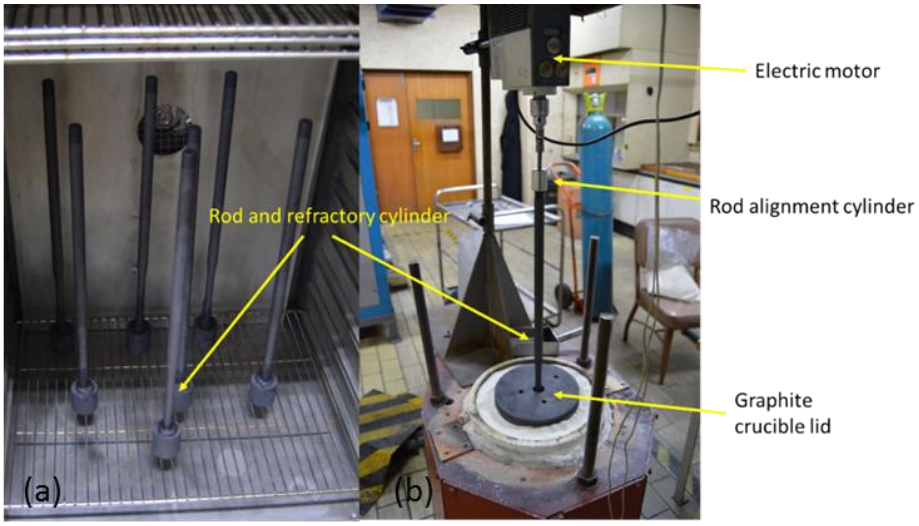

Figure A9: Graphite rod and refractory cylinder in the oven during baking (a) and rod connected to the electric motor (b)

Step 10

Lower the electric motor position to **ON.** Once the test has been completed the electric motor would then be move to **OFF** position, see Figure A10 and Figure A11.

Figure A10: Marked position for the rotating motor (a) and the refractory cylinder level when lowered to 'On' position (b)

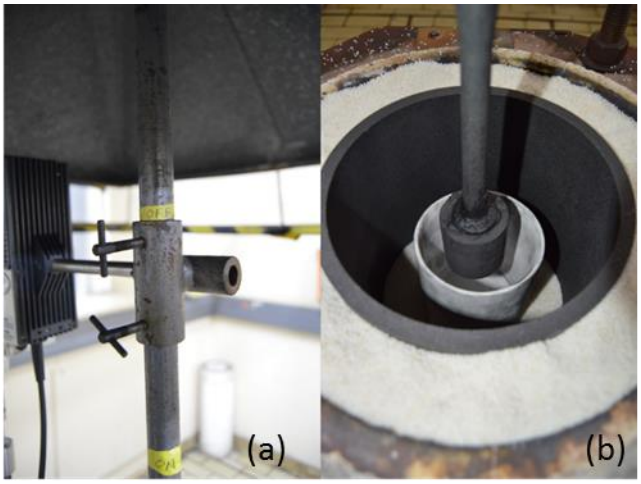

Figure A11: Marked positions for the rotating motor (a) and the refractory cylinder level when raised to 'OFF' position (b)

Step 11

- Open graphite crucible lid and pour in SiMn alloy sample in the alumina crucible to the level of 25 mm and place refractory cylinder on top the alloy.
- Cover the refractory cylinder and alumina crucible gap by adding alloy sample to cover 70% of the refractory height (i.e.35 mm/55 mm).
- Close graphite crucible lid, see Figure A12.

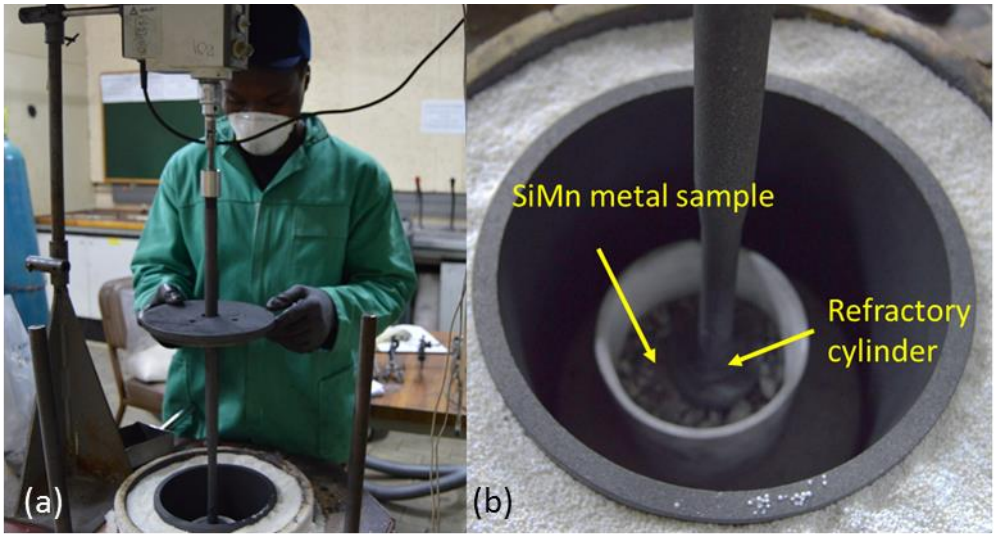

Figure A12: Opening the crucible lid (a) and the alloy sample added in the alumina crucible (b)

Step 12

Mount thermocouple stand, see Figure A13.

Figure A13: Thermocouple stand used for mounting tubes

Step 13

Insert 105 mm of thermocouple into the graphite crucible and mount it on the thermocouple stand, see Figure A14. Do for both thermocouples, one inside alumina crucible, one outside – see Figure A15. Insert argon pipe into the graphite tube near the alumina crucible.

.

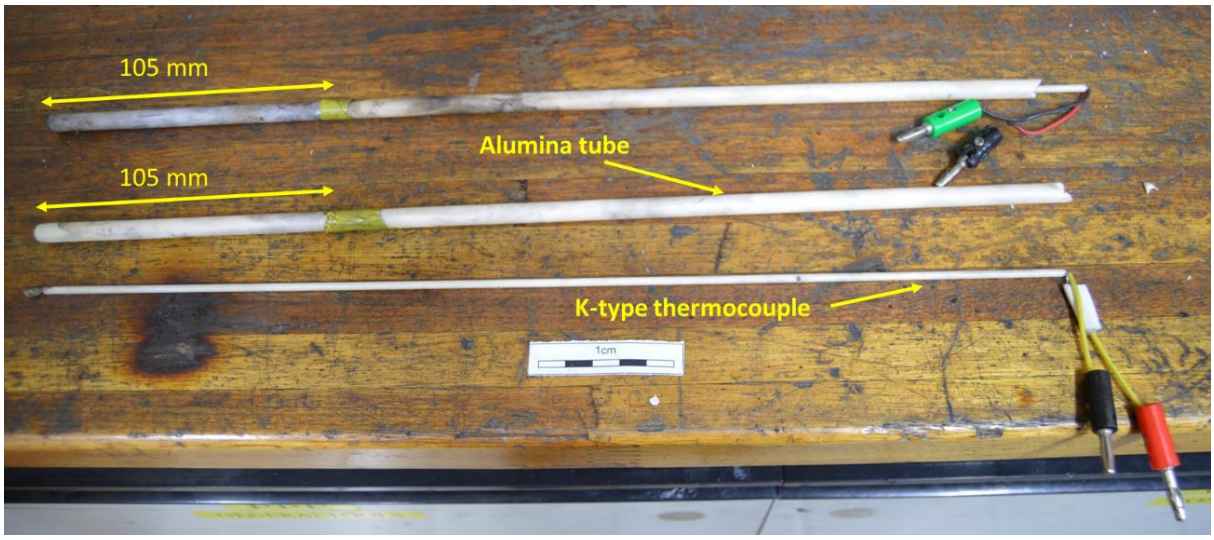

Figure A14: Thermocouple alumina tubes and welded K-type thermocouples

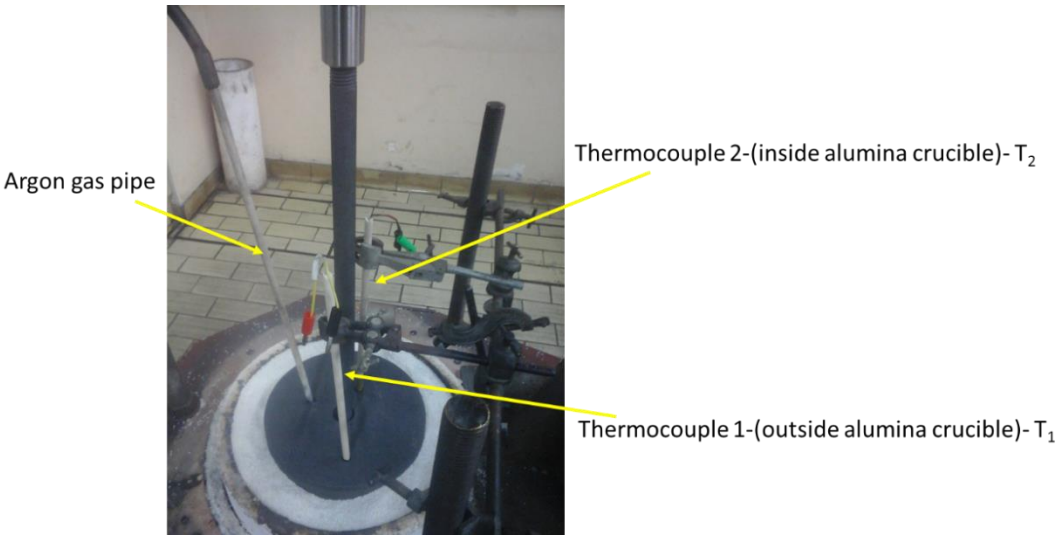

Figure A15: Thermocouples inserted through the graphite crucible lid

Step 14

Connect argon gas cylinder to the flow meter, see Figure A16.

Figure A16: Argon gas cylinders and a Fischer & Porter Model 10A6132M/B10 - 1/4" NPTF gas flow meter.

Step 15

Connect thermocouples to the Agilent 34970A temperature data readers and set the temperature setting to B-type and units in °C, see Figure A17.

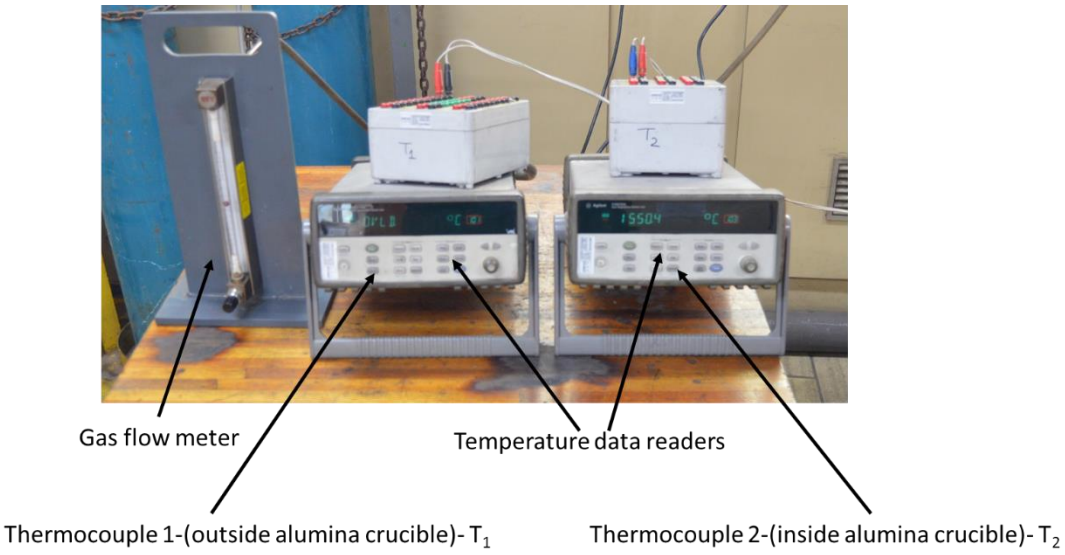

Figure A17: Agilent 34970A temperature data readers

Step 16

Fully cover the graphite crucible alumina bubbles, see *Figure 1*.

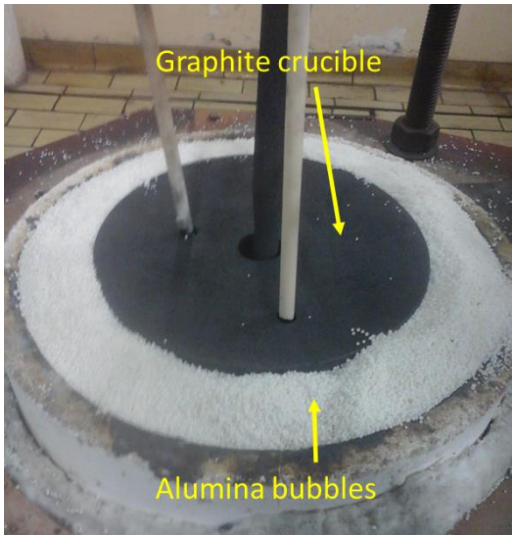

Figure 1: Graphite crucible fully covered by alumina bubbles

Step 17

Cut ceramic blanket (fibre frax) into small pieces Figure A19 (a) and cover the graphite crucible with the ceramic blanket, see Figure A19 (b).

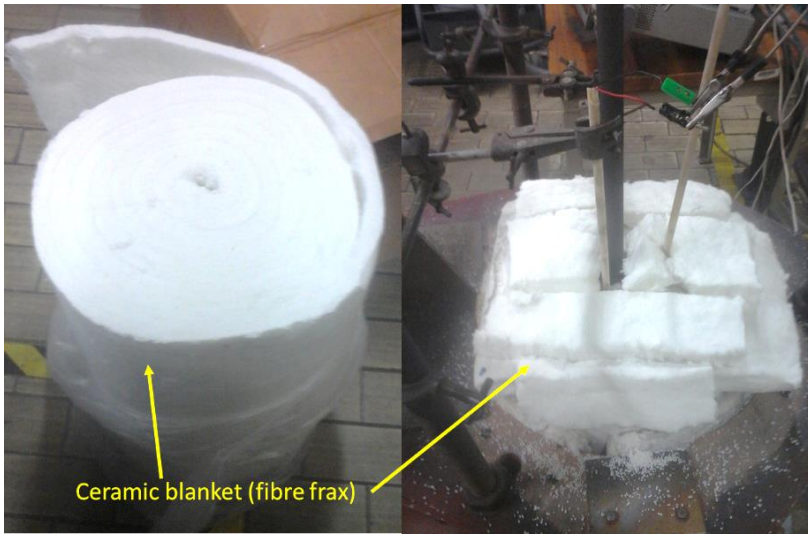

Figure A19: Ceramic blanket (a) and ceramic blanket pieces covering the graphite crucible lid (b)

Step 18

- Switch cooling water pump ON, see Figure A20 (a)
- Turn main switch on the furnace ON, see Figure A20 (b)
- Turn cooling water ON, see Figure A20 (c)
- Turn the Heat ON, see Figure A20 (c)
- Set Power knob to 2.5kW, see Figure A20 (c)

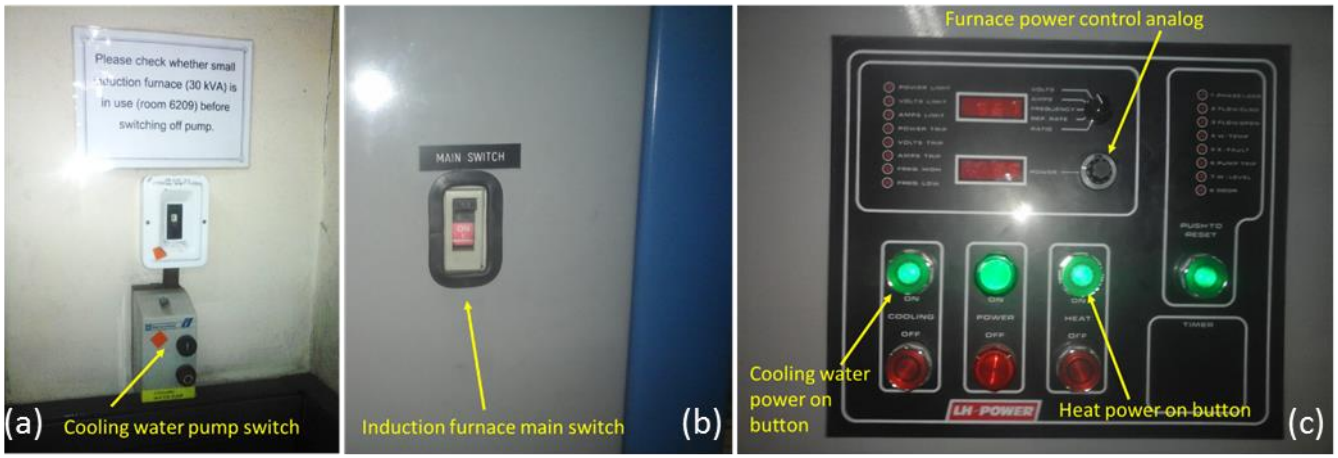

Figure A20: Power supply switches

Step 19

- Open Argon gas main valve, see Figure A21 (a)
- Set argon supply flow rate to the flow meter valve at 20 l/min, see Figure A21 (a)
- Set argon gas flow meter at scale level 10, which is equivalent to Argon gas flow of 5.8 Nl/min see Figure A21(b)

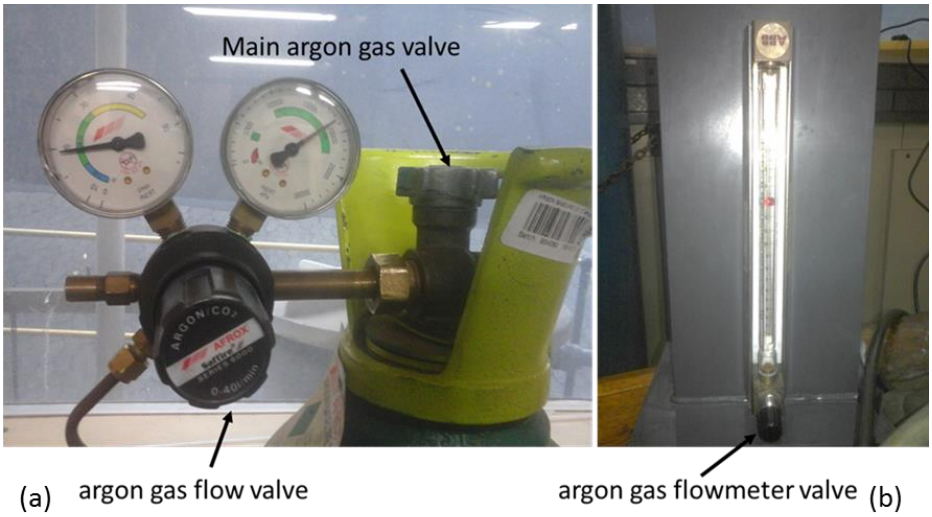

Figure A21: Argon gas regulator (a) and a Fischer & Porter Model 10A6132M/B10 - 1/4" NPTF gas flow meter (b)

Step 20

- Run experiment, see Figure A22.
- On completion reduce furnace power down to zero kW (using power analog).
- Switch the ("heat on") furnace controls off, using heat off button, leaving cooling water and argon gas running.

Figure A22: Complete rotating finger experiment (left) and closer view (right)

Challenges and solutions discovered during the trial run

Flames

At temperatures above 1000°C, there was a noticeable flame around the graphite rod inlet hole, and the flame grew bigger as the temperatures approached the set-point. The concern with the flames was that the graphite rod will oxidise and break. The second concern was that the electric motor, holding the graphite rod would result in thermal damage due to the excessive heat from the flames.

Solution(s):

The initial approach was to cover the furnace with more ceramic blankets, and especially focusing on the area below the electric motor, see Figure A23.

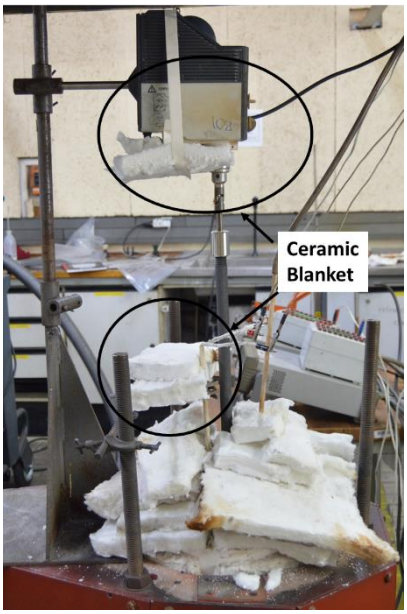

Figure A23: Ceramic blankets under the electric motor

The other solution is to redesign the graphite rod such that, it is wider at the bottom and also 5cm longer than the initial graphite rod, see Figure A24. This will allow the electric motor to be mounted at a higher position and the thicker rod will result in less oxidation.

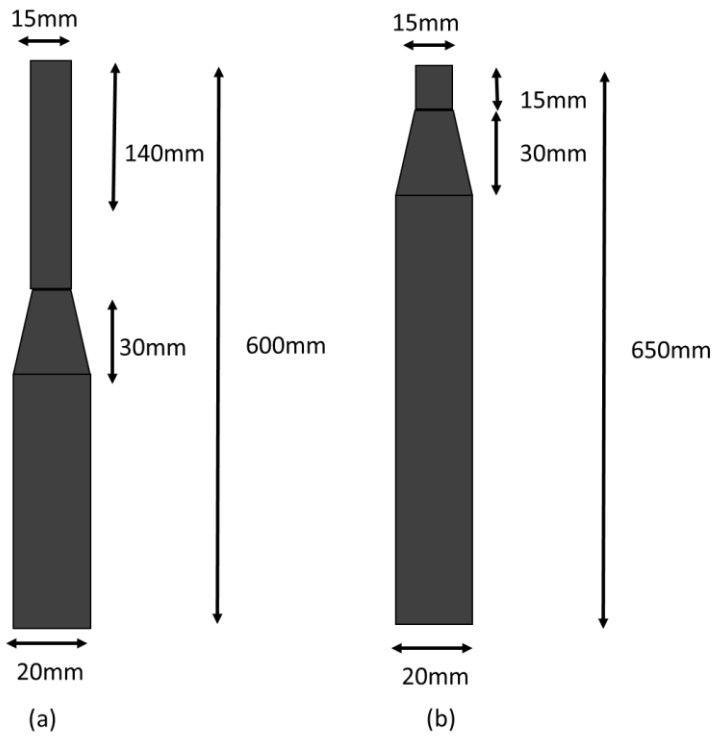

Figure A24: Graphite rod (a) initial and (b) final design

Thermocouple stuck inside the alloy upon cooling

The thermocouple in the first test got stuck inside the alloy as it cooled, the thermocouple most probably slipped inside upon completion of the experiment, see Figure A25.

Solution(s):

Both thermocouples are partially removed and mounted at a higher level from the furnace after the experiment has been completed and this allowed preservation of the thermocouples. For thermocouple safety reasons, the length of the thermocouple alumina tube going inside the furnace as seen in Figure A14, was changed from 105 mm to 95 mm.

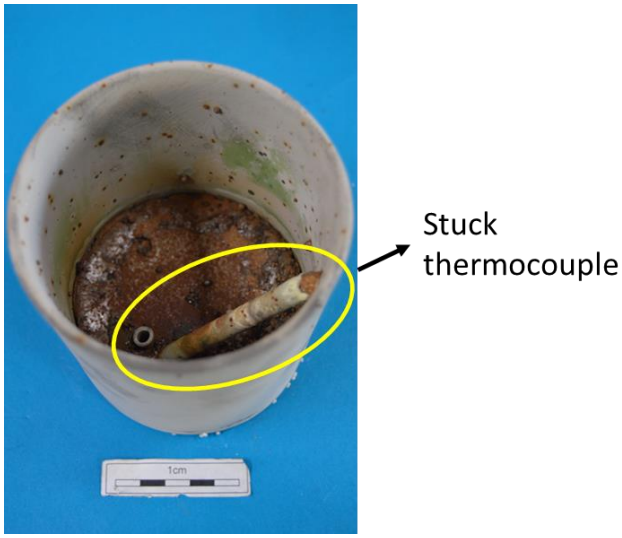

Figure A25: Thermocouple stuck inside crucible

Thermocouple not reading on the data logger

Occasionally, one or more thermocouples were not reading on the data logger. One of the reasons for a failing thermocouple was when the two thermocouple wire strands were touching or when the thermocouple wire burnt out.

Solution(s):

The burnt-out thermocouple was easily solved by removing the thermocouple wire and re-joining the junction and reinserting the thermocouple wire slowly to avoid thermal shock. The two wire strands were insulated using high-temperature tape to keep them apart (prevent them from touching) as well as protect them from the flames around the graphite rod inlet hole.

Inconsistent alloy mass addition

Since the intention of the trial run was to see if the experiment will actually work, not everything was fixed, for example, the alloy additions were guided by the level of alloy on the bottom (25 mm) as seen in Figure A12. After the alloy was added inside the alumina crucible, the refractory cylinder was placed inside the alumina crucible and lowered such that the cylinder sits on top of the alloy. Then more alloy was added around the refractory cylinder to cover the refractory cylinder and alumina crucible gap by adding alloy sample to cover 70% of the refractory height (i.e.35 mm/55 mm). As a result the mass of alloy added was inconsistent. Table A.1 contains the mass of the alloy used in the trial test runs.

Table A.1: Mass of alloy used in each test during the trial run.

	Test 1	Test 2	Test 3	Test 4	Test 5	Test 6
Mass before (g)	1316.2	1293.1	1233.4	1255.0	1282.4	1243.0
Mass After (g)	251.2	244.9	181.4	172.2	190.2	189.6
Mass added (g)	1065.0	1048.2	1052.0	1082.8	1092.2	1053.4
Average (g)	**1065.6**					
Std dev (g)	**18.1**					

Solution(s):

From Table A.1 the values of alloy were not far off from each other, when using height as an alloy addition guideline, with an average of 1066 grams alloy added. In order to have a constant volume of molten alloy in the experiment, the alloy mass will be fixed to 1100 grams. This will also allow the volume of the molten alloy to be constant in each test.

Electric motor start-up

Once at the set point, the electric motor needs to be started up gradually to avoid the breakage of the refractory cylinder from the graphite rod.

Solution(s):

The electric motor needs to be set at speed 1, which is equivalent to 40 rpm. Once turned on, it needs to start rotating and the speed increased at every minute, up to speed 4, which is equivalent to 100 rpm. Similarly, when switching off, the speed must be reduced every minute, till back at speed 1, then the motor can be switched off.

Calibration of the electric motor was also done prior to the method development using an Ono Sokki digital tachometer HT-4200. The calibration results can be seen in Figure A26, where the relative error between the electric motor reading and the tachometer readings was an

average of 9%. The rpm readings decreased due to the weight of the graphite rod and refractory cylinder, hence the same rpm was achieved and at a higher value of the electric motor speed knob. The Tachometer readings were still in agreement with the electric motor speed

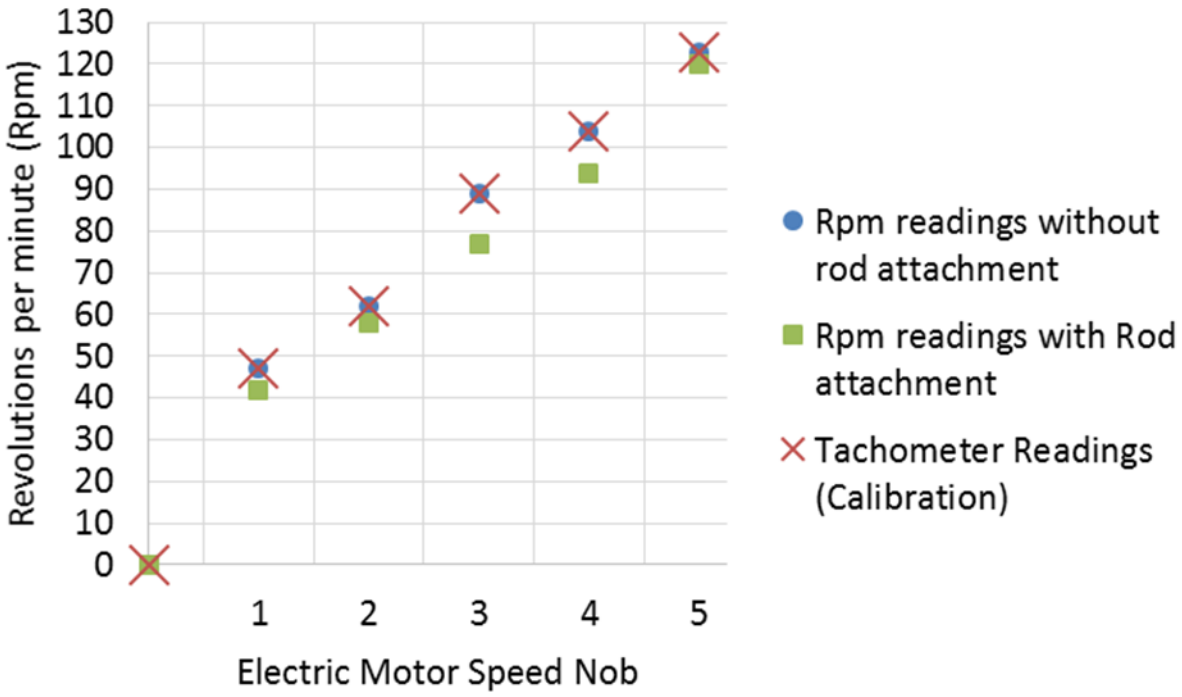

Figure A26: Electric motor calibration curve

Oxidation of the graphite crucible lid

The increase in the set point temperature increased the graphite crucible lid oxidation on the surface exposed to the atmosphere.

Solution(s):

The oxidation of the graphite lid affects the external equipment only, as it generates a flame that might cause thermal damage to the electric motor. The solution to this will be increasing the coverage of alumina bubbles around the graphite crucible lid, and placing the ceramic blanket, so as to reduce the extent of oxidation taking place on the surface of the lid. In Figure A27 (b), it can be seen that the oxidations doesn't affect the inside of the crucible, thus verifying that the atmosphere inside the crucible is inert.

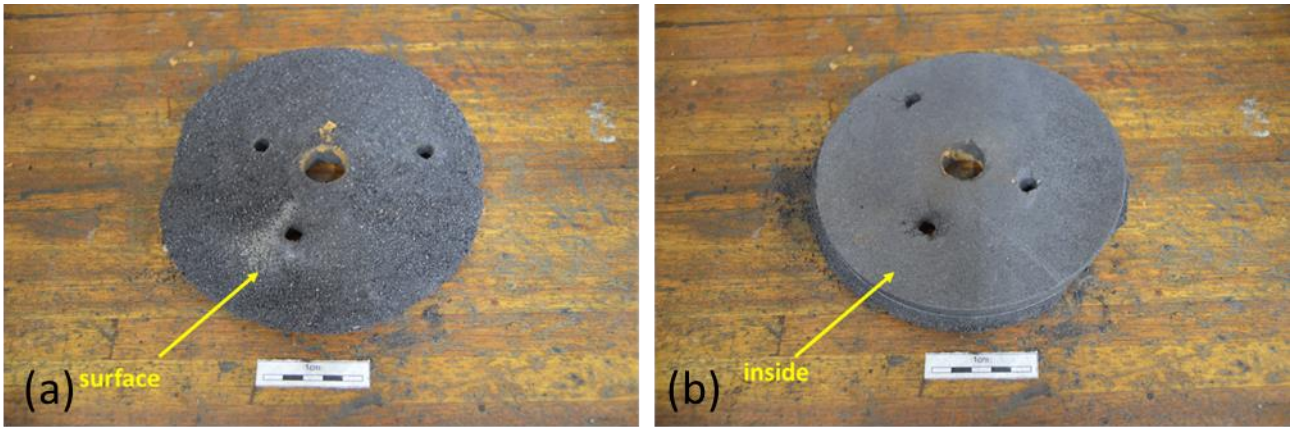

Figure A27: oxidised outside surface (a) and unoxidised inside surface of the graphite lid surface (b)

APPENDIX B: POST MORTEM SAMPLE PREPARATION

Samples were first dried in an oven overnight at 105°C in order to remove any moisture that the samples could have picked up during shipping from South Africa to Norway, see Figure B1. The samples were removed from the oven and allowed to cool off before resuming with the sample preparations.

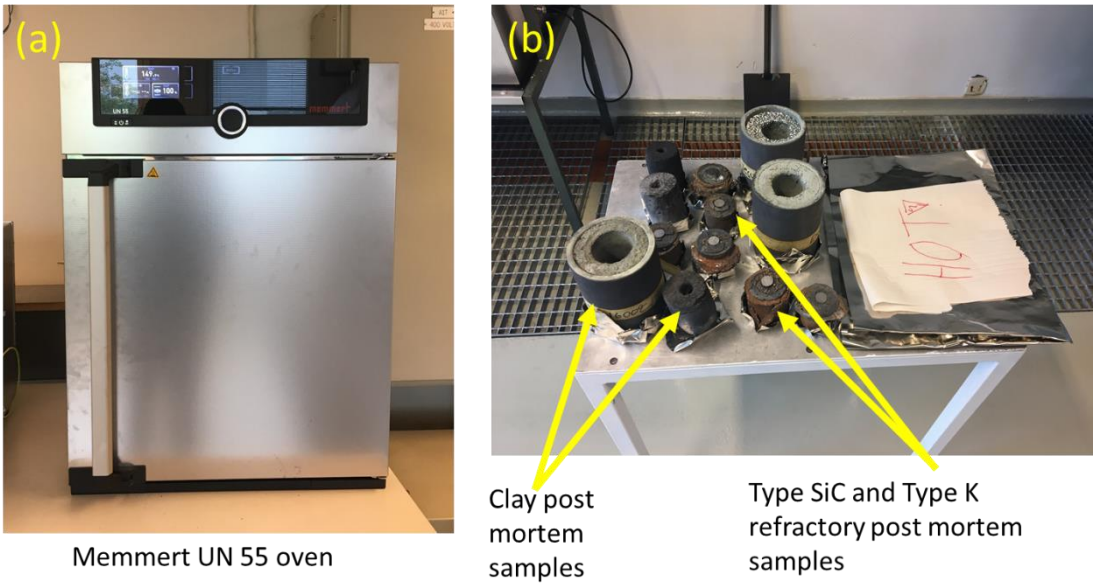

Figure B1: (a) Oven (b) Refractory post mortem samples

The next step after the type SiC and type K refractory samples cooled off, was to hold them in resin in order to avoid them crumbling when cutting the samples into a smaller workable size, Figure B2. This was achieved by first preparing the Epofix epoxy resin and hardener in a 25:3 ratio.

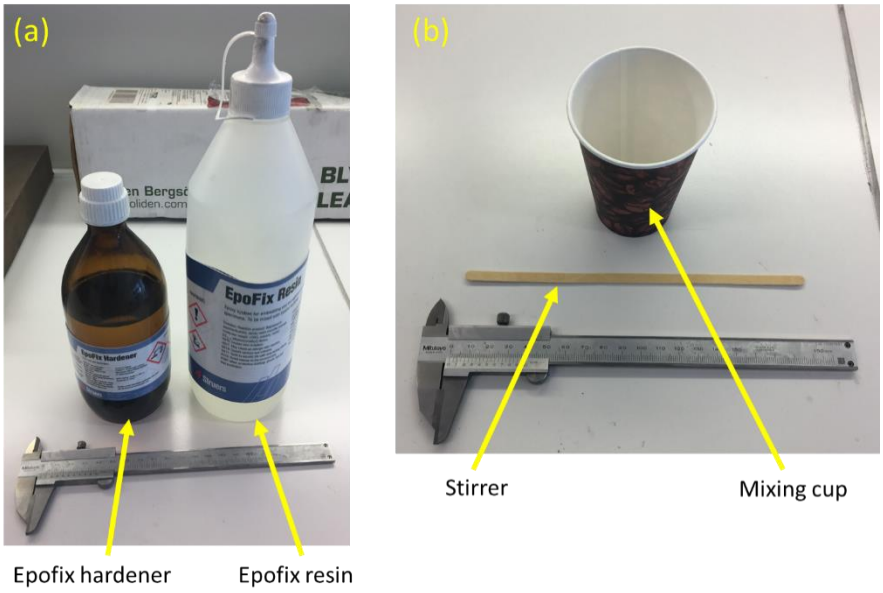

Figure B2: Material used to prepare the resin and hardener mixture

Batches of 143 g Epofix epoxy resin (125g) and hardener (18g) were then poured into containers containing the refractory samples under vacuum using a Stuers CitoVac machine. Figure B3 shows the procedure used to prepare the final samples, where the irregular shaped refractory cylinders, Figure B3(a), were cut in half using an electric saw machine with a SiC blade, Figure B3(b) and the samples were even cut further and put into resin so allow parts that were not well infiltrated by the epoxy resin, Figure B3(c) to be fully covered. The final samples, Figure B3(g), were then taken for grinding and polishing.

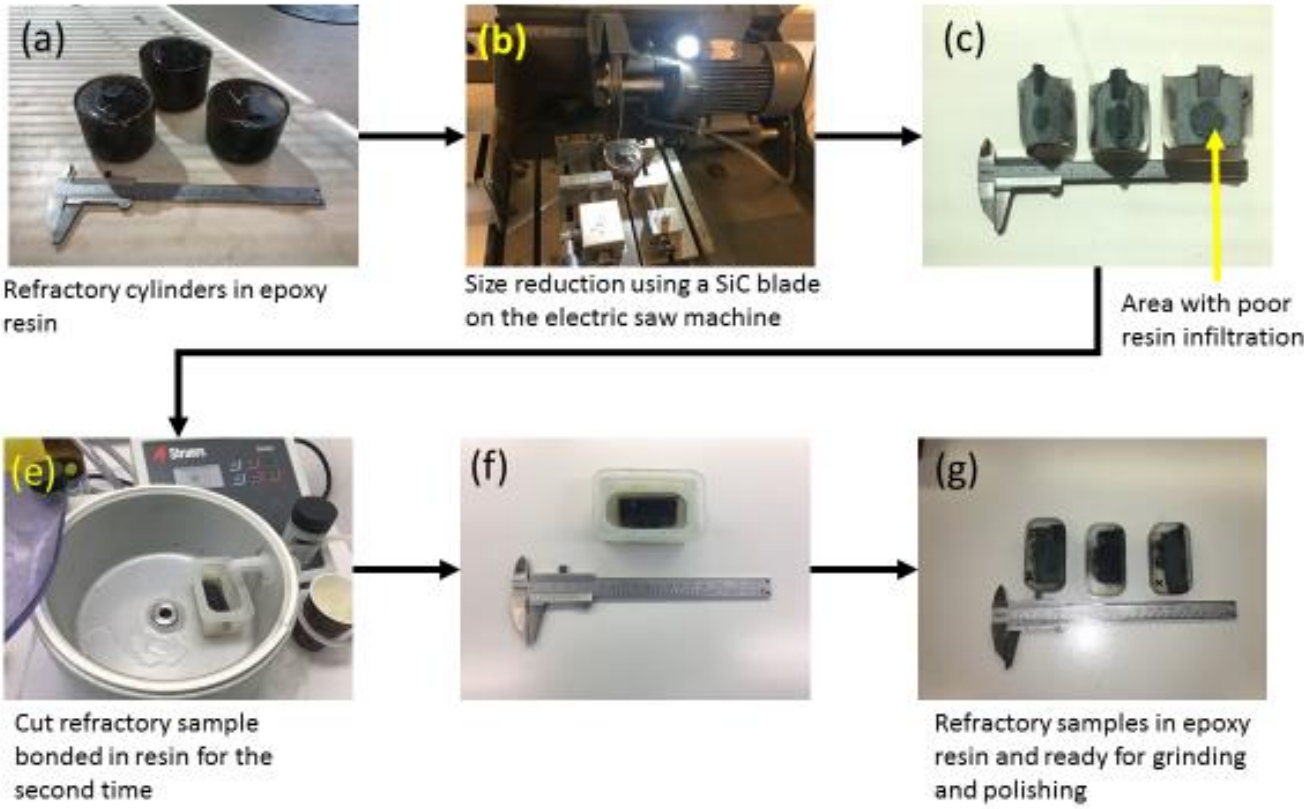

Figure B3: SEM-EDS sample preparation procedure before grinding and polishing

Epoxy resin embedded samples, Figure B3(g), were then ground in a Struers RotaForce 4 machine in order to expose the surface of the refractory material. The 80 grit diamond place was first used for 30 minutes, with the rotation at 150 rpm and water as the lubricant. The next steps in which a 220, 600, 1200 and 2400 grit diamond plates were used, were all done in 3 minutes each with the rotation at 150 rpm and water as the lubricant, Figure B4.

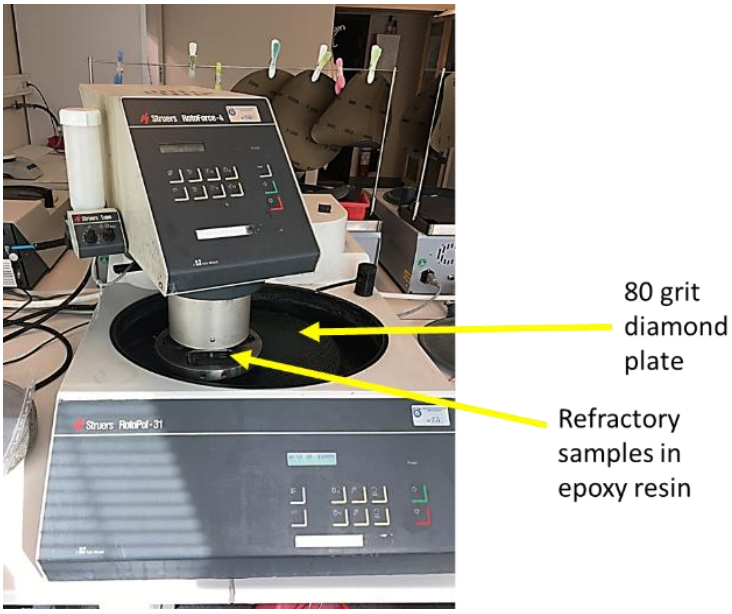

Figure B4: Stuers RotaForce4 sample grinding machine

APPENDIX C: MECHANICAL TESTING RESULTS

Appendix C contains the results obtained from the mechanical testing which was conducted after the equipment design and method development. The main observation was that the refractory wear was due to erosion and corrosion.

Test 1 and 2- Temperature at 1550° C

Figure C1 shows the refractory wear profile for both the K-type and SiC type refractories at 1550° C. The wear thickness was calculated by measuring the difference in diameter of the original and reacted refractory cylinder. In Figure C1 it can be observed that at 1550° C SiC-type refractory had more wear than the K-type refractory, and this is evident by the SiC-type curve reaching a higher wear thickness of 9.3 mm compared to a lower wear thickness of 4.8 mm in the K-type refractory. The wear thickness measurements will be repeated in the optimised test work to allow a higher degree of confidence in the results. Wear observations are in agreement with FactSage™ at 1550° C where the SiC-type refractory wore out more than the K-type (Banda, Steenkamp and Matinde, 2016). It is also interesting to note that SiC-type had some type of expansion in the top layers of the cylinder, the curve was in the build-up zone where the diameter of the refractory cylinder increased. It is suspected that this could have been due to material infiltrating the refractory pores and further investigations on the cause of the expansion will be done.

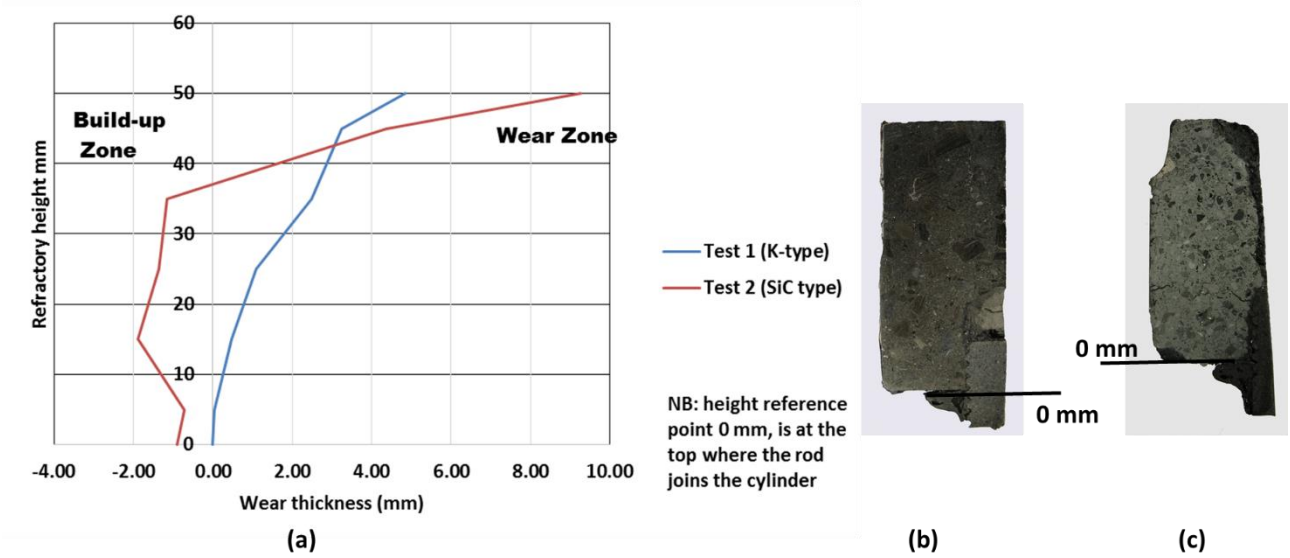

Figure C1: Wear profile (a), Test 1(b) and Test 2 (c) at temperature of 1550° C

Figure C2 and Figure C3 are the SEM-EDS analyses of the K-type and SiC-type refractory respectively. SiC-type was more severely infiltrated by SiMn alloy than K-type, as is evident by greater areas that are in white, i.e. the SiMn alloy phase.

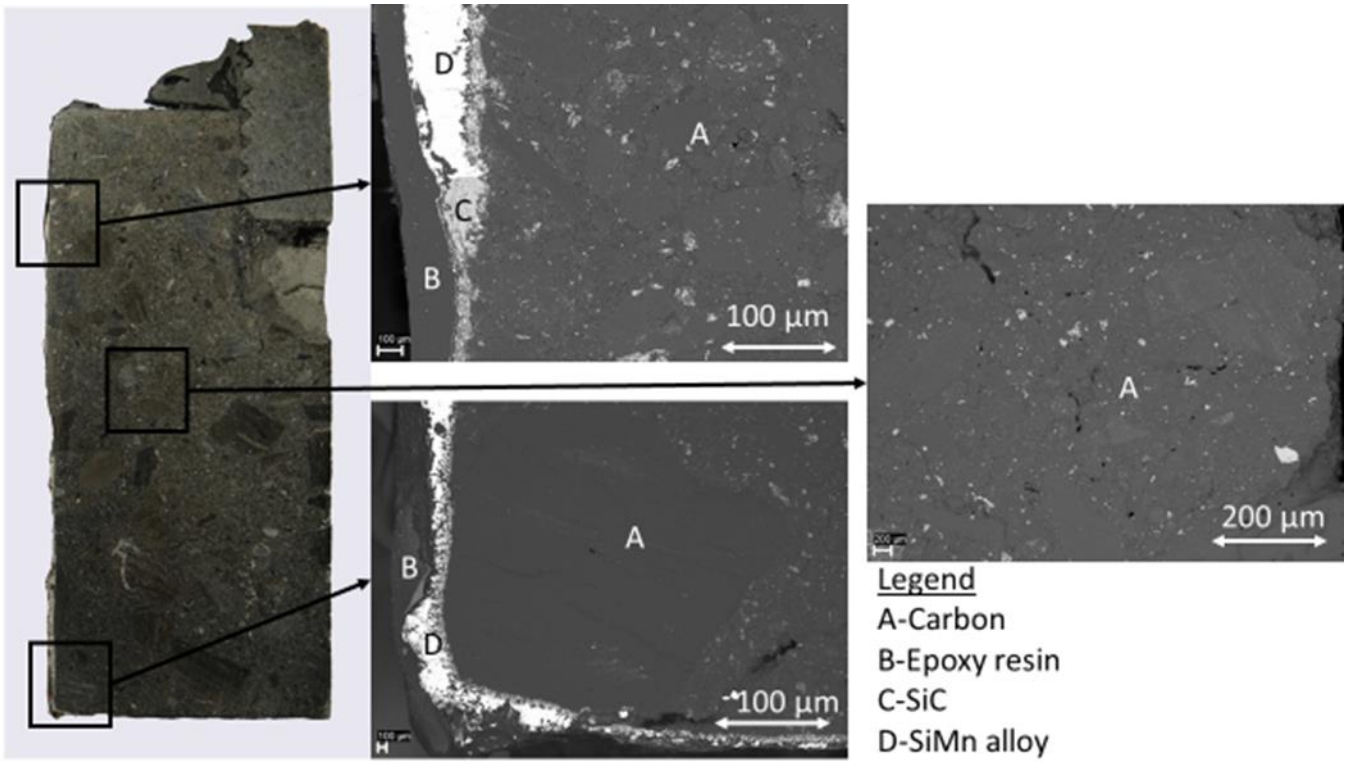

Figure C2: Test 1 (K-type) refractory cylinder, polished cross section and SEM-EDS images

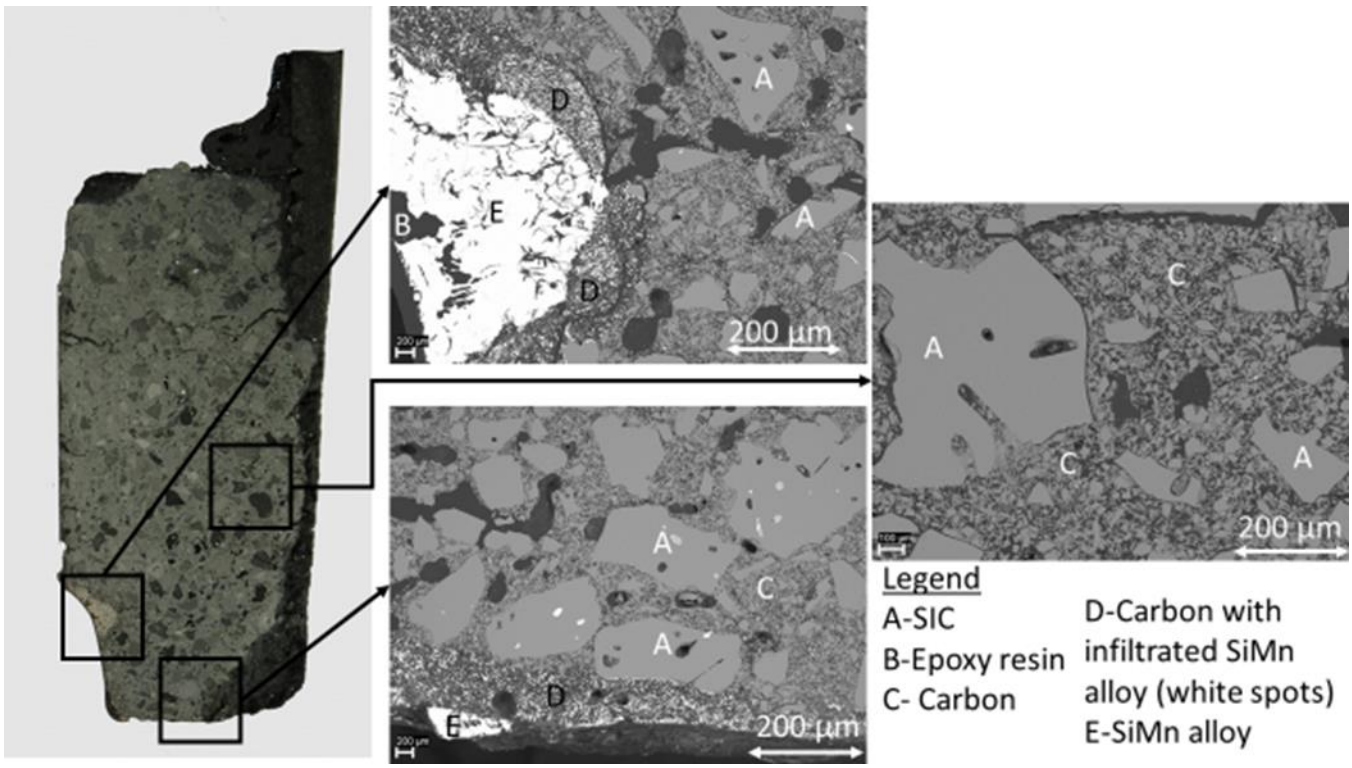

Figure C3: Test 2 (SiC-type) refractory cylinder, polished cross section and SEM-EDS images

Test 3 and 4- Temperature at 1600°C

Figure C4 shows the erosion wear profile for both the K-type and SiC type refractories at 1600° C. The wear thickness was also calculated by measuring the difference in diameter of the original and reacted refractory cylinder. In Figure C4 it can be observed that at 1600° C SiC-type refractory had worn more than the K-type refractory (as was the case for experiments conducted at 1550°C). This is evident by the SiC-type curve reaching a higher wear thickness of 13.7 mm compared to a lower wear thickness of 9.4 mm in the K-type refractory. Wear observations are in agreement with FactSage™ at 1600° C where the SiC-type refractory wore out more than the K-type. Neither SiC-type nor K-type showed signs of physical expansion as both the curve were in the wear zone, compared to SiC-type refractory at 1550° C.

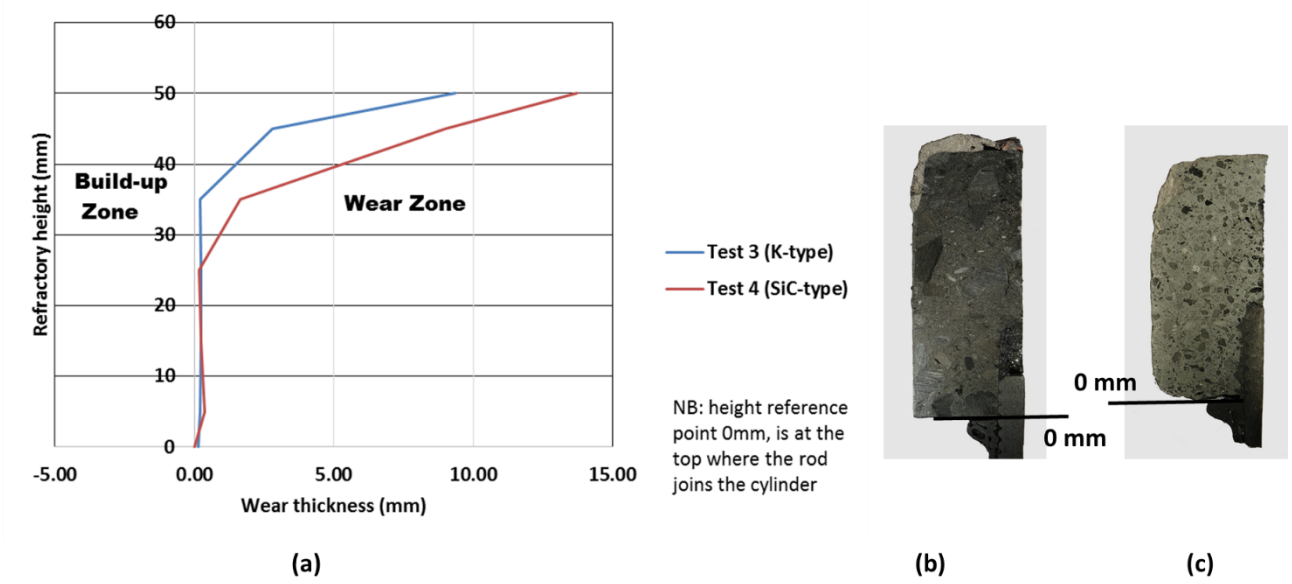

Figure C4: Wear profile (a), Test 3 (b) and Test 4 (c) at temperature of 1600° C

Figure C5 and Figure C6 are the SEM-EDS images of the two refractory cylinders. As was the case in Test 1 and 2, the SiMn alloy did not infiltrate the K-type refractory to the same extent as the SiC-type refractory. The temperature increase by 50° C, resulted in an increase in fluidity of the alloy, hence it also contributed to greater SiMn alloy infiltrations in the K-type and SiC-type refractory. The carbon binder phase in the SiC-type alloy also resulted in more infiltration, which was evident by more SiC precipitation and got mechanically worn out. Again it is observed that the alloy seems to remain attached to the surface of K-type refractory cylinder

and acts to replace the refractory material that has worn out, whilst in the SiC-type refractory, the alloy seems to attach to the refractory by filling in the pores of the cylinder.

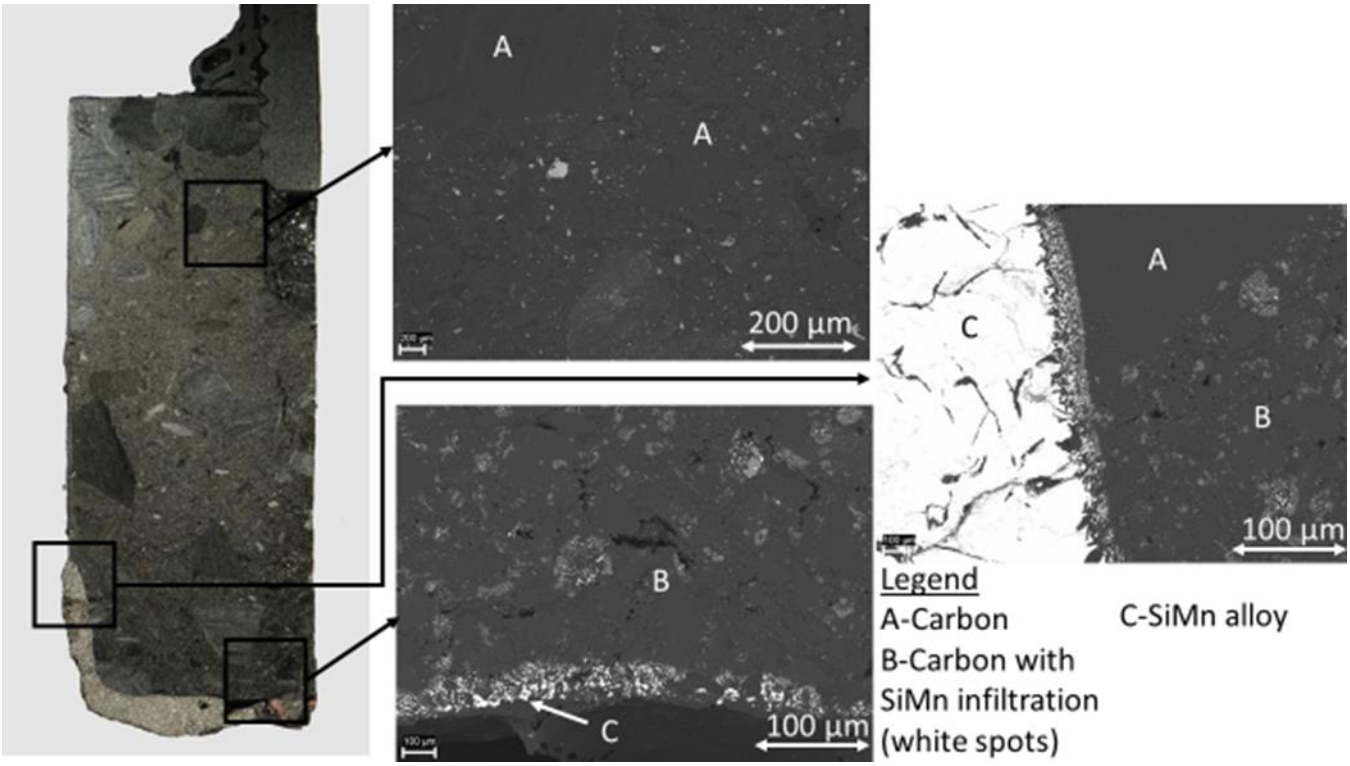

Figure C5: Test 3 refractory cylinder (K-type), polished cross section and SEM-EDS images

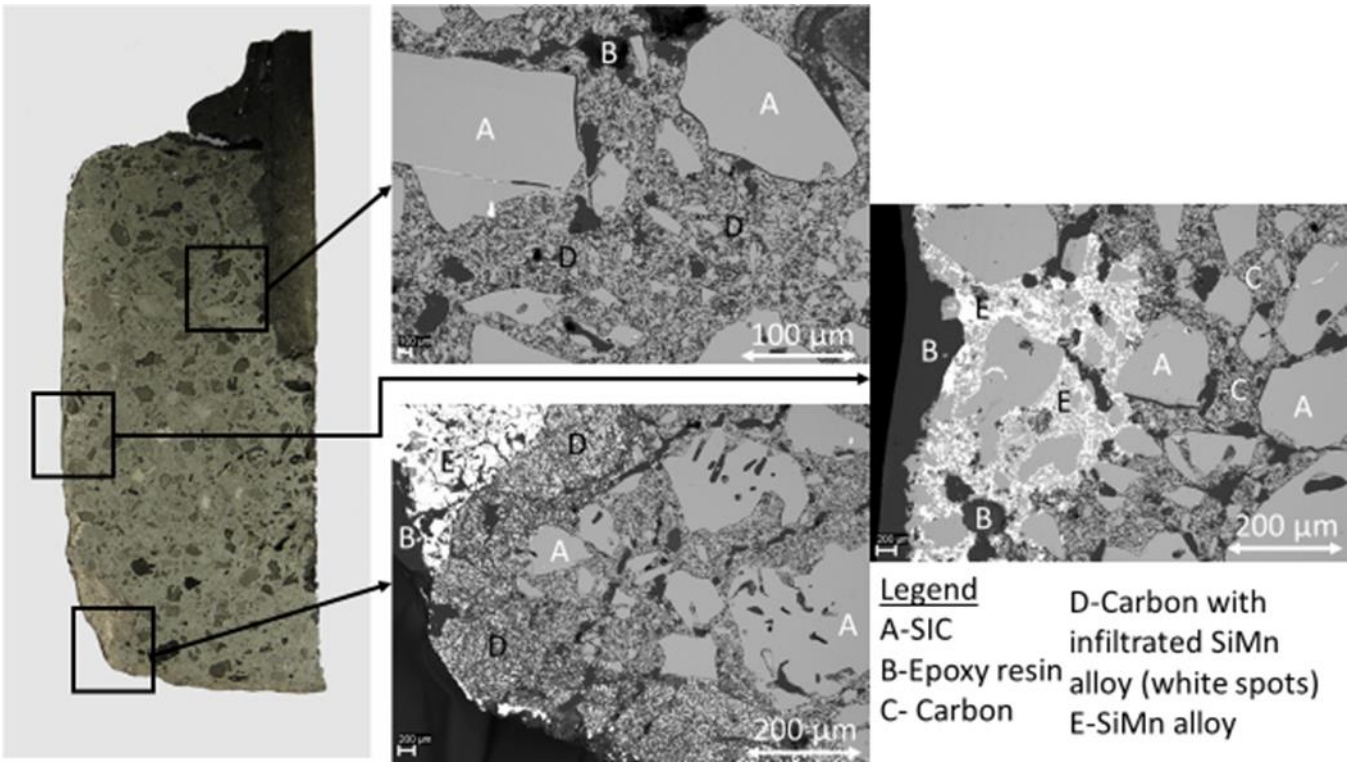

Figure C6: Test 4 refractory cylinder (SiC), polished cross section and SEM-EDS images

Test 5 and 6- Temperature at 1650°C

Figure C7 shows the erosion wear profile for both the K-type and SiC type refractories at 1650° C. The wear thickness was also calculated by measuring the difference in diameter of the original and reacted refractory cylinder. In Figure C7 it can be observed that at 1650° C SiC-type refractory also had more wear than the K-type refractory, and this is also evident by the SiC-type curve reaching a higher wear thickness of 20.3 mm compared to a lower wear thickness of 7.6 mm in the K-type refractory. Wear observations are in agreement with FactSage™ at 1650° C where the SiC-type refractory wore out more than the K-type. SiC type and K-type in both tests 5 and 6 respectively also did not have evident physical expansion as both the curve were in the wear zone, compared to SiC-type refractory at 1550° C.

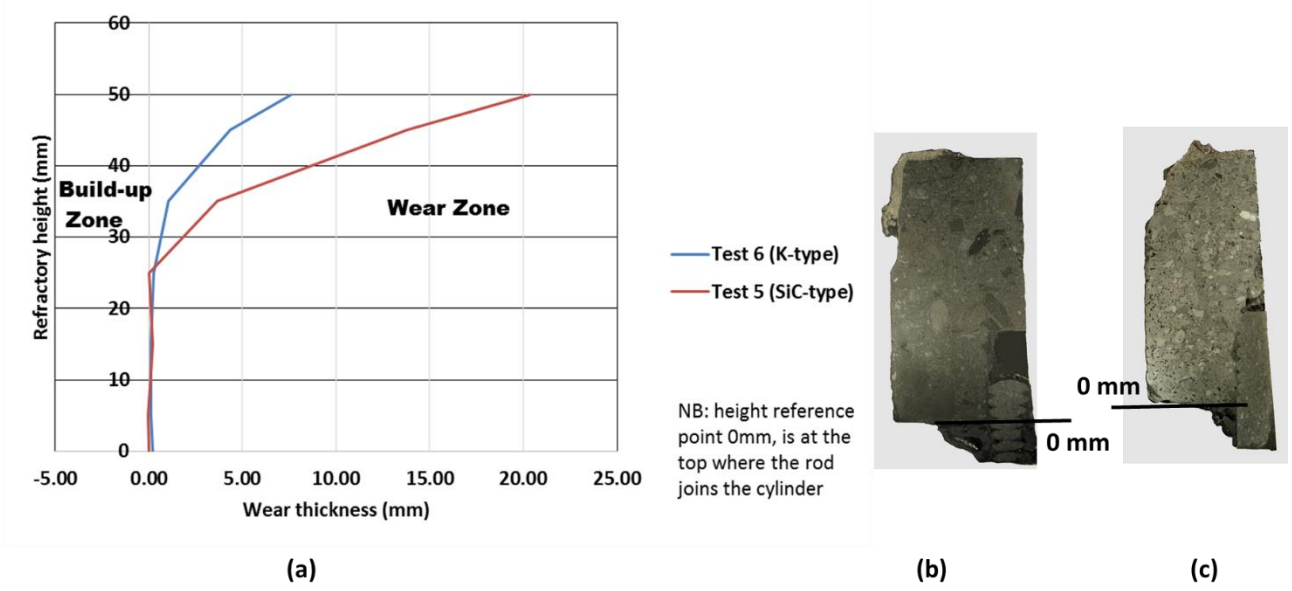

Figure C7: Wear profile (a), Test 5(b) and Test 6 (c) at temperature of 1650° C

Figure C8 and Figure C9 are the SEM-EDS images of the two refractory cylinders. Similarly to Test 1, 2, 3 and 4, the K-type refractory cylinder did not result in major SiMn alloy infiltrations compared to the SiC-type refractory. The increase in alloy fluidity due to the temperature increase by a further 50° C, also contributed to greater SiMn alloy infiltrations in the K-type and SiC-type refractory. The carbon binder phase is the SiC-type alloy also resulted in more infiltration, which can be also assumed that more SiC precipitation occurred and got mechanically worn out. In comparison to the SiC-type refractory from the previous tests at 1500° C and 1600° C, there was more infiltration of the alloy at 1650° C, to about 15 mm from the surface and 25 mm from the base. Again it is observed is that the alloy seems to remain

attached to the surface of K-type refractory cylinder and acts to replace the refractory material that has worn out, whilst in the SiC-type refractory, the alloy seems to attach to the refractory by filling in the pores of the cylinder.

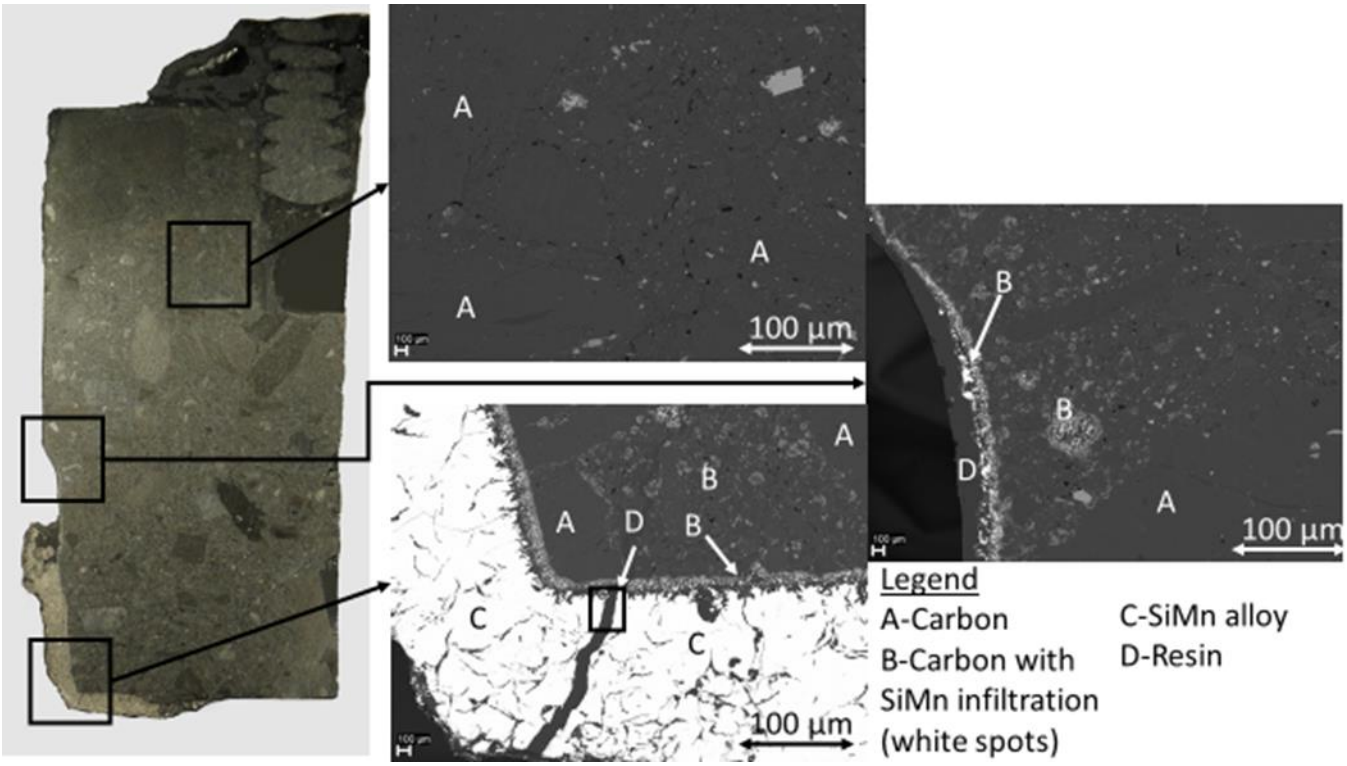

Figure C8: Test 5 refractory cylinder (K-type), polished cross section and SEM-EDS images

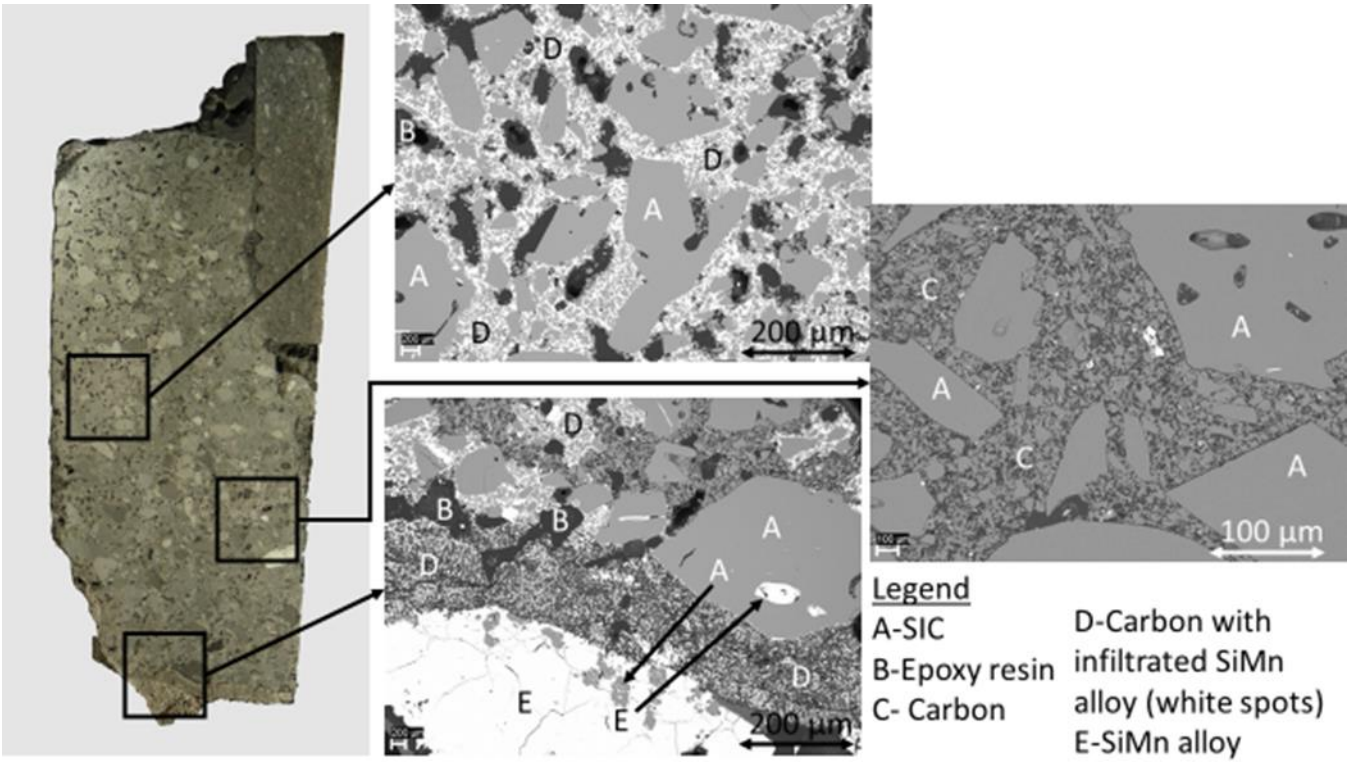

Figure C9: Test 6 refractory cylinder (SiC), polished cross section and SEM-EDS images

Summary

The experimental trial runs were successful in developing the rotating finger experimental set-up and creating a standard procedure to build the rig. The challenges that were encountered allowed solutions to be found and implemented to allow an optimised experimental set-up. Further investigation in the root cause of refractory expansion will be done.

Thermodynamic calculations conducted in FactSage™ 6.4 indicated that SiC would form as a product when SiC and the K-type is in contact with the SiMn alloy, with the SiC refractory wearing out the most (Banda, Steenkamp and Matinde, 2016). The SiC-type got worn out more since it had a higher porosity and as the Si in the alloy was reacting with the carbon binder, forming SiC which dissolved away through erosion wear, hence increasing the rate of wear of SiC refractory than the K-type refractory. K-type has a lower porosity than SiC-type (Banda, Steenkamp and Matinde, 2016), and this would explain why the SiMn alloy infiltration was lower, and ultimately less material was washed away during the refractory rotations.

At 50 mm diameter, i.e. at the base of the SiC-type refractory, the thickness got worn out from 9.3 mm at 1550° C to 20.3 mm at 1650° C. At 55 mm diameter, i.e. at the base of the K-type refractory, the thickness got worn out from 4.8 mm at 1550° C to 7.6 mm at 1650° C. The porous nature of the SiC-type refractory, inability to form a surface alloy layer, and increased alloy fluidity played a role in wearing the SiC-type refractory more than the K-type refractory.

From the experimental results, the first indications are as expected when compared to the FactSage™ calculations, and these findings will be confirmed through optimised experimental work.

APPENDIX D: POST MORTEM ALLOY ANALYSIS RESULTS

Appendix D contains the alloy analytical results used to calculate and plot the carbon uptake into the alloy with temperature. The equation D1 was used to calculate the difference in each species between the as-received alloy species and the post-mortem alloy species.

$$\Delta Composition = speciesA(SiMn\ \ post-mortem) - speciesA(SiMn2) \qquad \text{(D1)}$$

Table A.2: As-received SiMn2 alloy normalized composition (in mass %).

	SiMn2			
	Fe	Mn	Si	C
average	15.5	67.8	14.5	2.2
Std Dev	0.2	0.3	0.1	0

Table A.3: Type K-SiMn alloy post-mortem analysis (in mass %) at 1550°C (dynamic test).

Type K 1550°C				
	Fe	Mn	Si	C
Average	15.6	66.1	16.6	2.6
Normalized	15.4	65.5	16.4	2.6
Std Dev	0.2	0.2	0.1	0.0
Δcomposition	-0.1	-2.3	1.9	0.4

Table A.4: Type SiC-SiMn alloy post-mortem analysis (in mass %) at 1550°C (dynamic test).

	Fe	Mn	Si	C
Average	15.3	65.7	17.9	2.3
Normalized	15.1	64.9	17.7	2.3
Std Dev	0.3	0.3	0.1	0.0
Δcomposition	-0.4	-2.9	3.2	0.1

Table A.5: Type K-SiMn alloy post mortem analysis (in mass %) at 1600°C (dynamic test).

	Fe	Mn	Si	C
Average	15.4	65.8	16.5	2.7
Normalized	15.3	65.5	16.5	2.7
Std Dev	0.4	0.4	0.1	0.0
Δcomposition	-0.2	-2.3	2.0	0.5

Table A.6: Type SiC-SiMn alloy post-mortem analysis (in mass %) at 1600°C (dynamic test).

	Fe	Mn	Si	C
Average	15.7	56.4	16.7	2.4
Normalized	17.2	61.8	18.3	2.6
Std Dev	0.5	0.6	1.2	0.0
Δcomposition	0.2	-11.2	2.3	0.2

Table A.7: Type K-SiMn alloy post-mortem analysis (in mass %) at 1650°C (dynamic test).

	Fe	Mn	Si	C
Average	15.2	65.7	16.9	2.8
Normalized	15.1	65.3	16.8	2.8
Std Dev	0.3	0.6	0.1	0.0
Δcomposition	-0.4	-2.5	2.3	0.6

Table A.8: Type SiC-SiMn alloy post-mortem analysis (in mass %) at 1650°C (dynamic test).

	Fe	Mn	Si	C
Average	16.0	56.7	17.6	2.4
Normalized	17.2	61.2	19.0	2.6
Std Dev	0.2	0.4	0.2	0.0
Δcomposition	0.5	-10.9	3.1	0.3

Table A.9: Type K-SiMn alloy post-mortem analysis (in mass %) at 1550°C (static test).

	Fe	Mn	Si	C
Average	14.4	66.7	17.6	2.4
Normalized	14.3	66.0	17.4	2.3
Std Dev	0.2	0.2	0.2	0.0
Δcomposition	-1.2	-1.6	2.9	0.2

Table A.10: Type SiC-SiMn alloy post-mortem analysis (in mass %) at 1550°C (static test).

	Fe	Mn	Si	C
Average	14.1	65.7	17.9	2.3
Std Dev	0.2	0.1	0.2	0.0
Δcomposition	-1.4	-2.1	3.4	0.1

Table A.11: As-received SiMn composition (in mass %) used for 15% Si composition tests.

SiMn (15%)				
	Fe	Mn	Si	C
average	15.5	67.8	14.5	2.2
Std Dev	0.2	0.3	0.1	0.0

Table A.12: Type SiC (Si-15 mass %) post-mortem SiMn alloy.

Type SiC (15%) Post-mortem				
	Fe	Mn	Si	C
Average	15.7	56.4	16.7	2.4
Normalized	17.2	61.8	18.3	2.6
Std Dev	0.5	0.6	1.2	0.0
Δcomposition	1.7	-6.0	3.8	0.4

Table A.13: Type K (Si-15 mass %) post-mortem SiMn alloy.

Type K (15%) Post-mortem				
	Fe	Mn	Si	C
Average	15.4	65.8	16.5	2.7
Normalized	15.3	65.5	16.5	2.7
Std Dev	0.4	0.4	0.1	0.0
Δcomposition	-0.1	-2.0	2.0	0.5

Table A.14: Synthetic SiMn composition (in mass %) used for 17% Si composition tests.

SiMn (17%)				
	Fe	Mn	Si	C
Average	15.7	67.1	17.1	2.1
Normalized	15.4	65.7	16.8	2.1
Std Dev	0.1	0.4	0.2	0.0

Table A.15: Type SiC (Si-17 mass %) post-mortem SiMn alloy.

Type SiC (17%) Post-mortem				
	Fe	Mn	Si	C
Average	15.6	58.9	18.3	2.2
Normalized	16.4	62.0	19.2	2.3
Std Dev	0.1	0.4	0.2	0.0
Δcomposition	0.7	-5.1	2.1	0.2

Table A.16: Type K (Si-17 mass %) post-mortem SiMn alloy.

Type K (17%) Post-mortem				
	Fe	Mn	Si	C
Average	15.4	59.5	18.3	2.6
Normalized	16.1	62.1	19.1	2.7
Std Dev	0.2	0.3	0.8	0.0
Δcomposition	0.4	-5.0	2.0	0.5

Table A.17: Synthetic SiMn composition (in mass %) used for 18% Si composition tests.

SiMn (18%)				
	Fe	Mn	Si	C
Average	15.4	66.9	17.7	2.1
Normalized	15.1	65.5	17.4	2.1
Std Dev	0.4	0.2	0.5	0.0

Table A.18: Type SiC (Si-18 mass %) post-mortem SiMn alloy.

Type SiC (18%) Post-mortem				
	Fe	Mn	Si	C
Average	15.4	58.8	18.5	2.1
Normalized	16.2	62.0	19.5	2.3
Std Dev	0.0	0.4	0.1	0.0
Δcomposition	0.8	-5.0	1.8	0.1

Table A.19: Type K (Si-18 mass %) post-mortem SiMn alloy.

Type K (18%) Post-mortem				
	Fe	Mn	Si	C
Average	15.4	59.9	17.9	2.2
Normalized	16.1	62.8	18.7	2.4
Std Dev	0.1	0.0	0.1	0.0
Δcomposition	0.7	-4.1	1.0	0.2

APPENDIX E: MECHANICAL WEAR MEASUREMENT CALIBRATION

Appendix E contains the mechanical wear calibration conducted with a vernier caliper. The specification of refractory samples from the manufacturer indicated that the cylinders were 55 mm height and 50 mm diameter. The refractory samples were measured 3 times and the error of the calculation was quantified. Equation E1 was used to calculate the average, equation E2 was used to calculate the standard deviation and equation E3 was used to calculate the percentage error in the measurement method.

$$\bar{x} = \frac{x_1+x_2+\cdots+x_n}{n} \quad \text{(E1)}$$

$$s = \sqrt{\frac{\sum(x-\bar{x})^2}{n-1}} \quad \text{(E2)}$$

$$Percentage\ error = \left|\frac{V_m-V_e}{V_e}\right| \times 100\% \quad \text{(E3)}$$

Table E1: Type K mechanical wear calibration. Values in mm.

K-type					
Height	**1**	**2**	**3**	**Average**	**% error**
0	49.7	49.62	49.48	49.60	0.8
5	49.65	49.71	49.55	49.64	0.7
15	49.68	49.83	49.51	49.67	0.7
25	49.75	49.73	49.54	49.67	0.7
35	49.73	49.7	49.55	49.66	0.7
45	49.61	49.65	49.57	49.61	0.8
50	49.54	49.72	49.6	49.62	0.8
Average				**49.64**	**0.72**
Standard Deviation				**0.03**	**0.06**

Table E2 : Type K mechanical wear calibration. Values in mm.

SIC-type					
Height	**1**	**2**	**3**	**Average**	**% error**
0	50.53	51.06	50.91	50.83	1.67
5	51.37	51.57	51.18	51.37	2.75
15	51.21	52.39	51.45	51.68	3.37
25	50.93	51.64	50.94	51.17	2.34
35	50.65	50.72	50.53	50.63	1.27
45	50.22	50.2	50.14	50.19	0.37

50	50	50.1	50.04	50.05	0.09
Average				**50.85**	**1.69**
Standard Deviation				**0.61**	**1.21**

APPENDIX F: REFRACTORY MASS LOSS CALCULATIONS

Appendix F contains the refractory mass loss calculations and procedure.

Step 1: Autodesk Fusion 360 free 3D CAD/CAM design software was used to draw the refractory 3D models using the refractory wear profile dimensions. The volume of the cylinders were then recorded from the software results.

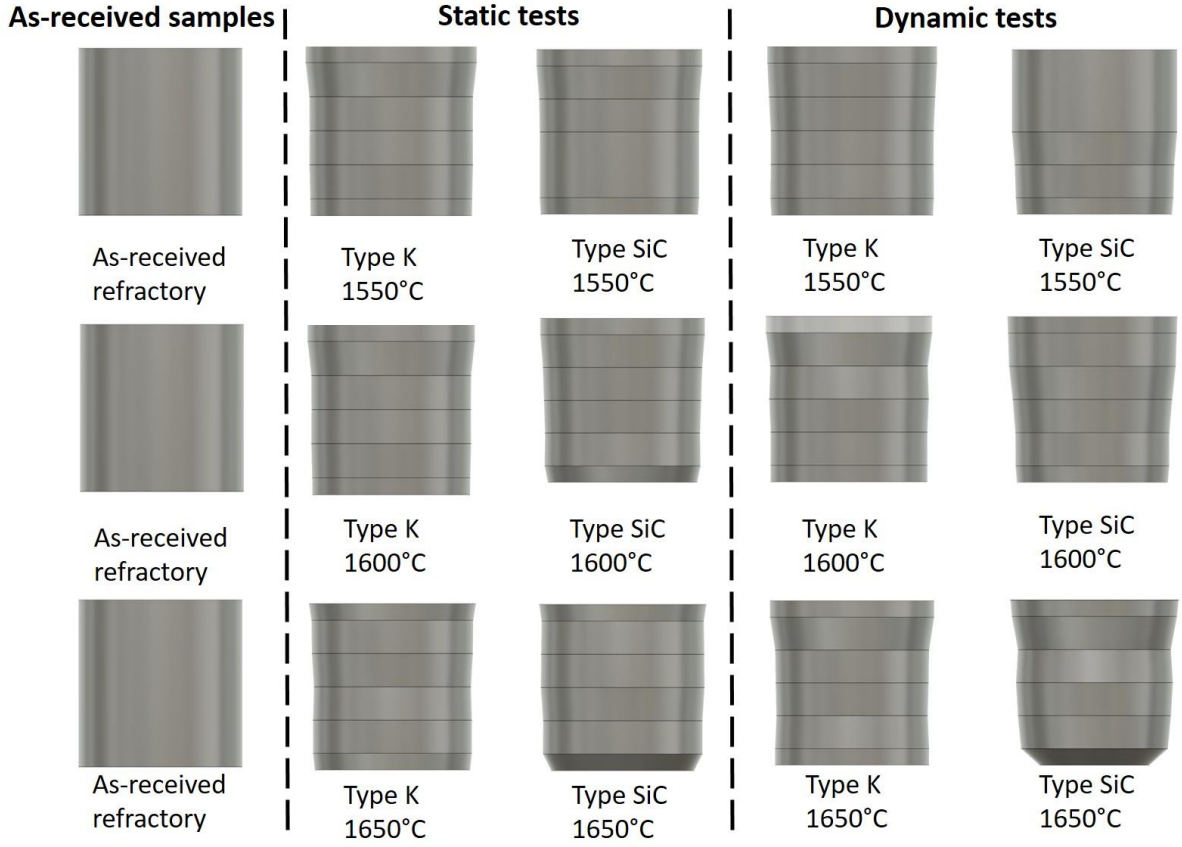

Figure F1: 3D refractory wear representation of the actual experimental refractory wear under static and dynamic conditions as temperature was varied with Si mass % fixed.

Step 2: Volume loss (ΔV) was then calculated using equation F1. Mass loss (Δm) was then calculated using equation F2.

$$\Delta V = V_{Initial} - V_{final} \quad \text{(F1)}$$

$$\Delta m = \Delta V \times \rho_{refractory} \quad \text{(F2)}$$

Where:

ΔV= Volume loss

Δm= Mass loss

ρ_refractory = density of the refractory

$V_{Initial} - V_{final}$ = Initial and final volume respectively

Table F1: volume and mass loss calculations

	Volume (mm^3)	ΔVolume (loss) mm^3	Mass loss type K (g)	Mass loss type SiC (g)
Density (g/mm^3)			0.00148	0.00232
Original	98170		145.29	228.15
Test1	90790	7380	10.92	
Test2	90950	7220	10.69	
Test3	89710	8460	12.52	
Test4	92460	5710		13.27
Test5	90730	7440		17.29
Test6	91150	7020		16.31
Test7	92840	5330	7.89	
Test8	90110	8060	11.93	
Test9	87850	10320	15.27	
Test10	94920	3250		7.55
Test11	91150	7020		16.31
Test12	84960	13210		30.70

Step 3: FactSage™ Mass loss (Δm) was then calculated using equation F4.

$$\Delta m = m_{Initial} - m_{final} \quad \text{(F4)}$$

Where:

Δm= Mass loss

$m_{Initial} - m_{final}$ = Initial and final mass respectively

Table F2: FactSage™ mass loss calculations

Temperature (°C)	Type K (g)	Type K adjusted (g)	Mass loss type K (g)	Type SiC (g)	Type SiC adjusted(g)	mass loss type SiC (g)
25	100	145.29	0.00	100	228.1	0.00
1550	99.5	144.57	0.73	97.7	222.9	5.25
1600	99.3	144.27	1.02	97	221.3	6.84
1650	99	143.84	1.45	96.2	219.5	8.67